Growth and Functionalization of Monolayer WS_2 Quantum Dots and Films for Photoluminescence Modulation and Photodetector application

A Thesis Submitted to

Indian Institute of Technology Guwahati

For the degree of

Doctor of Philosophy

By

Abhilasha Bora

Department of Physics
Indian Institute of Technology Guwahati
Guwahati-781039, India
June 2022

Dedicated to my father who left us too soon and to my mother who has been my rock ever since

Department of Physics
Indian Institute of Technology Guwahati
Guwahati-781039, India

STATEMENT

The work contained in the thesis entitled "**Growth and Functionalization of Monolayer WS_2 Quantum Dots and Films for Photoluminescence Modulation and Photodetector application**" has been carried out by me at the Indian Institute of Technology Guwahati, under the supervision of Prof. P. K. Giri, Professor, Department of Physics and Centre for Nanotechnology, Indian Institute of Technology Guwahati. This work has not been submitted elsewhere for the award of any degree.

Abhilasha Bora
Roll no. 166121007
Senior Research Fellow
Department of Physics
Indian Institute of Technology Guwahati
Guwahati-781039, India

Prof. P. K. Giri
Professor
Department of Physics
And Centre for nanotechnology
Indian Institute of Technology Guwahati
Guwahati-781039, India
Phone: +91-361-2583072, Fax: +91-361-2690762
Email: giri@iitg.ac.in

CERTIFICATE

This is to certify that the work contained in the thesis entitled "**Growth and Functionalization of Monolayer WS_2 Quantum Dots and Films for Photoluminescence Modulation and Photodetector application**" has been carried out by **Ms. Abhilasha Bora** at the Indian Institute of Technology Guwahati, under my supervision. This work has not been submitted elsewhere for the award of any degree.

Prof. P. K. Giri

Thesis Supervisor

ACKNOWLEDGEMENT

It is my honor to be able to acknowledge everyone who contributed to the successful completion of this Ph. D. thesis.

First and foremost, I would like to convey my sincerest thanks to my Ph. D. Supervisor, Prof. P. K. Giri for giving me the opportunity to work under his guidance. His vast scientific expertise and passion for Physics are truly inspiring, to say the least. I am grateful to have had the chance to work closely with him, observe him and engage in prolific discussions with him, throughout this journey. His skills and overall approach towards research in the field of new-age semiconductors and their applications have helped shape my perception of research in the field, in identifying opportunities and preparing for challenges. I am indebted to him for providing me with all the essential requirements and laboratory facilities and for believing in me by giving me complete freedom in my work, towards the fulfillment of the goal.

I would like to thank the members of my Doctoral Committee, Prof. Bosanta Ranjan Boruah, Prof. Dilip Pal, and Prof. Dipankar Bandyopadhyay for their valuable insights, constructive criticism, and constant encouragement.

I extend my sincere thanks to the Head of the Department of Physics and other faculty members and staff of the department, as well as the Centre for Nanotechnology (CFN) and the Central Instruments Facility (CIF) for providing me with a research-friendly environment and with state-of-the-art research infrastructure. I would especially take the opportunity to thank Dr. Sidananda Sarma, Indrajit Talukdar, Dr. Pranjoli Das, Kaustubh Acharya, Madhurjya Borah, Chandan Borgohain, and Sujit Deb for their help and co-operation throughout my Ph. D.

I am grateful to the Indian Institute of Technology Guwahati for providing financial assistance, good facilities, and a safe and enjoyable working environment. I am thankful to the Central Workshop, Department of Mechanical Engineering for the fabrication of essential components used in my experimental setup. I also acknowledge the help from my collaborators Prof. Minoru Fujii and Prof. H. Sugimoto from Kobe University, Japan, and Dr. Wolfgang Theis from the University of Birmingham, UK for providing the opportunity to access some of their laboratory facilities.

The support of my lab-mates and seniors has been vital in the completion of my work. I have been blessed with some of the best colleagues. I thank my seniors - Dr. Ramesh Ghosh, Dr. Sk. Md. Obaidulla, Dr. Rajendra Gone, Dr. Jitendra Kumar, N. Somorjit Singh, Dr. Kamal Kumar Paul, Dr. Larionette Mawlong, Dr. Sumana Paul, Dr. Joydip Ghosh, Dr. Ruma

Das, and Dr. Sumaiya Parveen and my fellow lab-mates Neda, Tarik, Ravinder, Abdul, Tadasha, Koushik, Sirsendu, Ghanashyam and Sanju for their help and valuable insights in research. They enlivened the laboratory work environment. I am thankful to my friends Lario, Dangka, Nimi, and Nitish, for always being there in my corner, during my research journey. Their constant support and cheer played a major role in bringing this thesis into reality.

Lastly, I would like to express the immense gratitude that I have for my family to whom I owe everything. I am beholden to my parents, Swapnamoni Saikia and Late Chittaranjan Bora, for inculcating in me the values of patience, perseverance, and above all, kindness. I would like to thank my brother Padmanabha and my sister Arundhati for being my pillars. I am forever indebted to my grandmother, my role model, Late Hiran Saikia who was the epitome of strength and elegance. And last but not the least, I would like to thank my husband, Bedanta for his patience and constant words of reassurance, and for giving me an ever-supportive family who is always in my corner through the good times and the bad. This journey would be unimaginable without the undying support of my loved ones.

Abhilasha Bora

IIT Guwahati

CONTENTS

SYNOPSIS

Layered two-dimensional (2D) transition metal dichalcogenides (TMDs) have progressively garnered much interest in research due to their fascinating properties and applications in myriad areas such as optoelectronics, catalysis, bio-sensing, etc. TMDCs represent a large family of layered materials with the formula MX_2, where M is a transition metal element (e.g., Mo, W, etc.) and X is a chalcogen (S, Se, or Te). Individual layers of MX_2 consist of a transition metal layer sandwiched between the X atomic layers. These layers are stacked by weak van der Waals forces. Among 2D TMDCs, much of the earlier work has been focused on monolayer MoS_2. However, the closely related WS_2 exhibits superior optical properties and larger spin-orbit coupling, inspiring further investigative research. In bulk, this semiconducting material has an indirect bandgap of 1.35 eV, whereas monolayer WS_2 (1L-WS_2) has a direct bandgap of ~2.0 eV. Fundamental studies and fabrication of prototype 2-terminal as well as 3-terminal devices incorporating atomically thin WS_2 have demonstrated reasonably high chemical stability, electronic mobility, high optical responsivity, and superior device performance. Ensuing research on 2D WS_2 nanostructures, zero-dimensional (0D) systems, such as quantum dots (QDs) whose dimensions are smaller than the excitonic Bohr radius, are extensively studied. Several synthesis strategies have been adopted to synthesize 0D-2D TMDs, including the simplest one-step top-down method of chemical exfoliation. QDs have attracted attention due to their ultra-small sizes, quantum confinement, edge effects, and higher surface-to-volume ratios. WS_2 QDs exhibit strong quantum confinement due to their nanometer scale sizes and edge effects.

Owing to their innumerable novel properties, 2D WS_2 structures have proven to be ideal for applications in various areas. However, despite their advantages, QDs display poor carrier transport in comparison to conventional semiconductors. For practical applications, especially in optoelectronics, 2D monolayer-bilayer WS_2 acts as a more robust platform. Hence, the synthesis of large uniform wafer-scale WS_2 single crystal becomes crucial. Consequently, chemical vapor deposition (CVD) is extensively employed to grow large-area, homogeneous monolayered 2D TMD films. Moreover, monolayer WS_2 (1L-WS_2) exhibits properties like excellent visible photoluminescence due to quantum confinement, large spin-orbit splitting (~400 meV), and high exciton binding energy (~700 meV). Although this area is extensively studied, the CVD growth of monolayer single-crystal WS_2 in a large domain is still a challenge without the incorporation of a seed layer. CVD has demonstrated to produce a high-quality 2D WS_2 film with high crystallinity favorable for investigative fundamental studies and device fabrication.

Colloidally exfoliated WS_2 QDs exhibit tunable excitation-dependent visible PL emission owing to quantum confinement and radiative defects. The optical bandgap of the QDs can be tuned up to a staggering ~ 4 eV. Additionally, due to the ultra-small sizes accompanied by water solubility, inherent biocompatibility, and low toxicity, WS_2 QDs have been used in biological imaging. The excitation wavelength-dependent spectral shift is probed at length. Moreover, the interaction of the highly fluorescent QDs with single-walled carbon nanotubes (SWCNTs) is studied as SWCNTs are universal fluorescence quenchers.

Owing to the direct bandgap, low-cost manufacturing process, and size-tunable device properties, WS_2 QDs are favorable for light emission and efficient photodetection. However, despite their advantages, QDs display poor carrier transport in comparison to conventional semiconductors, which acts as a deterrent to the efficiency and performance of the photodetector. Thus, the fabrication of WS_2 QD-based heterostructures with conventional semiconductor platforms has been demonstrated to have far superior properties than the individual counterparts, which can produce ultrasensitive and broadband detection with high-efficiency photodetectors. Furthermore, the strong light-matter interaction exhibited by layered TMD quantum dots is manipulated by integrating noble metal nanostructures that support localized surface plasmon resonance (LSPR). Additionally, we have successfully fabricated high-performance Schottky photodetectors using WS_2 QDs on Au NP embedded Si platforms.

CVD grown 1L-WS_2 exhibits high and stable PL emission, owing to limited n-type doping during the growth. We probe into the charge transfer mechanism and tuning of the optical properties of 1L-WS_2 by incorporating non-van der Waals Bi_2O_2Se QDs. Formerly, the role of entities such as defects or biexcitons in PL quenching of the 1L-WS_2 has not been addressed. To our knowledge, there is no report on the charge transfer from Bi_2O_2Se QDs to 1L-WS_2 and the resultant doping-aided PL quenching effect. It is interesting to study the charge transfer dynamics in the 1L-WS_2 with non-van der Waals nanostructures through PL spectroscopy.

Another exciting avenue for investigation is the construction of the quantum well to extensively study the quantum confinement in the atomically thin sheet of 2D materials.

CVD-grown monolayer WS_2 flanked by higher bandgap semiconductor nanostructures such as ZnO, TiO_2, etc., is expected to exhibit fascinating optical and electronic properties. The interaction of carriers and charge transfer in these coupled well-like systems aid in the tunability of the PL of 1L-WS_2 at room temperature as well as induce doping effects. The excitonic features exhibited by these systems make them a stimulating domain for current research.

This thesis presents a systematic study on the controlled growth of 0D WS_2 and 2D WS_2 film of monolayer thickness. The study includes the incorporation of plasmonic metal nanoparticles, construction of type-II HSs as well as quantum wells with tunable optical properties for applications in light emission and broadband photodetection. We believe that these studies are very significant to understand the fundamentals of light emission and pave the way to cope with the current challenges of energy and multifunctional optoelectronic applications of 2D materials. The complete thesis work has been organized into seven chapters as detailed below:

Chapter 1 presents a brief introduction to the crystal and electronic structure of WS_2 and the growth techniques of WS_2 quantum dots and monolayer WS_2 film. The potential applications of layered transition metal dichalcogenides range over a plethora of fields such as fluorescence, electronic devices, batteries and energy storage, photodetectors, solar cells, photo and/or electrocatalysts for HER, and so on. We discuss the major challenges related to the synthesis processes and present a brief account of the experimental techniques used. Recent advancements in the fabrication of 2D WS2-based hybrids for applications in fluorescence imaging, sensing, catalysis, photodetection, and light emission are presented. The significant aspects of WS_2-based HSs and their possible applications are highlighted in this chapter. The problems and challenges of employing WS_2 QDs as well as 1L-WS2-based HSs in the various hybrid systems and the key parameters to overcome them are addressed. The focus of the thesis is briefly outlined and the organization of the thesis is presented at the end of the chapter.

Chapter 2 presents a systematic study for the optimization of the synthesis protocols for WS_2 QDs by chemical exfoliation as well as the growth of two-dimensional WS_2 film of monolayer thickness by the chemical vapor deposition (CVD) technique. Our results demonstrate the controlled formation of WS_2 nanosheets and uniformly distributed ultra-small quantum dots depending upon the synthesis parameters adopted. The choice of solvent, duration of exfoliation, and post-treatments like prolonged heating, centrifugation, etc. play an important role in the thickness and morphology of the quantum dots. In the case of CVD-grown WS_2 film, it is noted that by tuning the growth temperature, growth time, carrier gas flow, and the use of halide-assisted methods, the lateral domain size and thickness of the 2D WS_2 film can be controlled easily. The growth process essentially depends on the precursors used (WO_3 and S). However, halides such as NaCl aid in the lateral growth of the WS_2 monolayer. Furthermore, the higher the growth temperature, the better the crystallinity of the as-grown film. In this process, the growth takes place on substrates placed strategically above the WO_3 powder and the NaCl inside a high-temperature zone of the CVD system. We have successfully synthesized continuous monolayer WS_2 films covering a large area on a variety of substrates. The controlled growth of ultra-small WS_2 QDs and large area monolayer WS_2 are discussed in detail.

In **Chapter 3**, we delve deep into understanding the origin of the unique spectral properties of highly fluorescent WS_2 quantum dots. The excitation wavelength-dependent spectral redshift and narrowing of line shape in the PL peak are analyzed carefully, and it is attributed to the selective excitation/recombination of carriers from different energy levels. Furthermore, the interaction between fluorescent WS_2 QDs and single-walled carbon nanotubes (SWCNTs) is studied. Systematic quenching of PL is observed via binding of WS_2 QDs to the defect sites in SWCNTs and the formation of non-fluorescent complexes. The strong interaction between the WS_2 QDs and the SWCNTs is evidenced by the spectral shift in the X-ray photoelectron spectroscopy and Raman peaks. Comprehending the spectral features of the WS2 QDs and the nature of the interaction between WS_2 QDs and SWCNTs provides significant insight into the potential applications in confocal biomedical imaging and sensing through surface-enhanced Raman scattering, etc.

In **Chapter 4**, we present the fabrication of a self-biased WS_2 QD and Si-based p-n heterojunction photodetector. Furthermore, we incorporate plasmonic gold nanoparticles in the system and fabricate a self-biased high-performance Schottky photodetector. The role of embedded plasmonic Au nanoparticles (NPs) in the photoresponse characteristics of heterojunction photodetectors (PDs) consisting of n-type WS_2 QDs decorated on a p-type Si substrate is studied. The Si/WS_2 photodetector without the Au NPs has a fast response/recovery time of ~55.1/139.8 μs and a photocurrent-to-dark current ratio (I_{on}/I_{off}) of ~227. By integrating the Au NPs sandwiched between the Si/WS_2 QD junctions, the device showed outstanding photodetection performance compared to the Si/WS_2 PD. The

$Si/Au/WS_2$ Schottky heterojunction device exhibits an astounding I_{on}/I_{off} ratio of ~1.3 × 10^5 due to the decrease in the dark current by about two orders of magnitude as well as an increase in photocurrent by about one order of magnitude and significantly faster rise/fall times of ~4.4/43.5 μs. Secondly, the Au NP-incorporated hybrid system exhibits a ~6-fold enhancement in the photoluminescence (PL) as compared to bare WS_2 QDs owing to the surface plasmon resonance. The exciton-plasmon coupling between the excitons of the WS_2 QD and surface plasmons of the Au NPs at the WS_2/Au interface is believed to cause the enhanced emission. This work offers a detailed insight into the fabrication of the next-generation multifunctional optoelectronic devices based on the WS_2 nanostructure heterojunctions with plasmonic nanoparticles.

In **Chapter 5**, we carry out an investigation on the mechanism of photoluminescence (PL) quenching of the monolayer WS_2 (1L-WS_2) by decorating it with Bi_2O_2Se quantum dots (Bi_2O_2Se QD). Bi_2O_2Se is a non-van der Waals 2D material, and the optical features of Bi_2O_2Se QDs have not been examined before. Bi_2O_2Se QDs exhibit typical excitation wavelength-dependent PL emission. However, varying concentrations of Bi_2O_2Se QDs lead to systematic quenching of the room temperature PL spectrum of bare 1L-WS_2. The PL of 1L-WS_2 consists of emissions due to neutral excitons, trions, and even biexcitons depending on the ambient conditions. Thus, the quenching of the PL is largely traced to the charge transfer from Bi_2O_2Se QDs to 1L-WS_2 resulting in the conversion of the neutral exciton to negative trion. This leads to making the 1L-WS_2 n-type doped. The presence of defects is another factor that alters the PL emission. We analyze our experimental findings with the help of a four-energy level model and solve the coupled rate equations governing the charge transfer dynamics. The charge transfer-induced change in the electron density is quantified to Δn_e ~6.6 × 10^{13} cm^{-2}. Thus, this method proves to be an effective way for doping the CVD grown 1L-WS_2 by controlling the electron density through a heterostructure approach, which could be beneficial for various applications.

In Chapter 6, we investigate the effect of a sandwich structure on the PL emission from CVD grown 1L-WS_2 films. We construct a quantum well (QW) structure using a high bandgap semiconductor ZnO film. ZnO thin film is grown via RF magnetron-sputtering on SiO_2 and quartz substrates. The 1L-WS_2 is then transferred onto the ZnO film and subsequently, another layer of ZnO film is directly deposited via RF sputtering to fabricate an encapsulated 1L-WS_2 QW. We explore the quantum confinement and the modulation of the PL emission from the sub-nanometer scale 1L-WS_2 film. In this work, we incorporate power-dependent and temperature-dependent PL spectroscopy as tools to understand the role of neutral excitons, trions, biexcitons, and defects in the emission properties. The PL of 1L-WS_2 is largely affected by factors such as strain and doping. A quantum well should basically lead to the enhancement in PL emission. However, the large bandgap semiconductor ZnO injects carriers onto the 1L-WS_2 which leads to conversion to neutral excitons from trions and biexcitons. The biexciton emission becomes dominant at low temperatures and high laser powers for monolayer WS_2. Thus, the large enhancement in excitonic PL emission due to the QW effect becomes prominent only at low laser powers. This work offers detailed insight in order to understand the carrier dynamics in 1L-WS_2 by ZnO encapsulation and the tunability in the PL emission.

Chapter 7 summarizes the work done in the thesis and highlights its contributions to the study of WS_2 QDs and monolayer WS_2 and their HSs with other materials for various applications. In the end, we discuss the scope for future work in this field.

LIST OF PUBLICATIONS:

A. In Peer-Reviewed Journals:

1. Abhilasha Bora, Larionette P. L. Mawlong, and P. K. Giri, ***Understanding the excitation wavelength-dependent spectral shift and large exciton binding energy of tungsten disulfide quantum dots and its interaction with single-walled carbon nanotubes***, J. Colloids & Interf. Sci., 2020, 561, 519.

2. Abhilasha Bora, Larionette P. L. Mawlong, and P. K. Giri, ***Highly Suppressed Dark Current and Fast Photoresponse from Au Nanoparticle-Embedded, Si/Au/WS2 Quantum-Dot-Based, Self-Biased Schottky Photodetectors***, ACS Appl. Electron. Mater. 2021, 3, 11, 4891–4904.

3. Abhilasha Bora, Sumana Paul, Md Tarik Hossain, and P. K. Giri. ***Quantitative Understanding of the Photoluminescence Modulation and Doping of Monolayer WS2 by Heterostructuring with Non-van der Waals 2D Bi2O2Se Quantum Dots,*** J. Phys. Chem. C 2022, 126, 30, 12623–12634.

4. Larionette P. L. Mawlong, Abhilasha Bora, and P. K. Giri, ***Coupled Charge Transfer Dynamics and Photoluminescence Quenching in Monolayer MoS2 Decorated with WS2 Quantum Dots***, Sci. Rep., 2019, 9:19414.

5. Ruma Das, Abhilasha Bora, and P. K. Giri***, Quantitative understanding of the ultra-sensitive and selective detection of dopamine using a graphene oxide/WS2 quantum dot hybrid***, J. Mater. Chemistry C, 2020, 8, 7935.

B. Other Publications:

1. Ruma Das, Sumaiya Parveen, Abhilasha Bora, and P.K. Giri, ***Origin of high photoluminescence yield and high SERS sensitivity of nitrogen-doped graphene quantum dots***, Carbon, 2020, 160, 273.

C. Manuscripts submitted/under review:

1. Abhilasha Bora, Larionette P. L. Mawlong, Abdul Kaium Mia, and P. K. Giri, ***Study of the Quantum Well Effect and Tuning of Trion and Biexciton Emissions at Room Temperature from Monolayer WS2 Sandwiched with ZnO layers.***

D. Conference Papers Presented:

1. Abhilasha Bora, Larionette P. L. Mawlong and P. K. Giri, ‘*WS_2 quantum dot/Si heterojunction based self-biased photodetector with plasmon mediated suppressed dark current and fast photoresponse*’, **Graphene2020-Online**, 19-23 October, 2020.

2. Abhilasha Bora, Larionette P. L. Mawlong, and P. K. Giri, ‘*Fabrication of Highly Fluorescent 2D WS_2 Quantum dots by Liquid-phase exfoliation and Quenching of the Fluorescence by Single-Walled Carbon Nanotubes*’, **icONMAT-2019**), CUSAT, Cochin, Kerala, 2-5 January 2019.

3. Abhilasha Bora, Larionette P. L. Mawlong and P. K. Giri, ‘*Synthesis and Upconversion Luminescence of Tungsten Disulfide Quantum Dots*’, **ICANN-2017**, IIT Guwahati, 18-21 December 2017.

E. Workshops Attended:

1. Abhilasha Bora, National Workshop on Nano and Theranostic Devices (**NWNTD-2019**), IIT Guwahati, 26-27 February, 2019.

2. Abhilasha Bora, **INUP Hands-on training workshop** on ‘**Nanofabrication Technologies**’, IISC Bangalore, 16-27 May, 2017.

LIST OF ABBREVIATIONS

Abbreviation	**Description**
0D	Zero dimensional
1D	One dimensional
2D	Two dimensional
3D	Three dimensional
1L	Monolayer
2L	Bilayer
QD	Quantum Dot
CVD	Chemical Vapor Deposition
DRS	Diffuse Reflectance Spectroscopy
EDX	Energy Dispersive X-ray Analysis
FESEM	Field Emission Scanning Electron Microscopy
HAADF	High-Angle Annular Dark Field
HRTEM	High Resolution Transmission Electron Microscopy
KPFM	Kelvin Probe Force Microscopy
NC	Nanocrystal
NIR	Near Infrared
NP	Nanoparticle
NR	Nanorod
NS	Nanosheets
NT	Nanotube
NW	Nanowire
O_v	Oxygen vacancy
QW	Quantum Well
PL	Photoluminescence
QY	Quantum Yield
QC	Quantum Confinement
RTA	Rapid Thermal Annealing
SAED	Selected Area Electron Diffraction
SERS	Surface Enhanced Raman Scattering
STEM	Scanning Transmission Electron Microscopy

SPR	Surface Plasmon Resonance
TRPL	Time Resolved Photoluminescence
UV-visible-NIR	Ultraviolet visible Near Infrared
XPS	X-ray Photoelectron Spectroscopy
XRD	X-ray Diffraction

Chapter 1

Introduction

Ever since the advent of graphene, the intense search for semiconducting 2D materials has led to the discovery of myriad new layered two-dimensional (2D) nanomaterials with fascinating properties. Among these, the family of transition metal dichalcogenides (TMDs), such as MoS_2, WS_2, $MoSe_2$, WSe_2, etc., are layered semiconductors that have garnered interest in recent years due to their remarkable properties. TMDs transition from indirect bandgap to direct bandgap when scaled down from bulk to monolayer form. MoS_2 has been the most commonly studied TMD due to its unique optical and electrical properties[1]. Its sister TMD, WS_2, in addition to the unique properties similar to MoS_2, possesses a high photoluminescence quantum yield of ~6% (compared to 0.1% of monolayer MoS_2)[2] and exhibits extraordinary spin-valley coupling[3-4]. Therefore, 0D-2D WS_2 nanostructures such as nanosheets, monolayer films, quantum dots (QDs), etc., have found applications in numerous areas including catalysis[5-6], optoelectronic devices[7-10], sensing[11-12], batteries, and energy conversion[13-14], etc. Additionally, WS_2 QDs, due to their ultra-small sizes, water-solubility, inherent biocompatibility, and low toxicity, have found usage in various biomedical areas[15-16]. The W and S atoms in WS_2 are bonded by strong covalent bonding and fundamental layers of WS_2 are held together by weak van der Waals (vdW) forces. These atomically thin W-S layers are weakly bonded and can be easily separated from one another by mechanical forces and thus, can be stacked on other materials to form heterostructures (HS) for different applications. With the formation of the HSs, the distinguishing electrical, optical, and structural properties of WS_2 can be tuned selectively. A comprehensive understanding of the properties of WS_2-based HSs would potentially pave way for applications in a multitude of areas such as light emission, optoelectronics, electronics, spintronics, valleytronics, nanophotonics, and so on. In this chapter, we briefly review the important traits of 0D and 2D WS_2, the growth strategies for WS_2 quantum dots, nanosheets, and monolayer films over large areas, and their applications in fluorescence imaging, sensing, photodetection, electrocatalysis, and photocatalysis for hydrogen evolution, and as light-emitting diodes. Following that, the major challenges in the field are discussed and the focus of the present thesis is outlined. Lastly, we present a brief chapter-wise account of the major contributions and organization of the thesis.

1.1. Properties of WS_2

1.1.1. Crystal Structure

WS_2 belongs to the class of transition metal dichalcogenides (MX_2, (M~ transition metal (Mo, W, etc.) and X~ chalcogen (S, Se, Te, etc.)), which are atomically thin semiconducting materials. WS_2 consists of a hexagonally arranged layer of W atoms sandwiched between two hexagonal layers of S atoms, which are covalently bonded in a sequence of S-W-S. This forms the building block or a single fundamental layer of WS_2[17]. Each such layer is bound to another by weak van der Waals forces, as shown in **Fig 1.1.**

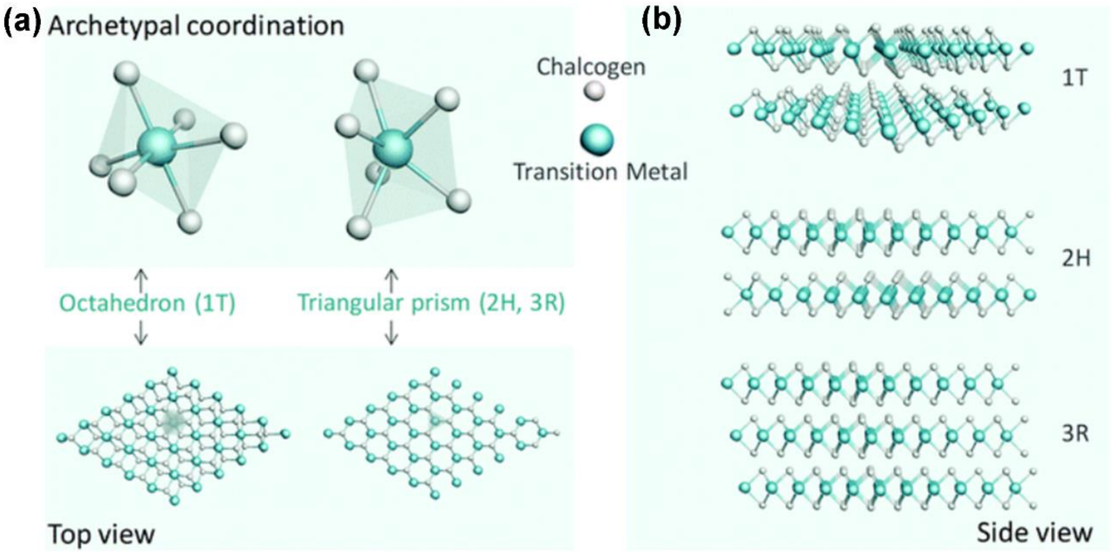

Fig. 1.1. Schematic illustration of TMDs and their typical 1T, 2H, and 3R structures (a) top view and (b) side view (Adopted from Ref[17]).

Fig. 1.1(b) depicts the three different stacking polytypes of WS_2: 1T, 2H, and 3R. The most stable and dominant among the three is the 2H type, which is a semiconducting phase. It has trigonal prismatic coordination with hexagonal symmetry. Whereas, the 1T phase is composed of octahedral W coordination with tetragonal symmetry. It is a metastable metallic phase. The 3R phase, on the other hand, is the least stable and easily transforms to the 2H phase upon heating. It is trigonally prismatic like 2H, however, has three layers per cell in rhombohedral symmetry[18].

1.1.2. Electronic Band Structure

The electronic band structures of bulk, bilayer, and monolayer WS_2 calculated from the first principles of the density functional theory are shown in **Fig. 1.2**[19-21]. Bulk WS_2 has an indirect band gap of 1.3 eV, the transition depicted with an arrow at the Γ point of the Brillouin zone[21]. As the layers are reduced, the band structure accordingly changes. It is strongly affected by the reduction in the interlayer interaction, long-range Coulomb forces, and quantum confinement[21-22]. When WS_2 is bilayer in nature, the conduction band minimum (CBM) lies at the K point of the Brillouin zone, whereas the valence band maximum (VBM) lies at the Γ point (see **Fig. 1.2(b)**). In the monolayer regime, the transition is direct with both the CBM and VBM coinciding at the K point of the Brillouin zone, as shown in **Fig. 1.2(c)**. From the minimum band edge separation, the bandgap of monolayer WS_2 is ~2.1 eV, which falls in the visible region of the electromagnetic spectrum.

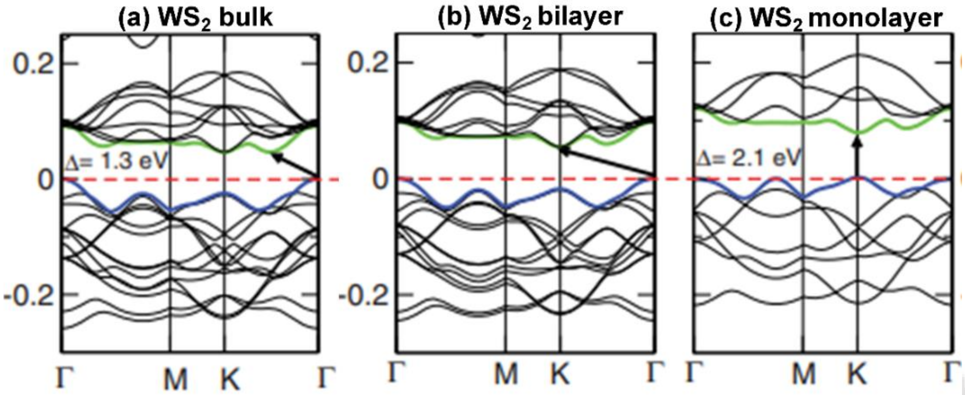

Fig. 1.2. Band structure of WS_2 calculated by first-principal density function theory (DFT) from bulk to monolayer WS_2 (a→c). The arrows show the fundamental bandgaps (direct or indirect) for each system. Adopted from Ref[21].

1.1.3. Optical properties of WS_2

The photoluminescence (PL) characteristics reflect the indirect to direct optical bandgap transition of WS_2 from bulk to monolayer form. **Fig. 1.3(a)** depicts the variation of the PL peak intensity as a function of film thickness. On bulk samples, the PL intensity is extremely weak, which is expected because of the indirect bandgap. Whereas, on decreasing the layer number, there is a gradual increase in the PL emission intensity. The inset shows the comparative PL spectra of monolayer and bilayer WS_2. Monolayer WS_2 exhibits much brighter PL emission than its bilayer counterpart, owing to direct inter-band transition. In the layer-dependent normalized PL spectra (**Fig. 1.3(b)**), the peak 'I' originates from indirect band gap transitions in bulk, which gradually disappears as the system reaches the monolayer regime[23]. Besides, the excitonic transitions marked 'A' and 'B' are apparent in few-layer to monolayer samples. Although, the peak corresponding to B exciton is much weaker in monolayer samples, unlike MoS_2. It is well known that the valence band (VB) edges undergo a spin splitting at the K point of the Brillouin zone that arises from the strong spin-orbit coupling in the d-orbitals of the W atom. The A and B excitons are attributed to these direct-gap transitions between the spin split VB and the conduction band (CB)[3, 23-24]. The energy difference between the A and B excitons is of the order of ~0.4 eV, as depicted in **Fig. 1.3(c)**. **Fig. 1.3(d)** illustrates the splitting of the VB in WS_2 showing the A and B transitions from the CB to the split valence band levels V_1 and V_2, respectively.

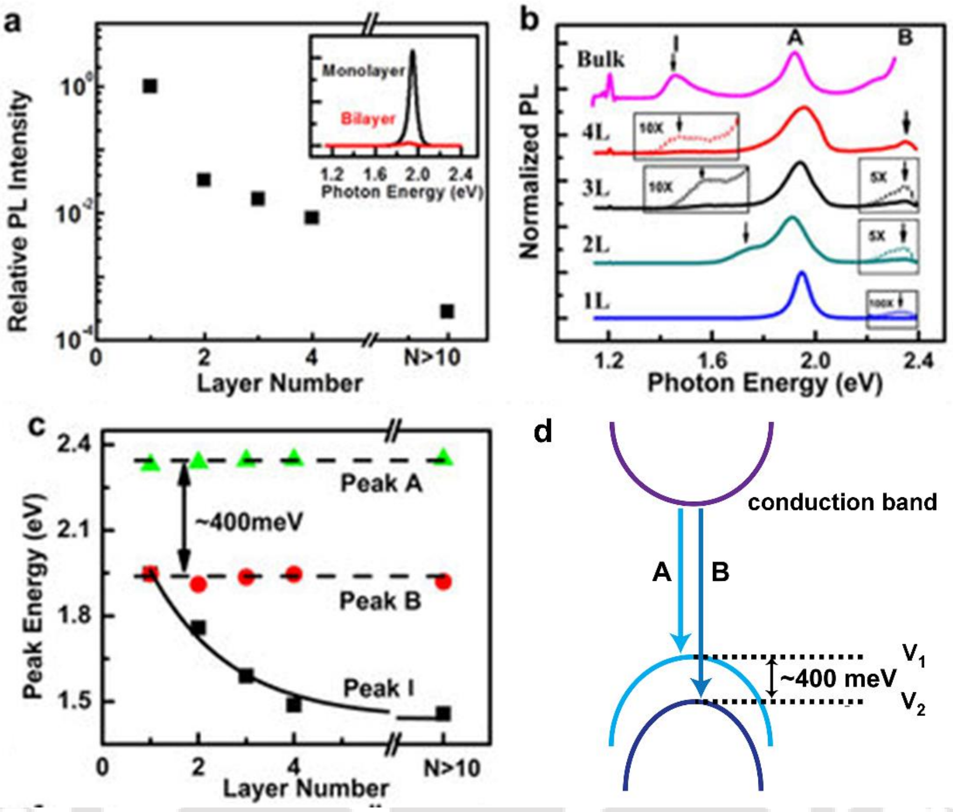

Fig. 1.3. (a) The relative PL intensity of WS_2 as a function of film layer number under the same conditions. Inset shows the PL spectra of monolayer and bilayer WS_2. (b) The normalized PL spectra (with respect to peak A) of WS_2. 'I' indicates the luminescence from indirect gap inter-band transition, and 'A' and 'B' are the direct-gap transitions from the split valence band edge to the conduction band edge at K points. (c) The peak positions of I, A, and B transitions as a function of the film thickness in WS_2. Adopted from Ref[23]. (d) Schematic illustration of the valence band splitting and transitions related to A and B excitons in monolayer WS_2.

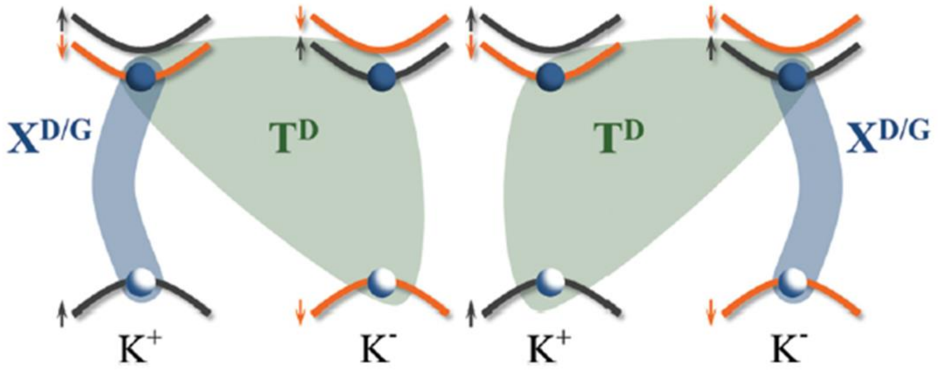

Fig. 1.4. Schematic illustration of possible configurations for the neutral (blue shade) and the negatively charged dark (green shade) excitons located at the K± valleys. The grey (orange) curves indicate the spin-up (spin-down) sub-bands. The electrons (holes) in the conduction (valence) band are represented by blue (white) circles. Adopted from Ref[4].

In addition to the splitting of the VB from the strong spin-orbit coupling, monolayer WX_2 exhibit a splitting of the CB that occurs at 11-40 meV. As such, two types of excitonic states are possible, depending on the spin selection rule – 1) the spin allowed bright exciton, formed by an electron in the highest conduction level and a hole in the highest valance level, at the K point; and 2) the spin forbidden dark state, which is formed by an electron in the lowest conduction level and a hole in the highest valance level, at the K point. The bright exciton, as the name suggests, combines radiatively and thus, emits light. While, the spin forbidden dark state is completely non-radiative and reduces the overall light emission from WS_2, especially at low temperatures[3, 25]. In **Fig. 1.4**, the '+' sign in '$K^{\pm}$' stands for spin-up (grey) state, and '-' indicates spin down (orange). The transitions marked in blue correspond to the dark excitonic state and the green transitions are those of dark trions (see **Fig. 1.4**)[26]. Tuning of the excitonic PL is of paramount importance for various practical applications.

1.2. Synthesis of 0D-2D WS_2

There have been numerous efforts to synthesize controllable, large-scale, high-quality WS_2 nanostructures using various top-down and bottom-up approaches for fundamental studies as well as practical applications. In this section, we discuss a few growth strategies for WS_2 nanosheets, quantum dots, and monolayer films.

1.2.1. Mechanical exfoliation

Mechanical exfoliation is a top-down synthesis route that yields high-quality mono- to few-layer WS_2 films of good crystallinity and facilitates the study of its intrinsic properties. In this process, a small amount of high-quality bulk WS_2 powder is stuck to an adhesive tape. Repeated mechanical peeling is carried out and ultimately pressed onto a suitable substrate. Several WS_2 flakes are obtained on the substrate, of different shapes, sizes, and layer numbers. This method is quick and cost-effective, however, offers relatively very low yield, and hence, is not useful for large-scale synthesis.

1.2.2. Intercalation and Chemical exfoliation

Due to the weak interlayer bonding of TMDs in general, brute forces can be easily applied for the separation of these layers from one another. Chemical exfoliation and ion intercalation are great ways to synthesize quality 0D-2D TMD nanostructures on a large scale, for various applications.

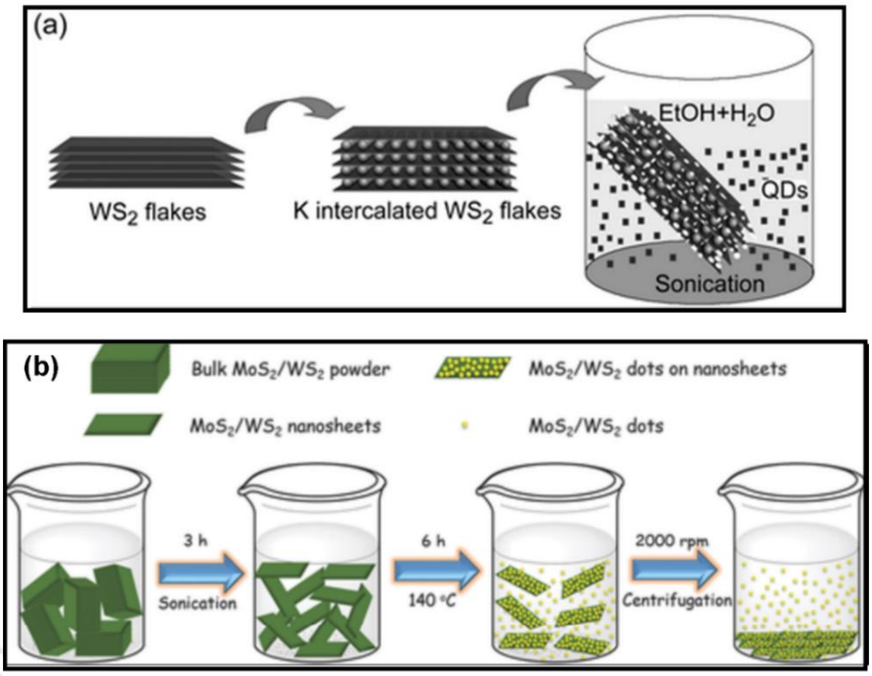

Fig. 1.5. (a) Schematic of K intercalation of WS$_2$ powder, followed by sonication. (b) Schematic of chemical exfoliation in NMP/DMF for the synthesis of nanosheets and quantum dots. Adopted from Refs[15, 27].

Alkali metal ions such as Na$^+$, Li$^+$, and K$^+$ aid in weakening the interlayer binding forces[28-29]. Interestingly, upon Li intercalation, TMDs tend to attain the metastable 1T phase instead of the thermodynamically stable 2H phase[30]. **Fig. 1.5(a)** depicts the experimental scheme for K intercalation, where sonication of bulk WS$_2$ is carried out in presence of K "chunks" in a medium of EtOH/H$_2$O. The exposure to air during ultrasonication aids in the expansion of the interlayer distance, and ultimately separation of layers leads to the synthesis of nanosheets as well as QDs. In this process, however, dialysis needs to be followed to remove the K$^+$ impurities from the solution[27].

Xu et. al used a simple facile method of solvent exfoliation of MoS$_2$ as well as WS$_2$ in dimethyl formamide (DMF). The schematic of the experiment is displayed in **Fig. 1.5(b)**. The dispersion obtained post-sonication was heated and allowed to settle for several hours. Then, centrifugation was carried out to segregate uniformly distributed highly fluorescent QDs[15]. Other solvents that can be used for the process are N-methyl-2-pyrrolidinone (NMP), dimethylimidazolidinone (DMEU), etc. The excess solvent from the as-exfoliated nanosheets/QDs can be easily dried off and redispersed in a suitable solvent, such as water, ethanol, etc, for further use. There have been several studies based on colloidally/chemically exfoliated WS$_2$ nanostructures and their applications[31-34]. However, the prolonged ultrasonication process leads to high defect densities in the as-prepared 0D-2D WS$_2$

nanostructures, which can be a limitation occasionally in specific areas which require high-quality/purity materials.

1.2.3. Physical and chemical vapor deposition

Various physical vapor deposition (PVD) methods have been reported to obtain high-quality WS_2 films with control over thickness and uniformity by magnetron sputtering[35], pulsed laser deposition (PLD)[9], etc. However, the films synthesized through these routes have a possibility of high defect density, unevenness, and non-stoichiometric polycrystallinity, and are often considered expensive. Therefore, when it comes to the growth of thin films of atomic-level thickness of high quality, chemical vapor deposition (CVD) is by far one of the most reliable methods. There have been numerous reports on the growth of WS_2 monolayers by CVD, using different growth parameters, such as precursors, growth pressure, temperature, duration of growth, carrier gas, and so on.

Xu et. al have grown triangular monolayer WS_2 flakes of domain sizes ~10-15 µm using a CVD technique. They employed a low reaction temperature (500 °C) and used WS_2 and $Na_2S_2O_3$ as precursors in a sealed quartz tube (see **Fig. 1.6(a)**). The growth was allowed to take place for 60 min at atmospheric pressure[36]. Another group used WCl_6 and H_2S vapors as W and S sources for the synthesis of monolayer WS_2, as shown in **Fig. 1.6(b)**[37]. WCl_6 was kept at 90 °C in a stainless-steel bubbler. Ar was used as the carrier gas, with a small amount of H_2, that acts as a chemical etchant aiding in a reduced nucleation density[38] and also, aids in the reduction of W^{6+} to W^{4+}, promoting monolayer WS_2 growth[39]. The reaction temperature was set at 600 °C and chamber pressure was maintained at ~4.5 Torr[37]. Kang et. al studied the effect of H_2 gas flow on the CVD growth keeping the Ar gas flow fixed at 100 sccm. The schematic of their experimental setup is presented in **Fig. 1.6(c)**. The precursors WO_3 and S powders were placed as shown in the schematic setup. The growth temperature and pressure were maintained at 900 °C and 9 Torr, respectively. The density and size of the as-prepared WS_2 monolayer crystals increased with H_2 gas flow[40]. **Fig. 1.6(d)** shows the schematic setup of a multi-zoned furnace used for CVD growth. The WO_3 powder and the growth substrates were kept in zone 1 and zone 2, respectively. As the high temperature (920 °C) of zone 1 affected zone 0, due to insufficient thermal insulation, S powder was placed outside zone 0 and a heating belt was used. The growth pressure was set at 0.16 Torr and growth was allowed to happen for 60 min[41].

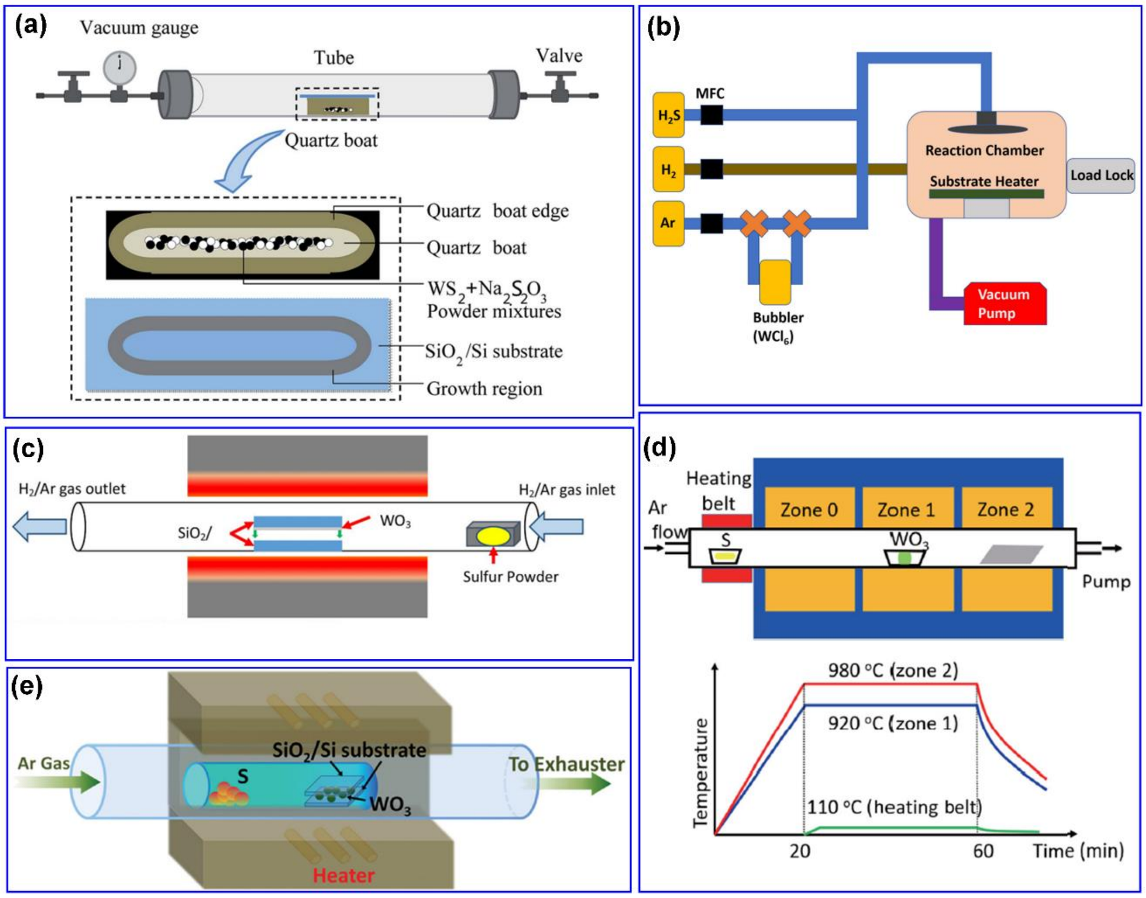

Fig. 1.6. CVD growth of monolayer WS$_2$ using (a) WS$_2$ and Na$_2$S$_2$O$_3$ as precursors. Adapted from Ref[36]. (b) WCl$_6$ and H$_2$S vapors as precursors, adapted from Ref[37]. (c) a one-zone furnace and Ar/H$_2$ carrier gas with varying H$_2$ concentrations. Adapted from the Ref[40]. (d) a 3-zone furnace and Ar carrier gas. Adapted from Ref[41]. (e) a semi-sealed growth setup and WO$_3$ sandwiched between substrates. Adapted from the Ref[42].

Since the melting point of WO$_3$ is ~1300 °C, researchers have proposed the use of a semi-sealed setup to ensure the requisite WO$_3$ vapor pressure for optimum monolayer growth. **Fig. 1.6(e)** depicts one such experimental system. Ar was used as the carrier gas and direct sulfurization of WO$_3$ powder sandwiched between two SiO$_2$/Si substrates was carried out at 750 °C[42]. A similar approach was adopted by Lan et.al, as well, where the WO$_3$ powder was kept in close proximity to the substrates in a semi-sealed quartz boat, ensuring a high WO$_3$ partial pressure with respect to that of the setup. The transport of S vapor was optimized by keeping the pressure of the furnace high during the growth[43]. Xie et al. have grown high-quality WS$_2$ monolayers at atmospheric pressure and varying the growth temperature in the range of 750-850 °C[44]. WO$_3$ and S were used as precursors and a halide-assisted approach was adopted for large area WS$_2$ monolayers. They employed a smaller quartz tube inside the furnace and magnets to control the temperature of the S and the time of introduction, to ensure optimum growth. As compared to the case of monolayer MoS_2, large-area growth of monolayer WS_2 is a challenging task and several growth parameters affect the growth process.

1.3. WS_2 Based Heterostructures

In recent years, WS_2-based HSs with different materials have been extensively studied to tune their multifunctional properties. Several techniques have been developed for the construction of high-quality HSs using atomically thin 2D WS_2 films, as well as 0D quantum dots with other materials. The combined properties of different materials in the WS_2-based HSs can create new products with novel and remarkable properties that can immensely raise the potential of WS_2 to be used in various applications. The properties of WS_2 can be engineered by forming HSs with the following: (a) other semiconductors[45-46], (b) graphene-based materials[47-48], (c) plasmonic nanostructures[49-50], (d) 2D van der Waals materials[48, 51], (e) 2D non-van der Waals materials[52], (f) organic and inorganic perovskites[53] and so on. For instance, the formation of WS_2-based heterostructures could be a promising approach to improve the photoconduction or photocatalytic activity of WS_2, utilizing effective charge separation and reduced recombination of photoinduced electron-hole pairs. Additionally, the weak interlayer van der Waals forces make the isolation of individual layers attainable by simple exfoliation techniques. As such, stacking of these layers with different materials irrespective of their crystal lattice mismatch is easily achieved. In the following section, we attempt to briefly cover some of the practical applications where WS_2 and WS_2-based heterostructures have been employed.

1.4. Application of WS_2 and its Heterostructures

The most distinctive characteristic of TMDs in general is the transition from a small indirect bandgap in their bulk form to a widened direct bandgap in the monolayer regime. Owing to its remarkable properties, such as finite bandgap, absorption in the UV-Visible region, good carrier mobility, and flexibility to form HSs, WS_2 has attracted substantial interest for fundamental studies on light-matter interactions and a wide range of applications. The formation of WS_2-based HSs allows to enhance or tune these properties and likewise, brings in the prospects of further comprehensive studies and next-generation applications. In this section, we will discuss a few of the promising areas where 0D-2D WS_2 and its HSs have been utilized such as in fluorescence imaging, sensors, solar cells and photodetector, photocatalytic hydrogen production, light-emitting devices, etc.

1.4.1. Photoluminescence and Imaging

Owing to their strong fluorescence, water solubility, and low toxicity, WS_2 QDs have been used as non-toxic fluorescence labels for the detection of biological cells using confocal fluorescence microscopy. **Fig. 1.7.** shows the cellular images of MDCKII cells using WS_2 QDs[27]. The QDs permeate the cell cytoplasm but do not penetrate the nuclei. **Fig. 1.7(a)** shows WS_2 QD stained cells, where the QDs agglomerate around the nuclei. The MDCKII nuclei were stained with DAPI (4',6-diamidino-2-phenylindole) (see **Fig. 1.7 (b)**). In **Fig. 1.7(c)**, the cell cytoplasm is stained with WS_2 QDs, and the nuclei are stained with DAPI. The cell nuclei along with the cytoplasm and the boundary between cells are clearly observed. Note that the emission range of both DAPI and the QDs is ~400-650 nm. **Fig. 1.7(d)** is an overlay image of **Fig. 1.7(b, c).** Therefore, WS_2 QDs have been useful in high contrast bioimaging applications and hence, considered suitable in the field of clinical diagnostics. Another group, Xu et. al utilized confocal imaging to detect HeLa cells incubated in Dulbecco's modified Eagle's medium (DMEM) containing WS_2 QDs, which entered into cells by endocytosis, but similar to the case described above, could not enter the nuclei. Thus, there was no disruption to the genetic sequence, implying low cytotoxicity of the fluorescent probes[15].

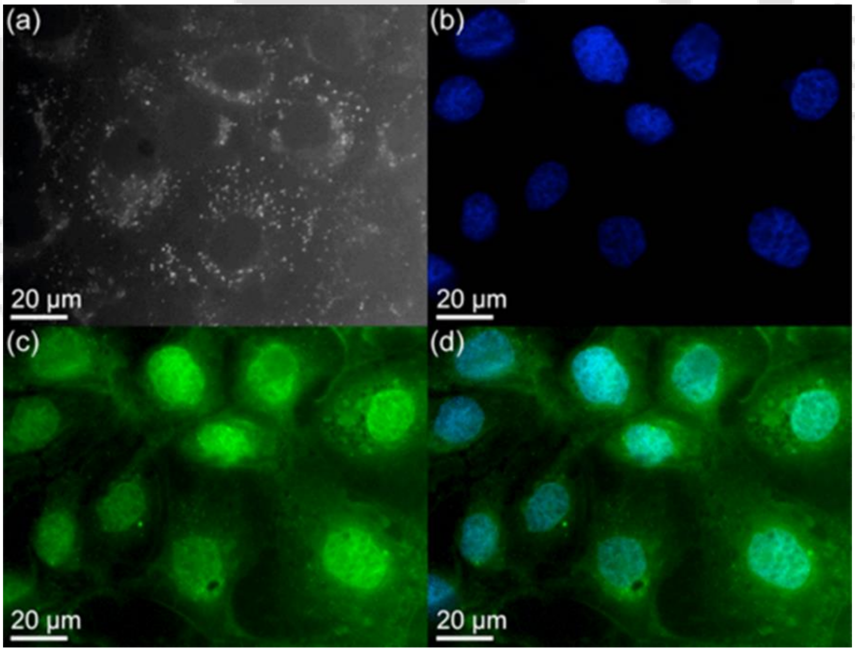

Fig. 1.7. (a) Agglomerated WS_2 QDs surrounding each nucleus (cells are stained by WS_2 QDs only). (b) Individual nucleus stained with DAPI. (c) The cell nucleus and cytoplasm were stained with DAPI and WS_2 QDs, respectively. (d) The overlay image of panels b and c. Adapted from the Ref[27].

1.4.2. Sensors

The low-cost solution processing and highly fluorescent nature of TMD QDs pave way for the fabrication of effective sensors of various ions, pollutants, chemicals, neurotransmitters, etc. Hang et. al have successfully developed carbon QD/WS_2 QD-based sensors for the detection of H_2O_2 as well as glucose. The PL of the hybrid system was systematically quenched in the presence of H_2O_2 or glucose, with a limit of detection (LOD) of ~60 μM[54]. WS_2 QDs offer abundant active edge sites that make them promising candidates for applications in environmental monitoring, biochemistry, and biomedical areas.

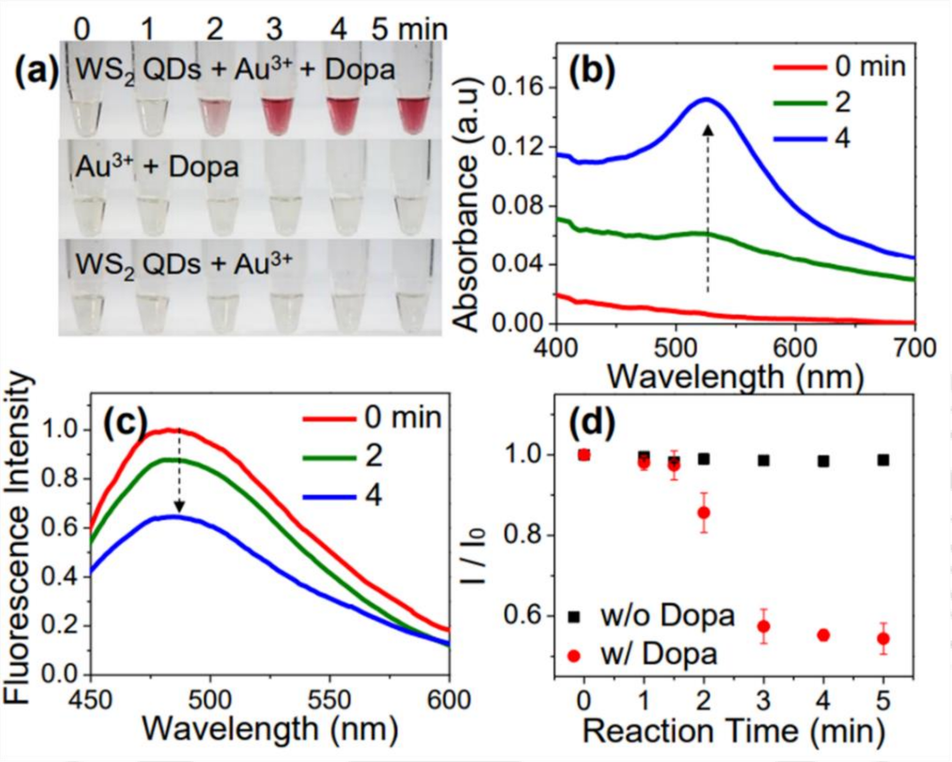

Fig. 1.8. (a) Optical images for the solutions; WS_2 QDs + Au^{3+} ions + Dopa, Au^{3+} ions + Dopa, and WS_2 QDs + Au^{3+} ions. The concentrations of Au^{3+} and Dopa were 250 and 12.5 μM, respectively. (b) Absorption spectra of the solution consisting of WS_2 QDs + Au^{3+} ions + Dopa, showing the plasmonic absorption of Au NPs. (c) Fluorescence response of WS_2 QDs in the solution of WS_2 QDs + Au^{3+} ions + Dopa, showing a quenching response. (d) Quenching response kinetics of WS_2 QD fluorescence in the absence and the presence of Dopa. I0 and I were the fluorescence intensities of WS_2 QDs including Au^{3+} ions before and after the addition of Dopa, respectively. Adapted from the Ref[55].

Fig. 1.8 depicts the detection of Dopamine (Dopa) with WS_2 QDs[55]. When Au^{3+} ions and Dopa were simultaneously added to the QD solution, Au NPs are formed in minutes (**Fig. 1.8(a)**), which is confirmed by the absorption spectra (see **Fig. 1.8(b)**). Systematic quenching was observed with increased incubation time, as shown in **Fig. 1.8(c)**. In other words, when Dopa was in presence of Au^{3+} ions, fluorescence quenching occurred due to the formation of Au NPs, which was attributed to fluorescence resonance energy transfer (FRET) between the rapidly-formed Au NPs and the QDs. **Fig 1.8(d)** depicts the gradual decrease of the PL intensity in presence of Dopa with time[55]. To examine the selectivity, the group examined various types of interference compounds and neurotransmitters, such as ascorbic acid, uric acid, glucose, adenosine triphosphate, and dopamine derivatives like epinephrine, and norepinephrine. No fluorescence quenching was observed in the presence of any of these other interference materials verifying that the WS2 QD fluorescent sensor is highly selective in dopamine detection. Singh et. al developed a highly efficient and selective WS_2 QD-based Fe^{3+} sensor and explored the fluorescence quenching mechanism in detail. The LOD was of the order ~1.32 μM[56]. Another group devised a fluorescence sensing strategy for the detection of glucose, based on the different influences of Fe^{2+} and Fe^{3+} ions on the fluorescence of WS_2 QDs[57]. Glucose, in the presence of glucose oxidase, generated H_2O_2 which in turn led to oxidation of Fe^{2+} to Fe^{3+}. The Fe^{3+} ions quenched the fluorescence of the hydrothermally synthesized WS_2 QDs via the mechanism of photoinduced electron transfer. The detection limit of glucose was as low as 0.3 μM[57]. The sensing applications of WS_2 QDs have been reported for a diverse range of chemicals including the detection of 2,4,6-trinitrophenol (TNP), which is a member of the family of nitroaromatic (NA) explosives. The LOD was 0.3 μM. The mechanism of the associated fluorescence quenching constituted electron transfer, FRET, and the inner filter effect (IFE)[58]. Hence, WS_2-based nanostructures have proven to have immense potential in the fields of optical sensing, biosensing, bioimaging, etc.

1.4.3. Electrocatalytic and Photocatalytic Hydrogen Production

Addressing the global energy crisis and accompanied climate change is the ultimate need of the hour. The overconsumption of fossil fuels with rapid civilization has raised the urgency to look for alternative energy sources. As such, hydrogen production via water splitting has been regarded as the cleanest energy resource.

Over the years, nanostructures of TMDs like MoS_2 and WS_2 have garnered significant attention as potential efficient catalysts for water splitting. Xu et. al compared the electrocatalytic activity of MoS_2 and WS_2 composites (combination of QDs and nanosheets) with the conventional noble electrocatalyst, Pt. Both MoS_2 and WS_2 exhibited excellent catalytic activity, owing to two main factors– (a) the QDs embedded on the respective nanosheets are defect-rich and offer abundant active edge sites for hydrogen evolution reaction (HER); (b) the random stacking of the exfoliated nanosheets offered greater surface to volume ratio aiding in enhanced electron transfer between the active edge sites and underlying electrode[15, 59]. Another group developed 2H-WS_2 and 1T-WS_2 nanostructure-based catalysts for photocatalytic hydrogen production[60]. Moreover, TiO_2, owing to its broad absorption characteristics, was used to form TiO_2:WS_2 composites and the catalytic activities were compared. **Fig. 1.9(a)** displays the band alignment of TiO_2 with 2H- and 1T-WS_2. Under illumination, the TiO_2 produced H_2 gas at a rate of 700 µmol g^{-1} h^{-1}, although, the nanocomposite of TiO_2:1T-WS_2 exhibited a superior H_2 production rate of ~2570 µmol $g^{-1}h^{-1}$, as shown in **Fig. 1.9(b)**. The photocatalytic activity of the TiO_2 composite with the semiconducting 2H-WS_2 was much diminished, which was attributed to more recombination in the system. Recently, Lai et. al reported the photocatalytic activity of few-layer WS_2-MoS_2 that produced H_2 gas at a remarkable rate of ~10 µmol g^{-1} h^{-1}. The composite catalyst retained its performance after multiple cycles, showing outstanding stability[61]. These noble metal-free co-catalysts are, however, still considered inferior to conventional Pt/Pd co-catalysts, when it comes to stability and catalytic activity.

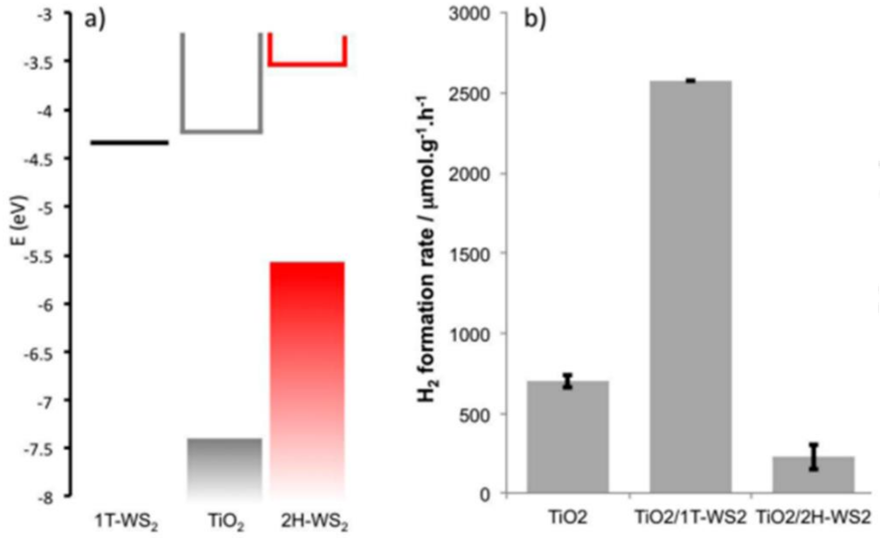

Fig. 1.9. HER activity WS_2 based HS. (a) Electronic band alignment between TiO_2 and synthesized 1T-WS_2 and 2H-WS_2 nanostructures. (b) Photocatalytic hydrogen production rates for TiO2 and the TiO_2:1T-WS_2 and TiO_2:2H-WS_2 nanocomposites. Adapted from the Ref[60].

1.4.4. Photodetectors and Solar cells

The excellent light absorption and tuneable optical bandgaps of TMD systems make them excellent contenders for the fabrication of electronic and optoelectronic devices, especially photodetectors and solar cells. WS_2-based HSs with even conventional semiconductors like Si, Ge, etc., greatly boost the performance of the devices. Wu et al. demonstrated a high-performance self-powered WS_2 film/Si heterojunction photodetector (PD) that could perform broadband photodetection[62]. The device showed a fast photoresponse of ~16/29 µs under 980 nm illumination and at 0 bias. Lan et al. reported a highly responsive and stable Zener photodiode based on n-WS_2 film/p-Si heterojunction[63]. **Fig. 1.10** depicts the schematic of an ultrabroadband photodetector based on the HS $WS_2/AlO_x/Ge$. Reduction of the defect density of a multi-layer WS_2 film was carried out using AlO_x-aided surface passivation. The fabricated device was self-powered with an ultrabroad detection range of ~200 nm to 4.6 µm[64]. Besides conventional semiconductors, several WS_2 heterojunction photodetectors have been fabricated using a variety of other TMDs, semiconductors, plasmonic NPs, and so on. Li et. al developed a high-performance photodetector based on lateral monolayer MoS_2/WS_2 heterojunctions[8]. The device exhibited a high responsivity of 576 A/W.

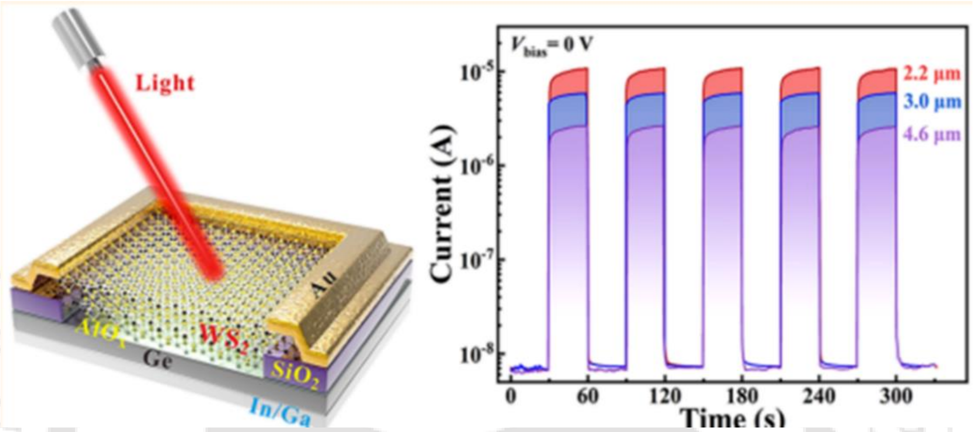

Fig. 1.10. Schematic diagram of the $WS_2/AlO_x/Ge$ heterojunction photodetection device. Temporal photoresponse of the device to IR light illumination wavelengths 2.2, 3.0, and 4.6 µm at zero bias. Adapted from the Ref[64].

The performance parameters of some of the WS_2 films/QD and WS_2-based heterojunction photodetectors are summarized in **Table 1.** The distinct properties of the WS_2 heterojunction devices lay the foundation for advancements in other multifunctional optoelectronic applications.

Table 1: Performance parameters of WS_2 heterojunction photodetectors.

Materials	Wavelength Range (nm)	Responsivity (A/W)	Detectivity (Jones)	Rise/fall time	Ref
$WS_2/AlO_x/Ge$	200-4600	0.63	4.3×10^{11}	9.8/12.7 µs	64
MoS_2/WS_2	405-635	576	$\sim 10^{11}$	-	8
WS_2/graphene	UV	1814.3	7.5×10^{12}	2/2.9 s	65
WS_2/MoS_2	~532	4.36×10^{-3}	4.4×10^{13}	4/4 ms	66
2D-WS_2/Si	265-3043	0.22	1.5×10^{12}	16/29 µs	62
WS_2 film	visible	53.3	1.2×10^{11}	-	9
Au/WS_2 nanosheets	405	~3	4.9×10^{11}	7.8/37.2 ms	67

Monolayer WS_2 films, QDs, and WS_2-based heterostructures have also acquired an interest in the development of stable, cost-effective, high-performance solar cells over the past few years. For industrial photovoltaic applications, solar cells are required to be highly stable and have a high-power conversion efficiency (PCE). High-quality WS_2 films have proven to act as efficient hole transport layers (HTL). Wang et. al have utilized chemically exfoliated WS_2 nanosheets as HTL in an organic solar cell[68]. The device exhibited a high-power conversion efficiency (PCE) of ~ 15.75%. Cao et. al fabricated WS_2 flake-incorporated perovskite solar cells that exhibited a boosted PCE of ~21.1%, with excellent stability[69]. Thus, WS_2 offers great potential as HTL for stable and efficient heterojunction photovoltaic devices, which paves a way for designing highly efficient WS_2-based solar cells in the future. Moreover, WS_2, like MoS_2, has been argued to be an emerging candidate for stable, efficient, and low-cost counter electrodes in dye-sensitized solar cells offering high PCEs[70-73], which is beneficial given the current global environmental and energy crisis.

1.4.5. Light-emitting diode (LED)

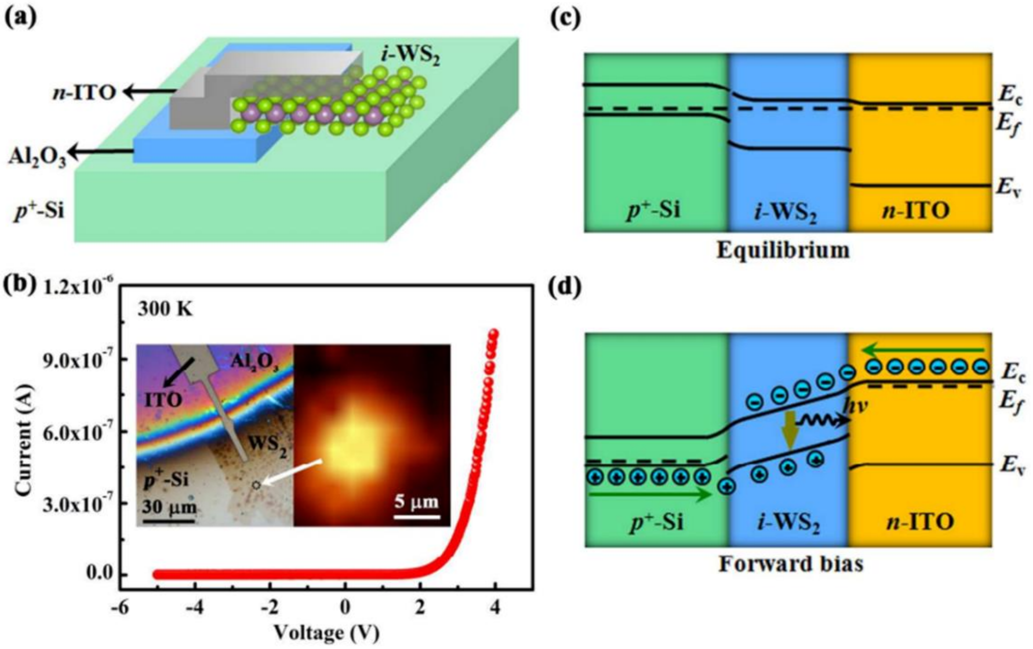

Fig. 1.11. (a) Schematic of the p^+-Si/i-WS_2/n-ITO heterojunction LED. (b) Room temperature I-V characteristic of the p^+-Si/i-WS_2/n-ITO heterojunction LED. Inset shows the high magnification optical images of the LED device and EL mapping image as the white arrow indicated. (c, d) Band diagram of the p^+-Si/i-WS_2/n-ITO heterojunction in equilibrium condition and under forward bias, respectively[74].

Lately, light-emitting diodes or LEDs have gradually replaced conventional lighting sources owing to their low cost and low power consumption and thus, being environment friendly. Among new-age 2D materials, researchers have endeavoured to fabricate suitable TMD heterojunction-based light-emitting devices, owing to the efficient direct band-gap recombination and easy stacking ability. Several LED architectures have been suggested in the past.

Yang et. al demonstrated electrically tuneable chiral electroluminescence (EL) of 1L-WS_2 by constructing a p-i-n heterojunction LED[74]. The schematic is shown in **Fig. 1.11(a).** Here, heavily p-doped Si and n-ITO injected holes and electrons into i-WS_2, respectively and Al_2O_3 acted as an insulating layer. The I-V characteristics showed rectifying nature of the device (**Fig. 1.11(b)**) and the LED had a turn-on voltage of ~2 V. The inset of **Fig. 1.11(b)** depicts the fabricated device and the EL image. **Fig. 1.11(c)** illustrates the band diagram of the heterojunction under the equilibrium condition. There is a large valence band offset of 1.23 eV between p^+-Si and 1L-WS_2. On forward biasing (**Fig. 1.11(d)**), the holes from p^+-Si are injected into monolayer WS_2, while the larger valence band offset between 1L-WS_2 and ITO forms a barrier blocking the injected holes from leaking into the n-type layer. The electrons and holes injected from adjacent layers can give rise to efficient radiative recombination in the 1L-WS_2. Additionally, by varying the forward injection current, it was possible to obtain net circularly polarized light emission from the LED[74]. The fabrication of valley-LEDs opens up avenues for the incorporation of rich new physics in developing more unconventional 2D optoelectronic devices.

Andrzejewski et. al employed mechanically exfoliated WS_2 flakes to fabricate red LEDs with organic p-conductive layers (PEDOT: PSS/poly-TPD) on ITO-coated glass substrates, serving as hole supporting layers and ZnO NPs as electron supporting layers. The monolayer WS_2 flakes sandwiched between these layers showed pronounced electroluminescence in the visible red region of the spectrum. The fabricated light emission device had an external quantum efficiency (EQE) of 0.27% and exhibited a luminance of ~50 Cd/m^2. Thus, it showed promise as an upscaled LED if the flakes are replaced by large-area monolayer WS_2[10]. The group also fabricated the first-ever flexible LED using 2D WS_2 as the active layer and ITO-coated flexible PEN substrates. On application of bias voltage, the device had a red-light emission at ~652 nm and exhibited a luminance of 1 Cd/m^2. The devices showed rectifying behaviour in their I−V characteristics. Interestingly, bending the substrate allowed precise monitoring of any wavelength shift[7]. The performance parameters of some of the WS_2 films/QD and WS_2-based heterojunction LEDs are tabulated below (see **Table 2).**

Table 2: Performance parameters of WS_2 and WS_2-based heterostructure LEDs.

Device	Emission wavelength (nm)	Operating Voltage (V)	EQE (%)	Maximum luminance (Cd/m^2)	Ref
ITO/WS_2/Si	~625-635	2	-	-	74
ITO/ PEDOT: PSS/poly-TPD/WS_2 flakes/ZnO NP/Al	red	12	0.27	50	10
ITO/ PEDOT: PSS/poly-TPD/WS_2 flakes/MoS_2/Al	red	6	-	-	10
ITO/ PEDOT: PSS/PVK/WS_2 QDs/ZnMgO NC/Ag	white	10	-	507	75
PEN+ITO/ PEDOT: PSS/poly-TPD/1L-WS_2/ZnO NP/Al	652	9	-	1	7
ITO/ PEDOT: PSS/poly-TPD/1L-WS_2/ZnO QD/Al	red	7	0.01	1	76

1.5. Challenges in Fabrication and Applications of WS_2-Based Heterostructures

Over the last few years, there has been extensive research on the fundamental aspects of the synthesis and applications of layered TMDs. However, few challenges still remain in the large-scale and reproducible growth of uniform, large-area, and high-quality monolayer WS_2 for practical applications on the industrial scale. Mechanically exfoliated WS_2 or MoS_2 flakes, although of superior quality, are produced at much low yields. Additionally, in the case of chemical exfoliation techniques, the control over the layer number, purity, and phases of WS_2 still are issues that need to be addressed. Also, further control over vapor deposition strategies for stable, large-scale, defect-free, easily processed WS_2 is desirable. Moreover, doping of WS_2 would be a useful technique to enhance the ability of charge transport and tune other properties. Secondly, the formation of WS_2-based HS with different materials that are semiconducting, plasmonic, etc., would allow us to tune the unique properties of WS_2 to our advantage for a wide range of applications. An in-depth understanding of the innate optical properties of WS_2 and the effect of HS formation on them is crucial to having a grasp of the resultant light-matter interactions. Furthermore, we believe band structure engineering of WS_2 by the formation of various HS can help to achieve superior performances in optoelectronic and electronic devices. Thus, further exhaustive studies in the field of the charge carrier dynamics of 2D WS_2 in different hybrid systems are imperative. This will be significant not only for various future applications but also in achieving a fundamental understanding of the 2D TMD systems.

1.6. Focus of the Present Thesis

WS_2, like its sister TMD MoS_2, has displayed immense potential in new-age semiconductor research. Although the zero-dimensional QDs have been used extensively, their spectral features are not completely understood. Moreover, in the development of optoelectronic devices, QDs exhibit limited carrier mobility compared to two-dimensional monolayer films. However, challenges still remain in the synthesis procedures. In the present thesis, we endeavoured for controlled growth of large-area monolayer WS_2 and explored its HSs with other semiconductors to understand the underlying charge transfer mechanisms and modulation of their optical properties. The main objectives of the present thesis are as follows:

- Top-down controlled synthesis of WS_2 QDs by liquid exfoliation.
- Controlled growth of large-area monolayer WS_2 by CVD technique and study of the effect of growth conditions on the thickness and flake size of WS_2.
- Detailed analysis of excitation wavelength-dependent photoluminescence spectrum of the WS_2 QDs and study of interaction with single walled carbon nanotubes.
- Fabrication of p-n heterojunction photodetector based on Si/WS_2 QDs heterostructure and incorporation of Au nanoparticles to fabricate high-performance Schottky Si/Au/WS_2 photodetector.
- PL modulation of monolayer WS_2 by heterostructuring with non-van der Waals Bi_2O_2Se QDs and quantitative analysis involving coupled charged transfer dynamics to explain the systematic decrease in the PL peak intensity of WS_2 with Bi_2O_2Se QDs.
- Tunability of the PL emission by the encapsulation of WS_2 film with high band gap ZnO and study of the quantum well effect on the exciton dynamics of monolayer WS_2.

1.7. Organization of the Thesis

The work done is presented in a thesis organized into seven chapters. In **Chapter 1,** we have introduced the material and its important properties and laid out a brief overview of the literature on the different growth techniques and the promising applications of 2D, 0D WS_2, and its heterostructures. The motivation and focus of the present thesis are discussed at the end. **Chapter 2** presents the controlled synthesis of WS_2 quantum dots by chemical exfoliation and high-quality large-area monolayer WS_2 via CVD by monitoring various growth parameters, such as duration, post-treatments, growth pressure/temperature, precursors, etc. **Chapter 3** demonstrates a simple two-step top-down synthesis process of the WS_2 QDs by prolonged liquid exfoliation followed by centrifugation and the in-depth study of its photoluminescence behaviour. We have further investigated the systematic quenching of the PL intensity of these QDs in presence of Single walled carbon nanotubes (SWCNTs) of different defect densities. In **Chapter 4,** we fabricated a high-performance Si/Au NP/WS_2 QD Schottky photodetector (PD). The WS_2 QDs act as the n-type semiconductor on Au NP embedded p-type Si platforms and the device exhibits highly suppressed dark current and fast response. In **Chapter 5**, we have grown a WS_2 film of monolayer thickness and investigated the modulation of the PL and doping caused by decorating it with Bi_2O_2Se QDs. We have conducted a thorough quantitative examination using the four-energy level model to explain the associated charge transfer dynamics in the quenching of the PL in the 1L-WS_2/Bi_2O_2Se QD system. **Chapter 6** demonstrates the tunability of the PL of 1L-WS_2 when encapsulated by a higher bandgap semiconductor, ZnO in a quantum well-like structure. We have explored the power-dependent and temperature-dependent variation of the PL to identify the contributing recombination channels in the emission characteristics of the system. **Chapter 7** summarizes the significant findings and lays out the important highlights of the present thesis and the future scope of the work.

References

1. Mak, K. F.; Lee, C.; Hone, J.; Shan, J.; Heinz, T. F., Atomically Thin ${\Mathrm{Mos}}_{2}$: A New Direct-Gap Semiconductor. *Physical Review Letters* **2010**, *105*, 136805.

2. Yuan, L.; Huang, L., Exciton Dynamics and Annihilation in Ws2 2d Semiconductors. *Nanoscale* **2015**, *7*, 7402-7408.

3. Upadhyay, B.; Thakur, D.; Pramanick, B.; Bhandari, S.; Balakrishnan, V.; Pal, S. K., Anomalous Emission Behavior of Excitons at Low Temperature in Monolayer and Ws₂. *Journal of Physics D: Applied Physics* **2022**, *55*, 235105.

4. Zinkiewicz, M., et al., Neutral and Charged Dark Excitons in Monolayer Ws2. *Nanoscale* **2020**, *12*, 18153-18159.

5. wu, Z.; Fang, B.; Bonakdarpour, A.; Sun, A.; Wilkinson, D.; Zan, X., Ws2 Nanosheets as a Highly Efficient Electrocatalyst for Hydrogen Evolution Reaction. *Applied Catalysis B: Environmental* **2012**, *125*, 59–66.

6. Fan, X.; Wang, S.; An, Y.; Lau, W., Catalytic Activity of Ms 2 Monolayer for Electrochemical Hydrogen Evolution. *The Journal of Physical Chemistry C* **2015**, *120*.

7. Andrzejewski, D.; Oliver, R.; Beckmann, Y.; Grundmann, A.; Heuken, M.; Kalisch, H.; Vescan, A.; Kümmell, T.; Bacher, G., Flexible Large-Area Light-Emitting Devices Based on Ws2 Monolayers. *Advanced Optical Materials* **2020**, *8*, 2000694.

8. Li, C.; Zhu, J.; Du, W.; Huang, Y.; Xu, H.; Zhai, Z.; Zou, G., The Photodetectors Based on Lateral Monolayer Mos2/Ws2 Heterojunctions. *Nanoscale Research Letters* **2021**, *16*, 123.

9. Zeng, L.; Tao, L.; Tang, C.; Zhou, B.; Long, H.; Chai, Y.; Lau, S. P.; Tsang, Y. H., High-Responsivity Uv-Vis Photodetector Based on Transferable Ws2 Film Deposited by Magnetron Sputtering. *Scientific Reports* **2016**, *6*, 20343.

10. Andrzejewski, D.; Hopmann, E.; John, M.; Kümmell, T.; Bacher, G., Ws2 Monolayer-Based Light-Emitting Devices in a Vertical P–N Architecture. *Nanoscale* **2019**, *11*, 8372-8379.

11. Li, X.; Li, X.; Li, Z.; Wang, J.; Zhang, J., Ws2 Nanoflakes Based Selective Ammonia Sensors at Room Temperature. *Sensors and Actuators B: Chemical* **2017**, *240*, 273-277.

12. Järvinen, T.; Lorite, G. S.; Peräntie, J.; Toth, G.; Saarakkala, S.; Virtanen, V. K.; Kordas, K., Ws₂ and Mos₂ Thin Film Gas Sensors with High Response to Nh₃ in Air at Low Temperature. *Nanotechnology* **2019**, *30*, 405501.

13. Nandi, D. K.; Sen, U. K.; Dhara, A.; Mitra, S.; Sarkar, S. K., Intercalation Based Tungsten Disulfide (Ws2) Li-Ion Battery Anode Grown by Atomic Layer Deposition. *RSC Advances* **2016**, *6*, 38024-38032.

14. Vakili-Nezhaad, G. R.; Gujarathi, A. M.; Al Rawahi, N.; Mohammadi, M., Performance of Ws2 Monolayers as a New Family of Anode Materials for Metal-Ion (Mg, Al and Ca) Batteries. *Materials Chemistry and Physics* **2019**, *230*, 114-121.

15. Xu, S.; Li, D.; Wu, P., One-Pot, Facile, and Versatile Synthesis of Monolayer Mos2/Ws2 Quantum Dots as Bioimaging Probes and Efficient Electrocatalysts for Hydrogen Evolution Reaction. *Advanced Functional Materials* **2015**, *25*, 1127-1136.

16. Liao, W.; Zhang, L.; Zhong, Y.; Shen, Y.; Li, C.; An, N., Fabrication of Ultrasmall Ws(2) Quantum Dots-Coated Periodic Mesoporous Organosilica Nanoparticles for Intracellular Drug Delivery and Synergistic Chemo-Photothermal Therapy. *OncoTargets and therapy* **2018**, *11*, 1949-1960.

17. Zhu, C.; Gao, D.; Ding, J.; Chao, D.; Wang, J., Tmd-Based Highly Efficient Electrocatalysts Developed by Combined Computational and Experimental Approaches. *Chemical Society Reviews* **2018**, *47*, 4332-4356.

18. Wang, Q. H.; Kalantar-Zadeh, K.; Kis, A.; Coleman, J. N.; Strano, M. S., Electronics and Optoelectronics of Two-Dimensional Transition Metal Dichalcogenides. *Nature Nanotechnology* **2012**, *7*, 699-712.

19. Fu, Q.; Xiang, B., Monolayer Transition Metal Disulfide: Synthesis, Characterization and Applications. *Progress in Natural Science: Materials International* **2016**, *26*.

20. Terrones, H.; López-Urías, F.; Terrones, M., Novel Hetero-Layered Materials with Tunable Direct Band Gaps by Sandwiching Different Metal Disulfides and Diselenides. *Scientific Reports* **2013**, *3*, 1549.
21. Kuc, A.; Zibouche, N.; Heine, T., Influence of Quantum Confinement on the Electronic Structure of the Transition Metal Sulfide TS${}_{2}$. *Physical Review B* **2011**, *83*, 245213.
22. Kang, J.; Tongay, S.; Zhou, J.; Li, J.; Wu, J., Band Offsets and Heterostructures of Two-Dimensional Semiconductors. *Applied Physics Letters* **2013**, *102*, 012111.
23. Zeng, H., et al., Optical Signature of Symmetry Variations and Spin-Valley Coupling in Atomically Thin Tungsten Dichalcogenides. *Scientific reports* **2013**, *3*, 1608.
24. Zhu, B.; Zeng, H.; Dai, J.; Gong, Z.; Cui, X., Anomalously Robust Valley Polarization and Valley Coherence in Bilayer Ws₂. *Proceedings of the National Academy of Sciences* **2014**, *111*, 11606-11611.
25. Zhang, X.-X.; You, Y.; Zhao, S. Y. F.; Heinz, T. F., Experimental Evidence for Dark Excitons in Monolayer ${\Mathrm{Wse}}_{2}$. *Physical Review Letters* **2015**, *115*, 257403.
26. Liu, E.; van Baren, J.; Liang, C.-T.; Taniguchi, T.; Watanabe, K.; Gabor, N. M.; Chang, Y.-C.; Lui, C. H., Multipath Optical Recombination of Intervalley Dark Excitons and Trions in Monolayer ${\Mathrm{Wse}}_{2}$. *Physical Review Letters* **2020**, *124*, 196802.
27. Lin, L.; Xu, Y.; Zhang, S.; Ross, I. M.; Ong, A. C. M.; Allwood, D. A., Fabrication of Luminescent Monolayered Tungsten Dichalcogenides Quantum Dots with Giant Spin-Valley Coupling. *ACS Nano* **2013**, *7*, 8214-8223.
28. Ghorai, A.; Midya, A.; Maiti, R.; Ray, S. K., Exfoliation of Ws2 in the Semiconducting Phase Using a Group of Lithium Halides: A New Method of Li Intercalation. *Dalton Transactions* **2016**, *45*, 14979-14987.
29. Wu, Y., et al., Unexpected Intercalation-Dominated Potassium Storage in Ws2 as a Potassium-Ion Battery Anode. *Nano Research* **2019**, *12*, 2997-3002.
30. Eda, G.; Yamaguchi, H.; Voiry, D.; Fujita, T.; Chen, M.; Chhowalla, M., Photoluminescence from Chemically Exfoliated Mos2. *Nano Letters* **2011**, *11*, 5111-5116.
31. Xu, D.; Xu, P.; Zhu, Y.; Peng, W.; Li, Y.; Zhang, G.; Zhang, F.; Mallouk, T. E.; Fan, X., High Yield Exfoliation of Ws2 Crystals into 1–2 Layer Semiconducting Nanosheets and Efficient Photocatalytic Hydrogen Evolution from Ws2/Cds Nanorod Composites. *ACS Applied Materials & Interfaces* **2018**, *10*, 2810-2818.
32. Lin, H.; Wang, J.; Luo, Q.; Peng, H.; Luo, C.; Qi, R.; Huang, R.; Travas-Sejdic, J.; Duan, C.-G., Rapid and Highly Efficient Chemical Exfoliation of Layered Mos2 and Ws2. *Journal of Alloys and Compounds* **2017**, *699*, 222-229.
33. Desai, J. A.; Adhikari, N.; Kaul, A. B., Chemical Exfoliation Efficacy of Semiconducting Ws2 and Its Use in an Additively Manufactured Heterostructure Graphene–Ws2–Graphene Photodiode. *RSC Advances* **2019**, *9*, 25805-25816.
34. Adilbekova, B.; Lin, Y.; Yengel, E.; Faber, H.; Harrison, G.; Firdaus, Y.; El-Labban, A.; Anjum, D. H.; Tung, V.; Anthopoulos, T. D., Liquid Phase Exfoliation of Mos2 and Ws2 in Aqueous Ammonia and Their Application in Highly Efficient Organic Solar Cells. *Journal of Materials Chemistry C* **2020**, *8*, 5259-5264.
35. Ghosh, J.; Mawlong, L. P. L.; G. B, M.; Pattison, A. J.; Theis, W.; Chakraborty, S.; Giri, P. K., Solid-State Synthesis of Stable and Color Tunable Cesium Lead Halide Perovskite Nanocrystals and the Mechanism of High-Performance Photodetection in a Monolayer Mos2/Cspbbr3 Vertical Heterojunction. *Journal of Materials Chemistry C* **2020**, *8*, 8917-8934.
36. Xu, Z.; Lv, Y.; Li, J.; Huang, F.; Nie, P.; Zhang, S.; Zhao, S.; Zhao, S.; Wei, G., Cvd Controlled Growth of Large-Scale Ws2 Monolayers. *RSC Advances* **2019**, *9*, 29628-29635.
37. Campbell, W. R.; Reale, F.; Sundaram, R.; Bending, S. J., Optimisation of Processing Conditions During Cvd Growth of 2d Ws2 Films from a Chloride Precursor. *Journal of Materials Science* **2022**, *57*, 1215-1229.

38. Lee, X.; Li, X.; Zang, X.; Zhu, M.; He, Y.; Wang, K.; Xie, D.; Zhu, H., Role of Hydrogen in Chemical Vapor Deposition Growth of Mos2 Atomic Layers. *Nanoscale* **2015**, *7*.

39. Ammerlaan, J. A. M.; Boogaard, D. R. M.; van der Put, P. J.; Schoonman, J., Chemical Vapour Deposition of Tungsten by H2 Reduction of Wc16. *Applied Surface Science* **1991**, *53*, 24-29.

40. Kang, K. N.; Godin, K.; Yang, E.-H., The Growth Scale and Kinetics of Ws2 Monolayers under Varying H2 Concentration. *Scientific Reports* **2015**, *5*, 13205.

41. Cao, E.; Lin, W.; Sun, M.; Liang, W.; Song, Y., Exciton-Plasmon Coupling Interactions: From Principle to Applications. *Nanophotonics* **2018**, *7*, 145.

42. Cong, C.; Shang, J.; Wu, X.; Cao, B.; Peimyoo, N.; Qiu, C.; Sun, L.; Yu, T., Synthesis and Optical Properties of Large-Area Single-Crystalline 2d Semiconductor Ws2 Monolayer from Chemical Vapor Deposition. *Advanced Optical Materials* **2014**, *2*, 131-136.

43. Lan, F.; Yang, R.; Xu, Y.; Qian, S.; Zhang, S.; Cheng, H.; Zhang, Y., Synthesis of Large-Scale Single-Crystalline Monolayer Ws2 Using a Semi-Sealed Method. *Nanomaterials* **2018**, *8*, 100.

44. Xie, Y.; Wang, G.; Wang, Z.; Nan, T.; Wang, H.; Wang, Y.; Zhan, Y.; Jie, W.; Ma, X., Growth of Monolayer Ws2 Single Crystals with Atmospheric Pressure Cvd: Role of Temperature. *MRS Advances* **2019**, *4*, 255-262.

45. Pak, Y., et al., Enhanced Photoresponse of Ws2 Photodetectors through Interfacial Defect Engineering Using a Tio2 Interlayer. *ACS Applied Electronic Materials* **2020**, *2*, 838-845.

46. Yao, J. D.; Zheng, Z. Q.; Shao, J. M.; Yang, G. W., Stable, Highly-Responsive and Broadband Photodetection Based on Large-Area Multilayered Ws2 Films Grown by Pulsed-Laser Deposition. *Nanoscale* **2015**, *7*, 14974-14981.

47. Huang, H.; Sheng, Y.; Zhou, Y.; Zhang, Q.; Hou, L.; Chen, T.; Chang, R.-J.; Warner, J. H., 2d-Layer-Dependent Behavior in Lateral Au/Ws2/Graphene Photodiode Devices with Optical Modulation of Schottky Barriers. *ACS Applied Nano Materials* **2018**, *1*, 6874-6881.

48. Tan, H.; Xu, W.; Sheng, Y.; Lau, C. S.; Fan, Y.; Chen, Q.; Tweedie, M.; Wang, X.; Zhou, Y.; Warner, J., Lateral Graphene-Contacted Vertically Stacked Ws2/Mos2 Hybrid Photodetectors with Large Gain. *Advanced Materials* **2017**, *29*.

49. Du, W.; Zhao, J.; Zhao, W.; Zhang, S.; Xu, H.; Xiong, Q., Ultrafast Modulation of Exciton–Plasmon Coupling in a Monolayer Ws2–Ag Nanodisk Hybrid System. *ACS Photonics* **2019**, *6*, 2832-2840.

50. Lin, Z.; Luo, P.; Zeng, W.; Lai, H.; Xie, W.; Deng, W.; Luo, Z., Improvement of Photoelectric Properties of Mos2/Ws2 Heterostructure Photodetector with Interlayer of Au Nanoparticles. *Optical Materials* **2020**, *108*, 110191.

51. Xue, Y., et al., Scalable Production of a Few-Layer Mos2/Ws2 Vertical Heterojunction Array and Its Application for Photodetectors. *ACS Nano* **2016**, *10*, 573-580.

52. Fang, C.; Han, J.; Yu, M.; Liu, W.; Gao, S.; Huang, K., Ws2/Bi2o2se Van Der Waals Heterostructure with Straddling Band Configuration for High Performances and Broadband Photodetector. *Advanced Materials Interfaces* **2022**, *9*, 2102091.

53. Yang, A., et al., Giant Enhancement of Photoluminescence Emission in Ws2-Two-Dimensional Perovskite Heterostructures. *Nano Letters* **2019**, *19*, 4852-4860.

54. Hang, D.-R.; Sun, D.-Y.; Chen, C.-H.; Wu, H.-F.; Chou, M. M. C.; Islam, S. E.; Sharma, K. H., Facile Bottom-up Preparation of Ws2-Based Water-Soluble Quantum Dots as Luminescent Probes for Hydrogen Peroxide and Glucose. *Nanoscale Research Letters* **2019**, *14*, 271.

55. Kim, M.-J.; Jeon, S.-J.; Kang, T. W.; Ju, J.-M.; Yim, D.; Kim, H.-I.; Park, J. H.; Kim, J.-H., 2h-Ws2 Quantum Dots Produced by Modulating the Dimension and Phase of 1t-Nanosheets for Antibody-Free Optical Sensing of Neurotransmitters. *ACS Applied Materials & Interfaces* **2017**, *9*, 12316-12323.

56. Singh, V. K., et al., In Situ Functionalized Fluorescent Ws2-Qds as Sensitive and Selective Probe for Fe3+ and a Detailed Study of Its Fluorescence Quenching. *ACS Applied Nano Materials* **2019**, *2*, 566-576.

57. Duan, X.; Liu, Q.; Wang, G.; Su, X., Ws2 Quantum Dots as a Sensitive Fluorescence Probe for the Detection of Glucose. *Journal of Luminescence* **2019**, *207*, 491-496.

58. Pallikkarathodi Mani, N.; Cyriac, J., Hydrothermal Synthesis of Ws2 Quantum Dots and Their Application as a Fluorescence Sensor for the Selective Detection of 2,4,6-Trinitrophenol. *New Journal of Chemistry* **2020**, *44*, 10840-10848.

59. Xie, J.; Zhang, H.; Li, S.; Wang, R.; Sun, X.; Zhou, M.; Zhou, J.; Lou, X. W.; Xie, Y., Defect-Rich Mos2 Ultrathin Nanosheets with Additional Active Edge Sites for Enhanced Electrocatalytic Hydrogen Evolution. *Advanced Materials* **2013**, *25*, 5807-5813.

60. Mahler, B.; Hoepfner, V.; Liao, K.; Ozin, G. A., Colloidal Synthesis of 1t-Ws2 and 2h-Ws2 Nanosheets: Applications for Photocatalytic Hydrogen Evolution. *Journal of the American Chemical Society* **2014**, *136*, 14121-14127.

61. Lai, G.-J.; Lyu, L.-M.; Huang, Y.-S.; Lee, G.-C.; Lu, M.-P.; Perng, T.-P.; Lu, M.-Y.; Chen, L.-J., Few-Layer Ws2–Mos2 in-Plane Heterostructures for Efficient Photocatalytic Hydrogen Evolution. *Nano Energy* **2021**, *81*, 105608.

62. Wu, E.; Wu, D.; Jia, C.; Wang, Y.; Yuan, H.; Zeng, L.; Xu, T.; Shi, Z.; Tian, Y.; Li, X., In Situ Fabrication of 2d Ws2/Si Type-Ii Heterojunction for Self-Powered Broadband Photodetector with Response up to Mid-Infrared. *ACS Photonics* **2019**, *6*, 565-572.

63. Lan, C.; Li, C.; Wang, S.; He, T.; Jiao, T.; Wei, D.; Jing, W.; Li, L.; Liu, Y., Zener Tunneling and Photoresponse of a Ws2/Si Van Der Waals Heterojunction. *ACS Applied Materials & Interfaces* **2016**, *8*, 18375-18382.

64. Wu, D., et al., Ultrabroadband and High-Detectivity Photodetector Based on Ws2/Ge Heterojunction through Defect Engineering and Interface Passivation. *ACS Nano* **2021**, *15*, 10119-10129.

65. Singh, V. K.; M. Yadav, S.; Mishra, H.; Kumar, R.; Tiwari, R. S.; Pandey, A.; Srivastava, A., Ws2 Quantum Dot Graphene Nanocomposite Film for Uv Photodetection. *ACS Applied Nano Materials* **2019**, *2*, 3934-3942.

66. Wu, W.; Zhang, Q.; Zhou, X.; Li, L.; Su, J.; Wang, F.; Zhai, T., Self-Powered Photovoltaic Photodetector Established on Lateral Monolayer Mos2-Ws2 Heterostructures. *Nano Energy* **2018**, *51*, 45-53.

67. Gao, W., et al., 2d Ws2 Based Asymmetric Schottky Photodetector with High Performance. *Advanced Electronic Materials* **2021**, *7*, 2000964.

68. Wang, X.; Liu, P.; Yap, B.; Xia, R.; Wong, W.-Y.; He, Z., High-Quality Ws2 Film as a Hole Transport Layer in High-Efficiency Non-Fullerene Organic Solar Cells. *Nanoscale* **2021**, *13*, 16589-16597.

69. Cao, J.; Tang, G.; You, P.; Wang, T.; Zheng, F.; Zhao, J.; Yan, F., Enhanced Performance of Planar Perovskite Solar Cells Induced by Van Der Waals Epitaxial Growth of Mixed Perovskite Films on Ws2 Flakes. *Advanced Functional Materials* **2020**, *30*, 2002358.

70. Keawphaisan, L.; Harnchana, V.; Pimanpang, S.; Amornkitburung, V., Hydrothermal Synthesis of the Composited Ws2–W5o14–Mwcnts for High Performance Dye-Sensitized Solar Cell Counter Electrodes. *Journal of Materials Science: Materials in Electronics* **2017**, *28*, 18765-18772.

71. Rashidi, S.; Rashidi, S.; Heydari, R. K.; Esmaeili, S.; Tran, N.; Thangi, D.; Wei, W., Ws2 and Mos2 Counter Electrode Materials for Dye-Sensitized Solar Cells. *Progress in Photovoltaics: Research and Applications* **2021**, *29*, 238-261.

72. Hussain, S.; Shaikh, S. F.; Vikraman, D.; Mane, R. S.; Joo, O.-S.; Naushad, M.; Jung, J., Sputtering and Sulfurization-Combined Synthesis of a Transparent Ws2 Counter Electrode and Its Application to Dye-Sensitized Solar Cells. *RSC Advances* **2015**, *5*, 103567-103572.

73. Wu, M.; Wang, Y.; Lin, X.; Yu, N.; Wang, L.; Wang, L.; Hagfeldt, A.; Ma, T., Economical and Effective Sulfide Catalysts for Dye-Sensitized Solar Cells as Counter Electrodes. *Physical Chemistry Chemical Physics* **2011**, *13*, 19298-19301.

74. Yang, W., et al., Electrically Tunable Valley-Light Emitting Diode (Vled) Based on Cvd-Grown Monolayer Ws2. *Nano Letters* **2016**, *16*, 1560-1567.

75. Yin, W.; Bai, X.; Chen, P.; Zhang, X.; Su, L.; Ji, C.; Gao, H.; Song, H.; Yu, W. W., Rational Control of Size and Photoluminescence of Ws2 Quantum Dots for White Light-Emitting Diodes. *ACS Applied Materials & Interfaces* **2018**, *10*, 43824-43830.
76. Andrzejewski, D.; Myja, H.; Heuken, M.; Grundmann, A.; Kalisch, H.; Vescan, A.; Kümmell, T.; Bacher, G., Scalable Large-Area P–I–N Light-Emitting Diodes Based on Ws2 Monolayers Grown Via Mocvd. *ACS Photonics* **2019**, *6*, 1832-1839.

Chapter 2

Controlled Growth of WS_2 Quantum dots by liquid exfoliation and Monolayer WS_2 film by Chemical Vapor Deposition

In this chapter, we discuss controlled synthesis strategies for WS_2 quantum dots by chemical exfoliation and monolayer WS_2 films by chemical vapor deposition (CVD). Our results demonstrate the formation of nanosheets, quantum dot clusters, and uniformly distributed ultra-small quantum dots by a simple top-down colloidal exfoliation. We have found that synthesis parameters such as the choice of solvent, and post-treatments like prolonged heating, centrifugation, etc., play an important role in the size and overall morphology of the quantum dots. On the other hand, for the growth of two-dimensional (2D) monolayer WS_2 films via CVD, we consider three different approaches. It can be noted in the subsequent sections that tuning several factors such as the growth temperature, duration, gas pressure, use of halide-assisted methods, the lateral size, and the thickness of the 2D WS_2 film can be controlled. The growth process essentially depends on the precursors used (WO_3 and S). In the first process, we use a relatively lower temperature of ~750 °C to grow triangular 1L-WS_2 flakes. To improve upon the lateral dimension of the WS_2 film and the film's overall crystalline quality, we raise the substrate temperature to 1000 °C, in the second process. By making adjustments to the growth temperature and duration, we were able to grow large-area mono- to bilayer WS_2. Next, to ensure high-quality monolayer growth, we adopt a halide-assisted technique, in the third process. Halides such as NaCl aid in the lateral growth of the WS_2 layer. The substrate temperature was varied from 800 to 940 °C. We find that the higher the growth temperature, the better the crystallinity of the as-grown film. We have successfully synthesized continuous monolayer WS_2 films on a variety of substrates. The strategic placement of growth substrates above the WO_3 powder and the NaCl inside the high-temperature zone of the CVD system plays an important role in nucleation and large area growth. Herein, we present a systematic account of the controlled synthesis of ultra-small WS_2 QDs and the optimized growth of large-area monolayer WS_2 film.

2.1. Synthesis of WS_2 nanosheets and quantum dots by liquid exfoliation

2.1.1 Introduction

Ever since the discovery of graphene, layered two-dimensional (2D) transition metal dichalcogenides (TMDs) have progressively garnered attention in semiconductor research due to their fascinating properties and applications in a multitude of areas[1-5]. TMDs represent a large family of layered materials with the formula MX_2, where M is a transition metal and X is a chalcogen. A single layer of MX_2 consists of hexagonally arranged covalently bonded M atoms sandwiched between similarly bonded X atomic layers. These individual building blocks are stacked by weak van der Waals forces. Tungsten disulfide or WS_2 is a TMD that is closely related to MoS_2 and has recently inspired investigative research owing to its superior optical properties and larger spin-orbit coupling[5-7].

As such, zero-dimensional (0D) systems, such as quantum dots (QDs) have attracted attention due to their ultra-small sizes, quantum confinement, edge effects, and higher surface-to-volume ratios. Several synthesis strategies have been adopted to synthesize 0D-2D WS_2 nanostructures by various methods, such as hydrothermal synthesis[8-9], chemical exfoliation[10-11], Li^+/K^+ intercalation[12-13], pulsed laser deposition[14-15], CVD[16-17], magnetron sputtering[18-19], etc. Among these methods, colloidally exfoliated WS_2 QDs exhibit excellent light absorption, tunable visible PL emission owing to quantum confinement, water solubility, and low-cost solution processing, which opens up avenues for different applications. The morphology of these QDs can be determined greatly by various post-processing techniques.

2.1.2 Experimental section

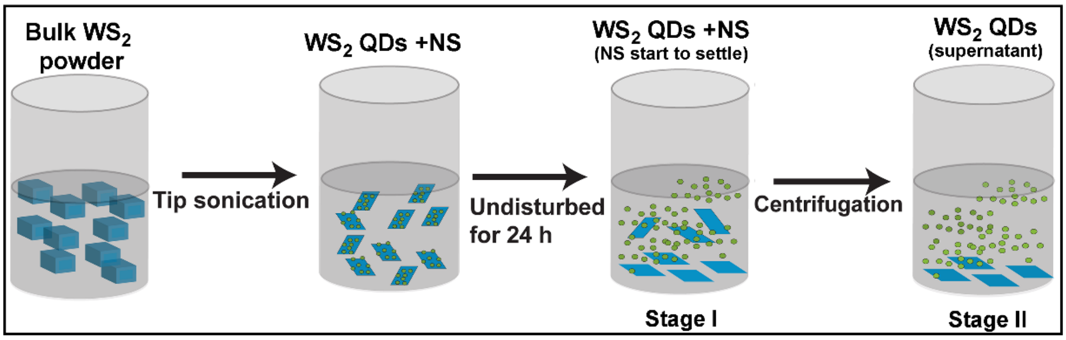

Fig. 2.1. Schematic of the synthesis process of WS_2 quantum dots via chemical exfoliation.

Mono- to bi-layer WS_2 quantum dots (QDs) and WS_2 nanosheets (NS) were directly synthesized via a top-down liquid exfoliation method. 80 mg of WS_2 powder (Sigma Aldrich, 99%) was dispersed in 80 ml N-methyl-2-pyrrolidinone (NMP) (Alfa Aesar, HPLC grade, 95%) in a beaker and sonicated using an ultrasonic homogenizer (Sonic Ruptor 250, Omni International) with an ultrasonic frequency output of 20 kHz for 15 hours. The exfoliation was carried out in an iced bath to eliminate any heating effect that might be caused in the process.

The obtained suspension was allowed to settle overnight. At this stage, the solution consists of WS_2 QDs as well as NS (see **Fig. 2.1** (Stage I)). To segregate the QDs from the NS, centrifugation is carried out at different rates: 4000 rpm, 8000 rpm, and 12000 rpm for 45 minutes at a controlled temperature of 4 °C. The colorless supernatant contained the WS_2 QDs, and the settled residue consisted of a mixture of WS_2 QDs and WS_2 nanosheets (Stage II, **Fig. 2.1**). The steps involved in the synthesis of WS_2 QDs are shown schematically in **Fig. 2.1.**

2.1.3 Characterization techniques

The morphology, size, and structural properties of the as-prepared WS_2 QDs have been studied by a transmission electron microscope (TEM) (JEOL-JEM 2010 operated at 200 kV). Samples for the TEM analyses have been prepared on carbon-coated Cu grids of 400 mesh size (Pacific Grid, USA). Atomic force microscopy (AFM) (Cypher, Oxford Instruments) images were acquired to confirm the layer thickness of the WS_2 QDs. UV-Vis-NIR absorbance spectroscopy measurements of the samples were recorded using a commercial spectrophotometer (PerkinElmer, UV win Lab). The steady-state PL measurements were performed by using a Xe lamp, coupled to a commercial spectro-fluorimeter (Horiba Scientific, Fluoromax-4). X-ray Photoelectron Spectroscopy (XPS) was employed to study the elemental composition of the as-prepared WS_2 QDs (Ulvac-Phi, Inc.). Crystallinity, defects, etc. in the WS_2 QDs have been studied by a high-resolution micro-Raman spectrometer (LabRam HR800, Jobin-Yvon) with excitation wavelengths (λ_{ex}) 532 nm (Ar ion laser). The excitation source was focused with a 100X objective lens, a spot size of 1 µm, and a laser power of 1.5 mW, and the signal was collected by a CCD in a backscattering geometry sent through a multimode fiber grating of 1800 grooves/mm.

2.1.4 Results and Discussions

2.1.4.1 Morphology Studies

The typical morphological properties of the as-prepared WS_2 QDs and NS were studied using TEM imaging. **Fig. 2.2(a)** shows the bright-field TEM image of the WS_2 QD embedded NS. Note that it corresponds to Stage I of the synthesis process. The QDs almost exhibit uniform size. TEM images were acquired for the QDs obtained after centrifugation. **Fig. 2.2(b)** displays the WS_2 QDs obtained at the centrifugation rate of 4000 rpm. The QD diameters vary in the range of ~2-14 nm, with the size averaging at ~6.3 nm. The QDs obtained after centrifugation at 8000 rpm display a narrower log-normal distribution (see **Fig. 2.2(c)**), the average size of the QDs being ~4.7 nm. However, the QDs obtained after a higher centrifugation rate of 12000 rpm exhibit a more uniform size distribution (see **Fig 2.2(d)**). The sizes vary in the range of ~1.5-5 nm, with an average QD diameter of ~2.4 ± 0.1 nm, as shown in the inset of **Fig 2.2(d)**. Given the narrow size distribution and smaller size, we carry out further experiments on these QDs. Thus, any further mention of the WS_2 QDs corresponds to the QDs obtained after 12000 rpm, unless mentioned otherwise.

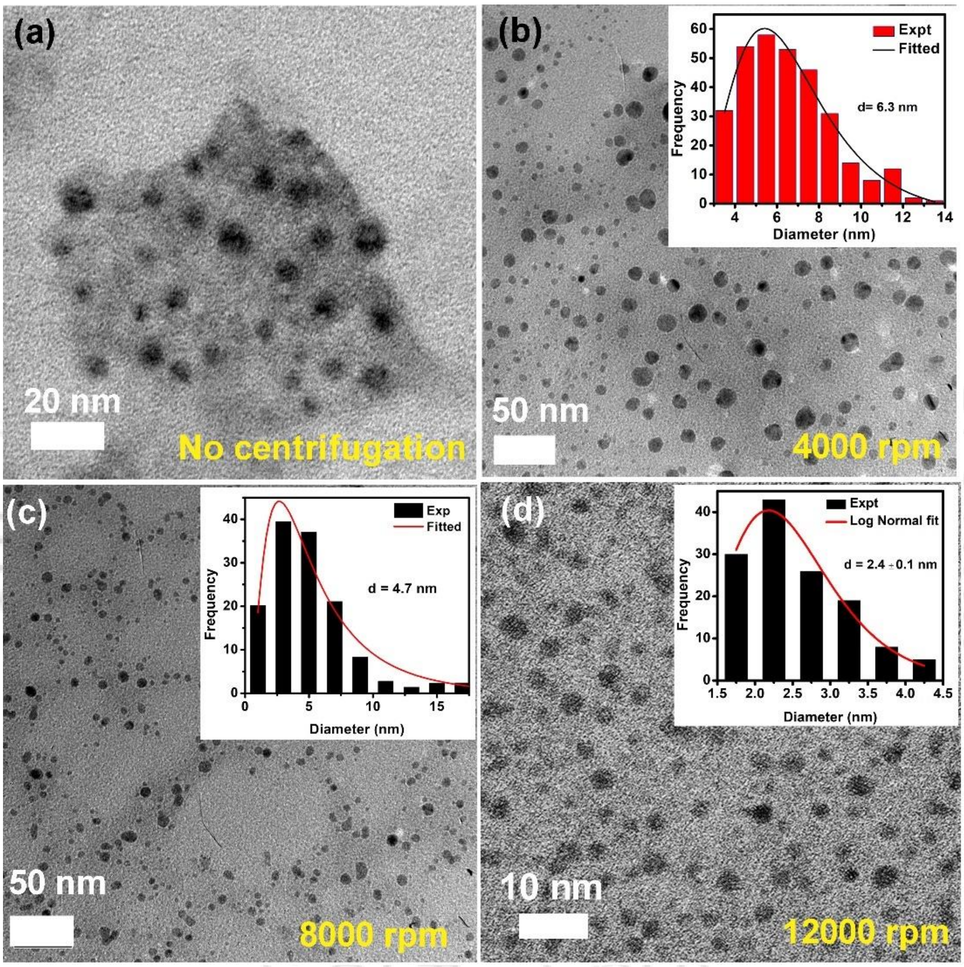

Fig. 2.2. (a) TEM image of the WS_2 QDs and the NS before centrifugation. TEM images of the WS_2 QDs obtained at the centrifugation rates (b) 4000 rpm, (c) 8000 rpm, and (d) 12000 rpm, respectively. The insets display the respective QD size distributions with log-normal fitting.

Fig. 2.3(a-c) exhibits the high-resolution TEM (HRTEM) images of WS_2 QDs. The images confirm the crystalline nature of the QDs. The insets show the Gatan software processed IFFT images of single WS_2 QDs that display clear lattice planes with a spacing of 0.23 nm corresponding to the (103) plane of WS_2. **Fig. 2.3(d)** shows an AFM image of the as-prepared WS_2 QDs. The height profile (inset) is obtained across the green line and it confirms the presence of monolayer as well as bilayer QDs.

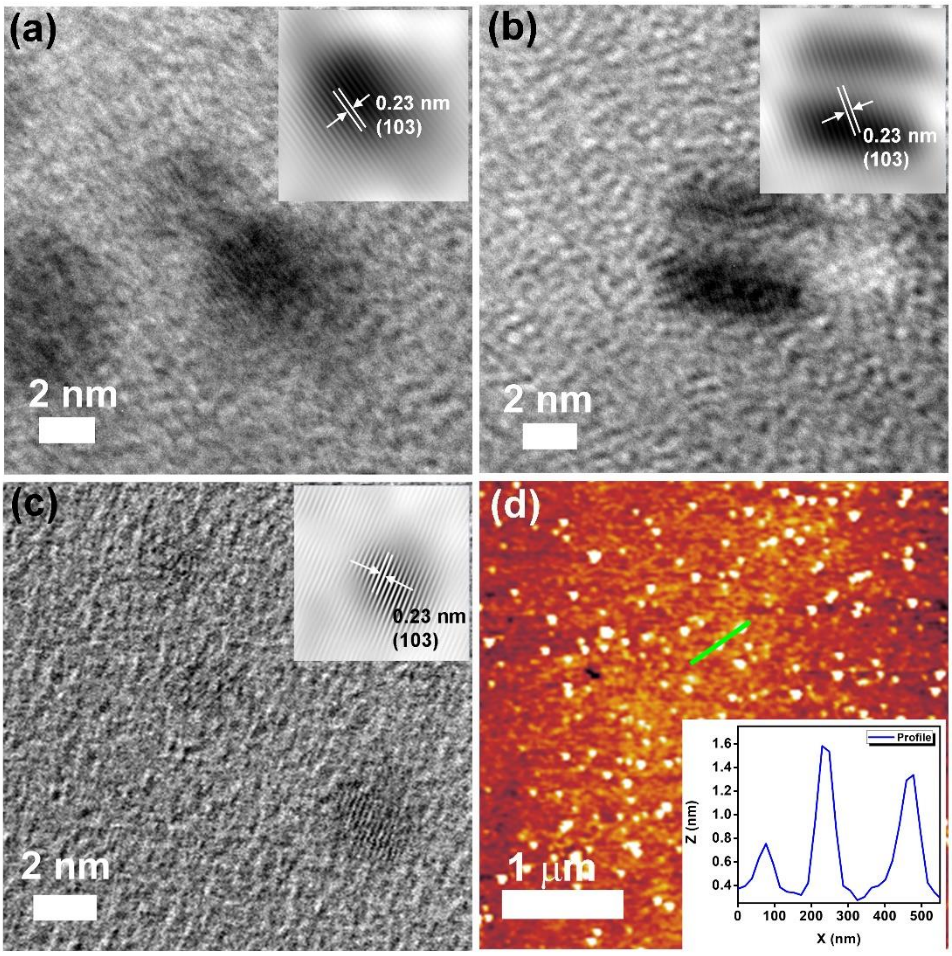

Fig. 2.3. (a-c) HRTEM lattice images of WS_2 QDs. Insets show the respective IFFT images of the lattice planes of WS_2. (d) AFM image of WS_2 QDs. The inset shows the height profile across the green line showing the presence of monolayer and bilayer QDs.

2.1.4.2 Optical analysis

To further investigate the properties of the as-prepared nanostructured WS_2 QDs and nanosheets, the samples were characterized by absorption spectroscopy. **Fig. 2.4(a)** shows the UV–vis absorption spectra of bulk WS_2 as a reference. **Fig. 2.4(b)** depicts the UV-Vis absorption spectra for the sample obtained at Stage I of the synthesis process, before centrifugation. There are clear signatures of the QDs as well as NS in the sample. WS_2 QDs exhibit strong UV absorbance, while the peak around ~620 nm corresponds to the layered nanosheets and is attributed to the optical transition at the K point of the Brillouin zone[10, 20-21]. This feature is, however, absent in the absorption spectrum of the WS_2 QDs. There is a strong UV absorption peak at ~297 nm (see **Fig. 2.4(c)**). It is to be noted that the sample used for this measurement is obtained after centrifugation at 12000 rpm. There is a broad absorption tail extending over the visible region. This property is typical of WS_2 QDs[22]. To determine the optical band gap of the as-prepared QDs, we use the Tauc plot for direct bandgap semiconductors. The inset of **Fig. 2.4(c)** shows the bandgap of the WS_2 QDs as ~3.48 eV.

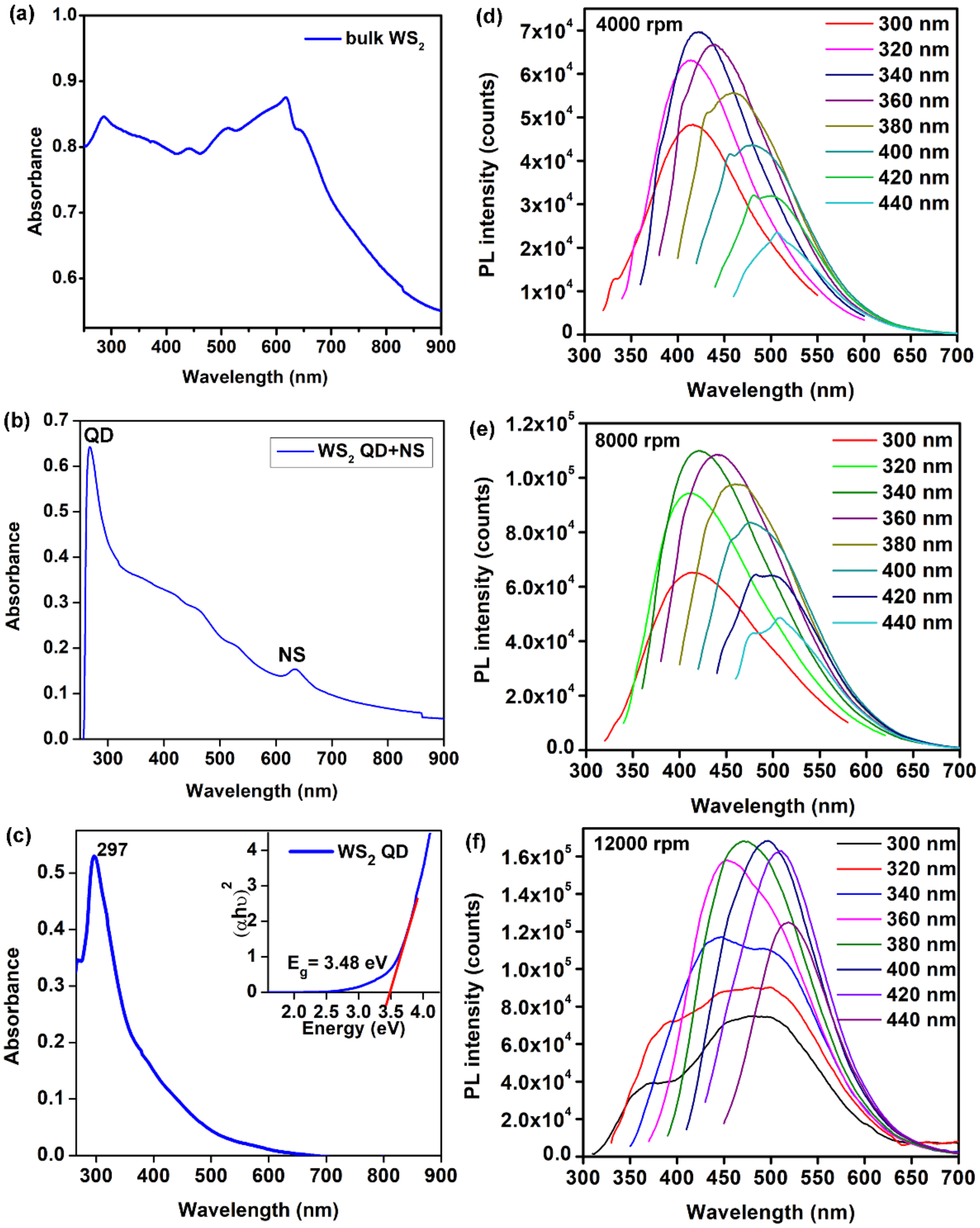

Fig. 2.4. UV-Vis absorption spectra for (a) bulk WS_2 powder, (b) WS_2 QDs and NS, and (c) WS_2 QDs. Excitation wavelength-dependent PL spectra of WS_2 QDs obtained from different centrifugation rates: (d) 4000 rpm, (e) 8000 rpm, and (f) 12000 rpm.

The excitonic Bohr radius of WS_2 QDs is ~1.2 nm[23-24]. Thus, the expected quantum confinement effect of the as-prepared WS_2 QDs was studied and characterized with the excitation-dependent PL spectra. The excitation wavelength (λ_{ex}) was varied from 300 nm to 440 nm using a monochromator and a Xenon lamp. **Fig. 2.4(d, e)** display the spectra for the

QDs corresponding to 4000 and 8000 rpm, respectively. In both cases, the PL intensity is maximum for the λ_{ex} ~340-360 nm. The emission spectra are broad and exhibit redshift with the increase in the λ_{ex}. Note that these QD samples exhibit broad-size distributions, as discussed in the previous section. However, the QDs obtained at 12000 rpm exhibit a narrower size distribution. Likewise, the corresponding λ_{ex} dependent PL spectra differ from the former case. The emission spectra are broad at lower λ_{ex} and become gradually narrower and exhibit a systematic redshift with the increase in the λ_{ex} (see **Fig. 2.4(f)**). Thus, it is clear that apart from the quantum size effect, the PL emission is essentially contributed by recombination at different selective states, depending on the wavelength of excitation. The contributing recombination pathways are discussed in detail in **Chapter 3**.

2.1.4.3. Compositional and Structural analysis

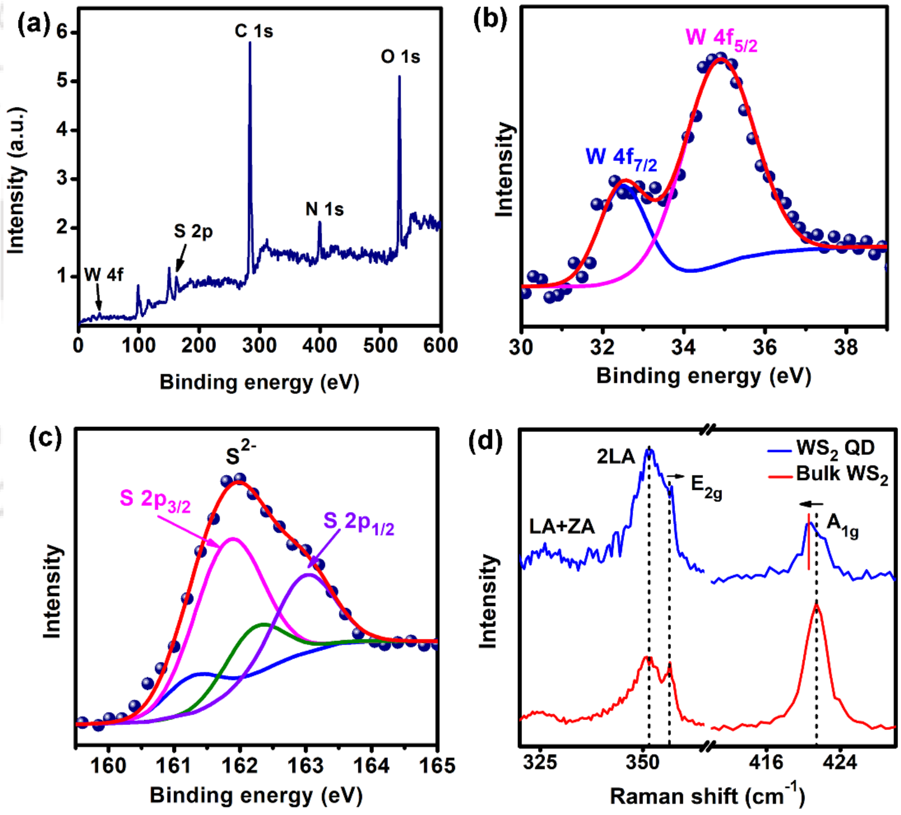

Fig. 2.5. (a) XPS survey scan of as-prepared WS_2 QDs. XPS spectra of the WS_2 QD showing (b) W 4f and (c) S 2p respectively. The symbols are the experimental data, and the solid curves are the Gaussian fittings. (d) Comparative Raman spectra of bulk WS_2 and WS_2 QDs films at excitation of 532 nm Ar laser.

The chemical composition of the as-prepared WS_2 QDs was determined using XPS analysis. **Fig. 2.5(a)** depicts the full range XPS survey scan spectrum for the WS_2 QDs. In addition to W 4f and S 2p peaks, there is the presence of C 1s (~284 eV), N 1s (~399 eV), and

O 1s (~531 eV) peaks. The carbon contamination is well known in XPS analysis, and the presence of N may be due to the residual trace of NMP, which was used for the sample preparation[10, 25]. In **Fig. 2.5(b),** the broad W 4f envelope is fitted with peaks at 32.5 eV and 34.8 eV, which are known to be from W $4f_{7/2}$ and W $4f_{5/2}$, respectively. These peaks correspond to the 4^+ oxidation state of W, which concur with previous reports for 2H-WS_2[22]. The S 2p XPS of the WS_2 QDs is displayed in **Fig. 2.5(c).** The peaks at ~161.8 eV and ~162.9 eV correspond to the S $2p_{3/2}$ and S $2p_{1/2}$, respectively, and are attributed to the divalent sulfide ions (S^{2-}). Additionally, there are extra peaks at 161.4 eV (with 10.3 % spectral weight) and 162.1 eV (with 14.4 % spectral weight) in the S-2p spectra of the WS_2 QDs, which are due to the presence of surface defects (S vacancies) in the WS_2 QDs. These defects are created during the synthesis by the liquid phase chemical exfoliation[22, 26].

Micro-Raman measurements were carried out on WS_2 QD and bulk powder using Ar laser excitation at 532 nm. **Fig. 2.5(d)** shows that the bulk WS_2 powder has two characteristic Raman modes E_{2g} (356.6 cm^{-1}) and A_{1g} (421.4 cm^{-1}), which correspond to the in-plane vibration and the out-of-plane vibration of the W-S bond of 2H WS_2. In addition to these characteristic modes, there is another mode at 351.5 cm^{-1} that is ascribed to the second-order longitudinal acoustic mode (2LA)[27-28]. Additionally, the low-intensity peak at 325.6 cm^{-1} is assigned to a combination of acoustic processes, LA, from longitudinal acoustic mode and ZA, attributed to out-of-plane acoustic phonons. WS_2 QDs also exhibit a similar Raman spectrum with a marginal blue shift in the E_{2g} peak by 0.4 cm^{-1} and a redshift in the A_{1g} peak by 0.8 cm^{-1} due to the decrease in the number of layers in the as-prepared WS_2 QDs, as compared to the bulk counterpart. The presence of these Raman modes confirms good crystallinity of the as-prepared WS_2 QDs[10]. Note that there is an increase in the relative intensity of the 2LA mode in the QDs that is attributed to the reduction of layer number and lateral size of WS_2 due to the confinement effect on the Raman acoustic phonon mode[28].

More exhaustive analyses of the as-prepared WS_2 QDs are carried out using various spectroscopic tools in the subsequent chapters. Their optical and photoconduction properties have been utilized for photoluminescence-based applications and in developing optoelectronic devices.

2.2. Lower temperature growth of monolayer WS_2 flakes via chemical vapor deposition

2.2.1 Introduction

As discussed in the previous section, owing to their several novel properties, 2D WS_2 structures have proven to be ideal for applications in various areas. However, despite their advantages, QDs display poor carrier transport in comparison to their 1D, 2D, and 3D counterparts. For practical applications, especially in optoelectronics, 2D monolayer-bilayer WS_2 acts as a more robust platform. Hence, the synthesis of large uniform wafer-scale WS_2 single crystal becomes crucial. Consequently, among different methods, chemical vapor deposition (CVD) is extensively employed for the growth of large-area, homogeneous, and high-quality monolayer 2D TMD films. Moreover, monolayer WS_2 (1L-WS_2) exhibits properties like excellent visible photoluminescence due to quantum confinement, large spin-orbit splitting, and high exciton binding energy. CVD has proved to be reliable for producing high-quality 2D WS_2 films with high crystallinity favorable for investigating fundamental properties and device fabrication. Although this area is being extensively studied, the CVD growth of monolayer single-crystal WS_2 with a large domain size is still a challenge without the incorporation of a seed layer[29] or H_2 gas[30]. The process primarily depends on the precursors, WO_3 and S. To optimize controlled growth, besides varying the typical growth parameters, the proper design of a growth system plays a significant role. As such, given the melting point of WO_3 is as high as 1300 °C, the importance of a space-confined growth system is explored[31-32]. This is done to enhance the partial pressure of the WO_3 vapor[33], to obtain uniform 1L-WS_2 of large domain sizes.

2.2.2. Experimental details

A two-zone tube furnace was employed to grow two-dimensional WS_2 monolayer single crystal on SiO_2 substrates via the CVD process. The precursors used were 200 mg of Sulphur powder (Sigma Aldrich, 99.9% purity) and 3 mg of WO_3 powder (Sigma Aldrich, 99.9%). A smaller one-end sealed quartz tube was placed inside a 2-inch diameter quartz tube, such that the sealed side lay in heating zone 2. The purpose of the inner quartz tube is to locally confine WO_3 vapor and increase the partial pressure near the substrates to facilitate growth at a lower temperature. **Fig. 2.6(a)** displays the schematic setup for the CVD process. In the deposition zone, i.e., zone 2, the WO_3 powder was kept sandwiched between two SiO_2 substrates, such that the polished sides faced each other. The W side or zone 2 was heated up to 150 °C at a ramping rate of 10 °C/min, followed by purging with ultra-high purity Ar gas at 300 sccm for 30 min to remove the surface-adsorbed impurities. Subsequently, it was heated to 550 °C at a fast ramping rate, and then to 750 °C at a rate of ~3 °C/min. Sulfur was placed in the center of heating zone 1 in a quartz boat (see **Fig. 2.6(a)**). The distance between the precursors was maintained at 20 cm. Zone 1 was allowed to heat to 150 °C at the beginning of the growth time to facilitate sulfurization of WO_3. The temperature in zone 2 was kept at 750° C for 5 minutes for the growth and then the furnace was allowed to cool down to room temperature naturally. Ultra-high purity Ar gas was flowed at the rate of 100 sccm during the whole growth process maintaining a pressure of 1 mbar inside the tube. The temporal variation of temperature for both the heating zones is depicted in **Fig. 2.6(b).**

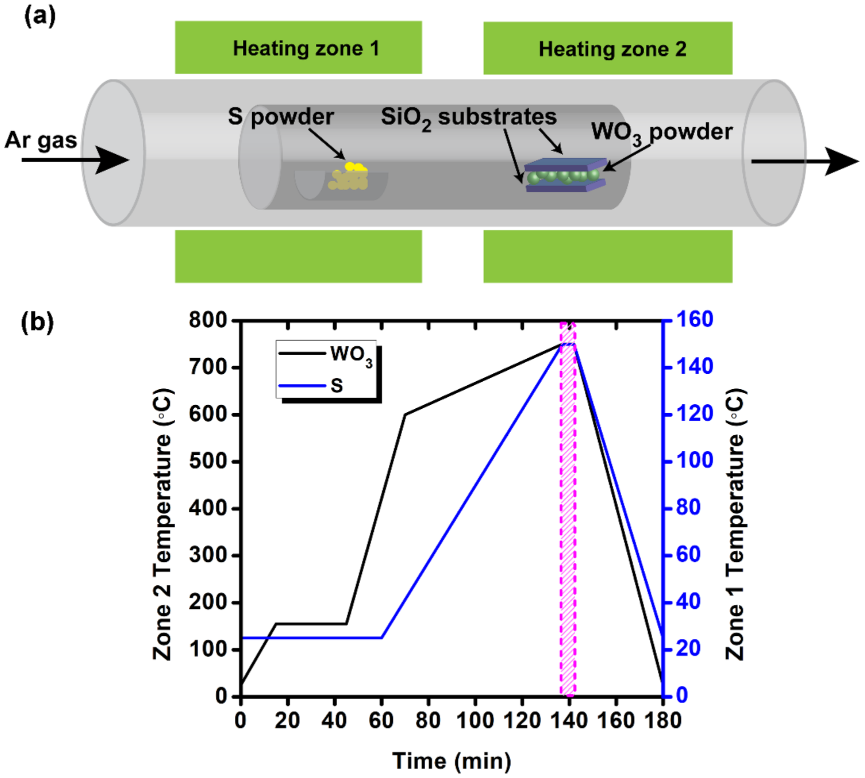

Fig. 2.6. (a) Schematic of the chemical vapor deposition (CVD) setup for the growth of monolayer WS_2 flakes on SiO_2 substrates. (b) Variation of temperature as a function of time at the WO_3 boat (Zone 2) and the sulfur boat (Zone 1) positions during the CVD process.

2.2.3 Characterization techniques

Atomic force microscopy (AFM) (Cypher, Oxford Instruments) images were acquired to confirm the layer thickness of the CVD-grown WS_2. Crystallinity, defects, etc. in the WS_2 QDs have been studied by a high-resolution micro-Raman spectrometer (LabRam HR800, Jobin-Yvon) with excitation wavelengths (λ_{ex}) 488 nm (Ar ion laser). The steady-state micro-PL measurements were performed by using the same micro-Raman spectrometer (LabRam HR800, Jobin-Yvon) with an excitation wavelength of 488 nm. X-ray photoelectron spectroscopy (XPS) with an Al Kα excitation was employed to study the elemental composition of the as-prepared 1L-WS_2.

2.2.4 Results and Discussions

2.2.4.1. Morphology study

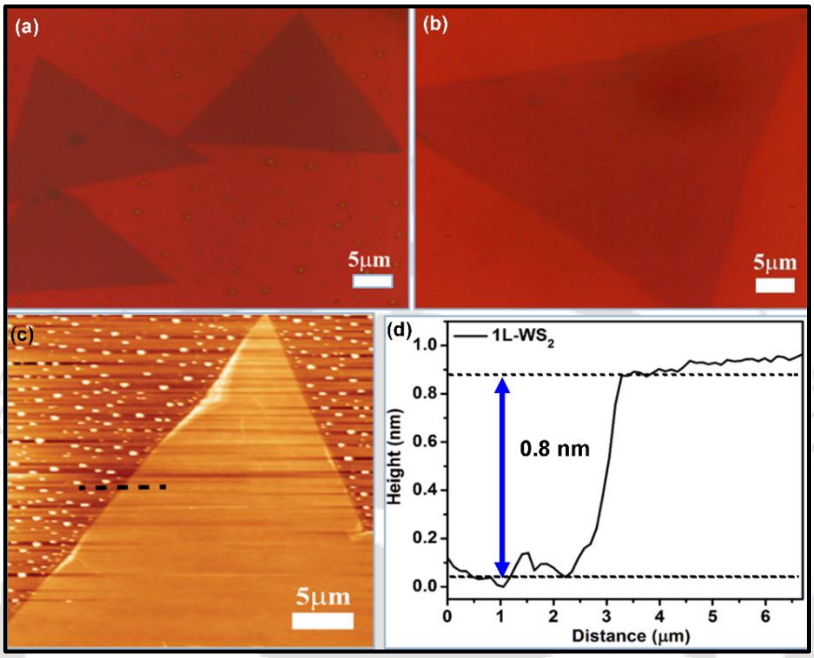

Fig 2.7. (a, b) Optical microscopy images of the triangular 1L-WS_2 flakes. (c) AFM image of the triangular 1L-WS_2 flake. (d) the height profile along the dashed line on (c).

The optical microscopy (OM) images of the CVD-grown WS_2 film are presented in **Fig. 2.7(a, b).** The lateral sizes of the triangular monolayered crystals lie in the range of 20-30 µm. To ascertain the layer number of the CVD-grown WS_2, AFM analysis is utilized. **Fig 2.7(c)** displays the AFM image of a single triangular WS_2 flake. The height profile along the black dotted line reveals a step height of ~ 0.8 nm, which corresponds to monolayer WS_2 (**Fig 2.7(d)**). Thus, the as-grown WS_2 layers are mostly monolayer in nature.

2.2.4.2. Micro-Raman and Photoluminescence study

Micro-Raman spectroscopy is a powerful tool in the characterization of 2D-WS_2, and all 2D-TMDs, in general. For comparison, the Raman spectrum corresponding to bulk WS_2 is shown with the CVD-grown WS_2 film in **Fig. 2.8(a)**. Laser excitation of 488 nm (Ar laser) was used for the measurement. The characteristic E_{2g} and A_{1g} modes of bulk WS_2 appear at 358.5 and 423.1 cm^{-1}, respectively. The CVD-grown WS_2, however, exhibits its A_{1g} mode at 418.5 cm^{-1}, thus showing a pronounced redshift of ~4.6 cm^{-1}. The frequency difference between these optical Raman modes, Δk, therefore, reduces from 64.6 cm^{-1}, in bulk, to 60.4 cm^{-1} in the CVD-grown WS_2. This is a clear indication of the formation of monolayer WS_2, in the process [28].

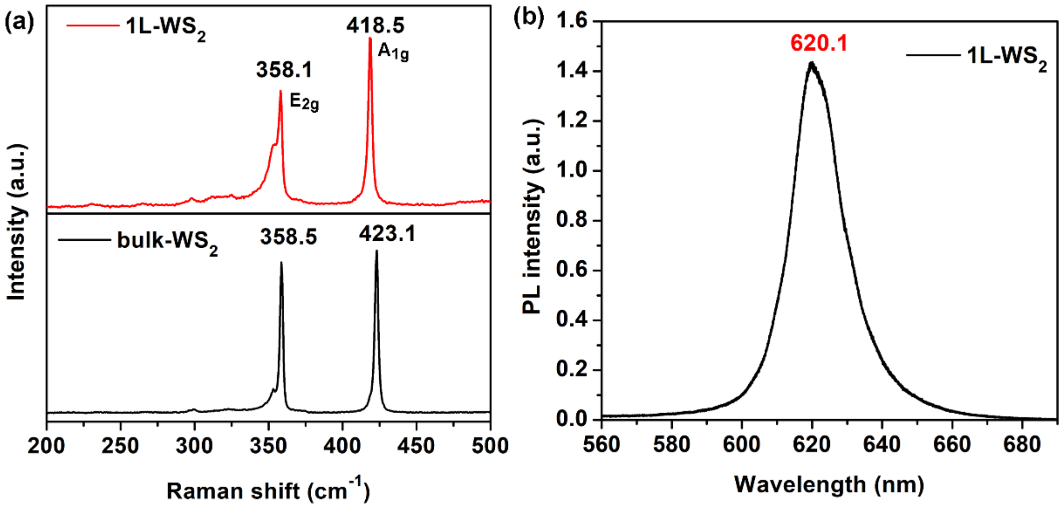

Fig 2.8. (a) Comparative micro-Raman spectra of bulk WS_2 and 1L-WS_2. (b) Micro-PL spectra of 1L-WS_2. The excitation wavelength used for the measurements is 488 nm.

Due to its direct bandgap, monolayer WS_2 exhibits a strong visible PL emission at room temperature. This feature is, however, absent in bulk WS_2 owing to its indirect band gap. Therefore, to confirm the growth of monolayer WS_2, PL measurements were carried out using laser excitation of 488 nm. The micro-PL spectrum obtained at the same spot shows a sharp PL emission spectrum with a peak position at ~620.1 nm (**Fig. 2.8(b)**). The sharp emission peak primarily corresponds to the A exciton emission derived from the direct bandgap transition from the conduction band minima to the valence-band maxima of 1L-WS_2. The overall emission, however, also consists of contributions from other excitonic states, which will be discussed in detail later. The recorded PL spectrum further ascertains the successful formation of 1L-WS_2[34].

2.3 CVD growth of monolayer WS_2 films

2.3.1 Introduction

The preceding section elucidated the experimental conditions involved in the CVD growth of monolayer WS_2. However, only the formation of small triangular 1L-WS_2 flakes was possible with the method, and it suffered from issues related to repeatability. Therefore, subsequently, we attempted to make a few adjustments to the CVD process parameters for the production of monolayer WS_2 of higher crystalline quality. The growth of WS_2 via CVD is essentially based on the reaction of WO_3 and S in the vapor phase. The growth temperature was tuned to 1000 °C, to ensure a higher vapor pressure of WO_3. However, it is to be noted that the growth of WS_2 via CVD is very sensitive to the sulfidation rate, which if not optimized, can prove to be detrimental to the growth of large-scale WS_2 film[33]. Thus, carrier gas flow and chamber pressure play a vital role in the process. Our study attempts to acquire a detailed understanding of the favorable conditions required for the controlled growth of monolayer WS_2.

2.3.2. Experimental details

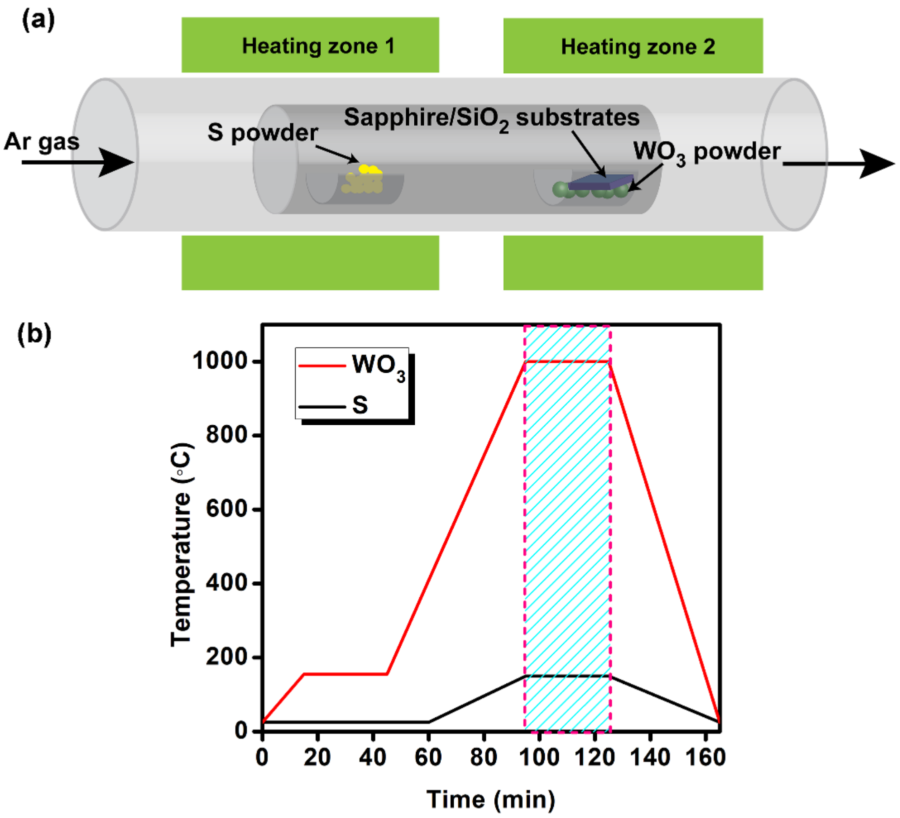

Fig. 2.9. (a) Schematic of the CVD) setup for the growth of monolayer WS_2 on Sapphire/SiO_2 substrates. (b) Temperature variation profile of the WO_3 and sulfur source positions during the CVD process.

A modified CVD process was adopted for the growth of monolayer WS_2. The growth temperature was fixed at 1000 °C. **Fig. 2.9(a)** shows the schematic of the CVD setup. The substrates are placed face down over the WO_3 powder in heating zone 2. Followed by the initial purging, zone 2 was programmed to heat to 1000 °C at a ramping rate of 17 °C/min. The growth pressure was maintained at ~0.8 mbar. The growth was allowed to take place for 30 min. The furnace was subsequently cooled down to room temperature naturally. **Fig. 2.9(b)** displays the variation of temperature of the heating zones with respect to time. The rest of the parameters matched those of the growth protocol discussed in the previous section.

2.3.3. Results and discussions

2.3.3.1. Morphology and Raman Study.

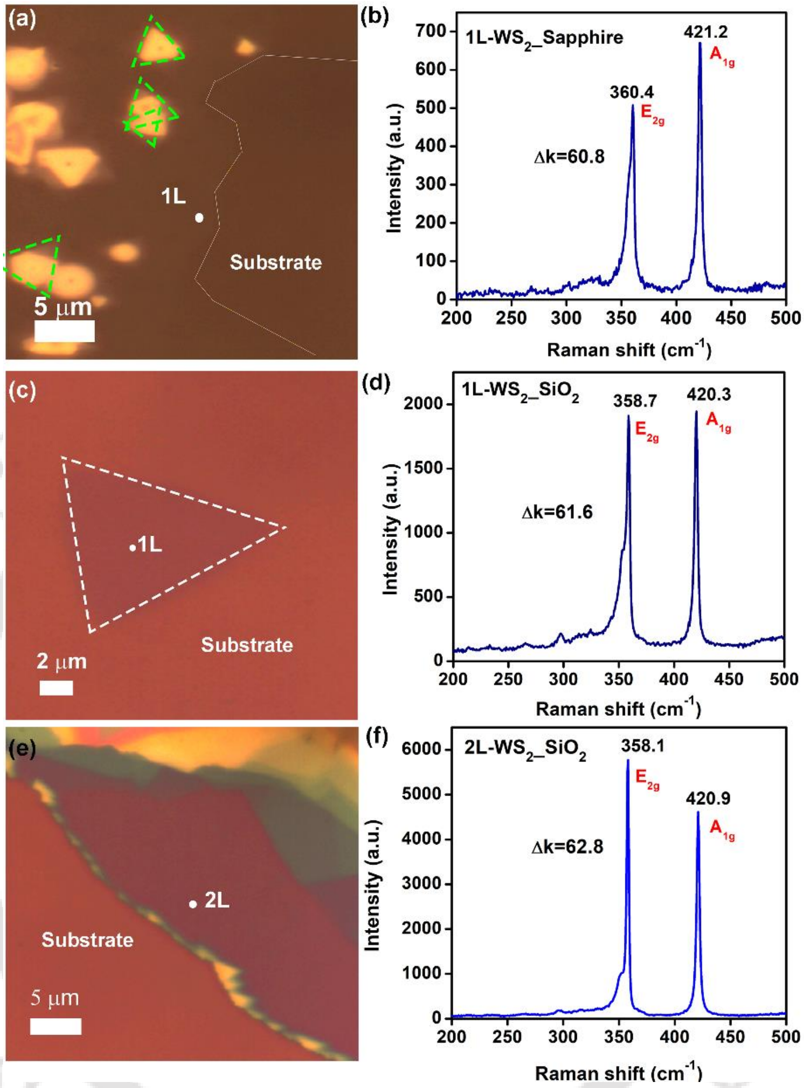

Fig. 2.10. (a) Optical microscopy image of CVD grown 1L-WS_2 on sapphire and (b) the corresponding Raman spectrum, (c) Optical microscopy image of CVD grown 1L-WS_2 on SiO_2, and (d) corresponding Raman spectrum, and (e) Optical microscopy image of 2L-WS_2 on SiO_2 and (f) corresponding Raman spectrum

Fig. 2.10. displays the optical microscope images of the CVD-grown WS_2 and the corresponding micro-Raman spectra acquired at the marked positions. Large area 1L-WS_2 is successfully grown on the sapphire substrate, however, smaller triangles of few-layer WS_2 are also apparent (few marked with green dashed lines), as depicted in **Fig. 2.10(a)**. To affirm the monolayered nature of the as-grown film, a Raman spectrum is acquired at the white spot. **Fig. 2.10(b)** shows the spectrum consisting of the characteristic E_{2g} and A_{1g} modes of WS_2 at 360.4 cm^{-1} and 421.2 cm^{-1}, respectively. The frequency difference of 60.8 cm^{-1} implies 1L-WS_2. Similarly, the number of layers in the triangular WS_2 flake on an SiO_2 substrate (in **Fig. 2.10(c)**)

was ascertained by the Raman spectrum displayed in **Fig 2.10(d)**[28]. The Δk amounts to 61.6 cm^{-1}. However, another position on the same SiO_2 substrate exhibited a film of higher contrast (**Fig. 2.10(e)**). The corresponding Raman spectrum **(Fig. 2.10(f)**) revealed that the characteristic E_{2g} and A_{1g} modes appear at 358.1 cm^{-1} and 420.8 cm^{-1}. The Δk of ~63 cm^{-1} implies a higher layer number. Thus, the experiment leads to mostly bilayer growth of WS_2 over a larger area.

2.3.3.1. Photoluminescence study

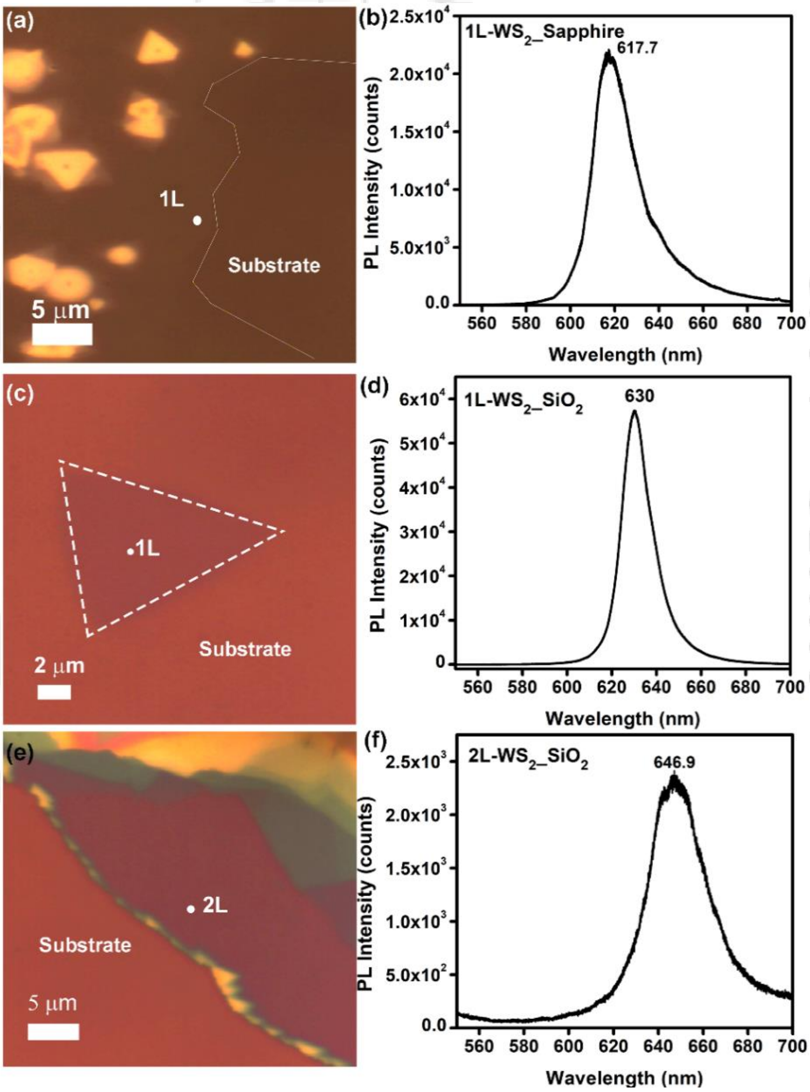

Fig. 2.11. (a) Optical microscopy image of CVD grown 1L-WS_2 and (b) corresponding PL spectrum on sapphire, (c) Optical microscopy image of CVD grown 1L-WS_2 and (d) corresponding PL spectrum on SiO_2, and (e) Optical microscopy image of 2L-WS_2 and (f) corresponding PL spectrum on SiO_2.

Micro-PL spectra were recorded for the as-grown WS_2 films on sapphire and SiO_2 substrates (see **Fig. 2.11**). Note that the spectra were recorded on the same spots where the micro-Raman spectra were acquired earlier. Although **Fig. 2.11(a-d)** correspond to 1L-WS_2, it is observed that there is a shift in the PL peak positions and a change in the PL intensity depending on the growth substrate. The effect of the substrate will be discussed in the next section. **Fig. 2.11(e)** displays an OM image of 2L-WS_2. The corresponding PL spectrum reveals an emission peak at ~647 nm. Also, the intensity is greatly reduced as compared to the monolayer counterpart. Thus, the recorded PL spectra at different locations further confirm the simultaneous growth of 1L-WS_2 as well as 2L-WS_2 on SiO_2 substrates by this method.

2.4. Salt-assisted CVD growth of large-area 1L-WS_2

2.4.1 Introduction

In the previous section, we were successfully able to grow larger area WS_2 films on Sapphire and SiO_2 substrates. Additionally, we have acquired an understanding of some of the vital experimental parameters for the synthesis. However, to improve upon the lateral growth of a monolayer film and reduce the possibility of few-layer growth, we incorporate a halide-assisted CVD process. Alkali metal halides such as NaCl react with the WO_3 to form a volatile tungsten oxyhalide species aiding the transport of W to the substrates[35]. Furthermore, an optimized quantity of NaCl kept in close proximity to the precursor WO_3 at the high-temperature zone facilitates in weakening of the interlayer adhesion governed by van der Waals forces[36-37], thus, limiting the possibility of the bilayer to multilayer growth.

In this section, we present a detailed study of the growth of monolayer WS_2 films via CVD at different growth temperatures (800-940 °C) and on different substrates (sapphire, SiO_2, and quartz). The film grown at 940 °C covers an area of a few hundred micrometers for all the substrates. The space-confined experimental setup is maintained to optimize the partial pressure of the WO_3 vapor. Also, to establish optimum control over the sulfidation rate, the S boat is kept further away from the WO_3 boat. Thus, homogenous growth of monolayer WS_2 film spread over a larger area is successfully achieved.

2.4.2. Experimental details

Large area 1L-WS_2 single crystals were grown via a halide-assisted CVD technique on various substrates, such as sapphire, quartz, and SiO_2. At first, 10 mg of the tungsten source, WO_3 powder is placed in a quartz boat towards the closed end of the inner one-end closed quartz tube, such that it lies in the center of the heating zone 2. For better lateral growth, we add an optimized quantity of NaCl (Merck, 99%), 1 cm away from the WO_3 powder, such that the ratio of NaCl to WO_3 lies between 1:7 to 1:10. The substrates face down are placed right above the precursor, as shown in **Fig. 2.12(a).**

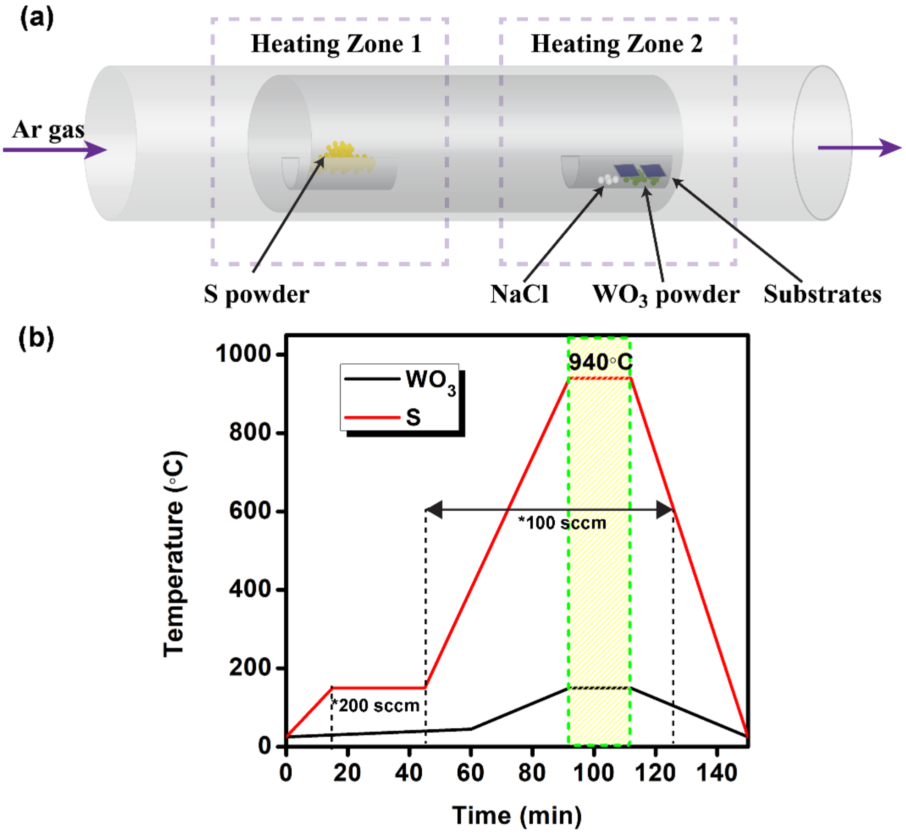

Fig. 2.12. (a) Schematic of the CVD setup for the growth of large-area WS_2 on various substrates. (b) Temperature variation profile of the WO_3 boat and the sulfur boat positions during the process. The growth temperature is 940°C. The asterisk * denotes the Ar gas flow rate.

At the upstream zone, 150 mg of Sulphur powder is kept in another quartz boat placed 25 cm away from the WO_3 boat. Zone 2 is heated up to 150 °C at a ramping rate of 10 °C/min, followed by purging with Ar gas at 300 sccm for 30 min before the growth to remove the surface-adsorbed impurities. Subsequently, the Ar gas flow rate is fixed at 100 sccm. The temperature of zone 2 is ramped at a rate of 17 °C/min up to different growth temperatures: 800 °C, 900 °C, and 940 °C. Depending on the set growth temperature, the duration of the ramping up varied. The growth duration was fixed at 15 min. At the beginning of the growth stage, the temperature of the sulfur, i.e., zone 1 reached 150 °C. The pressure inside the tube was maintained at ~0.5 mbar. The furnace was allowed to cool naturally after 15 min. However, the growth pressure was maintained till zone 2 reached 600 °C. The temperature variation profile of both precursor zones is presented in **Fig. 2.12(b).** It is to be noted that **Fig. 2.12(b)** corresponds to the experiment with a growth temperature of 940 °C.

2.4.3. Results and discussions

2.4.3.1. Morphology Studies

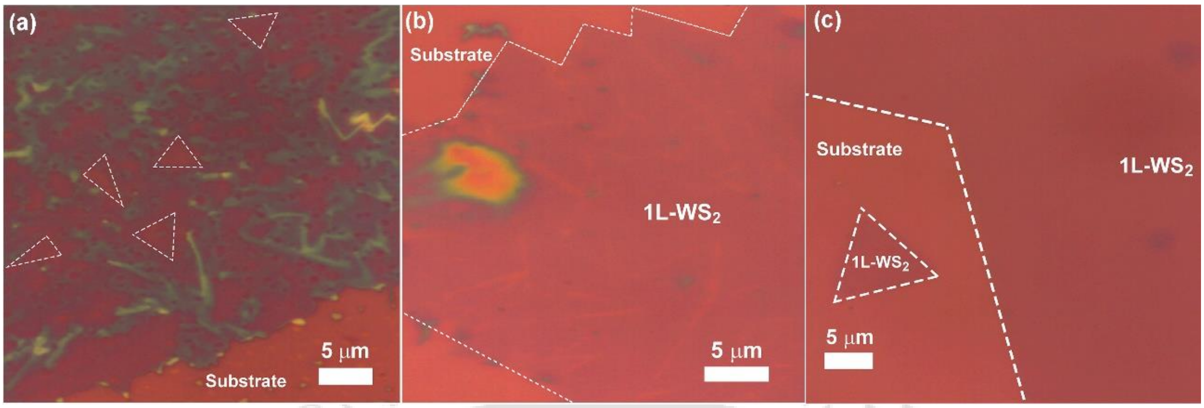

Fig. 2.13. Optical microscopy images of CVD-grown WS_2 on SiO_2 at (a) 800 °C, (b) 900 °C, and (c) 940 °C, respectively.

The optical microscopy images of the WS_2 film grown on SiO_2 substrates at different temperatures ranging from 800 to 940 °C are displayed in **Fig. 2.13(a-c)**. It is observed that under different growth temperatures, WS_2 flakes attain a triangular shape which was observed in earlier sections as well. The as-grown triangular flakes are seen to be interconnected to form a continuous film. The triangular or near triangular shape arises from the fact that the flake shape is determined by the growth rate of the WS_2 edges[38]. The film grown at 800 °C consists of a combination of monolayer to few-layer WS_2, as seen in **Fig. 2.13(a)**. The triangles marked with dotted lines are monolayered and are of the order ~5 μm. At a higher growth temperature, i.e., 900 °C (**Fig. 2.13(b)**), a uniform monolayer WS_2 film was successfully grown. However, the film appears to have grain boundaries and is not continuous over a large area. Lastly, in the case of the WS_2 grown at 940 °C (**Fig. 2.13(c)**), the film quality is observed to be superior. Smaller triangular flakes merge to form a sizably continuous and homogenous film over an area of the order of hundreds of micrometers with excellent uniformity.

Fig. 2.14(a-c) displays the OM images of the 1L-WS_2 films successfully grown on different substrates (SiO_2, quartz, and sapphire, respectively) at a growth temperature of 940 °C. The dotted lines mark the region of monolayer growth. To confirm the monolayer nature of the as-grown film, AFM is carried out for WS_2 grown on the SiO_2 substrate (**Fig. 2.14(d)**). The inset displays the height profile along the white line, which reveals a step height of ~ 0.8 nm, corresponding to monolayer WS_2. Thus, the salt-assisted CVD growth yields a large area of 1L-WS_2 film on a variety of substrates.

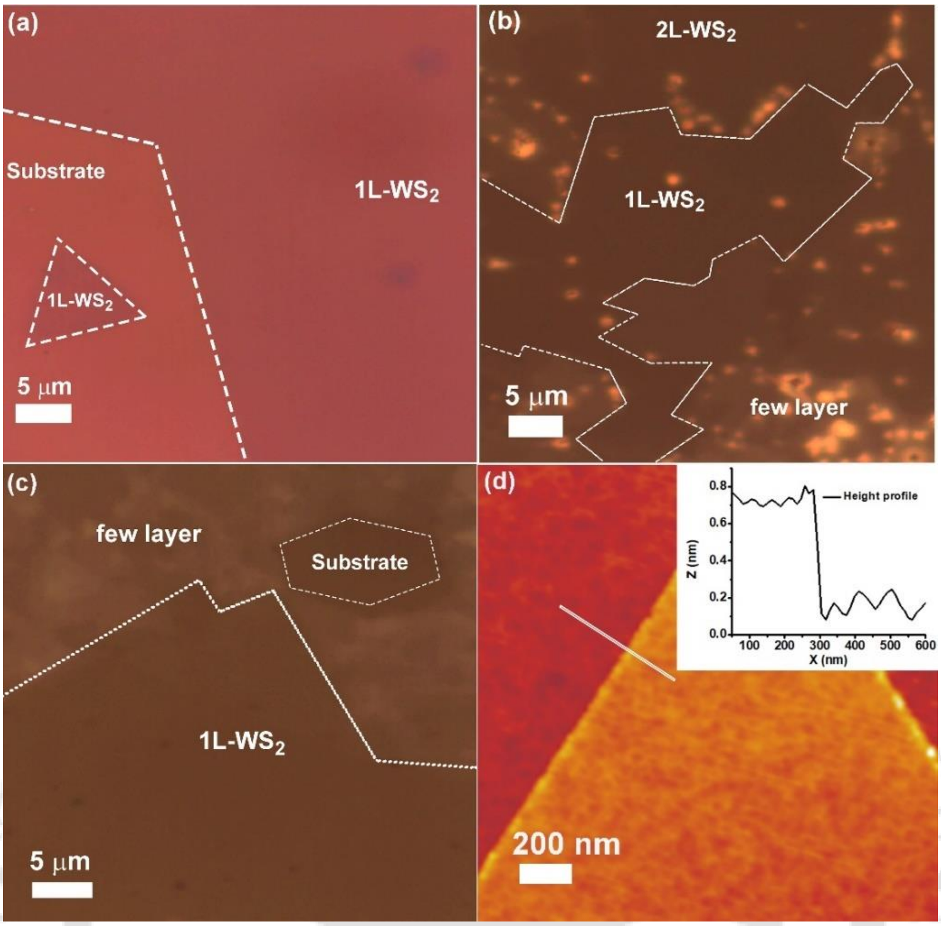

Fig. 2.14. Optical microscopy images of CVD grown 1L-WS_2 at 940 °C on (a) SiO_2, (b) Quartz, and (c) Sapphire substrates, respectively. (d) AFM image of CVD grown 1L-WS_2 on a SiO_2 substrate. The inset shows the height profile along the white line.

2.4.3.2. Raman Study

Fig. 2.15(a) shows the comparative micro-Raman spectra of the CVD-grown WS_2 at different growth temperatures in the range of 800-940 °C. Laser excitation of 488 nm was used for the Raman measurement. The Raman spectra show the presence of the two characteristic optical Raman modes (E_{2g} and A_{1g}), which correspond to the in-plane and the out-of-plane vibrations of the S atoms with respect to the W atoms, respectively, confirming good crystallinity of the as-grown WS_2 layer. The frequency difference between the two peaks (Δk) can be used to identify the layer number of TMDs[39]. At 800 °C, the spectrum was acquired in one of the dotted triangles, and Δk is found to be ~ 61 cm^{-1}, which confirms their monolayered nature[28]. The FWHM of the E_{2g} and A_{1g} modes were ~2.9 cm^{-1} and ~3.5 cm^{-1}, respectively, indicating good crystallinity. At higher temperatures, 900 and 940 °C, the Raman spectra analyses yielded Δk of ~ 61.6 cm^{-1} and 61.3 cm^{-1}, respectively. Note that there is an enhancement in the intensity with temperature.

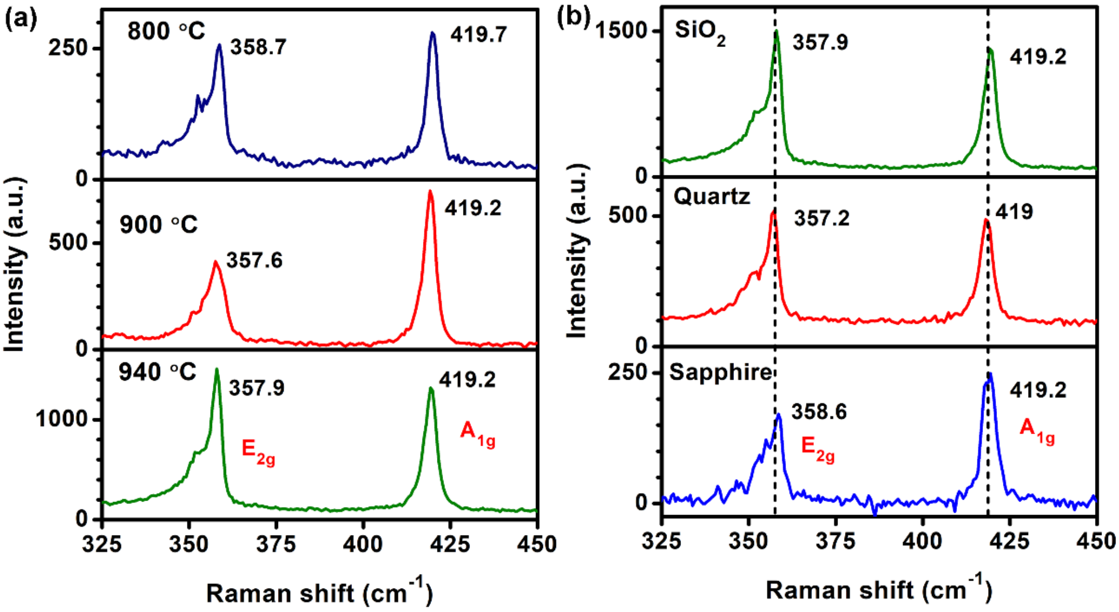

Fig. 2.15. (a) Comparative micro-Raman spectra of 1L-WS_2 grown on SiO_2 substrates by CVD at growth temperatures 800 °C, 900 °C, and 940 °C. (b) Comparative substrate-dependent micro-Raman spectra of 1L-WS_2 grown at 940 °C on SiO_2, quartz, and sapphire substrates.

All other parameters in these experiments were fixed, to solely study the effect of the growth temperature. With different growth temperatures, there is a difference in the concentration of precursors on the growth substrate. We find that the WS_2 film grown at 940 °C shows Raman peaks with higher intensities and narrower peak widths. Therefore, although the synthesis of monolayer WS_2 is possible over the said temperature range, there is an overall improvement in the film quality and the crystallinity of the as-grown WS_2 with an increase in the temperature. Furthermore, we observed similar results for the films grown on other substrates (see **Fig. 2.15(b)**). The Δk values are found to be ~61.0 ± 0.7 cm^{-1} for the WS_2 film on the different substrates, as tabulated in **Table 1**.

Table 1: Summary of the E_{2g} and A_{1g} Raman modes for the different substrates. The peak separation (Δk ~61 cm^{-1}) signifies the growth of monolayer WS_2.

Substrate	E_{2g} (cm^{-1})	A_{1g} (cm^{-1})	Δk (cm^{-1})
SiO_2	357.9	419.2	61.3
Quartz	357.2	419	61.7
Sapphire	358.6	419.2	60.4

The positions of the E_{2g} peak are seen to vary from substrate to substrate. This is primarily due to the built-in strain induced during the growth due to the difference in the thermal expansion coefficients (TEC) between the substrate and WS_2. The TEC of WS_2 is about one order higher than that of SiO_2, while it is almost comparable to that of sapphire[40-41]. The E_{2g} mode is believed to be more sensitive to uniaxial strain since it corresponds to in-plane vibrations[41-42]. Thus, the SiO_2 substrate introduces uniaxial strain in the WS_2 film, while for sapphire, it is nearly a strain-free film, as evident from the redshift in the E_{2g} mode by ~1.3 cm^{-1} with respect to SiO_2. On the other hand, the A_{1g} band is impacted by the doping level of the system[41]. Thus, the slight variation in the A_{1g} peak positions might be due to the presence of charged impurities at the interface between the WS_2 film and the substrate. Nevertheless, in all cases, the Δk values imply the growth of monolayer WS_2 film.

2.4.3.3. XPS Study

The elemental composition of the CVD grown 1L-WS_2 on an SiO_2 substrate is ascertained by the XPS study. **Fig. 2.16(a)** presents the survey scan spectrum of the sample over the range of 0-600 eV. In addition to W 4f (~34 eV) and S 2p (~162 eV) peaks, there are peaks corresponding to S 2s (~244 eV), W 4p (~425 eV), Si (~102 eV and ~153 eV) and O 1s (~531 eV). The O 1s peak may be due to the presence of WO_3 residue as well as due to the SiO_2 substrate.

Fig. 2.16(b) displays the high-resolution XPS spectra of W 4f for the 1L-WS_2. The peaks attributed to W $4f_{7/2}$ (~32.5 eV) and W $4f_{5/2}$ (~34.7 eV), respectively, verify the formation of highly crystalline 2H-WS_2. The additional peaks at 31.7 eV and 33.5 eV match with the 4th oxidation state of W of the metallic 1T-phase of WS_2, which concurs with the literature[15, 22]. The shoulder peak at 35.9 eV, which corresponds to the W^{6+} state of the oxide confirms the presence of unreacted WO_3. Additionally, a small peak corresponding to the W 5p state is evident in the spectrum. The high-resolution core-level spectrum corresponding to S 2p of the 1L-WS_2 is shown in **Fig. 2.16(c).** The presence of the S^{2-} states, S $2p_{3/2}$ and S $2p_{1/2}$ is confirmed by the peaks at 162.2 eV and 163.4 eV, respectively[41]. The as-grown samples of 1L-WS_2 contain sulfur vacancies as evident from the peaks at 161.2 eV and 162.7 eV[26], which collectively constitute ~16% of the spectrum.

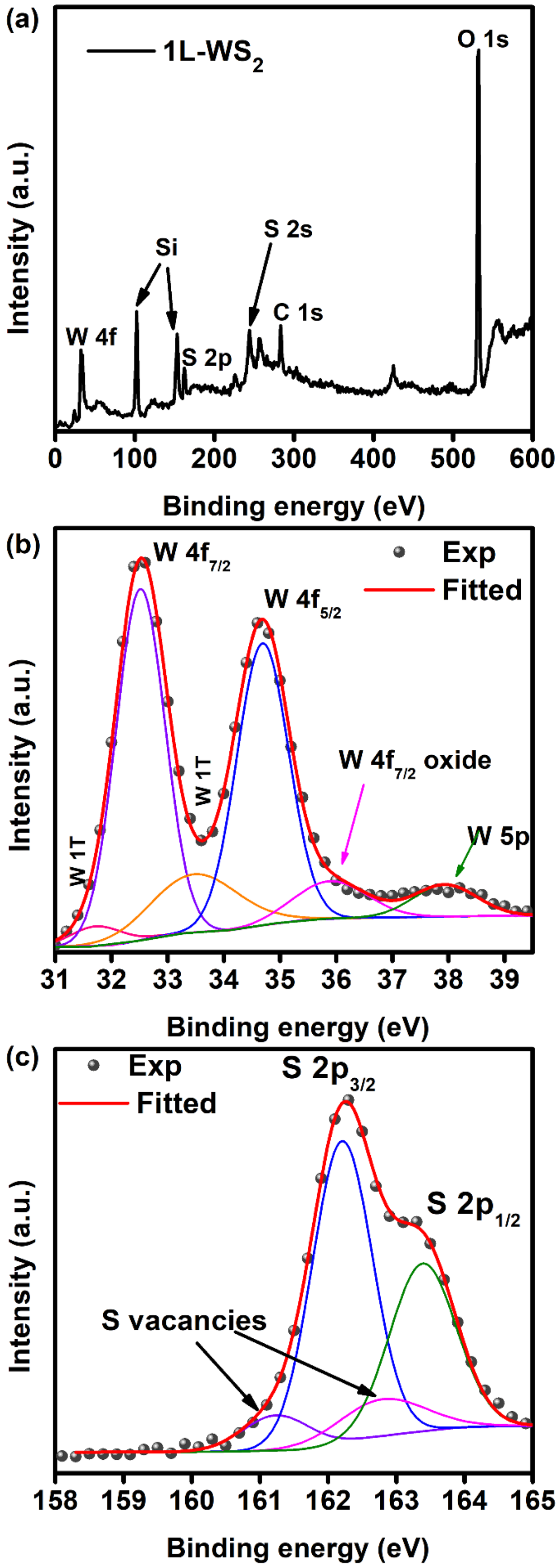

Fig. 2.16. (a) XPS survey scan spectrum of as-prepared 1L-WS_2. High-resolution XPS spectra of the 1L-WS_2 showing (b) W 4f and (c) S 2p respectively. The symbols are the experimental data, and the solid curves are the Gaussian fittings, with Shirley baseline.

2.4.3.4. Photoluminescence Study

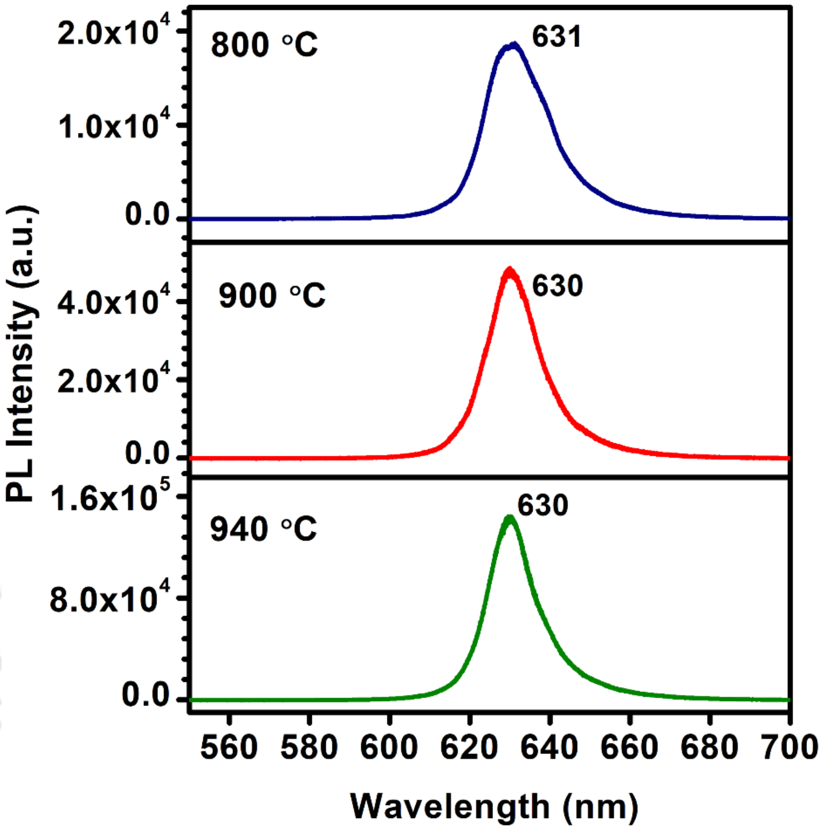

Fig. 2.17. Comparative micro-PL spectra of 1L-WS_2 grown on SiO_2 substrates by CVD at growth temperatures 800 °C, 900 °C, and 940 °C.

Fig. 2.17 shows the growth temperature-dependent PL spectra of 1L-WS_2 grown on SiO_2 substrates, taken at the same spots as the corresponding Raman spectra in **Fig. 2.15(a).** The emission characteristics are similar for each case, however, there is an overall enhancement in the intensity with higher growth temperature. **Fig. 2.18(a)** displays the comparative PL spectra on different substrates on a stacked plot. As discussed in **Section 2.4.3.2.**, the effect of the built-in strain determines the PL peak position, which differs from substrate to substrate. As expected, sapphire being the substrate with nearly no strain exhibits a blue shift with respect to the as-grown film on the SiO_2 substrate. Additionally, although the PL peak positions for SiO_2 and quartz substrate is nearly the same (~630 nm), the PL emission spectrum of the 1L-WS_2 on quartz is broader than that of the SiO_2 case. To understand the origin of the PL emission band, we deconvoluted each spectrum of the WS_2 film grown on different substrates by three Gaussian peaks (see **Fig. 2.18(b-d)**) – the neutral exciton or A_0 peak, derived from the direct bandgap of WS_2, the negative trion or A_{tr} peak, that arises from a three-body quasi excitonic state, and a defect bound X exciton. The negative trion emission is caused by light n-type doping of WS_2 due to the presence of a residual electron population in the system depending on the experimental conditions. We observed the presence of peak X at ~650 nm in all the samples, which is attributed to the radiative recombination of defect-bound excitons. The 1L-WS_2 film grown on an SiO_2 substrate shows the highest PL intensity, while the film grown on quartz shows the lowest intensity, measured under identical conditions. The deconvolution is carried out noting that the trion binding energy is of the order ~35 meV[34]. The spectral weight of A_0 is as high as ~74.5% for the SiO_2 substrate, while it is the lowest (~56.0 %) for the quartz case. The corresponding spectral weights of the A_{tr} are observed to be ~16.4% and ~ 24%, while the defect-bound X amounted to 9% and 20%, respectively. The PL spectrum of the 1L-WS_2 grown on sapphire is similar to that of SiO_2, however, the peak is substantially blue-shifted. The neutral excition A_0, trion A_{tr}, and defect X exciton, respectively, constitute 70.5%, 21.5%, and 8% of the overall spectrum. Thus, the spectral weights of the trion A_{tr} and the defect peak X are found to be highest in the case of WS_2 grown on the quartz substrate. The trion spectral weight is the lowest for the WS_2 grown on the SiO_2 substrate, explaining the highest PL intensity. Different weights of the constituents give rise to change in the overall peak positions for different substrates.

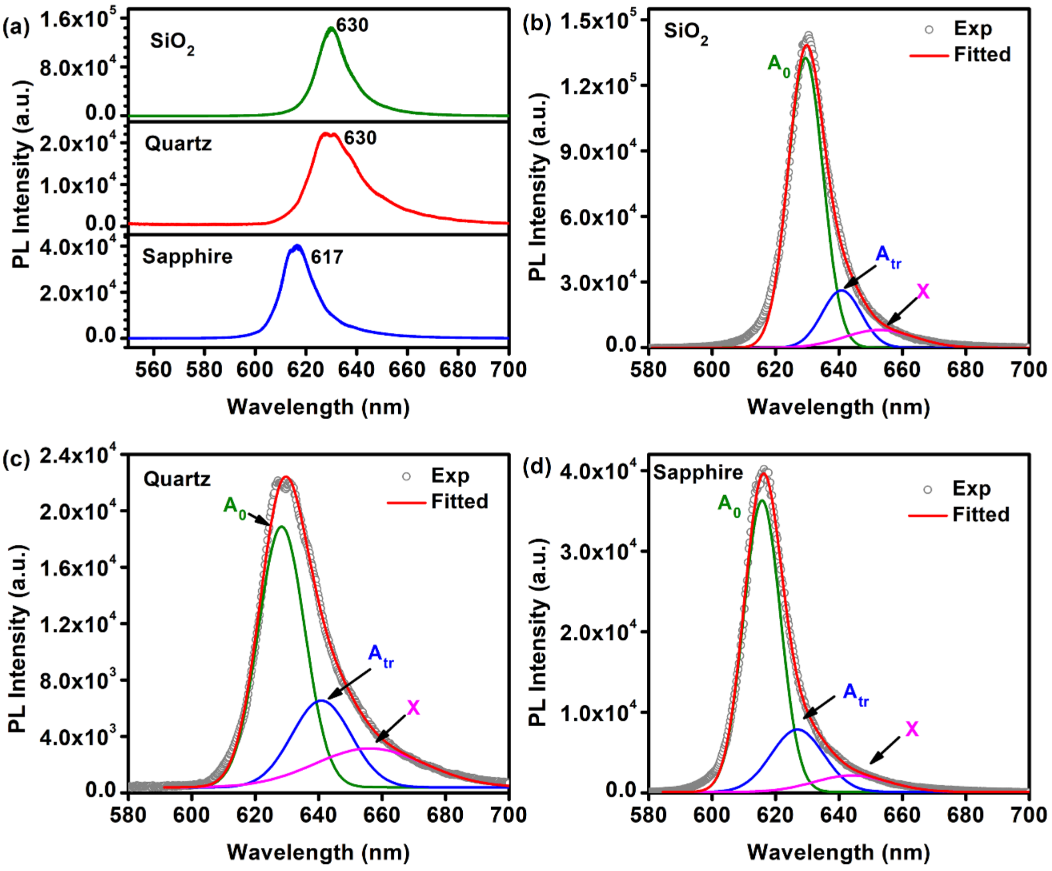

Fig. 2.18. (a) Comparative substrate-dependent micro-PL spectra of 1L-WS_2 grown at 940 °C on SiO_2, Quartz, and Sapphire substrates. Deconvoluted PL spectra of 1L-WS_2 grown on (b) SiO_2, (c) Quartz, and (d) Sapphire.

2.4.4. Growth Mechanism

We have successfully grown large area monolayer WS_2 film on different substrates (SiO_2, quartz, and sapphire), following previous reports on the CVD growth of WS_2[1, 32-33]. A space confined or semi-sealed system is crucial for the growth, to ensure optimum partial pressure of WO_3 vapor. At 750 °C, the vapor pressure of WO_3 is still low, which limited the domain size of the WS_2. However, at 1000 °C, even though the partial pressure of the WO_3 vapor increased, we believe it was accompanied by the increase in the S vapor pressure during the early phase of the growth, leading to a fast sulfidation rate. This occurred owing to the small separation between the precursors. To ensure the optimum sulfidation rate, the WO_3 and S boats were positioned at a distance of 25 cm away from each other. The substrates were kept face down over WO_3. NaCl was kept in close proximity to the W source to aid in the monolayer WS_2 formation of larger lateral domains[37]. The best growth was achieved at 940 °C where, due to the high partial pressure of WO_3 vapor, its molecules adhered to the surface of the substrate. Simultaneously, the vapor pressure of S increased and the reaction between S atoms and the WO_3 molecules took place over the substrate, which further led to the growth of monolayer WS_2.

2.5. Conclusion

To summarize, this chapter demonstrated firstly, the synthesis of highly fluorescent monolayer and bilayer WS_2 QDs using a simple top-down chemical exfoliation technique. The sizes of these QDs are easily controlled by post centrifugation rates. The elemental composition was ascertained via XPS and the crystallinity of the as-prepared QDs was confirmed by the Raman spectra. These low-cost solution-processed fluorescent WS_2 QDs stimulate a diverse range of applications in optoelectronics, bioimaging, and related areas. Moreover, they have the potential for the development of wearable devices based on flexible substrates. Further studies on the WS_2 QDs and their applications are presented in the next chapters. In the subsequent sections, we have demonstrated the growth of highly crystalline two-dimensional monolayer WS_2 flakes by the CVD technique at low (750 °C) and high (1000 °C) temperatures. Besides the growth temperature, several growth parameters such as precursors, growth pressure, duration, etc., were modified to understand the growth behaviors of WS_2. The precursors (WO_3 and S) were placed at different temperature zone in a two-zoned muffled furnace, which were controlled via precise heating profiles. This, along with the control over the carrier gas flow, allowed us to manipulate the required vapor pressure of precursors for optimum growth. Finally, we have shown a simple salt-assisted approach to growing high-quality, large-area continuous monolayer WS_2 film on different substrates by CVD. The influence of the change in the growth temperature (800-940 °C) was investigated to understand the effect on WS_2 growth. We have systematically studied the Raman and PL properties of the as-grown WS_2 on different substrates. We have briefly addressed the substrate-dependent built-in strain and doping effects. Thus, it is found that the growth substrates significantly affect the PL emission characteristics of the 1L-WS_2. Our results indicate that the large-area monolayer WS_2 grown on sapphire substrate contains fewer defects than that of the other substrates. The controlled synthesis procedures of these WS_2 QDs and monolayer films could further open avenues for investigations into the fundamentals of light-matter interactions in these 2D systems and thus, pave way for the development of various optoelectronic devices.

References

1. Lan, C.; Zhou, Z.; Zhou, Z.; Li, C.; Shu, L.; Shen, L.; Li, D.; Dong, R.; Yip, S.; Ho, J. C., Wafer-Scale Synthesis of Monolayer Ws2 for High-Performance Flexible Photodetectors by Enhanced Chemical Vapor Deposition. *Nano Research* **2018**, *11*, 3371-3384.
2. Bai, X., et al., Ultrasmall Ws2 Quantum Dots with Visible Fluorescence for Protection of Cells and Animal Models from Radiation-Induced Damages. *ACS Biomaterials Science & Engineering* **2017**, *3*, 460-470.
3. Li, X.; Zhang, J.; Liu, Z.; Fu, C.; Niu, C., *Ws 2 Nanoflowers on Carbon Nanotube Vines with Enhanced Electrochemical Performances for Lithium and Sodium-Ion Batteries*, 2018; Vol. 766.
4. Yao, Y.; Jin, Z.; Chen, Y.; Gao, Z.; Yan, J.; Liu, H.; Wang, J.; Li, Y.; Liu, S., Graphdiyne-Ws2 2d-Nanohybrid Electrocatalysts for High-Performance Hydrogen Evolution Reaction. *Carbon* **2018**, *129*, 228-235.
5. Feng, S., et al., Engineering Valley Polarization of Monolayer Ws2: A Physical Doping Approach. *Small* **2019**, *15*, 1805503.
6. Koperski, M.; Molas, M. R.; Arora, A.; Nogajewski, K.; Bartos, M.; Wyzula, J.; Vaclavkova, D.; Kossacki, P.; Potemski, M., Orbital, Spin and Valley Contributions to Zeeman Splitting of Excitonic Resonances in Mose ₂ , Wse ₂ and Ws ₂ Monolayers. *2D Materials* **2018**, *6*, 015001.
7. Norden, T.; Zhao, C.; Zhang, P.; Sabirianov, R.; Petrou, A.; Zeng, H., Giant Valley Splitting in Monolayer Ws 2 by Magnetic Proximity Effect. *Nature Communications* **2019**, *10*, 1-10.
8. Piao, M.; Chu, J.; Wang, X.; Chi, Y.; Zhang, H.; Li, C.; Shi, H.; Joo, M.-K., Hydrothermal Synthesis of Stable Metallic 1t Phase Ws₂ Nanosheets for Thermoelectric Application. *Nanotechnology* **2017**, *29*, 025705.
9. Yan, Y.; Zhang, C.; Gu, W.; Ding, C.; Li, X.; Xian, Y., Facile Synthesis of Water-Soluble Ws2 Quantum Dots for Turn-on Fluorescent Measurement of Lipoic Acid. *The Journal of Physical Chemistry C* **2016**, *120*, 12170-12177.
10. Xu, S.; Li, D.; Wu, P., One-Pot, Facile, and Versatile Synthesis of Monolayer Mos2/Ws2 Quantum Dots as Bioimaging Probes and Efficient Electrocatalysts for Hydrogen Evolution Reaction. *Advanced Functional Materials* **2015**, *25*, 1127-1136.
11. Zhao, H.; Wu, H.; Wu, J.; Li, J.; Wang, Y.; Zhang, Y.; Liu, H., Preparation of Mos2/Ws2 Nanosheets by Liquid Phase Exfoliation with Assistance of Epigallocatechin Gallate and Study as an Additive for High-Performance Lithium-Sulfur Batteries. *Journal of Colloid and Interface Science* **2019**, *552*, 554-562.
12. Ghorai, A.; Midya, A.; Maiti, R.; Ray, S. K., Exfoliation of Ws2 in the Semiconducting Phase Using a Group of Lithium Halides: A New Method of Li Intercalation. *Dalton Transactions* **2016**, *45*, 14979-14987.
13. Wu, Y., et al., Unexpected Intercalation-Dominated Potassium Storage in Ws2 as a Potassium-Ion Battery Anode. *Nano Research* **2019**, *12*, 2997-3002.
14. Godel, F., et al., Ws2 2d Semiconductor Down to Monolayers by Pulsed-Laser Deposition for Large-Scale Integration in Electronics and Spintronics Circuits. *ACS Applied Nano Materials* **2020**, *3*, 7908-7916.
15. Loh, T. A. J.; Chua, D. H. C.; Wee, A. T. S., One-Step Synthesis of Few-Layer Ws2 by Pulsed Laser Deposition. *Scientific Reports* **2015**, *5*, 18116.
16. Okada, M.; Sawazaki, T.; Watanabe, K.; Taniguch, T.; Hibino, H.; Shinohara, H.; Kitaura, R., Direct Chemical Vapor Deposition Growth of Ws2 Atomic Layers on Hexagonal Boron Nitride. *ACS Nano* **2014**, *8*, 8273-8277.
17. Xu, Z.; Lv, Y.; Li, J.; Huang, F.; Nie, P.; Zhang, S.; Zhao, S.; Zhao, S.; Wei, G., Cvd Controlled Growth of Large-Scale Ws2 Monolayers. *RSC Advances* **2019**, *9*, 29628-29635.
18. Koçak, Y.; Akaltun, Y.; Gür, E., Magnetron Sputtered Ws₂; Optical and Structural Analysis. *Journal of Physics: Conference Series* **2016**, *707*, 012028.

19. Weiß, V.; Seeger, S.; Ellmer, K.; Mientus, R., Reactive Magnetron Sputtering of Tungsten Disulfide (Ws2−X) Films: Influence of Deposition Parameters on Texture, Microstructure, and Stoichiometry. *Journal of Applied Physics* **2007**, *101*, 103502.

20. Epstein, I., et al., Near-Unity Light Absorption in a Monolayer Ws2 Van Der Waals Heterostructure Cavity. *Nano Letters* **2020**, *20*, 3545-3552.

21. Long, H.; Tao, L.; Tang, C. Y.; Zhou, B.; Zhao, Y.; Zeng, L.; Yu, S. F.; Lau, S. P.; Chai, Y.; Tsang, Y. H., Tuning Nonlinear Optical Absorption Properties of Ws2 Nanosheets. *Nanoscale* **2015**, *7*, 17771-17777.

22. Lin, L.; Xu, Y.; Zhang, S.; Ross, I. M.; Ong, A. C. M.; Allwood, D. A., Fabrication of Luminescent Monolayered Tungsten Dichalcogenides Quantum Dots with Giant Spin-Valley Coupling. *ACS Nano* **2013**, *7*, 8214-8223.

23. Li, R.-Z.; Dong, X.-Y.; Li, Z.-Q.; Wang, Z.-W., Correction of the Exciton Bohr Radius in Monolayer Transition Metal Dichalcogenides. *Solid State Communications* **2018**, *275*, 53-57.

24. Singh, V. K.; M. Yadav, S.; Mishra, H.; Kumar, R.; Tiwari, R. S.; Pandey, A.; Srivastava, A., Ws2 Quantum Dot Graphene Nanocomposite Film for Uv Photodetection. *ACS Applied Nano Materials* **2019**, *2*, 3934-3942.

25. Caigas, S. P.; Santiago, S. R. M.; Lin, T.-N.; Lin, C.-A. J.; Yuan, C.-T.; Shen, J.-L.; Lin, T.-Y., Origins of Excitation-Wavelength-Dependent Photoluminescence in Ws2 Quantum Dots. *Applied Physics Letters* **2018**, *112*, 092106.

26. Perrozzi, F.; Emamjomeh, S. M.; Paolucci, V.; Taglieri, G.; Ottaviano, L.; Cantalini, C., Thermal Stability of Ws2 Flakes and Gas Sensing Properties of Ws2/Wo3 Composite to H2, Nh3 and No2. *Sensors and Actuators B: Chemical* **2017**, *243*, 812-822.

27. Molas, M. R.; Nogajewski, K.; Potemski, M.; Babiński, A., Raman Scattering Excitation Spectroscopy of Monolayer Ws2. *Scientific Reports* **2017**, *7*, 5036.

28. Berkdemir, A., et al., Identification of Individual and Few Layers of Ws2 Using Raman Spectroscopy. *Scientific Reports* **2013**, *3*, 1755.

29. Lan, C.; Li, C.; Yin, Y.; Liu, Y., Large-Area Synthesis of Monolayer Ws2 and Its Ambient-Sensitive Photo-Detecting Performance. *Nanoscale* **2015**, *7*, 5974-5980.

30. Kang, K. N.; Godin, K.; Yang, E.-H., The Growth Scale and Kinetics of Ws2 Monolayers under Varying H2 Concentration. *Scientific Reports* **2015**, *5*, 13205.

31. Zhang, Y.; Yao, Y.; Getaye, M.; Yin, L.; Zhan, X.; Wang, F.; Wang, Z.; He, J., Recent Progress in Cvd Growth of 2d Transition Metal Dichalcogenides and Related Heterostructures. *Advanced Materials* **2019**, *31*.

32. Cong, C.; Shang, J.; Wu, X.; Cao, B.; Peimyoo, N.; Qiu, C.; Sun, L.; Yu, T., Synthesis and Optical Properties of Large-Area Single-Crystalline 2d Semiconductor Ws2 Monolayer from Chemical Vapor Deposition. *Advanced Optical Materials* **2014**, *2*, 131-136.

33. Lan, F.; Yang, R.; Xu, Y.; Qian, S.; Zhang, S.; Cheng, H.; Zhang, Y., Synthesis of Large-Scale Single-Crystalline Monolayer Ws_2 Using a Semi-Sealed Method. *Nanomaterials (Basel)* **2018**, *8*, 100.

34. Zhu, B.; Chen, X.; Cui, X., Exciton Binding Energy of Monolayer Ws2. *Scientific Reports* **2015**, *5*, 9218.

35. Li, S.; Wang, S.; Tang, D.-M.; Zhao, W.; Xu, H.; Chu, L.; Bando, Y.; Golberg, D.; Eda, G., Halide-Assisted Atmospheric Pressure Growth of Large Wse2 and Ws2 Monolayer Crystals. *Applied Materials Today* **2015**, *1*, 60-66.

36. Singh, A.; Moun, M.; Sharma, M.; Barman, A.; Kumar Kapoor, A.; Singh, R., Nacl-Assisted Substrate Dependent 2d Planar Nucleated Growth of Mos2. *Applied Surface Science* **2021**, *538*, 148201.

37. Wang, Z., et al., Nacl-Assisted One-Step Growth of Mos₂–Ws₂in-Plane Heterostructures. *Nanotechnology* **2017**, *28*, 325602.

38. Shu, H.; Chen, X.; Ding, F., The Edge Termination Controlled Kinetics in Graphene Chemical Vapor Deposition Growth. *Chemical Science* **2014**, *5*, 4639-4645.

39. Molina-Sánchez, A., Phonons in Single and Few-Layer Mos2 and Ws2. *Phys. Rev. B* **2011**, *84*.

40. Su, L.; Yu, Y.; Cao, L.; Zhang, Y., Effects of Substrate Type and Material-Substrate Bonding on High-Temperature Behavior of Monolayer Ws2. *Nano Research* **2015**, *8*, 2686-2697.

41. McCreary, K. M.; Hanbicki, A. T.; Singh, S.; Kawakami, R. K.; Jernigan, G. G.; Ishigami, M.; Ng, A.; Brintlinger, T. H.; Stroud, R. M.; Jonker, B. T., The Effect of Preparation Conditions on Raman and Photoluminescence of Monolayer Ws2. *Scientific Reports* **2016**, *6*, 35154.

42. Wang, F.; Kinloch, I. A.; Wolverson, D.; Tenne, R.; Zak, A.; O'Connell, E.; Bangert, U.; Young, R. J., Strain-Induced Phonon Shifts in Tungsten Disulfide Nanoplatelets and Nanotubes. *2D Materials* **2016**, *4*, 015007.

Chapter 3

Excitation Wavelength-dependent Spectral shift and large Exciton Binding Energy of WS_2 Quantum Dots and its interaction with Single-Walled Carbon Nanotubes

In this chapter, we investigate the origin of excitation wavelength-dependent spectral features and high fluorescence quantum yield in fluorescent 2D tungsten disulfide (WS_2) quantum dots (QDs) of sizes in the range of 2-4 nm. The chemically exfoliated WS_2 QDs possess a high optical bandgap and high fluorescence quantum yield of ~15% in the green region, without any functionalization. The broad photoluminescence (PL) spectrum consists of multiple peaks owing to emissions from excitonic transitions and defect-related transitions. The excitation wavelength-dependent redshift and narrowing of line shape in the PL peak are analyzed carefully, and it is attributed to the excitation/recombination of carriers from selective energy levels. The temperature-dependent PL analysis yields an exciton binding energy of ~302 meV evidencing upon large excitonic effect in the QDs. Furthermore, we study the interaction between fluorescent WS_2 QDs and single-walled carbon nanotubes (SWCNTs) and explore the mechanism of systematic quenching of PL of QDs by SWCNTs. The nature of the Stern-Volmer plot is found to be linear, and the time-resolved fluorescence measurements reveal that the quenching follows primarily the static type behavior. Our study further reveals that defect sites in SWCNTs primarily act as the binding sites for WS_2 QDs and form non-fluorescent complexes for effective quenching of the PL. These results reveal the nature of binding between WS_2 QDs and SWCNTs, which is important for their applications in biomedical imaging and sensing, such as surface-enhanced Raman scattering, etc.

3.1. Introduction

Bulk WS_2 is a semiconductor with an indirect band gap of 1.32 eV, while its monolayer counterpart has a direct band gap of ~2.02 eV[1-4]. Reduced dielectric screening results in enhanced Coulomb interactions leading to strong excitonic features of 2D monolayer WS_2 at room temperature. With its exfoliation and lateral size reduction down to quantum dots, WS_2 exhibits high room temperature photoluminescence (PL) due to the strong quantum confinement effect and surface edge effects[5-6]. These QDs exhibit a tunable direct band gap up to ~4 eV[7]. The 2D WS_2 nanostructures have found applications in a myriad of areas, as discussed in **Chapter 1 (Section**

1.4.), owing to their many unique properties. Excitation wavelength-dependent emission profiles have been reported for WS_2 QDs, though the origin of the same has not been addressed properly. The excitation-wavelength dependent change in emission color is very interesting, as it can serve as a multicolor biolabeling reagent[8]. Based on their high room temperature fluorescence, biosensors based on turn on- turn off fluorescence of these 2D semiconducting quantum dots, including graphene QDs[9] and MoS_2 QDs[10-11], etc., have been developed. Yan et al. utilized the fluorescence tunability of WS_2 QDs to fabricate a sensor for the determination of lipoic acid using Fe^{3+} ions as a quencher through photo-induced charge transfer[5]. The PL quantum yield of WS_2 QDs is usually higher than that of 2D sheets, which may be associated with the confinement effect and higher exciton binding energy. However, there is no report on the exciton binding energy of WS_2 QDs, though the same is known for the monolayer WS_2.

Single-walled carbon nanotubes (SWCNTs) are rolled over graphene sheets that are quasi-one-dimensional tubules having sharp densities of electronic states[12]. As universal fluorescence quenchers, single-walled and multi-walled CNTs effectively quench several fluorophores by Förster resonance energy transfer (FRET) from a donor (fluorophores) to an acceptor (CNT) or by the formation of ground state non-fluorescent complexes[12-15]. Das et al. reported a detailed analysis on the anomalous behavior of the PL intensity of the graphene QDs with varying concentrations of the SWCNTs[14]. However, there have been no reports on the effect of SWCNT on the emission properties of highly fluorescent TMD QDs, such as MoS_2, WS_2, etc. Thus, the fluorescence quenching mechanism of TMD QDs in the presence of SWCNTs has not been explored to date. In this chapter, the optical properties of the as-prepared WS_2 QDs are studied in detail. An in-depth study of the effect of SWCNTs on the fluorescence of the WS_2 QDs is carried out. The mechanism of PL quenching of WS_2 QDs is explored using various spectroscopic tools. There is an associated improvement in the structural quality and change in the electronic structure of the SWCNT with the attachment of the WS_2 QD on the SWCNT walls, which is observed for the first time.

3.2. Experimental details

3.2.1. Synthesis of WS_2 QDs by liquid exfoliation

WS_2 bulk powder was dispersed in NMP to carry out liquid exfoliation for a duration of 15 hours. The obtained suspension was centrifuged at a low temperature to separate the supernatant and the centrifugate. The synthesis procedure was described in detail in **Chapter 2**

(Section 2.1.2.). The excess solvent from the supernatant was evaporated, and the WS_2 QDs were redispersed in NMP at a concentration of 1 mg/ml for further use. The morphology, chemical composition and crystal structure are studied via TEM, AFM, XPS, and micro-Raman analyses.

3.2.2. General details of SWCNT used for Photoluminescence quenching

Commercially available SWCNTs having different amounts of structural defects were procured from Nanotech World Co. (Korea) (Purity>95%) (SWCNT1) and Sigma Aldrich (Purity~99%) (SWCNT2). For the typical quenching experiments, a homogenous solution in NMP of concentration 0.2 mg/ml was prepared by ultrasonication. Further dilutions were carried out to give a series of samples with different concentrations (2-50 μg/ml). Then, 1 ml of the as-prepared WS_2 QDs in NMP of concentration 1 mg/ml was mixed with 1 ml of the SWCNT1 solutions (2-50 μg/ml), i.e., in a 1:1 volume ratio. The resultant mixture was sonicated for 10 minutes. The PL spectra of the WS_2 QD solutions with the different concentrations of SWCNT1 were collected over the wavelength range of 425-750 nm under an excitation wavelength of 405 nm. The sample codes used for each concentration of the SWCNT1 are denoted as WS + C*x*, where *x* is the concentration of SWCNT1 in μg/ml. The concentration of the WS_2 QDs is fixed at 1 mg/ml. For comparison, we used SWCNTs with a lower concentration of defects (SWCNT2) than that of SWCNT1 to study the role of defects in SWCNTs on the efficiency of fluorescence quenching.

3.2.3. Characterization techniques

The morphology, size, and structural properties of the as-prepared WS_2 QDs and the WS_2 QD decorated SWCNT have been studied by a transmission electron microscope (TEM) (JEOL-JEM 2010 operated at 200 kV). X-ray photoelectron spectroscopy (XPS), (Ulvac-Phi, Inc.) was employed to study the elemental composition of the as-prepared WS_2 QDs and the WS_2 QD decorated SWCNT. Crystallinity, defects, etc. in the WS_2 QDs and SWCNT as well as the change in the crystallinity, and strain of the WS_2 QDs decorated SWCNT have been studied by a high-resolution micro-Raman spectrometer (LabRam HR800, Jobin-Yvon) with excitation wavelengths (λ_{ex}) 488 nm and 532 nm (Ar ion laser). The excitation laser light was focused with a 100× objective lens to a spot size of 1 μm, and the signal was collected by a CCD in backscattering geometry. UV-Vis-NIR absorbance spectroscopy measurements of the samples were recorded using a commercial spectrophotometer (PerkinElmer, UV win Lab). The steady-state PL and PL quantum yield measurements were performed by using a Xe lamp as well as an external laser, with an excitation wavelength of 405 nm, coupled to a commercial spectro-fluorimeter (Horiba Scientific, Fluoromax-4). Time-resolved PL (TRPL) measurements were carried out with 375 nm and 405 nm pulse laser excitations and a picosecond time-resolved luminescence spectrometer (Edinburg Instruments, FSP920). The room temperature PL measurements on WS_2 QDs were carried out in NMP solution and the contribution of NMP to the PL spectrum was subtracted in each case. For low-temperature PL, a thin film of the WS_2 QDs was used as the sample inside a liquid-nitrogen-cooled optical cryostat (Optistat DNV, Oxford Instruments). Fluorescence confocal imaging of the samples was obtained from a commercial confocal microscope (Zeiss LSM 880) with 405 nm Ar laser excitation.

3.3. Results and discussion

3.3.1. Morphology studies

The typical morphological properties of the as-prepared WS_2 QDs were studied using TEM imaging. **Fig. 3.1(a)** shows the high angle annular dark-field (HAADF) TEM image of the WS_2 QDs with nearly uniform sizes (diameter 2-4 nm). The narrow size distribution is fitted with a log-normal function, and the average diameter of the QDs is found to be 2.4 ± 0.1 nm, as shown in the inset of **Fig. 3.1(a).** The selected area electron diffraction (SAED) pattern (bottom inset of **Fig. 3.1(a)**) exhibits diffused rings that reveal the polycrystalline nature of the as-prepared WS_2 QDs. **Fig. 3.1(b)** exhibits the high-resolution TEM (HRTEM) image of WS_2 QDs depicting their crystalline nature. The inset shows a magnified HRTEM image of a single WS_2 QD with a lattice spacing of 0.23 nm corresponding to the (103) plane of WS_2. **Fig. 3.1(c)** shows the AFM image of the WS_2 QDs and the inset shows a height profile of the WS_2 QDs revealing the presence of bilayer and monolayer WS_2 QDs. The morphological changes of SWCNT1 before and after the interaction with WS_2 QD are observed from the TEM images as presented in **Fig. 3.1(d, e). Fig. 3.1(d)** shows the TEM image of pristine SWCNT1 that are composed of curled and bundles of carbon nanotubes with a length of >1μm. The TEM image of the functionalized SWCNT1 (concentration of 10 μg/ml) with WS_2 QDs (WS+C10) is depicted in **Fig. 3.1(e).** The WS_2 QDs (sizes~2-4 nm) are decorated on the walls of the bundled nanotubes and are also present in the region outside the nanotubes. The corresponding SAED pattern is displayed in the bottom right inset of **Fig. 3.1(e).** The indexed rings in the SAED pattern correspond to structural characteristics of both carbon/graphene and WS_2, indicating functionalization of SWCNT1 with WS_2 QDs. The TEM image of the WS_2 QD and SWCNT2 composite (WS+C10) is depicted in **Fig. 3.1(f),** which shows individual SWCNT with well-distributed WS_2 QDs.

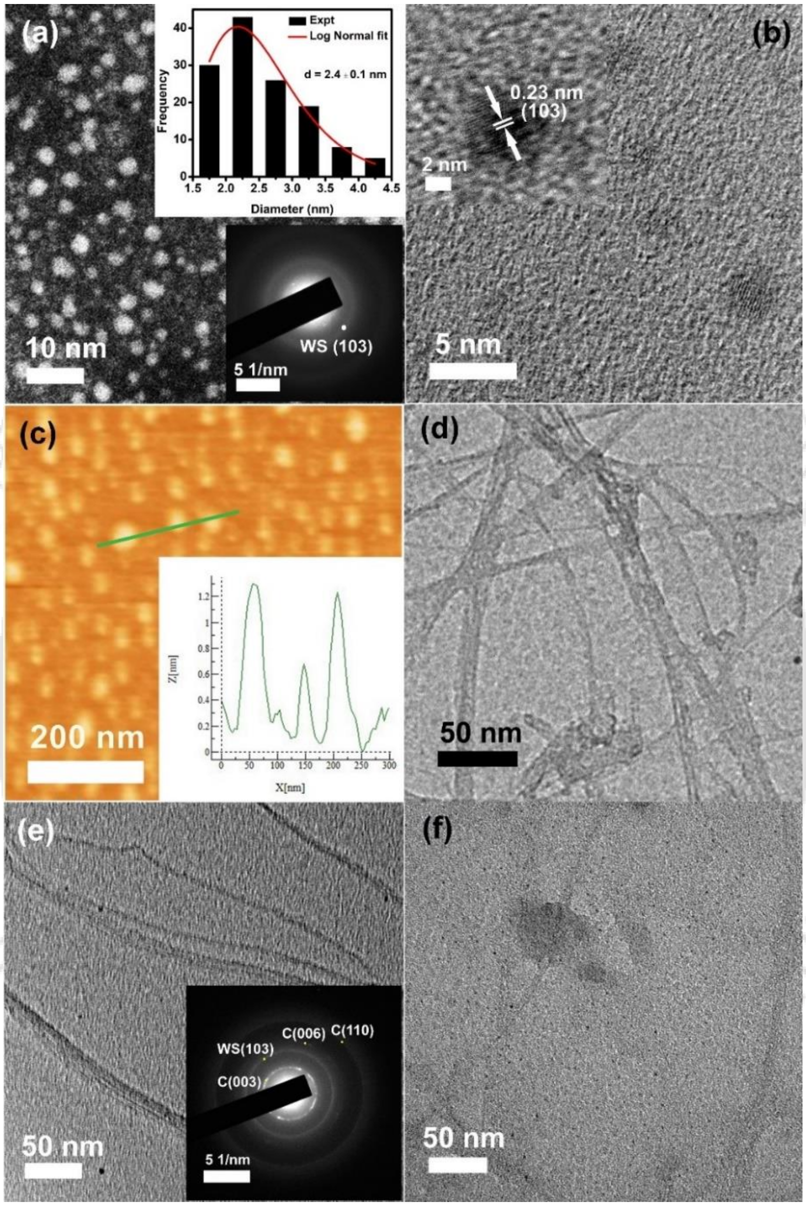

Fig. 3.1.: (a) HAADF TEM image of the WS_2 QDs. The top right inset shows the size distribution analysis for the sample. The bottom right inset displays the SAED pattern. (b) HRTEM lattice image of WS_2 QDs. The top left inset shows the magnified HRTEM image of WS_2 QDs showing a lattice d spacing of 0.23 nm indicating the (103) plane of WS_2. (c) AFM image of the WS_2 QDs. Inset displays the height profile of the WS_2 QDs corresponding to the green line. (d) TEM image of SWCNTs, (e) TEM image of WS_2 QD decorated SWCNTs. The white marked region shows the clear presence of QDs on SWCNT wall. The inset at the bottom displays the SAED pattern of the composite of WS_2 QD with SWCNT. (f) TEM image of the composite of WS_2 QD and less defective SWCNT (SWCNT2).

3.3.2. Structural and Compositional analysis

For structural analysis, micro-Raman measurements were carried out on WS_2 QD and bulk WS_2 powder using Ar laser excitation at 532 nm. Additionally, the elemental composition of the as-prepared WS_2 QDs was ascertained using XPS analysis. The analyses are discussed in detail in **Chapter 2, Section 2.1.4.3.** Our results are consistent with the AFM height profile analysis discussed in the previous section.

3.3.3. Optical analysis of WS_2 QDs

3.3.3.1. UV-Vis Absorption Study

Fig. 3.2(a) shows the UV-vis absorption spectrum of WS_2 QDs in dispersion. Monolayer WS_2 is known to exhibit two excitonic peaks A and B at ~615 nm and ~517 nm, respectively, originating from the direct transition from the spin-split valence band at the K point of the Brillouin zone. There are also transitions at the Γ point, which correspond to the C and D excitonic absorption peaks at the shorter wavelength region[3-4, 16]. However, in the case of WS_2 QDs studied here, excitonic absorption peaks are less distinct, though there is a strong absorption peak in the UV region at 294 nm. A similar absorption feature at ~297 nm was reported by Yin et al.[17] In the case of semiconductor quantum dots, a distinct excitonic absorption peak is usually observed besides the absorption edge. The peak at 294 nm is ascribed to excitonic transitions from deep level valence band states to the conduction band[18-19]. Note that here a broad absorption tail is observed in the blue to the green region and it may be partly due to the presence of defects in the WS_2 QDs. To extract the absorption features related to spin-orbit split B and A excitons in the WS_2 QDs, we have taken the first derivative of the absorption spectrum (inset of **Fig. 3.2(a)**)[20], that shows two prominent peaks at 319 nm and 379 nm, which are ascribed to the B and A excitons, respectively. From the Tauc plot (see **Fig. 3.2(b)**), the optical bandgap of the WS_2 QDs is estimated to be ~3.48 eV, which is much higher than that of the monolayer WS_2, due to quantum confinement effect in the ultrasmall QDs.

3.3.3.2. Photoluminescence Study

PL measurements were carried out for the as-prepared WS_2 QDs with different excitation wavelengths ranging from 300-480 nm (**Fig. 3.2(c)**). Interestingly, the QDs exhibit an excitation wavelength-dependent shift in the PL emission peak. With low wavelength excitation, the QDs display a broad emission spectrum, which gradually becomes narrower with the increase in the excitation wavelengths.

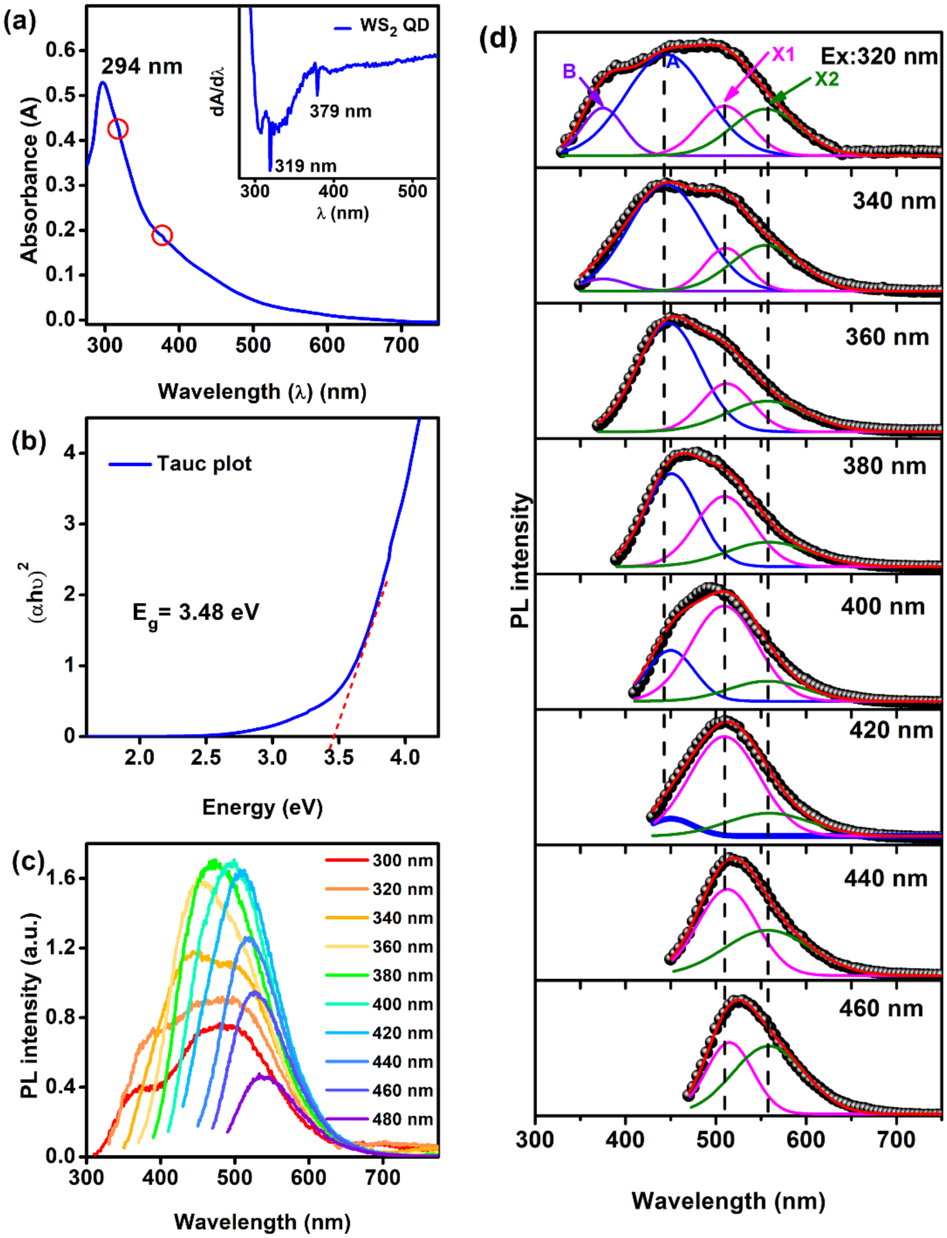

Fig. 3.2. (a) UV-vis absorption spectra of WS_2 QDs. The inset displays the first derivative of the absorption spectra showing prominent peaks at 319 nm and 379 nm owing to B and A excitons, respectively. (b) Tauc plot for the WS_2 QDs depicting a direct band gap of 3.48 eV. (c) PL spectra of WS_2 QDs with various excitation wavelengths (300-480 nm). Inset displays a digital photograph of the fluorescence emission of the WS_2 QDs at an excitation of 360 nm. (d) Gaussian fitting of the PL spectra for different excitation wavelengths in the range 320-460 nm. The vertical lines indicate the invariance of the individual peak positions for different excitation wavelengths.

A redshift is observed in the overall PL emission band with the increase in the wavelength of excitation owing to selective excitation of lower energy states, such as bound excitonic emissions. Excitation wavelength-dependent shift in the PL peak in WS_2 QDs has been reported by Yin et al., though it is not understood well[17]. The as-prepared WS_2 QDs exhibit a reasonably high PL quantum yield (QY) of ~15.4% at 405 nm excitation, without any functionalization. The following relation was used to evaluate the PLQY:

$$PLQY = \frac{E_C - E_A}{L_A - L_C} \times 100\% \qquad (1)$$

Here, E_C is the integrated luminescence of the sample (WS_2 QDs in solution) caused by direct excitation, E_A is the integrated luminescence from the solvent, NMP, L_C is the integrated excitation profile when the sample is directly excited by the incident beam and L_A is the integrated excitation profile from the solvent. The solvent was placed in the liquid sample holder inside the integrating sphere, and its integrated excitation profile (L_A) and integrated luminescence (E_A) were recorded. Next, the sample was placed in the liquid sample holder inside the integrating sphere, and similarly, the integrated excitation profile with the sample (LC) and integrated luminescence of the sample (EC) was obtained and corrected using the instrument correction file. Higher quantum yield has been reported for surface passivated WS_2 QDs and monolayer WS_2 sheets[21].

To further interpret the origin of the PL peak evolution, we have deconvoluted the PL spectra measured under different excitation wavelengths (320-460 nm), as shown in **Fig. 3.2(d).** The broad PL spectrum under the excitation of 320 nm is fitted with four Gaussian components, as shown in **Fig. 3.2(d),** namely the B exciton, the neutral exciton (A), and the defect bound excitons (X1 and X2). The B and A excitons centered at 375 nm and 445 nm, respectively, arise from direct gap transitions from the splitting of the valence band at K point to the conduction band. It is well understood that the valence band edge at the K valley is split due to strong spin-orbit coupling in the d orbitals of the W atoms[16, 18, 22]. The bound excitonic peaks at the longer wavelength region, centered at 510 nm and 555 nm, are believed to arise from the surface defect states and in-plane point defects arising from missing S atoms from the hexagonal lattice of WS_2[17, 23]. The relative intensities of bound exciton emissions increase at longer wavelengths of excitations. The X1 emission band intensity is highest for the excitation at 400 nm, whereas the X2 emission band intensity is highest under 460 nm excitation. Under the excitation of 460 nm, the PL spectrum fits well with two Gaussian peaks at ~515 nm and ~559 nm, respectively. These two peaks are attributed to the defect-bound and X2 (**Fig. 3.2(d)**). There is no contribution from B and A excitons for high wavelength excitations. Individual peak positions of B, A, X1, and X2 excitons are nearly independent of the excitation wavelength in the range of 320-460 nm. Note that the highest intensity of the PL emission is observed under the excitation of 380 nm. The details of the fitting parameters derived from the Gaussian deconvolution are provided in **Table 1**.

Table 1: Summary of the Gaussian fitting of PL spectra showing various excitonic species for WS$_2$ QDs.

Peaks	B exciton		A exciton		X1 exciton		X2 exciton	
Excitation wavelength (nm)	**Position (nm)**	**Spectral wt. (%)**	**Position (nm)**	**Spectral wt. (%)**	**Position (nm)**	**Spectral wt. (%)**	**Position (nm)**	**Spectral wt. (%)**
320	375	13	445	51	510	16	555	20
340	375	4	445	59	510	14	555	23
360	-	-	447	58	512	21	557	21
380	-	-	451	44	509	37	559	19
400	-	-	450	22	509	62	557	16
420	-	-	450	7	509	72	559	21
440	-	-	-	-	513	56	558	44
460	-	-	-	-	515	40	559	60

It is to be noted that for the excitation wavelengths >380 nm, the contribution from the A and B exciton is gradually reduced and hence the spectrum is narrower and red-shifted as compared to that of lower wavelength excitations. For the excitations of 440 and 460 nm, the PL emission is only due to the defect-bound X1 and X2 excitons, i.e., the contribution to the PL emission is only from the defect levels. Thus, the excitation wavelength-dependent PL spectral line shape and spectral shift are mainly due to the selective excitation/recombination of carriers at a certain range of energy levels depending on the energy of the excitation source. Note that the broadening in each peak is due to the size distribution of WS$_2$ QDs possessing a range of band gaps depending on their sizes. In the literature, the origin of excitation wavelength-dependent fluorescence in WS$_2$ QDs has been argued to be due to carrier localization where carriers transport to lower energy levels in the localized region before recombination[24]. Additionally, excitation wavelength-dependent fluorescence of graphene oxide has been attributed to out-of-plane strain[25]. However, in the present case, our results could be explained without invoking the strain effect. Note that we did not detect any strain in the lattice from the Raman analysis. The change in the line shape and spectral shift in PL can be well explained by the relative amplitude of each peak for different excitation energies.

To better understand the spectral line shape, PL excitation (PLE) spectra were recorded for the emission wavelengths 375 nm, 445 nm, 510 nm, and 560 nm, which are the emission peak positions for B, A, X1, and X2 excitons, respectively. For the 375 nm emission, the PLE spectrum shows a single excitation peak at ~318 nm, and for the 445 nm emission (A exciton), the PLE spectrum consists of a distinct peak at ~368 nm and a shoulder peak at ~318 nm, as shown in **Fig. 3.3(a).** The PLE spectra for the X1 and X2 band emissions are broad and asymmetric. To have a better understanding, we have deconvoluted the PLE spectrum for the A exciton emission (~445 nm) with 3 Gaussian peaks: 318 nm, 368 nm, and 405 nm corresponding to B, A, and X1 exciton absorption, respectively (**see Fig. 3.3(b)**). Based on the above, the band structure of the WS_2 QDs and related optical transitions are schematically shown in **Fig. 3.3(c),** where E_b refers to the exciton binding energy. Thus, the emission peak centered at 445 nm is contributed by three excitation processes, as revealed from PLE and absorption spectra: (1) at 318 nm, excitation from V_1 point to conduction band minimum (CBM) and subsequent recombination leading to B excitonic emission, (2) at 368 nm, excitation from V_2 point to CBM and subsequent recombination leading to A exciton emission and (3) excitation to the defect level at ~405 nm and subsequent recombination leads to bound exciton (X band) emission (see **Fig. 3.3(c)**). The points V_1 and V_2 correspond to the valence band maxima for the spin-valley split B and A excitons, respectively. The energy difference between the two points can be manipulated by controlling the lateral size of the WS_2 QDs[18].

3.3.3.3. Time-Resolved Photoluminescence Study

TRPL measurements were carried out for the WS_2 QDs at A-exciton and X1 band emission wavelengths. **Fig. 3.3(d)** shows the acquired TRPL spectra at 440 nm and 510 nm. Caigas et al. have previously reported a stretched exponential PL decay for undoped and doped WS_2 QDs. It was argued that the emission wavelength-dependent decay time was related to emission from localized states[24]. However, in our case, we observe that the TRPL decay spectrum in each case fits well with a bi-exponential decay function given by:

$$y = A_1 e^{-t/\tau_1} + A_2 e^{-t/\tau_2} \tag{2}$$

Here, τ_1 and τ_2 are the carrier lifetimes for the two main types of recombination processes involved, one being the decay of emission at V_1 or V_2 point and the other being the decay of the emission from the defect-related level[18]. A_1 and A_2 are the respective amplitudes of these processes and t is the instantaneous time. Using the equation, $\tau_{av} = \Sigma \frac{A_i \tau_i^2}{A_i \tau_i}$, we evaluate the average carrier lifetime to be 6.9 ns for the emission at 440 nm, while that of 510 nm emission peak comes out to be 9.2 ns. Higher τ_{av} for 510 nm emission is due to the bound state excitons, while the lower lifetime is due to the free excitons. Slow carrier recombination for the X1 band is a clear indication of carrier localization, consistent with the earlier report[24].

Note that a large Stokes shift between the absorption and emission peaks for X1 and X2 bands observed experimentally are characteristic of defect-bound emissions. Hence, the TRPL decay at higher emission wavelength (~510 nm) is mainly due to localized bound excitons. In the literature, the bi-exponential decay profile of monolayer WS_2 has been attributed to the band nesting effect[26], which may be present in our case of WS_2 QDs. Additionally, due to size distribution, each peak in the PL spectrum is broad and some overlap of emission wavelength may give rise to contribution from two different emission states.

3.3.3.4. Low-temperature Photoluminescence Study

To further investigate the excitonic properties of the as-prepared WS_2 QDs, temperature-dependent PL measurement was carried out in the temperature range of 100-350 K at a laser excitation of 355 nm (see **Fig. 3.3(e)**). As the temperature increases from 100 K to 350 K, there is a gradual decrease in the PL intensity. The PL intensity of WS_2 QDs is reduced by ~68% when the temperature increases from 100 K to 350 K. This decrease in the PL intensity could be due to the increase in the probability of the non-radiative recombination process with an increase in thermal energy. There is a slight redshift of the PL peak with an increase in the temperature. This is partly may be due to the reduction in the bandgap with the increase in temperature and partly due to the higher probability of emission from the radiative surface defect-related trap states at lower temperatures. The temperature dependence of the PL intensity can be expressed by the relation:

$$I_{RT} = \frac{I_{LT} \times K_{rad}}{K_{rad} + K_{nonrad}} \qquad (3)$$

Here, I_{RT} and I_{LT} are the PL intensities of WS_2 QDs at room temperature and at low temperature, respectively and K_{rad} and K_{nonrad} are the radiative and non-radiative recombination rates[27-28]. The electron relaxation and defect-trapping rate within the conduction and valence bands of a semiconductor are reported to be related to the non-radiative recombination rate[29]. From the temperature dependence of intensity, it is estimated that the non-radiative recombination rate is ~1.4 times the radiative recombination rate at room temperature.

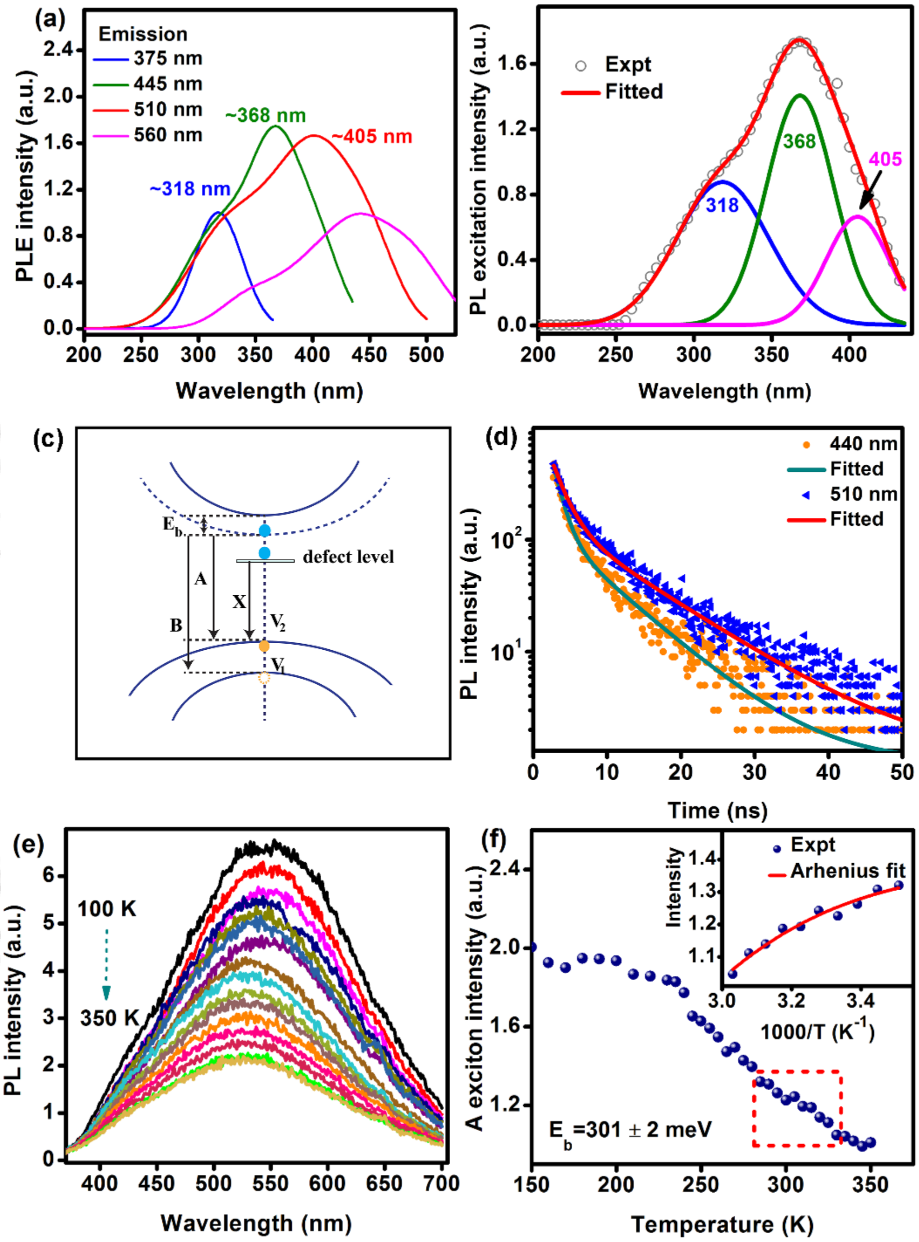

Fig. 3.3.: (a) PLE spectra of the WS_2 QDs for emission wavelengths of 375, 445, 510, and 560 nm. (b) Gaussian deconvolution of the PLE spectrum for emission at 445 nm. (c) Energy band diagram of WS_2 QDs showing the different excitonic transitions (A, B, X excitons) at the K point. (d) TRPL decay curves of WS_2 QDs recorded at 440 nm and 510 nm emissions for 375 nm excitation. The solid lines show the bi-exponential fit to the experimental data (symbols). (e) Temperature-dependent PL emission spectra for WS_2 QDs (film) using 355 nm laser excitation. (f) The variation of A exciton intensity with temperature for the WS_2 QDs. The inset shows the Arrhenius plot for the region 285-330 K (the red dashed box indicates the temperature range used for Arrhenius fit). The experimental data have been fitted with the Arrhenius equation to extract the exciton binding energy (E_b).

Thus, there is a reduction in the PL intensity with an increase in temperature. The PL spectra obtained for the entire temperature range of 100-350 K were deconvoluted using three Gaussian components, the A exciton, and the defect-bound X1 and X2 excitons. The PL peak intensity for the A exciton is extracted from the fitted spectra and plotted as a function of temperature in **Fig 3.3(f),** which shows a systematic decrease in intensity with an increase in temperature. The intensity of A exciton emission is decreased by ~60% when the temperature is increased from 100 K to 350 K. To estimate the thermal activation energy (E_a) of the recombination process in the as-prepared WS$_2$ QDs, the temperature-dependent intensity of excitonic emission can be expressed in terms of the Arrhenius equation:

$$I(T) = \frac{I_0}{1+C\exp\left(-\frac{E_a}{k_B T}\right)} \qquad (4)$$

Here I(T) and I_0 are the PL emission intensities of the A exciton at temperatures T and 0 K, respectively, and C is a constant. The temperature range of 285-330 K is considered to extract the thermal activation energy of ~301 ± 2 meV from the Arrhenius plot, as shown in the inset of **Fig. 3.3(f).** Since the evolution of only A-exciton intensity is considered in the plot, the measured E_a is assigned to the intrinsic exciton binding energy (E_b), which gives strong experimental evidence for the existence of the large excitonic effect in the as-prepared WS$_2$ QDs[3]. Our result is consistent with the experimental result reported by Chernikov et al.[20] for monolayer WS$_2$. The large exciton binding energy observed here is a manifestation of the strong Coulomb interactions and quantum confinement in the WS$_2$ QDs.

3.3.4. Study of the interaction between WS$_2$ QDs and SWCNTs

Next, we study the interaction of WS$_2$ QDs with SWCNTs through fluorescence studies and provide evidence for the WS$_2$ QDs/SWCNT complex formation facilitated by the defects in the SWCNT walls. Due to the biocompatibility of both WS$_2$ QDs[30], and SWCNTs and their potential medical applications, understanding the interaction between the WS$_2$ and SWCNTs is very important. We explore the effect of SWCNTs on the fluorescence quenching of WS$_2$ QDs. SWCNTs of different purity/defect content from two different sources (SWCNT1 and SWCNT2) were used to understand the role of defects in the interaction between the two species and the evolution in the PL spectra.

3.3.4.1. Raman analysis of the SWCNT/ WS$_2$ QD hybrid

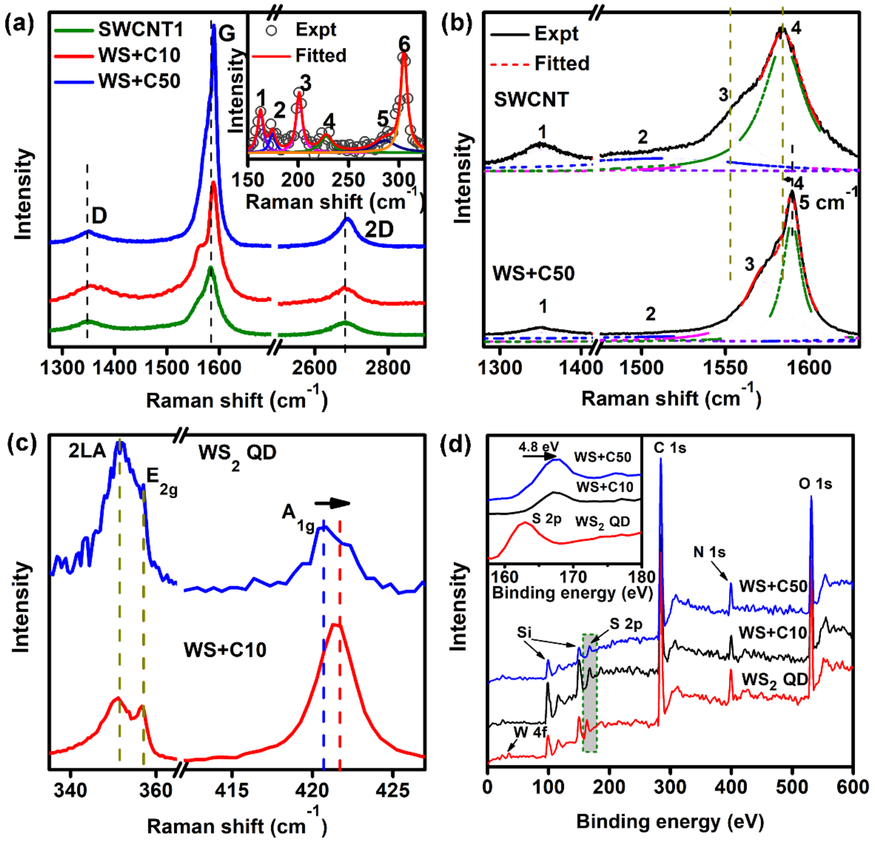

Fig. 3.4. (a) Comparison of the Raman spectra of bare SWCNT1 and the composites of WS_2 QD with SWCNT1 concentrations 10, 50 µg/ml. For the composites, the position of the G and 2D bands of SWCNT1 are blue-shifted. The inset shows the Lorentzian fitting of the Raman spectrum of pristine SWCNT1 showing the RBM modes. (b) The Lorentzian fittings of the Raman spectra in the range of 1280-1630 cm^{-1} for pristine SWCNT1 and WS+C50 composite. (c) Comparison of the Raman spectra of WS_2 QDs without and with SWCNT1. Peak shifts are indicated by vertical dashed lines. (d) Comparison of the XPS survey spectra of pristine WS_2 QDs without and with SWCNT1 at two different concentrations. The inset shows the high-resolution XPS S 2p spectra of WS_2 QDs without and with SWCNT1.

To understand the structure of the pristine SWCNTs and the SWCNTs functionalized with WS_2 QDs, laser micro-Raman measurements were carried out using 488 nm Ar ion laser excitation. **Fig. 3.4(a)** displays the comparison of the Raman spectra of the pristine SWCNT1 and the SWCNT1/WS_2 composites- WS+C10 and WS+C50. All three samples exhibit the characteristic first-order Raman bands of SWCNTs, namely the graphitic G band at ~1585 cm^{-1} as well as the radial breathing modes (RBM) in the range of 150-350 cm^{-1}. The Raman spectra also show the presence of the characteristic double resonance Raman modes, D and 2D bands[31]. In the composite sample, the shift in the D, G, and 2D bands is apparent from the vertical dashed lines passing through the respective peaks of pristine SWCNT1. We have deconvoluted the RBM modes with six Lorentzian peaks, as shown in the inset of **Fig. 3.4(a)** and calculated the diameters of the SWCNT1 using the formula $\omega_{RBM}= C/d_t$, where C is 248 cm^{-1} nm and d_t is the diameter in nm[31]. The analysis of the chiral indices reveals the presence of both semiconducting and metallic SWCNT1. The pristine SWCNT1 is a mixture of chiral and armchair types of nanotubes. The indices (15,7), (11,10), (11,7), and (10,2) represent their semiconducting chiral nature with diameters 1.53, 1.43, 1.23, and 0.87 nm, respectively, while the indices, (8,8) and (6,6) represent the metallic armchair SWCNT1 with diameters of 1.08 and 0.81 nm respectively (as shown in **Table 2**).

Table 2: Summary of the Raman RBM modes, the chiralities, and diameters of the pristine SWCNTs.

RBM (cm^{-1})	Diameter (nm)	Chirality	
		Semiconducting	Metallic
162.5	1.53	(15,7)	-
174.3	1.43	(11,10)	-
200.9	1.23	(11,7)	-
227.7	1.08	-	(8,8)
286.1	0.87	(10,2)	-
305.0	0.81	-	(6,6)

Fig. 3.4(b) depicts the comparison of Raman spectra of SWCNT1 without and with WS_2 QDs (WS+C10 and WS+C50). The vertical dashed lines show a blue shift of 5 cm^{-1} in the G-band of the Raman spectra of the SWCNT1 after functionalization with WS_2 QDs. This is indicative of a strong interaction between WS_2 QDs and SWCNTs. To obtain a detailed picture of the structural characteristics of the SWCNTs, each of the Raman spectra for the range 1200-1800 cm^{-1} is fitted with three Lorentzian peaks and one Breit-Wigner-Fano (BWF) line shape corresponding to the metallic SWCNT (**Fig. 3.4(b)**)[31]. For the pristine SWCNT1, peaks at 1350 cm^{-1} (peak 1) and 1584.6 cm^{-1} (peak 4) correspond to the D and G bands, respectively. The ratio of the intensities of the D to G bands (I_D/I_G) for the SWCNT1 is 0.23, which gives a measure of the defects present in the SWCNT1. Peaks 2 and 3 correspond to the asymmetric metallic BWF feature (~1532 cm^{-1})

and the Lorentzian band (~1573 cm^{-1}) for the semiconducting carbon nanotubes, respectively[14, 31]. The presence of both semiconducting and metallic nanotubes was further confirmed from the Raman frequency calculation using the equation, $\omega = \omega_0 + \beta/d^2$ where β = -47.7 cm^{-1} nm^2 for semiconducting and β = -79.5 cm^{-1} nm^2 for the metallic SWCNT1, ω_0 = Raman frequency of G band, i.e., 1584.6 cm^{-1}, the diameter of SWCNT1 was taken as d = 1.3 nm[32]. The calculated and measured values of the frequencies match well. The overtone of the D-band, another double resonance feature, the 2D band appears at 2682.3 cm^{-1}. We compared the Raman spectra of pristine SWCNT1 with that of the composite WS+C50. The Raman spectrum of WS+C50 was similarly deconvoluted into 3 Lorentzian peaks (D, G, and semiconducting bands) and one metallic BWF peak (**Fig. 3.4(b)**). The defect-related D-band and the first-order characteristic G-band appear at 1351.5 and 1589.6 cm^{-1}, respectively. The BWF band shifts to 1543.8 cm^{-1} and the Lorentzian peak corresponding to semiconducting SWCNTs appears at 1573 cm^{-1}. The defect-related overtone of the D-band, the 2D band shifts to 2689 cm^{-1}. Thus, the D, G, and 2D bands exhibit a blue shift of 1.5, 5.0, and 7.0 cm^{-1}, respectively, in the composite sample. This is indicative of the presence of uniaxial compressive strain in the nanotubes due to the attachment of WS_2 QD on the defect (vacant) sites on the walls of the SWCNT1[31, 33-34].

Interestingly, we notice a reduction in the I_D/I_G ratio upon functionalization of SWCNT by WS_2 QDs, which comes down to 0.08 from its pristine value of 0.23, indicating a substantial decrease in the defect density in the walls of SWCNTs in the composite system. Additionally, the semiconducting nature dominates in the composite with respect to the pristine SWCNT1, perhaps due to the loading of the semiconducting WS_2 QDs on the SWCNTs. The ratio of the integrated intensities of metallic to semiconducting band decreases from ~1.8 for pristine SWCNT1 to ~0.7 in the case of the composite WS+C50. This can be attributed to the decoration of semiconducting WS_2 QD on the SWCNT1 walls. There is an overall increase in the intensities of these bands accompanied by a decrease in the full width at half maxima (FWHM) of the G band from ~30 cm^{-1} for pristine SWCNT1 to ~13.5 cm^{-1} for the functionalized SWCNT1. This hints toward an overall improvement in the crystallinity and structural quality of SWCNT1 upon functionalization with WS_2 QDs.

Next, we study the effect of SWCNTs on the Raman spectra of WS_2 QDs using laser excitation of 532 nm. **Fig. 3.4(c)** represents the comparative Raman spectra of bare WS_2 QDs and the composite showing the presence of the characteristic modes of WS_2. The 2LA, E_{2g}, and A_{1g}

modes appear at 351.5 cm^{-1}, 357.0 cm^{-1}, and 420.6 cm^{-1}, respectively for pristine WS_2 QDs. In the WS_2/SWCNT composite, the A_{1g} peak blue shifts by 0.9 cm^{-1} indicating a charge transfer from WS_2 QDs to the SWCNT. This observable shift in the A_{1g} mode is attributed to the strong electron-phonon coupling[35]. The overall change in the Raman spectra of both WS_2 QDs and SWCNTs upon complex formation is indicative of strong binding between the QDs and the SWCNTs. **Fig. 3.4(d)** shows the comparison of the full range XPS spectra of the WS_2 QDs without and with SWCNTs at different concentrations. Characteristic peaks of W 4f and S 2p are present in all the samples. Interestingly, the S 2p peak shows a substantial upshift in the binding energy for composite samples (see the inset of **Fig. 3.4(d)**), indicating the strong interaction of WS_2 QDs with the defect sites of SWCNTs, since the defect density (D band intensity) was found to reduce in the composite sample as revealed from the Raman analysis discussed above. These results may imply a strong bonding and a kind of complex formation between the WS_2 QDs and SWCNTs.

3.3.4.2. Optical studies and PL quenching

Fig. 3.5(a, b) show the UV-vis absorption spectra of the SWCNT1 and the WS_2 QDs at different concentrations of SWCNT1 (defective), respectively. The absorption spectrum of the SWCNT1 (in **Fig. 3.5(a)**) is shown for the concentration of 10 μg/ml. There is an intense absorption peak in the UV region at 280 nm due to the π- π^* interacting plasmons in the case of metallic SWCNTs. The absorption in the wavelength range of 450-600 nm is attributed to the M_{11} band for metallic nanotubes, whereas in the IR range, i.e., 900-1200 nm, the S_{22} absorption band is due to the presence of semiconducting SWCNT1[36-38]. Thus, the absorption spectrum indicates the presence of both metallic and semiconducting nanotubes. The semiconducting S_{22} bands (~988 nm and ~1160 nm) are more prominent than the metallic M_{11} band. **Fig. 3.5(b)** depicts the comparison of the absorption spectra of the WS_2 QD without and with SWCNT1 (10 and 50 μg/ml). An enhancement in the absorption intensity is observed with an increase in the concentration of SWCNT1 indicating the formation of WS_2/SWCNT1 complexes. The higher absorption in the composite may be partly due to the absorption by the SWCNTs and partly due to the scattering by the SWCNTs. There is an intense absorption peak at 294 nm, which is attributed to the WS_2 QDs, as discussed earlier. In the UV region, the absorption peak results from the contribution of both the maximum peak of the WS_2 QD and π- π^* plasmons of the SWCNT1, and hence it is broader as compared to the plasmonic absorption band exhibited by only SWCNT1.

The M_{11} band of SWCNT1 is diminished with the formation of the composite, while the semiconducting S_{22} bands are prominent. This is consistent with our conclusion that there is a complex formation between the SWCNT1 and the semiconducting WS_2 QDs, which leads to an increase in the proportion of the semiconducting SWCNT1.

PL emission measurements were carried out for the WS_2 QDs and the composites with different concentrations of SWCNT1. **Fig. 3.5(c)** shows the acquired spectra of WS_2 QDs without and with SWCNT1 for concentrations in the range of 2-50 μg/ml. With the addition of the SWCNT1, which acts as a PL quencher, a systematic decrease in the PL emission intensity of WS_2 QDs is observed with increasing concentrations of SWCNTs. For a very low concentration of the SWCNT1 (2 μg/ml), the PL peak intensity decreases by about 10%. With a further increase in the concentration of the SWCNT1, a systematic decrease in the PL intensity is observed. At the concentration of 50 μg/ml, the PL peak intensity of WS_2 QDs is quenched by ~68%.

Note that with 405 nm excitation, the measured PL is contributed mainly by defect-related X1 and X2 bands in WS_2 QDs. Quenching of defect PL with the addition of SWCNTs clearly suggests that defect sites in WS_2 are passivated by the surface defects in SWCNTs. Similar quenching was also observed with UV excitation source, as discussed later. To understand the mechanism behind the fluorescence quenching of the WS_2 QDs by the SWCNT1, the fractional integrated PL intensities (I_0/I) with respect to the concentration of SWCNT1, x (in μg/ml) shown in **Fig. 3.5(d)** and the experimental data are fitted well with the linear Stern-Volmer equation[13, 39].

$$\frac{I_0}{I} = 1 + Kx \tag{5}$$

Here I_0 and I are the maximum PL emission intensities of WS_2 QDs and the composite WS_2/SWCNT1 respectively, K, Stern-Volmer quenching constant is found to be 0.039 μg^{-1} ml. Based on the PL quenching of the WS_2 QDs by SWCNT1, the presence of SWCNT1 can be detected by WS_2 QDs. We calculated the limit of detection (LOD) of the SWCNT1 using the relation, $LOD = \frac{3 \times S.D.}{K}$, where S.D. is the standard deviation of the intercept and K is the slope.[5] The LOD, in our case, is found to be equal to 1.5 μg/ml. The linear Stern-Volmer plot indicates the occurrence of either static or dynamic quenching. Static quenching takes place when there is a formation of a ground-state complex, i.e., complex formation before the excitation. While collisional or dynamic quenching occurs due to the depopulation of the excited states of the fluorophores leading to quenching of fluorescence[13].

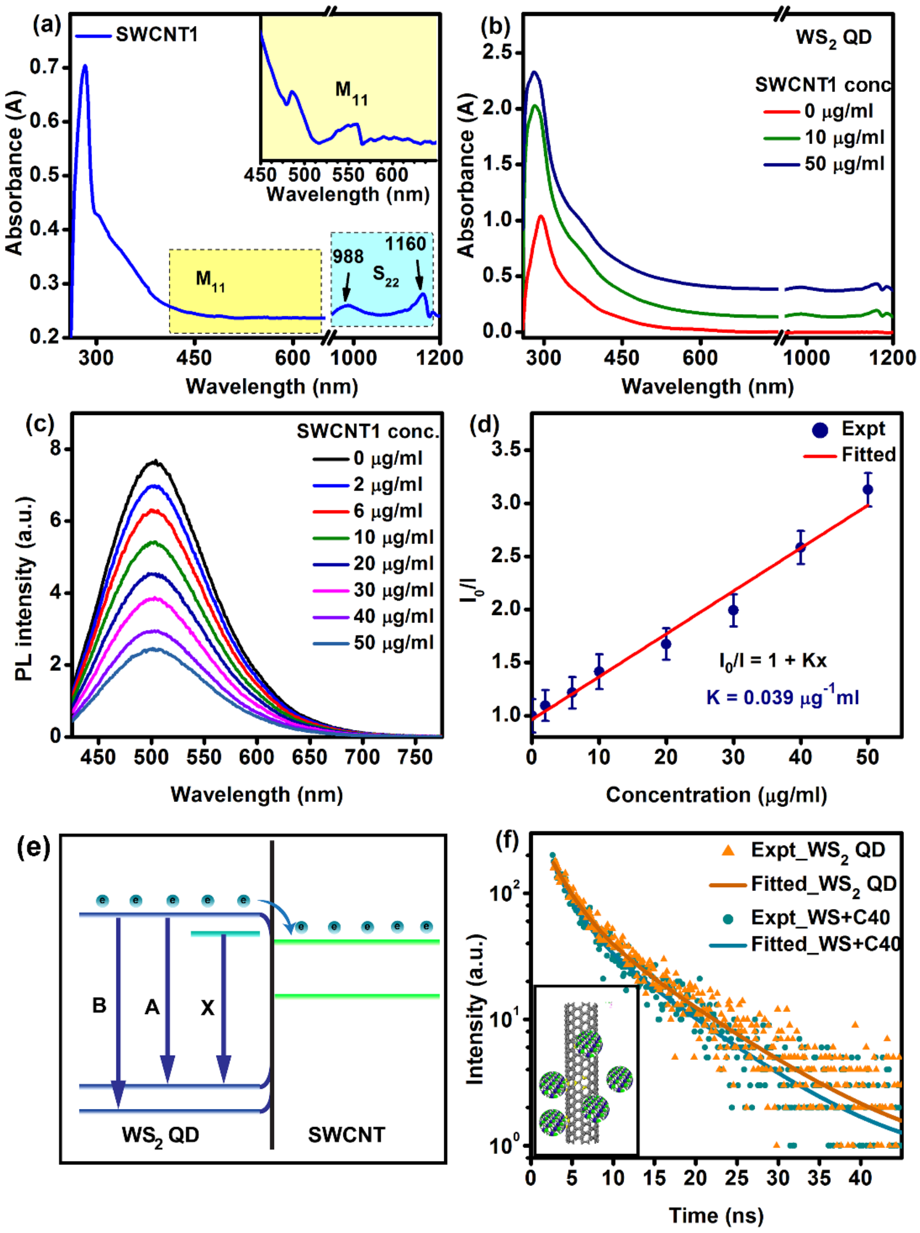

Fig. 3.5. UV-vis absorption spectra of (a) bare SWCNT1, and (b) WS_2 QDs without and with SWCNT1 at different concentrations. (c) Emission spectra of WS_2 QDs in the presence of different concentrations of SWCNT1 (0-50 μg/ml) for excitation wavelength 405 nm. (d) The Stern-Volmer plot of quenching for different concentrations of SWCNT1. (e) Schematic of the recombination and charge transfer process at the WS_2/SWCNT interface in the composite sample. (f) TRPL spectra of WS_2 QDs without and with SWCNT1 (40 μg/ml). The average carrier lifetimes are 8.8 ns and 8.1 ns, respectively. The solid line shows the bi-exponential fit to the experimental data (symbols). The inset shows a schematic of the WS_2 QD/ SWCNT complex.

Note that there is a possibility of charge transfer-induced partial quenching in the present case. **Fig. 3.5(e)** depicts a schematic of the band alignment and charge transfer as well as the recombination process for the WS_2/SWCNT composite. The work function of 2D WS_2 is ~4.6 eV[40], whereas that of SWCNTs is ~5.05 eV [41]. This difference in the work function enables charge transfer from WS_2 QD to SWCNT and also leads to suppression of carrier recombination. This is fully consistent with the Raman analysis of the WS_2 QDs that evidenced the complex formation and charge transfer induced spectral shift.

To discern the exact nature of quenching, TRPL measurements were carried out. **Fig. 3.5(f)** shows the TRPL decay profiles of WS_2 QD and WS_2/SWCNT1 composite for the SWCNT1 concentration of 40 μg/ml (WS+C40). The carrier lifetime is obtained from the decay curves fitted with the bi-exponential function. The WS_2 QDs, being highly fluorescent, have a τ_{av} of 8.8 ns. After the addition of SWCNT1, the average lifetime of the composite becomes 8.1 ns (for SWCNT1 concentration of 40 μg/ml). It is observed that with the change in the concentration of SWCNT1, the average carrier lifetime does not show any considerable change, i.e., $\tau \approx \tau_0$. Here, τ_0 and τ are the recombination lifetimes of WS_2 QDs in the absence and presence of SWCNT1, respectively. Thus, no substantial change in PL lifetime in the composite system, and the linear Stern-Volmer plot suggest that the PL quenching follows static quenching behavior due to the formation of ground state complexes. The ground state complexes are non-fluorescent. Hence, the fluorescence is quenched effectively due to the unavailability of fluorescent WS_2 QDs (fluorophores) that do not form any complexes. The WS_2 QDs, due to the presence of abundant edge sites, can form complexes with the highly defective SWCNT1 even at very low concentrations of the SWCNT1. This is consistent with the Raman analysis discussed earlier. Thus, the steady-state and time-resolved PL analyses provide clear evidence of static quenching of WS_2 QDs. Note that the complex formation is believed to be facilitated by the defect sites of SWCNTs and the edge sites of WS_2 QDs. A schematic of the SWCNT/WS_2 QD complex formation is shown in the inset of **Fig. 3.5(f).** The atomic sites marked in yellow color refer to the point defects in SWCNTs, where the WS_2 QDs are preferentially attached.

The quenching of fluorescence of WS_2 QDs was also studied using a 340 nm excitation, and the fluorescence emission here is contributed by the B and A excitons along with the defect-related emissions (see **Fig. 3.6(a)**). The fluorescence intensity of the WS_2 QDs is quenched by ~65%, which is similar to the 405 nm excitation case. The Stern-Volmer plot (**Fig. 3.6(b)**) yields the same quenching constant, K=0.039 μg^{-1} ml. Thus, the overall PL intensity is quenched with the addition of SWCNTs irrespective of the excitation energy, and this further confirms that the quenching is due to ground state WS_2/SWCNT complex formation. Another possible mechanism for quenching could be fluorescence resonance energy transfer (FRET).

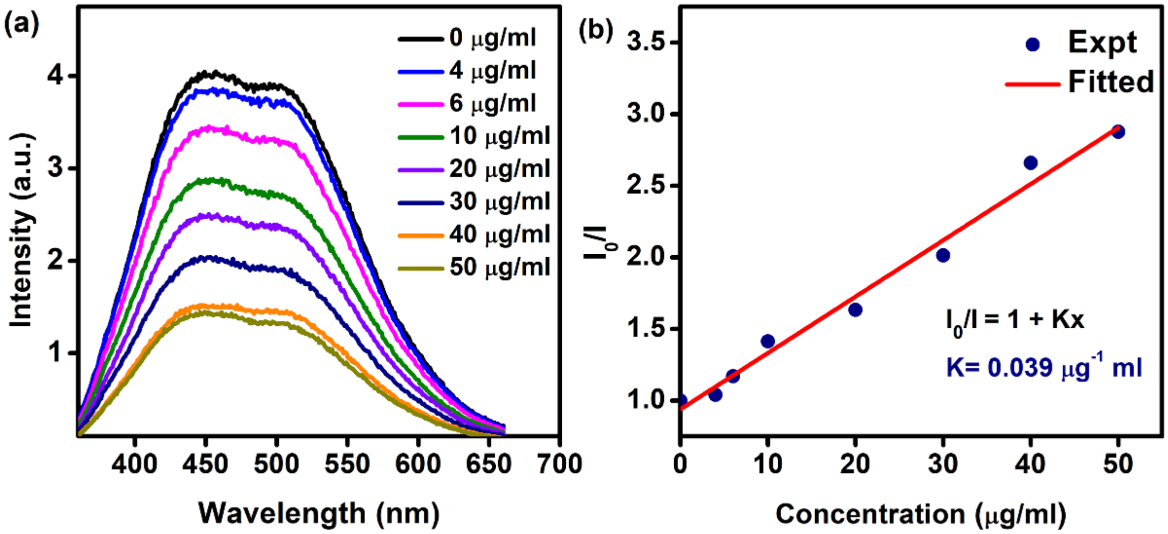

Fig. 3.6. (a) PL emission spectra of WS_2 QDs with the addition of different concentrations of SWCNT1 (0-50 μg/ml), with 340 nm excitation. (b) Stern-Volmer plot as a function of SWCNT1 concentration.

For FRET to take place, the essential condition is the overlap of energy between the donor and the acceptor molecules, i.e., the overlap of the emission spectra of the donor WS_2 QDs with the absorption of the acceptor SWCNTs. Despite the low absorption by SWCNTs in the region of emission of WS_2 QDs, any possible energy transfer cannot be completely ruled out for the A and B excitons of WS_2 QDs. However, no substantial change in the lifetime of the donor is observed in the composite sample, which essentially implies a negligible contribution of FRET in the quenching process. Thus, in the present case, quenching primarily occurs through the ground state complex formation.

The role of defects in the carbon nanotubes for the PL quenching was further ascertained by comparing the quenching efficiencies of SWCNT1 (more defective) and SWCNT2 (less defective) samples with different defect content. The comparative Raman spectra for SWCNT1 and SWCNT2 are shown in **Fig. 3.7(a).** For SWCNT1, the I_D/I_G ratio is ~0.23, as mentioned earlier, while for SWCNT2, the ratio is ~0.09. The I_D/I_G ratio is instrumental in the defect characterization of carbon nanotubes. The lower the ratio, the more defect-free are the SWCNTs[31]. Thus, the SWCNT2 sample contains a much lower density of defects, and the complex formation with WS_2 QDs is expected to be less efficient in this case as compared to SWCNT1. Note that in the case of SWCNT2, the shift in the G-band position with the addition of QDs is much lower (~1.5 cm^{-1}, see the inset of **Fig. 3.8(a)**) than that of SWCNT1 (~5 cm^{-1}).

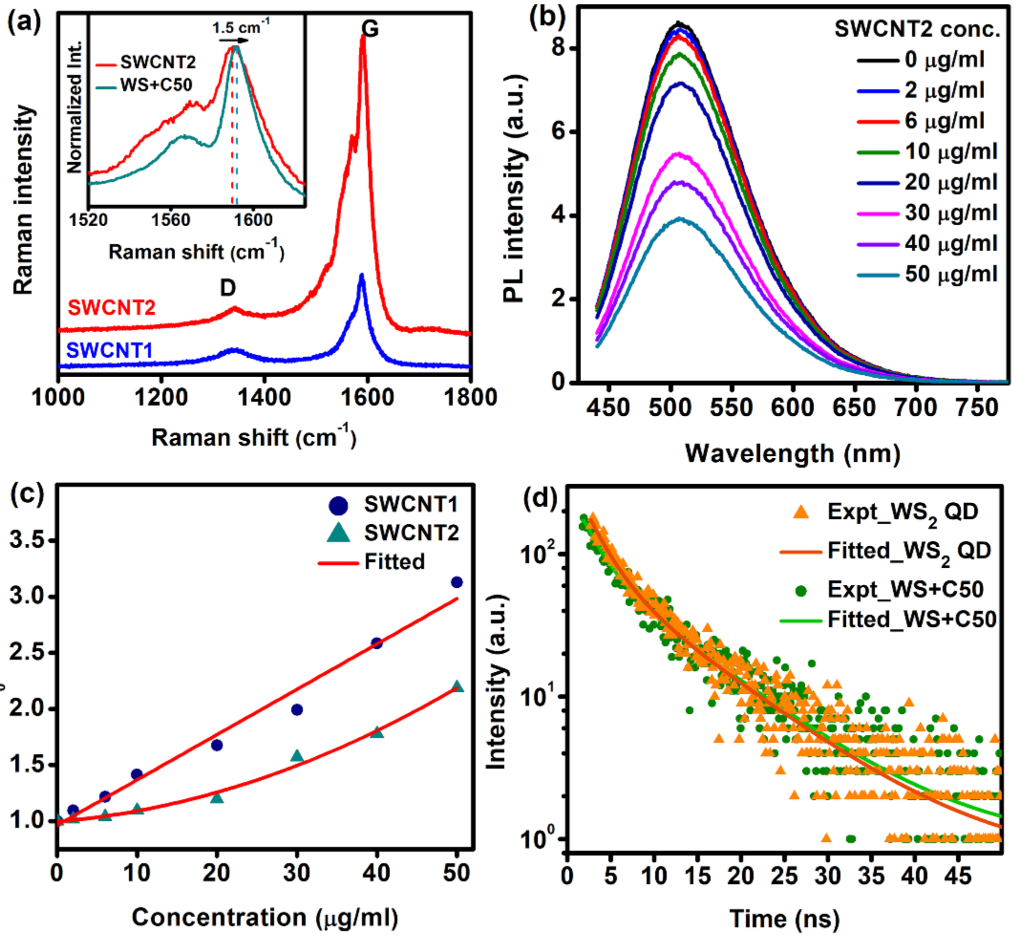

Fig. 3.7. (a) Comparative Raman spectra of SWCNT1 and SWCNT2 at laser excitation of 488 nm. The inset shows a comparison of the G band of the pristine SWCNT2 and WS_2/SWCNT2 composite showing a 1.5 cm^{-1} blue shift for the composite. (b) Evolution of the PL spectra WS_2 QDs in the presence of SWCNT2 (0-50 μg/ml) for 405 nm excitation. (c) Comparison of Stern-Volmer plots for SWCNT1 and SWCNT2. (d) TRPL spectrum of WS_2 QDs without and with SWCNT2 (50 μg/ml). The average carrier lifetimes are 8.8 ns and 9.1 ns, respectively. The solid line shows the fitted curve to the experimental data (symbols).

This implies a relatively weak interaction between QDs and SWCNT2, due to the fewer defect sites. **Fig. 3.7(b)** shows the acquired PL emission spectra of WS_2 QD in the absence and presence of less defective carbon nanotubes (SWCNT2), with concentrations ranging from 2-50 μg/ml. The PL of WS_2 is subsequently quenched in the presence of the SWCNT2. At 50 mg/ml, the PL emission intensity is reduced by 55%, which is much lower than the case of SWCNT1. Similar to the case of SWCNT1, the Stern-Volmer plot for SWCNT2 is shown in **Fig. 3.7(c)**. Note that for the SWCNT2, the quenching follows a nonlinear behavior and the quenching efficiency is much lower than that of SWCNT1 for the identical concentrations. The nonlinear quenching may be due to the combined effect of static and dynamic contributions[42]. The TRPL studies, on the other hand, show a negligible change in the average lifetime after the addition of SWCNT2 (**Fig. 3.7(d)**), which reveals that the contribution of dynamic quenching is very small. The quenching efficiency, in this case, is ~55%, which is much lower compared to highly defective SWCNT1 (~68%). Hence, the quenching efficiency is much higher in the case of more defective carbon nanotubes (SWCNT1), as the edge sites of QDs can easily bind to the defect sites of the carbon nanotubes. Note that WS_2 QDs also contain sufficient defects, as evident from the XPS and PL analyses. In particular, the edge sites of WS_2 QDs may easily attach to the defective sites of SWCNTs. Thus, the PL quenching is very efficient in the presence of the more defective SWCNT1, owing to its higher efficiency of complex formation.

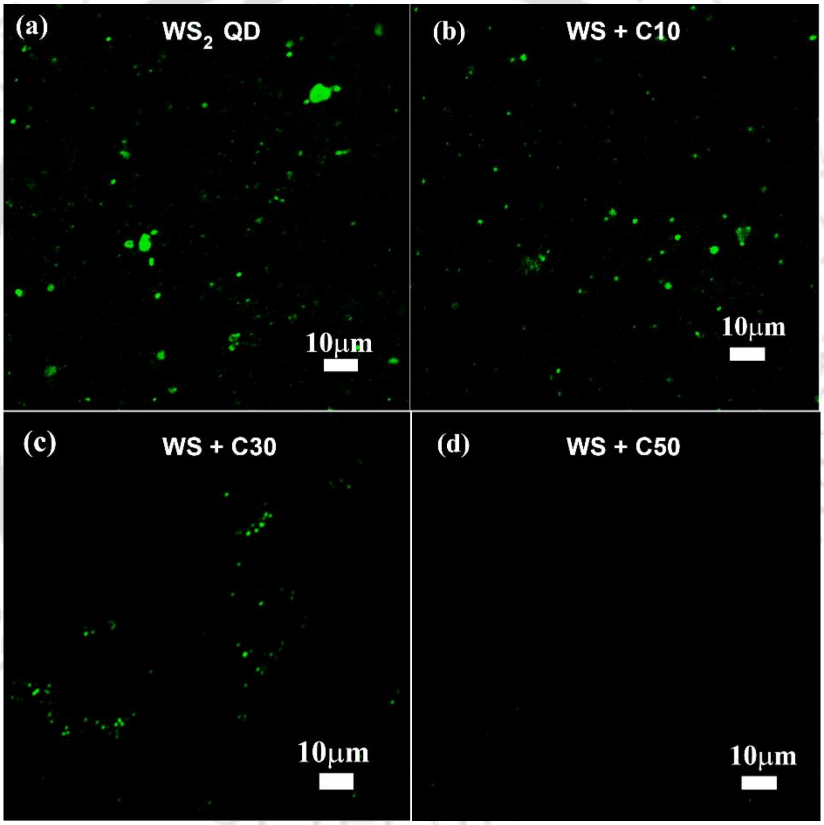

Fig. 3.8. Laser confocal microscopy images of (a) WS_2 QD and WS_2/SWCNT1 composites with SWCNT concentrations (b) 10 μg/ml, (c) 30 μg/ml, and (d) 50 μg/ml with excitation of 405 nm.

Fluorescence confocal imaging was carried out to directly visualize the fluorescence quenching of WS_2 QDs by SWCNT1. **Fig. 3.8** shows the confocal microscopy images of the WS_2 QDs and the composites of WS_2 QDs with the SWCNT1 at concentrations of 10, 30, and 50 μg/ml. For comparison, the confocal imaging was carried out under identical conditions at 405 nm excitation. The WS_2 QDs exhibit characteristic bright green emission, as evident from **Fig. 3.8(a).** On the other hand, the fluorescence images distinctively depict a gradual reduction in the fluorescence background with an increase in the concentration of SWCNT1 **(Fig. 3.8(b-d)).** This gives us direct evidence of the systematic quenching of fluorescence of the as-prepared WS_2 QD with the increase in the concentration of SWCNT1.

Based on our observations, we propose that during the ultrasonication process, the WS_2 QDs form complexes with SWCNT. The presence of ample surface edge sites/defects on the WS_2 QDs allow their attachment to the abundant defect sites on the carbon nanotube walls, which lead to the formation of non-fluorescent ground state complexes, primarily responsible for effective quenching of fluorescence[13, 42]. This attachment of WS_2 QDs on walls of the SWCNT, in turn, leads to charge transfer and further quenching of the PL intensity of the WS_2 QDs.

3.4. Conclusion

In summary, we have synthesized highly fluorescent WS_2 QDs using a liquid phase exfoliation technique. The average size of the QDs is ~2.4 nm. Analogous to monolayer WS_2, WS_2 QDs exhibit a direct optical band gap with a reasonably high PL yield (15.4%) at room temperature without any functionalization. The PL spectral analysis reveals that the excitation wavelength-dependent broad PL spectra result from different contributions from the excitonic transitions from the spin-orbit split band at the K point and emissions from defect levels. The temperature-dependent PL emission study indicates the presence of radiative defects. An exciton binding energy of ~301 meV is extracted from the Arrhenius fit to the temperature-dependent PL intensity of the A-exciton peak. We have demonstrated the efficient quenching of fluorescence of WS_2 QDs in the presence of SWCNTs with defective sidewalls. Furthermore, we have proposed a mechanism of WS_2/SWCNT complex formation supported by XPS and Raman analyses. We observed an overall improvement in the crystallinity of the SWCNTs by reduction of its defects with the help of WS_2 QDs, for the first time. Interestingly, even at a very low concentration of the SWCNT (2 μg/ml), the PL intensity of WS_2 QDs is partly quenched, and quenching is ~68% for SWCNTs concentration of 50 μg/ml. Our results reveal that quenching is static in nature, i.e., it is due to the formation of non-fluorescent WS_2/SWCNT ground state complexes leading to lesser availability of uncomplexed fluorescent QDs. Partial quenching also takes place due to charge transfer from WS$_2$ QDs to the SWCNTs due to the strong bonding between them. The quenching efficiency is shown to be higher for more defective SWCNT1 than that of less defective SWCNT2. The results are insightful in understanding the interaction between WS$_2$ QD and SWCNTs and regulating the fluorescence intensity of WS$_2$ QDs, which is important for various applications in biomedical areas, such as bio-imaging/sensing, drug delivery, etc.

References

1. Zhu, B.; Zeng, H.; Dai, J.; Gong, Z.; Cui, X., Anomalously Robust Valley Polarization and Valley Coherence in Bilayer Ws₂. *Proceedings of the National Academy of Sciences* **2014**, *111*, 11606-11611.
2. Gusakova, J.; Wang, X.; Shiau, L. L.; Krivosheeva, A.; Shaposhnikov, V.; Borisenko, V.; Gusakov, V.; Tay, B. K., Electronic Properties of Bulk and Monolayer Tmds: Theoretical Study within Dft Framework (Gvj-2e Method). *physica status solidi (a)* **2017**, *214*, 1700218.
3. Peimyoo, N.; Shang, J.; Cong, C.; Shen, X.; Wu, X.; Yeow, E. K. L.; Yu, T., Nonblinking, Intense Two-Dimensional Light Emitter: Monolayer Ws2 Triangles. *ACS Nano* **2013**, *7*, 10985-10994.
4. Zhu, B.; Chen, X.; Cui, X., Exciton Binding Energy of Monolayer Ws2. *Scientific Reports* **2015**, *5*, 9218.
5. Yan, Y.; Zhang, C.; Gu, W.; Ding, C.; Li, X.; Xian, Y., Facile Synthesis of Water-Soluble Ws2 Quantum Dots for Turn-on Fluorescent Measurement of Lipoic Acid. *The Journal of Physical Chemistry C* **2016**, *120*, 12170-12177.
6. Xu, S.; Li, D.; Wu, P., One-Pot, Facile, and Versatile Synthesis of Monolayer Mos2/Ws2 Quantum Dots as Bioimaging Probes and Efficient Electrocatalysts for Hydrogen Evolution Reaction. *Advanced Functional Materials* **2015**, *25*, 1127-1136.
7. Bayat, A.; Saievar, E., *Synthesis of Blue Photoluminescent Ws2 Quantum Dots Via Ultrasonic Cavitation*, 2017; Vol. 185.
8. Bai, X., et al., Ultrasmall Ws2 Quantum Dots with Visible Fluorescence for Protection of Cells and Animal Models from Radiation-Induced Damages. *ACS Biomaterials Science & Engineering* **2017**, *3*, 460-470.
9. Shi, J.; Lyu, J.; Tian, F.; Yang, M., A Fluorescence Turn-on Biosensor Based on Graphene Quantum Dots (Gqds) and Molybdenum Disulfide (Mos2) Nanosheets for Epithelial Cell Adhesion Molecule (Epcam) Detection. *Biosensors and Bioelectronics* **2017**, *93*, 182-188.
10. Zhong, Y.; Yi, T., Mos2 Quantum Dots as a Unique Fluorescent “Turn-Off–on” Probe for the Simple and Rapid Determination of Adenosine Triphosphate. *Journal of Materials Chemistry B* **2019**, *7*, 2549-2556.
11. Gan, Z.; Gui, Q.; Shan, Y.; Pan, P.; Zhang, N.; Zhang, L., Photoluminescence of Mos2 Quantum Dots Quenched by Hydrogen Peroxide: A Fluorescent Sensor for Hydrogen Peroxide. *Journal of Applied Physics* **2016**, *120*, 104503.
12. Zhu, Z.; Yang, R.; You, M.; Zhang, X.; Wu, Y.; Tan, W., Single-Walled Carbon Nanotube as an Effective Quencher. *Analytical and Bioanalytical Chemistry* **2010**, *396*, 73-83.
13. Lakowicz, J. R., *Principles of Fluorescence Spectroscopy*, 3rd ed.; Springer: New York, NY, 1983.
14. Das, R.; Rajender, G.; Giri, P. K., Anomalous Fluorescence Enhancement and Fluorescence Quenching of Graphene Quantum Dots by Single Walled Carbon Nanotubes. *Physical Chemistry Chemical Physics* **2018**, *20*, 4527-4537.
15. Karimi, B.; Arabi, A. M.; Najafi, F.; Shafiee Afarani, M., Cnt–Cdse Qds Nanocomposites: Synthesis and Photoluminescence Studies. *Journal of Materials Science: Materials in Electronics* **2018**, *29*, 13499-13507.
16. Zeng, H., et al., Optical Signature of Symmetry Variations and Spin-Valley Coupling in Atomically Thin Tungsten Dichalcogenides. *Scientific Reports* **2013**, *3*, 1608.
17. Yin, W.; Bai, X.; Chen, P.; Zhang, X.; Su, L.; Ji, C.; Gao, H.; Song, H.; Yu, W. W., Rational Control of Size and Photoluminescence of Ws2 Quantum Dots for White Light-Emitting Diodes. *ACS Applied Materials & Interfaces* **2018**, *10*, 43824-43830.

18. Lin, L.; Xu, Y.; Zhang, S.; Ross, I. M.; Ong, A. C. M.; Allwood, D. A., Fabrication of Luminescent Monolayered Tungsten Dichalcogenides Quantum Dots with Giant Spin-Valley Coupling. *ACS Nano* **2013**, *7*, 8214-8223.

19. Zhao, W.; Ghorannevis, Z.; Chu, L.; Toh, M.; Kloc, C.; Tan, P.-H.; Eda, G., Evolution of Electronic Structure in Atomically Thin Sheets of Ws2 and Wse2. *ACS Nano* **2013**, *7*, 791-797.

20. Chernikov, A.; Berkelbach, T. C.; Hill, H. M.; Rigosi, A.; Li, Y.; Aslan, O. B.; Reichman, D. R.; Hybertsen, M. S.; Heinz, T. F., Exciton Binding Energy and Nonhydrogenic Rydberg Series in Monolayer ${\Mathrm{Ws}}_{2}$. *Physical Review Letters* **2014**, *113*, 076802.

21. Amani, M.; Taheri, P.; Addou, R.; Ahn, G. H.; Kiriya, D.; Lien, D.-H.; Ager, J. W.; Wallace, R. M.; Javey, A., Recombination Kinetics and Effects of Superacid Treatment in Sulfur- and Selenium-Based Transition Metal Dichalcogenides. *Nano Letters* **2016**, *16*, 2786-2791.

22. Mak, K. F.; Lee, C.; Hone, J.; Shan, J.; Heinz, T. F., Atomically Thin ${\Mathrm{Mos}}_{2}$: A New Direct-Gap Semiconductor. *Physical Review Letters* **2010**, *105*, 136805.

23. Chow, P. K.; Jacobs-Gedrim, R. B.; Gao, J.; Lu, T.-M.; Yu, B.; Terrones, H.; Koratkar, N., Defect-Induced Photoluminescence in Monolayer Semiconducting Transition Metal Dichalcogenides. *ACS Nano* **2015**, *9*, 1520-1527.

24. Caigas, S. P.; Santiago, S. R. M.; Lin, T.-N.; Lin, C.-A. J.; Yuan, C.-T.; Shen, J.-L.; Lin, T.-Y., Origins of Excitation-Wavelength-Dependent Photoluminescence in Ws2 Quantum Dots. *Applied Physics Letters* **2018**, *112*, 092106.

25. Cushing, S. K.; Ding, W.; Chen, G.; Wang, C.; Yang, F.; Huang, F.; Wu, N., Excitation Wavelength Dependent Fluorescence of Graphene Oxide Controlled by Strain. *Nanoscale* **2017**, *9*, 2240-2245.

26. Liu, H.; Lu, J., Exciton Dynamics in Tungsten Dichalcogenide Monolayers. *Physical Chemistry Chemical Physics* **2017**, *19*, 17877-17882.

27. Nan, H., et al., Strong Photoluminescence Enhancement of Mos2 through Defect Engineering and Oxygen Bonding. *ACS Nano* **2014**, *8*, 5738-5745.

28. Mawlong, L. P. L.; Paul, K. K.; Giri, P. K., Direct Chemical Vapor Deposition Growth of Monolayer Mos2 on Tio2 Nanorods and Evidence for Doping-Induced Strong Photoluminescence Enhancement. *The Journal of Physical Chemistry C* **2018**, *122*, 15017-15025.

29. Splendiani, A.; Sun, L.; Zhang, Y.; Li, T.; Kim, J.; Chim, C.-Y.; Galli, G.; Wang, F., Emerging Photoluminescence in Monolayer Mos2. *Nano Letters* **2010**, *10*, 1271-1275.

30. Yong, Y.; Cheng, X.; Bao, T.; Zu, M.; Yan, L.; Yin, W.; Ge, C.; Wang, D.; Gu, Z.; Zhao, Y., Tungsten Sulfide Quantum Dots as Multifunctional Nanotheranostics for in Vivo Dual-Modal Image-Guided Photothermal/Radiotherapy Synergistic Therapy. *ACS Nano* **2015**, *9*, 12451-12463.

31. Dresselhaus, M. S.; Dresselhaus, G.; Saito, R.; Jorio, A., Raman Spectroscopy of Carbon Nanotubes. *Physics Reports* **2005**, *409*, 47-99.

32. Jorio, A., et al., G-Band Resonant Raman Study of 62 Isolated Single-Wall Carbon Nanotubes. *Physical Review B* **2002**, *65*, 155412.

33. Brar, V. W.; Samsonidze, G. G.; Dresselhaus, M. S.; Dresselhaus, G.; Saito, R.; Swan, A. K.; Ünlü, M. S.; Goldberg, B. B.; Souza Filho, A. G.; Jorio, A., Second-Order Harmonic and Combination Modes in Graphite, Single-Wall Carbon Nanotube Bundles, and Isolated Single-Wall Carbon Nanotubes. *Physical Review B* **2002**, *66*, 155418.

34. Liu, Z.; Zhang, J.; Gao, B., Raman Spectroscopy of Strained Single-Walled Carbon Nanotubes. *Chemical Communications* **2009**, 6902-6918.

35. Li, Z.; Ye, R.; Feng, R.; Kang, Y.; Zhu, X.; Tour, J. M.; Fang, Z., Graphene Quantum Dots Doping of Mos2 Monolayers. *Advanced Materials* **2015**, *27*, 5235-5240.

36. Berciaud, S.; Cognet, L.; Poulin, P.; Weisman, R. B.; Lounis, B., Absorption Spectroscopy of Individual Single-Walled Carbon Nanotubes. *Nano Letters* **2007**, *7*, 1203-1207.

37. Rance, G.; Marsh, D.; Nicholas, R.; Khlobystov, A., Uv-Vis Absorption Spectroscopy of Carbon Nanotubes: Relationship between the Pi-Electron Plasmon and Nanotube Diameter. *CHEMICAL PHYSICS LETTERS* **2010**, *493*, 19-23.
38. Weisman, R. B., Chapter 5 Optical Spectroscopy of Single-Walled Carbon Nanotubes. In *Contemporary Concepts of Condensed Matter Science*, Saito, S.; Zettl, A., Eds. Elsevier: 2008; Vol. 3, pp 109-133.
39. Choi, J.; Zhang, H.; Choi, J. H., Modulating Optoelectronic Properties of Two-Dimensional Transition Metal Dichalcogenide Semiconductors by Photoinduced Charge Transfer. *ACS Nano* **2016**, *10*, 1671-1680.
40. Wang, K., et al., Interlayer Coupling in Twisted Wse2/Ws2 Bilayer Heterostructures Revealed by Optical Spectroscopy. *ACS Nano* **2016**, *10*, 6612-6622.
41. Shiraishi, M.; Ata, M., Work Function of Carbon Nanotubes. *Carbon* **2001**, *39*, 1913-1917.
42. Singh, D. K.; Iyer, P. K.; Giri, P. K., Role of Molecular Interactions and Structural Defects in the Efficient Fluorescence Quenching by Carbon Nanotubes. *Carbon* **2012**, *50*, 4495-4505.

Chapter 4

Highly suppressed dark current and fast photoresponse in Au nanoparticle embedded Si/Au/WS₂ quantum dot-based self-biased Schottky photodetector

Two-dimensional semiconductor-based heterojunction photodetectors with ultra-low dark current and fast photoresponse are highly desirable for cutting-edge optoelectronic applications. Herein, we study the role of embedded plasmonic Au nanoparticles (NP) on the photoresponse characteristic of heterojunction photodetector (PD) consisting of n-type WS_2 quantum dots (QD) decorated on a p-type Si substrate. The Si/WS_2 photodetector without the Au NPs has a fast response/recovery time of ~55.1/139.8 μs and a photocurrent to dark current ratio (I_{on}/I_{off}) of ~227. By integrating the Au NPs sandwiched between the Si/WS_2 QD junction, the device showed outstanding photodetection performance compared to the Si/WS_2 PD. The Si/Au/WS_2 Schottky heterojunction device exhibits an astounding I_{on}/I_{off} ratio ~1.3×10^5 due to the decrease in dark current by about two orders of magnitude as well as an increase in photocurrent by about one order of magnitude and significantly faster rise/fall times of ~4.4/43.5 μs. The underlying mechanism behind the ultralow dark current and high on/off ratio is investigated in detail. The faster photoresponse is attributed to hot electron transfer as well as carrier tunneling from Au NPs to WS_2 QDs. The peak responsivity and detectivity of the fabricated Si/Au/WS_2 detector are estimated at ~276 A/W and ~ 4.3×10^{13} Jones, respectively, at an applied bias of 5 V and under 405 nm illumination. Notably, both devices function as self-powered PDs. Moreover, the Au NP incorporated hybrid system exhibits a ~6-fold enhancement in the photoluminescence (PL) as compared to bare WS_2 QDs owing to surface plasmon resonance. We use a theoretical model to calculate the field enhancement factor in the vicinity of WS_2 QDs due to the Au NPs and show that the experimental data match very well with the theoretical value at the chosen excitation wavelength. These results indicate that integrating plasmonic nanoparticles with the Si/WS_2 QD PD holds great potential for applications in future high-performance optoelectronic devices.

4.1. Introduction

In recent times, the family of layered 2D TMDs has drawn a great deal of attention in the field of optoelectronics on account of their fascinating properties, such as strong light-matter interaction and tunable bandgaps[1-6]. Among several semiconducting two-dimensional TMDs,

WS_2 has been widely studied due to its remarkable layer-dependent bandgap giving rise to a plethora of unique electrical and optical properties[7-10]. Zero-dimensional WS_2 QDs have excellent light absorption, tunable bandgap, water solubility, and low-cost solution processing. Despite these advantages, these QDs display poor carrier transport in comparison to conventional semiconductors, which is an immense hindrance to the efficiency and performance of the photodetection device. However, the WS_2 QD-based heterostructures have been demonstrated to have far more superior properties than their counterparts, which can produce ultrasensitive and broadband detection with high efficiency photodetectors.

There has been intensive research on van der Waals-based WS_2 heterostructures with materials such as Si,[11-13] graphene[5, 14], other TMDs (e.g., MoS_2, etc.)[14-16], plasmonic materials (Au, Ag, etc.)[17-19], TiO_2[20], etc. Among the various materials, hybrid nanostructures of WS_2 with Si have been thoroughly investigated. Wu et al. demonstrated a high-performance self-powered WS_2 film/Si heterojunction photodetector (PD) that could perform broadband photodetection[21]. Lan et al. reported a highly responsive and stable Zener photodiode based on n-WS_2 film/p-Si heterojunction[12]. However, WS_2 QD-based heterojunction photodetection on Si platforms remains unexplored. Furthermore, the strong light-matter interaction exhibited by layered TMD quantum dots can further be manipulated by integrating noble metal nanostructures that support localized surface plasmon resonance (LSPR)[17, 22-23]. These hybrid systems make for a promising platform for the development of high-performance photonic and optoelectronic devices[19]. In TMD-plasmon nanohybrid systems identified under a weakly coupled regime, plasmon-enhanced photoluminescence is observed. This phenomenon has been investigated for the enhancement of the PL emission intensity of monolayered TMDs[17, 22, 24-25]. Du et al. reported an extensive study of the steady-state and ultrafast response of monolayer WS_2-Ag nanodisk hybrid system[17]. In addition to the manipulation of optical properties, metal nanostructures are also used as efficient surface-enhanced Raman scattering (SERS) substrates[26]. To the best of our knowledge, the effect of Au NPs on the optical properties of WS_2 QDs is not yet explored. Further, the integration of WS_2 QDs with Au NPs grown by a physical deposition method is yet to be explored, which is most suitable for large-scale fabrication of high-performance devices. In this chapter, we fabricated a Si/WS_2 QD heterojunction-based PD and investigated the role of Au nanoparticles embedded at the heterojunction in its photodetection performance. We investigate the mechanism behind the superior performance of the Si/Au/WS_2 QD PD. WS_2 QDs act as a light-harvesting material, while the Au NPs underneath the WS_2 QDs serve as a carrier tunneling pathway and a medium for hot electron transfer for ultra-fast transport of photogenerated charge carriers. To explain the role of the plasmonic Au NPs quantitatively, we employ a theoretical model to calculate the field enhancement factor in the vicinity of WS_2 QD in presence of the Au NPs. The experimental results are consistent with the theoretical predictions in entirety.

4.2. Experimental procedure

4.2.1. Synthesis of WS_2 QDs

WS_2 QDs were synthesized using liquid exfoliation followed by centrifugation, as discussed in **Chapter 2 (Section 2.1.2.).** The excess solvent from the supernatant was then allowed to be evaporated with constant magnetic stirring at 750 rpm. The obtained dark residue of the WS_2 QDs was redispersed in ethanol at a concentration of 50 mg/l and used in device fabrication.

4.2.2. Growth of Au nanoparticles

The Au nanoparticles were grown by a two-step physical deposition/growth process. Firstly, an Au film was deposited on various substrates, such as p-type Si, SiO_2, and quartz, using the radio frequency (RF) magnetron sputtering technique. A 2-inch diameter high-purity Au sputter target (99.99%) was used for the process. The RF power was set at 8 W and the deposition was carried out for 15 minutes in an Ar gas atmosphere. The substrate holder was kept on rotation mode for a uniform deposition which resulted in an ultrathin Au film on various substrates. Next, a rapid thermal annealing system (RTA, Ulvac, Japan) was employed to reduce the deposited Au film into an array of Au NPs. The temperature for the RTA was set at 600°C for 3 minutes in Ar ambient condition. The ramping rate was fixed at 20 °C/s for both heating and cooling. RTA works in the principle of this rapid application of thermal energy resulting in the disintegration of the uniform metallic film which then again recrystallizes and nucleates to form nano-islands due to rapid cooling, yielding a high-quality array of NPs[27].

4.2.3. Fabrication of Si/WS_2 and $Si/Au/WS_2$ heterojunction photodetectors

The Si/WS_2 and $Si/Au/WS_2$ heterojunction photodetectors were fabricated for photocurrent measurements. 40 μl of WS_2 QDs in ethanol (50 mg/l) was dropped cast on a p-type Si substrate and Au NP coated p-Si substrate (Si/Au), which were then air-dried. This was optimized to ensure maximum coverage of the WS_2 QDs on the respective platforms for both the PDs so that the top contact is only in contact with the WS_2 layer. For electrical contacts, 200 nm thick Au film was deposited by thermal evaporation technique. The electrodes were deposited through a shadow mask, placed strategically, such that one electrode is in contact with p-Si and the other is in contact with the n-WS_2 QDs.

4.2.4. Characterization techniques

The details of the TEM, AFM, Micro-Raman, XPS, UV-Vis absorbance, and PL measurements of the WS_2 QDs have been discussed in **Chapter 2 (Section 2.1.3).** The size, distribution, and uniformity of Au NPs were studied by a field emission scanning electron microscope (FESEM; Sigma 300, Zeiss). X-ray photoelectron spectroscopy (XPS) was employed using a PHI X-tool automated photoelectron spectrometer (Ulvac-Phi Inc., Japan) to study the chemical environment of WS_2 QDs and the Au/WS_2 heterostructure. Raman spectra of the WS_2 QDs, as well as WS_2 QDs/Au NPs HS, have been acquired using a high-resolution micro-Raman spectrometer (LabRam HR800, Jobin-Yvon) with an excitation wavelength of 514 nm (Ar ion laser). Comparative PL measurements were carried out on thin films of the WS_2 QDs on Si and Au NP decorated Si using a commercial spectro-fluorimeter (Horiba Scientific, Fluoromax-4) and an external laser of excitation wavelength of 405 nm. Low-temperature PL measurement was performed for WS_2 QDs coated on Au NP decorated Si inside a liquid-nitrogen-cooled optical cryostat (Optistat DNV, Oxford Instruments). An external 405 nm laser was used as the excitation source. Time-resolved PL (TRPL) spectra were recorded using a time-resolved luminescence spectrometer (Edinburg Instruments, FSP920) using a 405 nm pulsed excitation source. Photocurrent measurements were done using a microprobe station (ECOPIA, EPS-500) connected to a source measure unit (Keithley 2400) and a 405 nm laser (CNI Laser) was used as the source of illumination. The device was illuminated using a focusing lens from the top such that photoexcitation took place in both WS_2 QDs and Si. A function generator was connected to the laser to generate laser pulses for photocurrent response measurement. The photocurrent response was digitized using a digital storage oscilloscope and the KickStart software. The 405 nm laser was used to measure the power-dependent responsivity and specific detectivity of the device. A 250 W Xenon lamp (Newport, USA) was used to measure the spectral responsivity and detectivity of the device. The excitation wavelength was chosen using a monochromator (Oriel Instruments, USA) attached to the lamp.

4.3. Results and discussion

4.3.1. Morphology studies

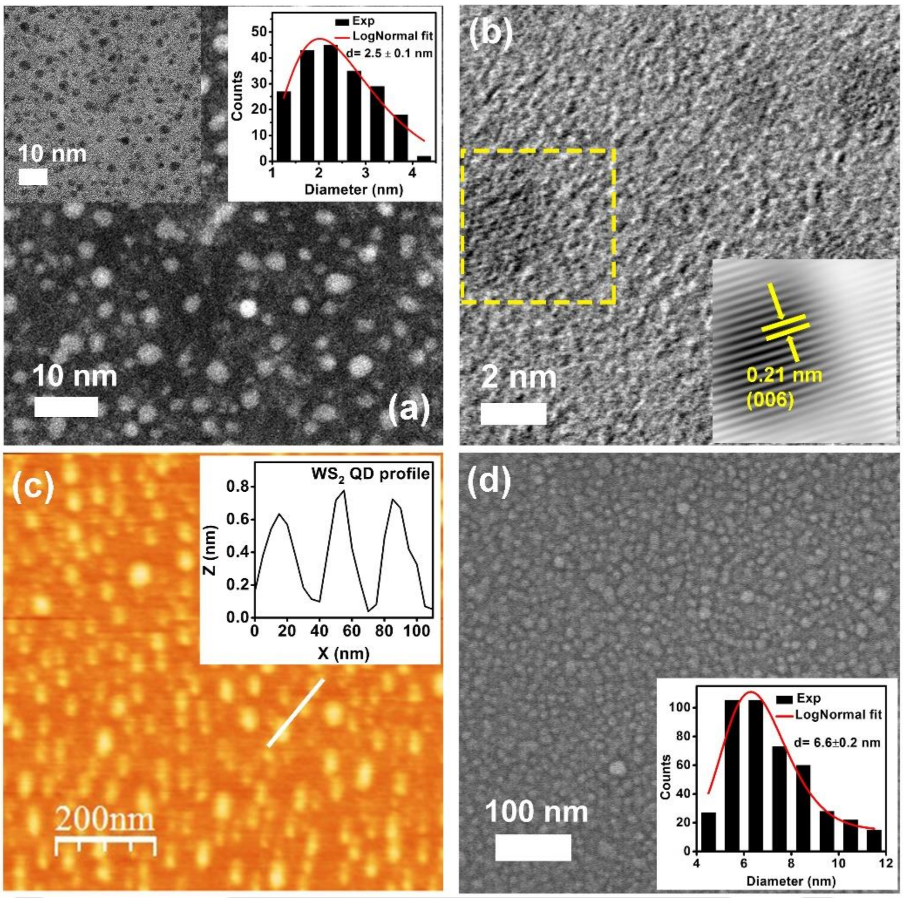

Fig. 4.1. (a) HAADF TEM image of the WS_2 QDs. The left inset displays the corresponding bright-field image. The top right inset shows a histogram of the size distribution of the WS_2 QDs along with the log-normal fit. (b) HRTEM lattice image of the WS_2 QDs; the inset shows the IFFT image of WS_2 lattice planes in the marked region. (c) AFM image of the WS_2 QDs. The inset shows the height profile of the WS_2 QDs along the white line. (d) FESEM image of the Au NPs on Si substrate. The inset displays a histogram of the size distribution of the Au NPs, showing an average size of 6.6 nm.

The size distribution and typical morphology of the WS_2 QDs were studied using HAADF-STEM. **Fig. 4.1(a)** shows the dark field TEM image of the WS_2 QDs showing a narrow size distribution (2-4 nm) which has been fitted with a log-normal function. The average diameter of the QDs is estimated at 2.5 ± 0.1 nm (right inset of **Fig. 4.1(a)).** The corresponding bright-field image is shown in the left inset of **Fig. 4.1(a). Fig. 4.1(b)** displays the high-resolution TEM (HRTEM) image of WS_2 QDs. Following further HRTEM analysis, using Gatan Digital Micrograph software, we obtain the inverse fast-Fourier transformed (IFFT) image of **Fig. 4.1(b)** (shown in the inset). The lattice d-spacing comes out to be 0.21 nm, which corresponds to the (006) plane of the WS_2 crystal. Atomic force microscopy (AFM) is used to determine the thickness or height profile of the WS_2 QDs. It is noteworthy that the lateral resolution of AFM is relatively low, while the vertical resolution is very high. The AFM image of the WS_2 QDs is shown in **Fig. 4.1(c).** The height profile of the WS_2 QDs along the white line reveals their thickness as ~8 Å (inset of **Fig. 4.1(c)**), which indicates that the QDs are mostly monolayer in nature[28]. The morphology of the as-synthesized Au NPs was studied using FESEM imaging.

Fig. 4.1(d) displays the FESEM image of the Au NPs showing a size distribution with diameters ranging from ~4 to 12 nm. The log-normal fit yields an average diameter of 6.6 ± 0.2 nm for the Au NPs (inset of **Fig. 4.1(d)**).

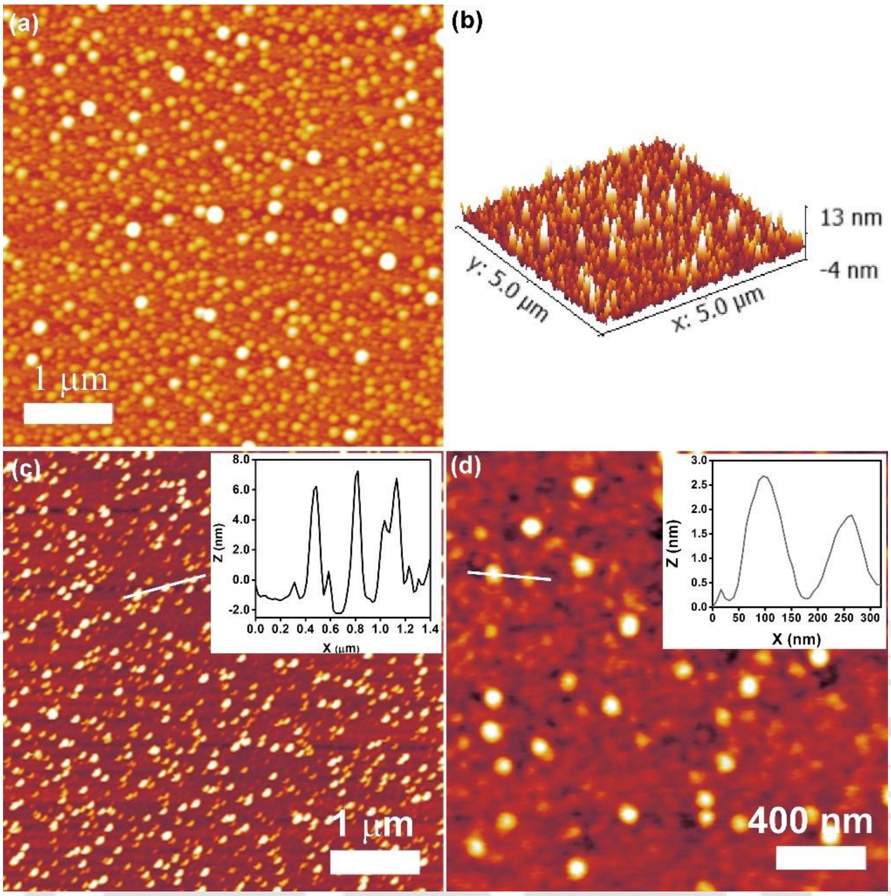

Fig. 4.2. (a) AFM image of WS_2 QDs on Si/WS_2 device. (b) Corresponding 3D height profile of the WS_2 QDs layer. (c) AFM image of Au NPs. (d) AFM image of Au NP/WS_2 QD system. Insets display the respective height profiles of the Au NPs (along the white lines).

Fig. 4.2(a) depicts the AFM image of the WS_2 QD layer on the Si/WS_2 device. There is optimum coverage of the QDs over the Si substrate, which ensures no Au atoms pass through the QDs during thermal deposition of electrodes. **Fig 4.2(b)** represents the corresponding three-dimensional profile of the WS_2 QDs revealing a total thickness of ~13 nm. The AFM image of the Au NPs is shown in **Fig. 4.2(c),** which reveals an average height of about ~6-8 nm. The AFM image of the WS_2 QD/Au NP system is displayed in **Fig. 4.2(d).**

4.3.2. Structural and compositional analysis

4.3.2.1. Micro-Raman analysis

Micro-Raman measurement was carried out on Si/WS_2 and Si/Au/WS_2 systems using a 514 nm Ar laser. WS_2 exhibits two characteristic Raman modes, E_{2g} (356.2 cm^{-1}) and A_{1g}

(420.8 cm^{-1}) as depicted in **Fig. 4.3(a),** which correspond to the in-plane vibration and the out-of-plane vibrations of the S atoms with respect to the W atoms in 2H WS_2, respectively.

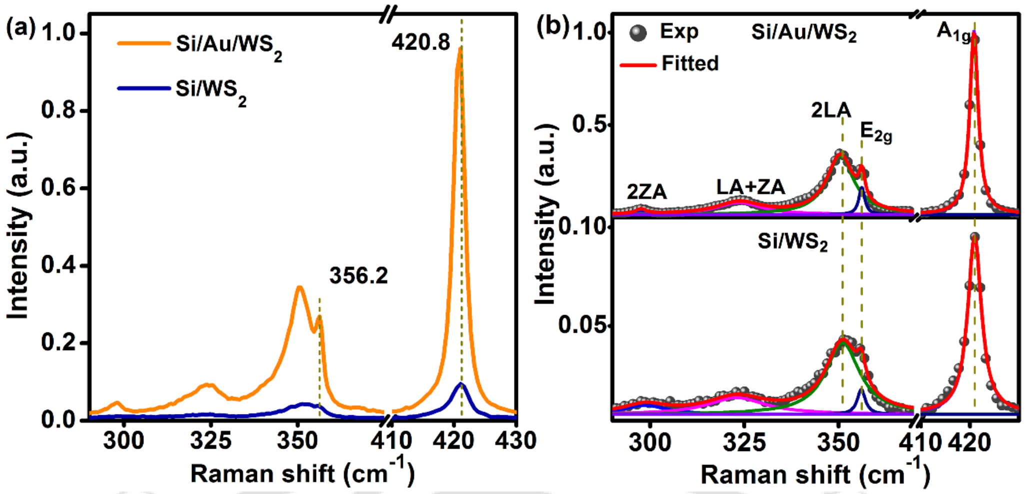

Fig. 4.3. (a) Comparative Raman spectra of WS_2 QDs on Si substrate and Si/Au substrate at excitation of 514 nm. (b) Deconvoluted Raman spectra of WS_2 QDs in Si/WS_2 and Si/Au/WS_2.

These two peaks are common to both Si/WS_2 and Si/Au/WS_2 samples. Interestingly, in the latter case, there is ~10 folds enhancement in the intensity of the A_{1g} mode of WS_2 QDs owing to the surface-enhanced Raman spectroscopy (SERS) effect caused by the Au NPs. Au NPs are well-known SERS materials that enhance the Raman signal via electromagnetic field enhancement[26]. The Raman spectra for both the cases are deconvoluted and a stacked plot is displayed in **Fig. 4.3(b).** In addition to the characteristic optical modes, WS_2 exhibits a high-intensity second-order longitudinal acoustic mode (2LA) at 351.1 cm^{-1} [29-30]. The peak at 325.6 cm^{-1} is ascribed to a combination of the longitudinal acoustic (LA) and out-of-plane acoustic vibrational (ZA) modes[30]. The presence of these Raman modes confirms good crystallinity in the as-prepared WS_2 QDs[31]. In the case of the Si/Au/WS_2 sample, these peaks exhibit a negligible shift, although there is a tenfold enhancement in the relative intensity of all the modes.

4.3.2.2. XPS Analysis

To further investigate the chemical composition/environment of the WS_2 QDs and the Au/WS_2 heterostructure, we employed X-ray photoelectron spectroscopy (XPS) analysis. **Fig. 4.4(a)** represents the survey scan XPS spectra of Si/WS_2 and Si/Au/WS_2. The survey scan corresponding to the WS_2 QDs clearly shows the peaks corresponding to W and S along with those of C, N, and O respectively, which are due to the solvent residue/contamination on the sample. In the case of Si/Au/WS_2, the additional Au 4f peak is observed in the spectrum. **Fig. 4.4(b)** depicts the XPS spectra of the core level W 4f for WS_2 QDs and Si/Au/WS_2. For WS_2

QDS, the peaks at 33.7 eV and 35.7 eV correspond to the 4th oxidation state of W and are ascribed to W $4f_{7/2}$ and W $4f_{5/2}$, respectively, confirming the formation of WS_2[32].

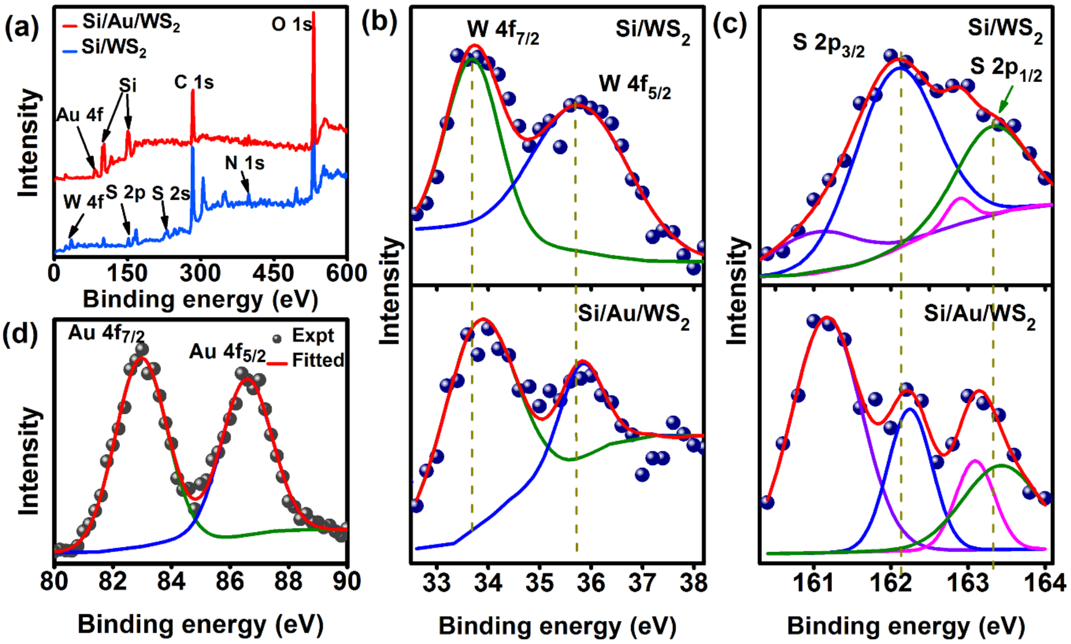

Fig. 4.4. (a) XPS survey scan spectra for Si/WS_2 and $Si/Au/WS_2$. (b, c) Comparative high-resolution XPS W 4f and S 2p spectra of WS_2 QDs on Si/WS_2 and $Si/Au/WS_2$. (d) High-resolution XPS spectrum of $Si/Au/WS_2$ showing Au 4f peaks. The solid lines are the Gaussian fittings of the experimental data (symbols) with Shirley baseline.

However, in the case of $Si/Au/WS_2$, there is a marginal shift of these peaks to 33.8 eV and 35.8 eV, respectively. This could be an indication of charge transfer from the Au NPs to the WS_2 QDs[33]. **Fig. 4.4(c)** displays the high-resolution S 2p XPS spectra of the WS_2 QDs and the $Si/Au/WS_2$. The peaks corresponding to the S^{2-} ions at ~162.0 eV and ~163.2 eV are attributed to the S $2p_{3/2}$ and S $2p_{1/2}$, respectively. The additional peaks at 161.0 eV (with a spectral weight of 13.6 %) and 162.9 eV (with a spectral weight of 2.6 %) in the S-2p envelope of the WS_2 QDs are due to S vacancies in the WS_2 QDs, which come into existence during the liquid exfoliation process[32, 34]. For the $Si/Au/WS_2$, the S peaks corresponding to S $2p_{3/2}$ and S $2p_{1/2}$ blue shift to 162.2 eV and 163.4 eV, respectively. The S vacancy-related peaks have effectively higher spectral weights in $Si/Au/WS_2$ (50.3% and 11.2%, respectively), which suggests an increase in the defect density in the WS_2 QDs for the heterostructure case. Additionally, the defect peaks also exhibit a similar blue shift of ~ 0.2 eV. The overall spectral shift, i.e., the upshift of the binding energies of W 4f and S 2p in Au/WS_2 is indicative of a shift of the Fermi level of the WS_2 QDs towards the conduction band due to the presence of the Au NPs. Here, the Au NPs act as a kind of n-type dopant for WS_2 QDs by the transfer of electrons to the WS_2 QDs[33, 35]. Note that the WS_2 QDs are drop cast on Au NP decorated Si substrate at room temperature and no further processing is carried out. Hence, the spectral shift due to any chemical reaction triggered by Au NPs is very unlikely. **Fig. 4.4(d)** depicts the high-resolution XPS spectrum of the core level Au 4f for Si/Au/WS_2, which comprises the peaks at 83.0 eV(Au $4f_{7/2}$) and 86.6 eV (Au $4f_{5/2}$) of elemental Au[36] confirming the presence of Au NPs in the Si/Au/WS_2 sample.

4.3.3. Optical studies on WS_2 QDs and Au/WS_2 hybrid

To study the optical characteristics of the Si/WS_2 and Si/Au/WS_2 HS, we acquire the diffused reflectance spectra (DRS) of both samples. The corresponding Kubelka-Munk function (F(R)) plots are presented in **Fig. 4.5(a)** which shows broad absorption in the range of 300-750 nm. The Si/Au/WS_2 HS exhibits higher absorption than the Si/WS_2 HS in the lower wavelength region. For bare Au NPs, we observed an absorption peak at ~510 nm, due to the surface plasmon resonance from the Au NPs (inset of **Fig. 4.5(a)**). It is induced by the creation and enhancement of the localized electromagnetic field in the vicinity of metallic Au NPs and is ascribed to the localized surface plasmon resonance (LSPR) peak of the as-synthesized Au NPs[25]. The UV-Vis absorption spectrum of bare WS_2 QDs in solution is presented in **Fig. 4.5(b)**. Although the characteristic excitonic peaks for monolayer WS_2 are absent in the case of WS_2 QDs, in the UV region there is a strong absorption. It is assigned to transitions from deep valence band states to the conduction band of WS_2 QDs[32, 37]. Such absorption features have been reported for MoS_2 and WS_2 QDs[31, 38]. A prominent absorption tail is evident in the visible region, which may be attributed to the presence of additional localized trap states in the WS_2 QDs. **Fig. 4.5(c)** displays the normalized PL spectra of WS_2 QDs with a range of excitation wavelengths (320-420 nm). The QDs display wavelength-dependent emission, which is mostly governed by their size distribution and emissions from multiple states[39]. The broad PL emission spectra exhibited at lower excitation wavelengths are attributed to polydispersity in the size which is common in colloidally synthesized QDs[31]. There is a gradual narrowing and spectral redshift with increasing excitation wavelengths, which becomes more apparent for longer excitation wavelengths. The mean position of the PL emission peak shifts from ~450 to 510 nm. The observed redshift in emission is due to the selective carrier recombination at lower energy levels that depends upon the excitation wavelength. Therefore, the PL emission band gradually becomes narrow as the excitation wavelength increases (or excitation energy decreases), because the emission is only from defect levels and excitonic contribution is negligible. The broad PL spectrum under 320 nm excitation has been deconvoluted with four Gaussian components- the B and A excitons centered at ~380 nm and ~450 nm, respectively, and the defect-bound excitons, X1, and X2 (see **Fig. 4.5(d)**). The B and A excitons arise from transitions to the spin-orbit split valence band at the K-K' point[32] from the conduction band. The giant splitting of the valence band is caused by strong spin-orbit coupling in the W atom of WS_2. However, with increasing excitation wavelength, the spectral weight of the B and A excitons steadily becomes negligible and the emission is only due to transitions from the defect levels.

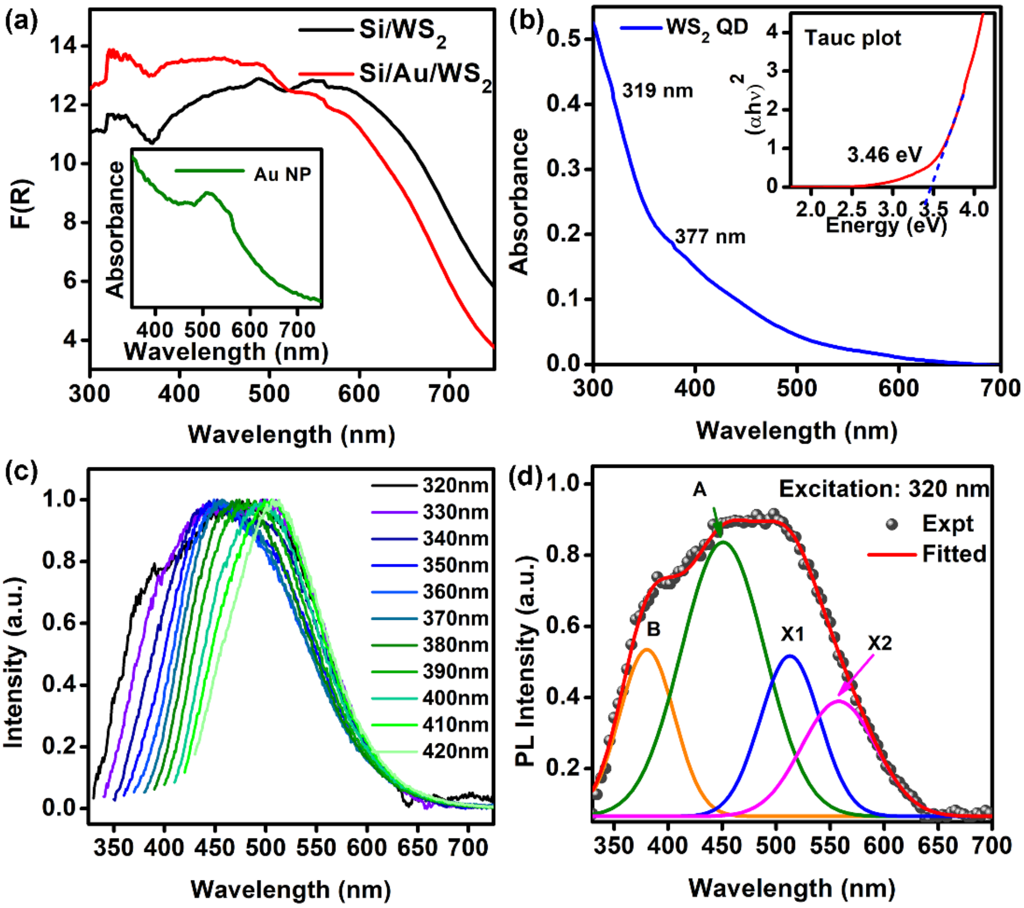

Fig. 4.5. (a) UV-vis DRS spectra of Si/WS_2 and $Si/Au/WS_2$ samples. Inset shows the UV-vis absorption spectrum of Au NPs on a Quartz substrate. (b) UV-Vis absorption spectrum of WS_2 QDs. Inset shows the corresponding Tauc plot indicating a bandgap of 3.46 eV. (c) Normalized excitation-dependent PL spectra for the excitation range of 320-420 nm. (d) Deconvoluted PL spectrum for WS_2 QDs under 320 nm excitation.

Next, to study the changes in luminescence emission properties of WS_2 QDs, while in the vicinity of Au NPs, we compare the PL spectra of Si/WS_2 QDs and $Si/Au/WS_2$ with a laser excitation of 405 nm at room temperature (**Fig. 4.6(a)**). The PL emission peak is observed at ~525 nm for both samples. Interestingly, the PL peak intensity for the $Si/Au/WS_2$ HS is observed to be enhanced by ~6 times compared to the bare Si/WS_2 QDs case. Note that in the HS sample, the WS_2 QDs are drop-cast on top of the Au NPs grown on the Si substrate. However, since the QDs are monolayered and are ultrasmall, the incident light can partially pass through them and interact with the underlying Au NPs. Subsequently, the QDs absorb the light scattered by Au NPs[23]. In addition, the light directly interacts with the QDs leading to an emission peak close to the SPR absorption peak of Au NPs, which in turn is absorbed by the Au NPs and enhances the local electric field. Thus, the enhanced PL emission is believed to arise from the combined effect of SPR and reabsorption by QDs. We have deconvoluted the PL spectrum of Si/WS_2 (**Fig. 4.6(b)**) using Gaussian fitting with three peaks: The A exciton (~450 nm) and two defect-related X1 and X2 peaks. It is noteworthy that for the excitations, $\lambda_{ex} \geq 400$ nm, the PL spectrum is largely dominated by bound excitonic emission[40]. For comparison, the Gaussian fitting of Si/Au/WS_2 is displayed in **Fig. 4.6(c)**. The spectral weight of the A exciton is boosted from 4.7% to 10.1% for the Au NP integrated system as compared to the bare Si/WS_2 case. In contrast, the overall contribution from the bound excitonic emissions was lesser in the Si/Au/WS_2 as compared to the bare WS_2 QDs on Si. Thus, in the Au integrated system, defects may be partly passivated by the Au NPs, giving rise to enhanced excitonic PL emission. Note that the overall increase in the PL intensity of the Si/Au/WS_2 system is mainly due to the local field enhancement by the plasmonic Au NPs as will be detailed later.

Next, the time-resolved PL spectra were recorded for the bare WS_2 QDs and Au/WS_2 coated on Si substrate. **Fig. 4.6(d)** displays the TRPL spectra at emission peak 540 nm for the excitation at 405 nm. The emission was selected at 540 nm to examine the effect of Au NP on the excitonic decay. Each decay spectrum fits well with a bi-exponential decay function:

$$y = A_1 e^{-t/\tau_1} + A_2 e^{-t/\tau_2} \qquad (1)$$

Here, τ_1 and τ_2 are the carrier lifetimes for the fast and the slow recombination processes[32, 41], and A_1 and A_2 are the respective strengths. We evaluate the average carrier lifetime (τ_{av}) for both the cases using the relation, $\tau_{av} = \Sigma \frac{A_i \tau_i^2}{A_i \tau_i}$. For Si/$WS_2$ case, τ_{av} is found to be 2.0 ns, while that for Si/Au/WS_2 case, comes out to be 0.5 ns. Thus, there is a significant decrease in the average carrier lifetime with the introduction of Au NPs. This may be because of the built-in field at the junction of the WS_2 QDs and Au NPs, leading to effective charge separation. The movement and loss of charges in opposite directions, avoiding recombination, effectively gives rise to faster decay of PL in the Au incorporated system. It may be noted that the recombination lifetime of WS_2 QDs/Si is lower than standalone WS_2 QDs[41], as discussed in Chapter 3, Section which is also attributed to charge separation at the junction between QDs to Si[42]. For a quantitative understanding of the mechanism behind the enhancement in the PL emission as well as Raman intensity, the field enhancement factor can be calculated for the Au NP incorporated system[43].

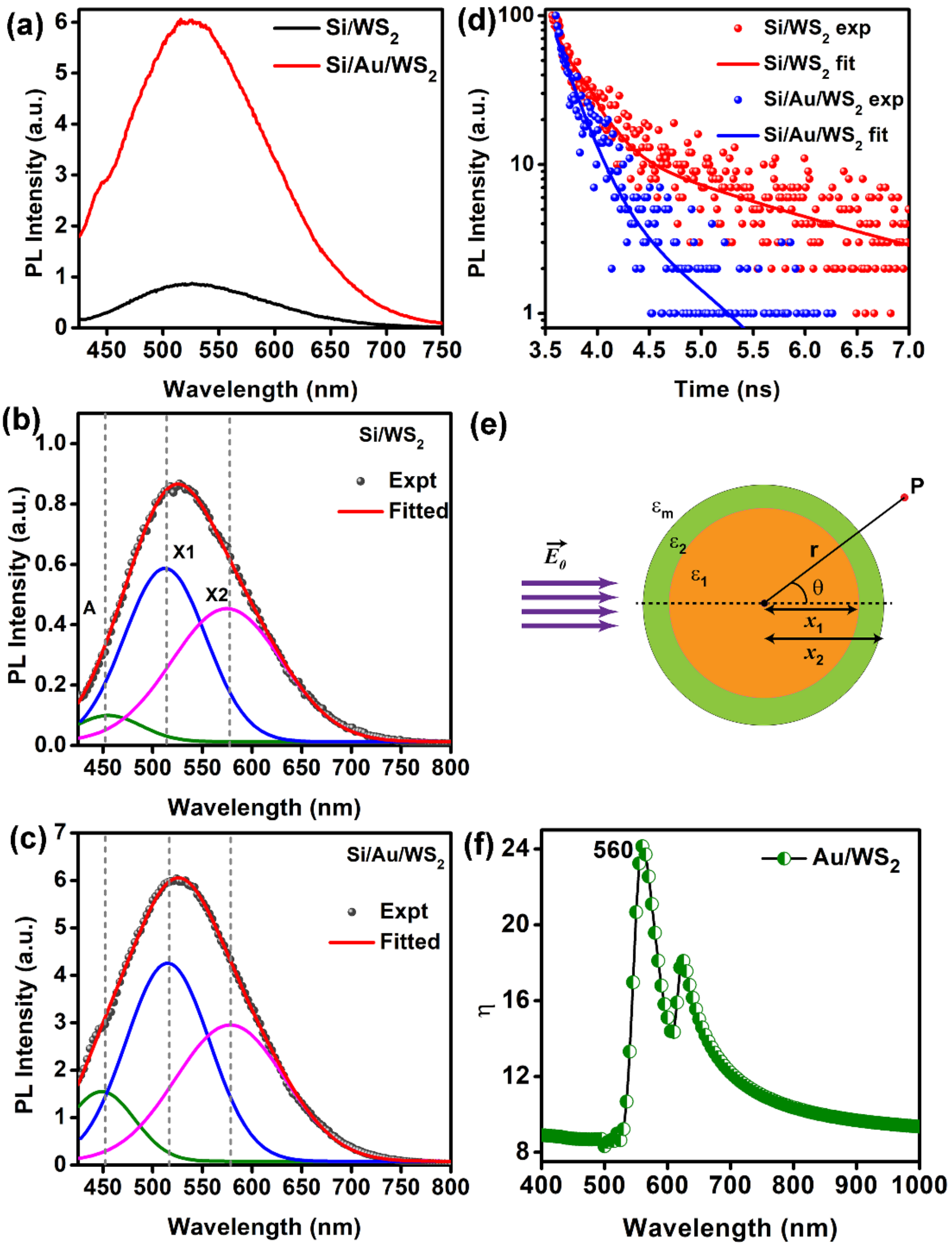

Fig. 4.6. (a) Comparative PL spectra of Si/WS$_2$ and Si/Au/WS$_2$ for excitation wavelength 405 nm. Deconvoluted PL spectrum under 405 nm excitation for (b) WS$_2$ QDs on Si (Si/WS$_2$) and (c) Au/WS$_2$ on Si (Si/Au/WS$_2$). (d) TRPL decay curves of Si/WS$_2$ and Si/Au/WS$_2$ recorded at ~540 nm for an excitation wavelength of 405 nm. The experimental data (symbols) are fitted with a bi-exponential decay function (solid lines). (e) Schematic illustration of a core-shell structure comprising an inner spherical core of Au NPs and an outer shell of WS$_2$ QDs in presence of an external electric field. (f) Calculated field enhancement factor (η) of the Au/WS$_2$ in air.

The magnification in the electromagnetic field intensities around Au NPs can be modeled by considering a concentric spherical core-shell structure consisting of an inner spherical core of radius x_1, dielectric constant ε_1, and an outer spherical shell of radius x_2, dielectric constant ε_2 placed in a medium with dielectric constant ε_m (**Fig. 4.6(e)**). Here, we consider the Au NP to be the inner spherical core surrounded by a concentric layer of WS_2 QDs. A uniform static electric field exists in the medium. The field enhancement factor (η) is defined in terms of the intensity ratio of the resultant field ($\overrightarrow{E_2}$) to the incident field ($\overrightarrow{E_0}$)[1], expressed as:

$$\eta = \frac{|\overrightarrow{E_2}|^2}{|\overrightarrow{E_0}|^2} = \left|1 + 2\frac{x_2^3}{r^3}\beta\right|^2 \tag{2}$$

$$\text{where, } \beta = \frac{(\varepsilon_2-\varepsilon_m)(\varepsilon_1+2\varepsilon_2)+f^3(\varepsilon_1-\varepsilon_2)(\varepsilon_m+2\varepsilon_2)}{(\varepsilon_2+2\varepsilon_m)(\varepsilon_1+2\varepsilon_2)+f^3(2\varepsilon_2-2\varepsilon_m)(\varepsilon_1-\varepsilon_2)} \tag{3}$$

Here, the dielectric constants ε_1, ε_2, and ε_m are complex functions of wavelength, i.e., $\varepsilon_j = \varepsilon_j' + i\varepsilon_j''$, where j = 1, 2, and m, where ε_j' and $\varepsilon_j''$are real entities. The η is dependent on the ratio of the radii of the core-shell structure, $f = \frac{x_1}{x_2}$ ~ 0.9, since x_1 ~ 6.8 nm and x_2 ~ 7.6 nm. We assume these values considering most of the WS_2 QDs are monolayer in thickness. The wavelength-dependent dielectric constants for Au and monolayer WS_2 were acquired from the literature[1-2]. The calculated η around a Au NP surrounded by WS_2 QDs in air is depicted in **Fig. 4.6(f).** The calculation of η is made at the observation point $\boldsymbol{r = x_2}$. We observed that the value of the field enhancement factor, η, is maximum for Au NP/WS_2 at λ~ 560 nm, and the corresponding η is found to be ~ 24 (see **Fig. 4.6(f)).** It is to be noted that at ~405 nm, η~8.8 i.e., at an excitation of 405 nm, the field is enhanced up to ~8.8 times in presence of the Au NP. This enhancement is evident in the rise in the PL intensity by 6 times in the Au NP incorporated system, i.e., Si/Au/WS_2 as compared to Si/WS_2 system. Thus, the PL enhancement factor closely matches the calculated field enhancement factor, η, from the theoretical model, considering a uniform WS_2 monolayer grown on the Au NPs. Thus, the Raman and PL enhancement factor in the Au incorporated system is primarily caused by the local field enhancement.

To gain further insight into the recombination mechanism for Au/WS_2 HS, we conducted temperature-dependent PL measurements with a laser excitation (405 nm) (see **Fig. 4.7(a)**). There is a systematic reduction in the PL emission intensity by ~22.4%, with the rise of temperature from 80 K to 350 K. This decrease in the PL emission intensity with rising temperature is believed to be due to the higher probability of non-radiative recombination over radiative recombination with the increasing thermal energy[44].

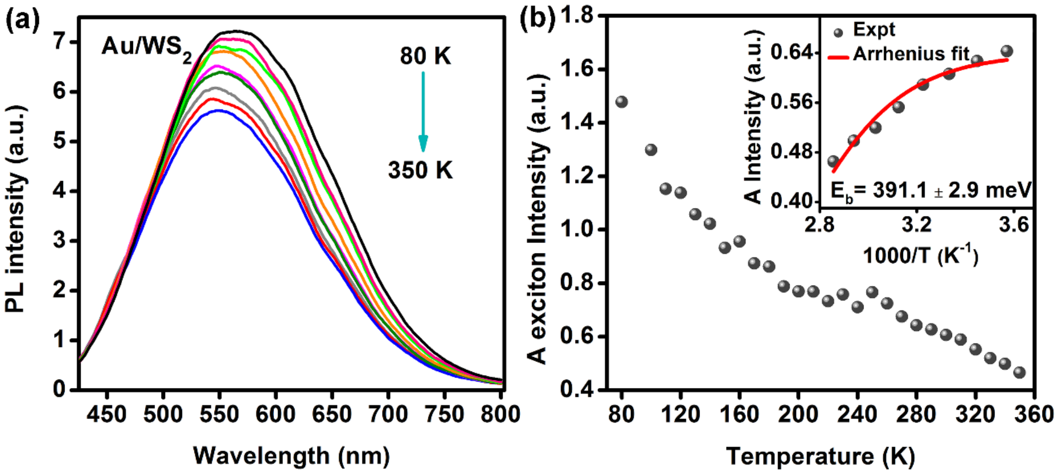

Fig. 4.7. (a) Temperature-dependent PL emission spectra of Si/Au/WS$_2$ measured in the range 80 to 350 K at regular intervals of 10 K. (b) Variation of A exciton peak intensity with temperature for the Si/Au/WS$_2$ case. The inset shows an Arrhenius plot for the region 280-350 K. Arrhenius equation fitting is carried out to compute the thermal activation energy (E$_a$).

A slight redshift in the PL peak is observed at lower temperatures. This redshift is attributed to increased emission from the radiative defect trap states. The characteristic A exciton intensity of the QDs in presence of the Au NPs is obtained from the fitted parameters of the PL spectra for all the temperatures and is plotted with respect to temperature in **Fig. 4.7(b)**. There is an apparent decline in the intensity of A excitonic emission with an increase in temperature. The thermal activation energy (E_a) for the Au/WS$_2$ HS is estimated using the Arrhenius equation:

$$I(T) = \frac{I_0}{1+Ce^{(-\frac{E_a}{K_B T})}} \tag{4}$$

I(T) and I$_0$ are the A exciton intensities corresponding to temperatures T and 0 K, respectively, and C is a proportionality constant. The E$_a$ indicates the non-radiative recombination for thermal quenching of photoluminescence as a higher temperature is approached. Thus, to compute the E$_a$ from the Arrhenius plot, data in the range 280-350 K is considered, which shows E$_a$ ≈391 meV, as shown in the inset of **Fig. 4.7(b)**. Here, E$_a$ can be assigned to exciton binding energy (E$_b$) as only the contribution of A excitonic emission is considered in the analysis. We noticed that there is an enhancement in the exciton binding energy of the WS$_2$ QDs with the integration of Au NPs in the system, as compared to the bare WS$_2$ QD system without the Au NPs (~301 meV), as discussed earlier[41]. Higher E$_b$ of the Au/WS$_2$ system is related to lesser dissociation of photo-generated excitons through non-radiative channels[4], resulting in enhanced PL emission.

4.3.4. Performance of Si/WS$_2$ and Si/Au/WS$_2$ Photodetectors

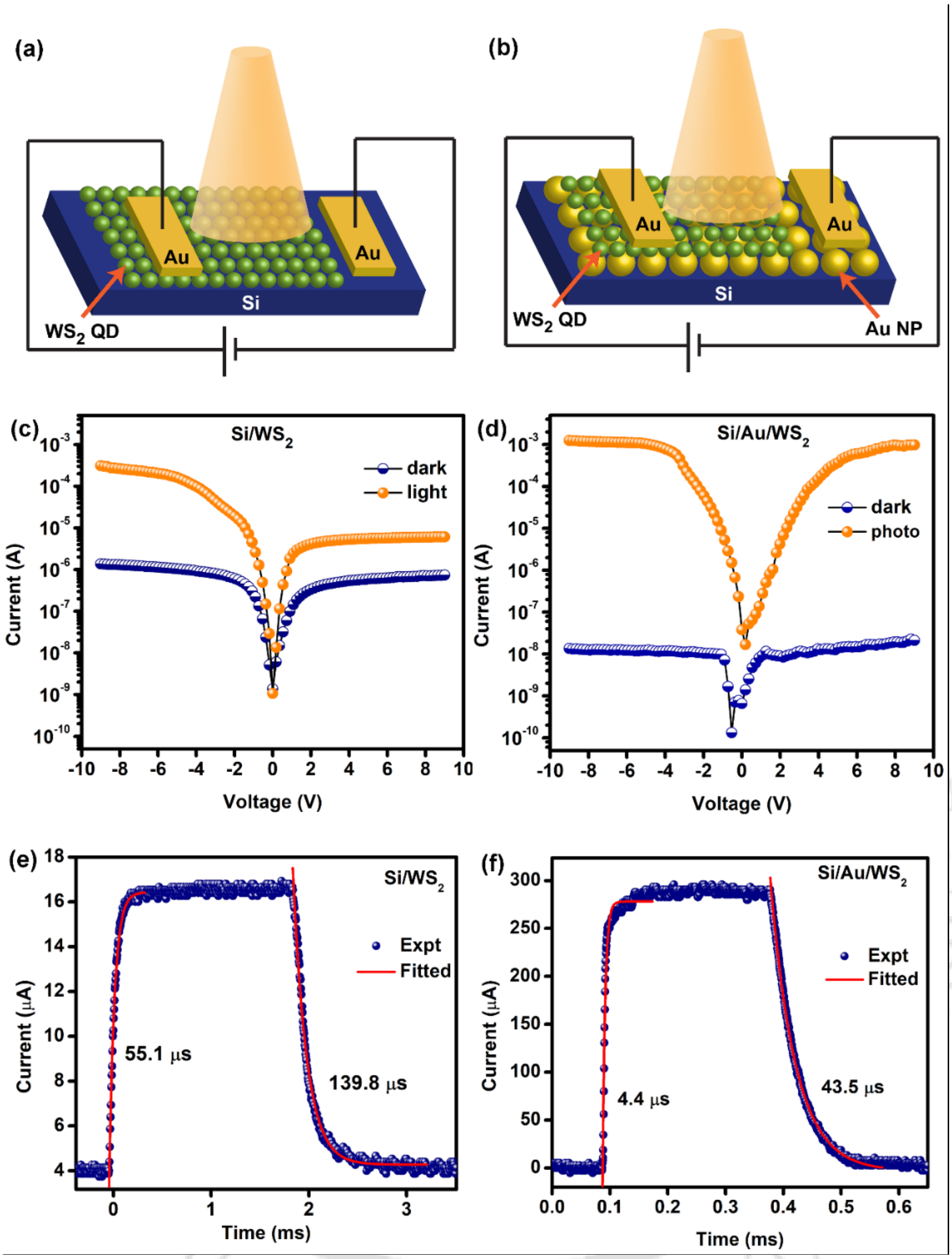

Fig. 4.8. Schematic illustrations of (a) Si/WS$_2$ and (b) Si/Au/WS$_2$ heterojunction-based photodetectors. I-V curves of the (c) Si/WS$_2$ heterojunction and (d) Si/Au/WS$_2$ heterojunction in dark and under the illumination of 12.9 mW/cm^2 at 405 nm. Temporal responses of the photocurrent for (e) Si/WS$_2$ and (f) Si/Au/WS$_2$ heterojunction photodetectors, measured at a reverse bias of 6 V under 405 nm light illumination. The solid line shows the fitting with a single exponential function.

In this section, we discuss and compare the performances of the Si/WS$_2$ and Si/Au/WS$_2$ heterojunction photodetector devices. The schematic representations of the heterojunctions as photodetectors, in reverse biased condition, are depicted in **Fig. 4.8(a, b)**, respectively. **Fig. 4.8(c)** displays the typical I-V characteristics of the Si/WS$_2$ photodetector in dark and in presence of light (under the excitation of 405 nm at ~12.9 mW/cm^2) under the bias. The dark current varied from -1.37 μA to 0.7 μA as the bias was swept from -9 to 9V, thus, yielding a nearly symmetric I-V characteristic. However, the photo I-V characteristic is asymmetric in nature compared to the dark I-V, i.e., the photocurrent under reverse bias is much higher than that under forward bias. At -9V bias, the I_{on}/I_{off} ratio is ~227, whereas at 9V, it is ~9. Therefore, under light, the p-Si/n-WS_2 behaves as a better rectifying junction. For comparison, the I-V characteristics for Si/Au/WS_2 photodetector under similar experimental conditions are depicted in **Fig. 4.8(d).** The I-V characteristic is fairly symmetric in nature, which indicates the formation of Schottky-type back-to-back contacts. Interestingly, the I_{on}/I_{off} ratio for the HS is ~1.3 $\times 10^5$, which is significantly higher (about 3 orders of magnitude) than the Si/WS_2 heterojunction. The photocurrent in the Si/Au/WS_2 is enhanced by more than one order of magnitude, which can be attributed to the enhanced electromagnetic field in the vicinity of the Au NP. However, the interesting aspect to be noted is the suppression of dark current by about two orders of magnitude in the Au NP incorporated system. The asymmetric Au NPs arrangement on the Si platform allows the achievement of a reasonably high built-in potential difference with the WS_2 QDs, which are randomly distributed on the Au/Si platform. Therefore, the dark current can be significantly suppressed under low operation voltages[45]. Moreover, the smaller dark current in Si/Au/WS_2 can be partly attributed to the higher thermal activation energy of the carriers in the Au NP incorporated system, as compared to the WS_2 QDs on bare Si[41]. Higher thermal activation energy would restrict thermal dissociation of excitons into free charge carriers, thus reducing the electrical conductivity in dark condition[46-47].

Fig. 4.8(e) shows the temporal photo-response of the Si/WS_2 photodetector under pulsed laser excitation of 405 nm. The measurement was carried out at -6V. To estimate the growth and decay time constants, a single exponential fitting ($I = I_0 + Ce^{-t/\tau}$) was done. The photocurrent growth/decay time constants were found to be 55.1/139.8 μs, whereas, for Si/Au/WS_2, the growth/decay time constants were 4.4/43.5 μs, which is an order of magnitude faster than that of the Si/WS_2 heterojunction PD, as shown in **Fig. 4.8(f).** Thus, the Si/Au/WS_2 heterojunction PD possesses a low dark current and a very fast photoresponse due to the incorporation of Au NPs. Such a behavior is facilitated by the strong built-in local electric field due to the incorporation of the plasmonic nanoparticles in the system. Besides, at the interface of WS_2 QDs and Au NPs, there may be charge transfer due to electron tunneling accompanied by hot electron transfer from Au NP to WS_2 QDs. Further discussion on the mechanism of charge transfer is presented later.

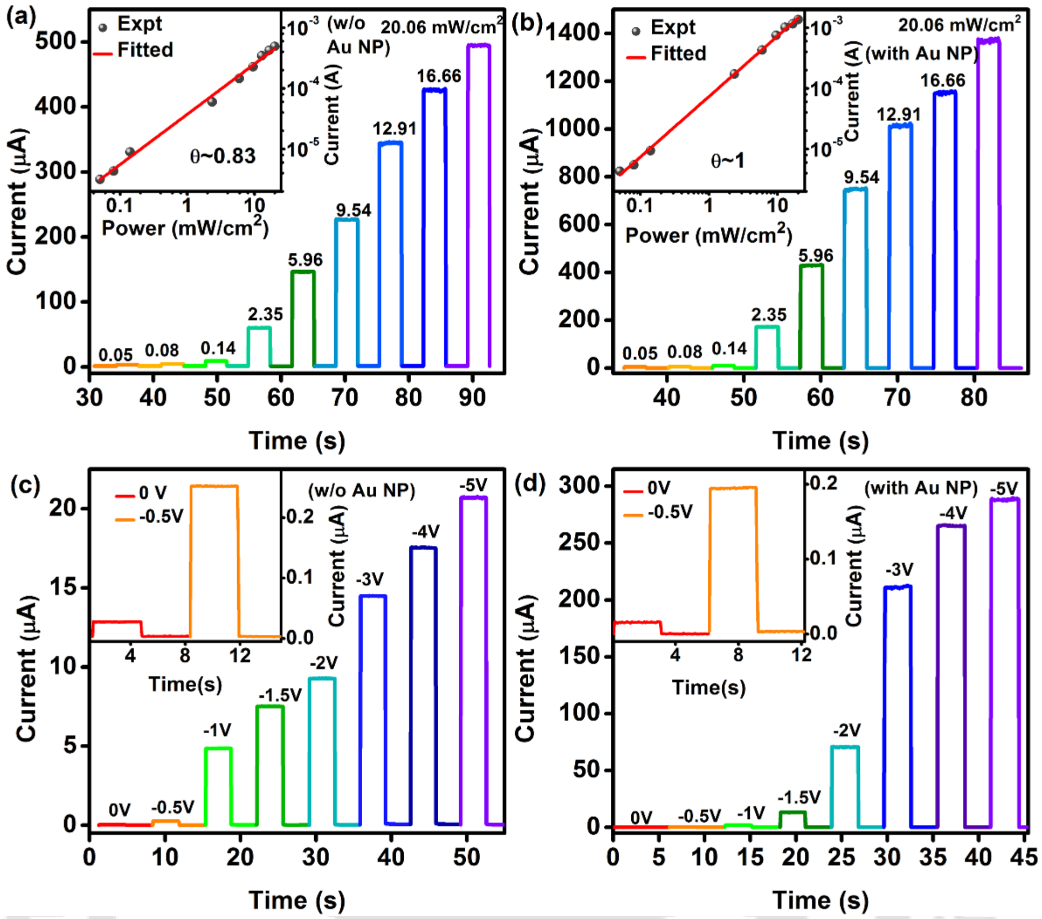

Fig. 4.9. Power dependent photocurrent responses of (a) Si/WS$_2$ and (b) Si/Au/WS$_2$ at -5V bias under pulsed illumination at different intensities in the range 0.05 mW/cm^2 to 20.06 mW/cm^2 of 405 nm laser. Respective insets depict the variation of photocurrent with power. (d) Voltage-dependent photocurrent response under pulsed laser excitation of 405 nm for (c) Si/WS$_2$ and (d) Si/Au/WS$_2$ heterojunctions. Respective insets show the magnified view of the photocurrents at 0 V and -0.5 V.

Next, we study the power-dependent photocurrent response of the Si/WS$_2$ and Si/Au/WS$_2$ at a constant bias of -5 V by varying the intensity of the pulsed laser excitation of 405 nm. With an increase in the irradiation power (0.05 mW/cm^2 to 20.06 mW/cm^2), there is a gradual increase in the photocurrent from 3 μA to 0.5 mA for Si/WS$_2$ (see **Fig. 4.9(a)**). We plot the variation of the photocurrent with incident laser power and fit the experimental data points with the power law, $I = AP^{\theta}$. Here, I is the photocurrent and P is the incident power and A is a proportionality constant. The exponent, θ, determines the response of photocurrent to light intensity and is found to be ~0.83. Ideally, θ should be 1.0, implying a linear relationship between the photocurrent and the incident light intensity. However, a sublinear behavior indicates the presence of certain trap states at the interface of the WS$_2$ QDs and Si, which might lead to carrier trapping/ recombination[6]. The variation of the photocurrent response with respect to incident power density was also studied for Si/Au/WS$_2$ under similar conditions, as shown in **Fig. 4.9(b).** As the illumination power was increased from 0.05 to 20.06 mW/cm^2, the photocurrent ascended from 4 μA to 1.4 mA. The power-law fitting indicates a perfectly linear relationship between photocurrent and the incident light intensity, i.e., $\theta \sim 1$, in this case. The presence of plasmonic NPs between the n-WS_2 and the p-Si essentially facilitates effective charge separation and inhibits the recombination process leading to the near-ideal behavior. Additionally, we monitor the change in the photo-response by keeping the laser power fixed at 12.9 mW/cm^2 and varying the applied bias voltages. **Fig. 4.9(c, d)** display the temporal responses of the photocurrent under different bias voltages for Si/WS_2 and Si/Au/WS_2 heterojunction PD. With the increase in the bias voltage, a systematic increase in the photocurrent was observed. Interestingly, both the photodetectors are observed to operate at zero bias voltage, as shown in the inset of **Fig. 4.9(c, d).** Hence, these devices can act as self-powered PDs. Under no external bias, the Si/WS_2 PD exhibits a current on/off (I_{on}/I_{off}) ratio of ~8, while the Si/Au/WS_2 photodetector, exhibits a pronounced I_{on}/I_{off} of about ~280, which shows its capability to detect very low optical signals under self-biased condition. Particularly, the Si/Au/WS_2 device exhibits photoresponse at a laser power of 500 nW/mm^2. Thus, the operation of the fabricated devices without requiring external bias is termed here as self-bias, in accordance with literature reports.

To discuss the overall performance of the self-powered photodetector, we need to address two of the significant figures of merits, which are responsivity (R) and specific detectivity (D*), given by the formulas[21, 48]:

$$R = \frac{(I_{ph} - I_d) \times 1000}{A \times P} \tag{5}$$

$$D^* = \frac{R}{\sqrt{2ej_d}} \tag{6}$$

Here, I_{ph} is the photocurrent, I_d is the dark current, P is the incident illumination power and A is the area of illumination. In equation (6), j_d refers to the dark current density. The measurement is carried out for -5V bias. We study these parameters as a function of incident power keeping the illumination wavelength fixed at 405 nm. The peak value of R for the Si/WS_2 detector is found to be 176.6 A/W, whereas, for Si/Au/WS_2, it is as high as ~246.2 A/W. **Fig. 4.10(a, b)** show the power dependence of the responsivities of both the devices. We have fitted the experimental data with the equation, $R = A'P^{\theta-1}$, where θ is the power-law exponent. The slope (θ-1) comes out to be ~ -0.16 for the Si/WS_2 PD, whereas it is ~0 for the Si/Au/WS_2 PD. This behavior is consistent with the power-law fitting of photocurrent with respect to the incident power (shown in **Fig. 4.10(a, b)**). The D* of the p-n heterojunction Si/WS_2 photodetector peaked at ~5.4×10^{12} Jones, while, the Schottky Si/Au/WS_2 detector exhibits a peak D* of ~4.3×10^{13} Jones, which is an order of magnitude higher. **Fig. 4.10(c, d)** shows the incident power dependence of the D* of both the heterojunction devices. The Au

NP embedded device shows a nearly flat response for D*, which is excellent for practical application.

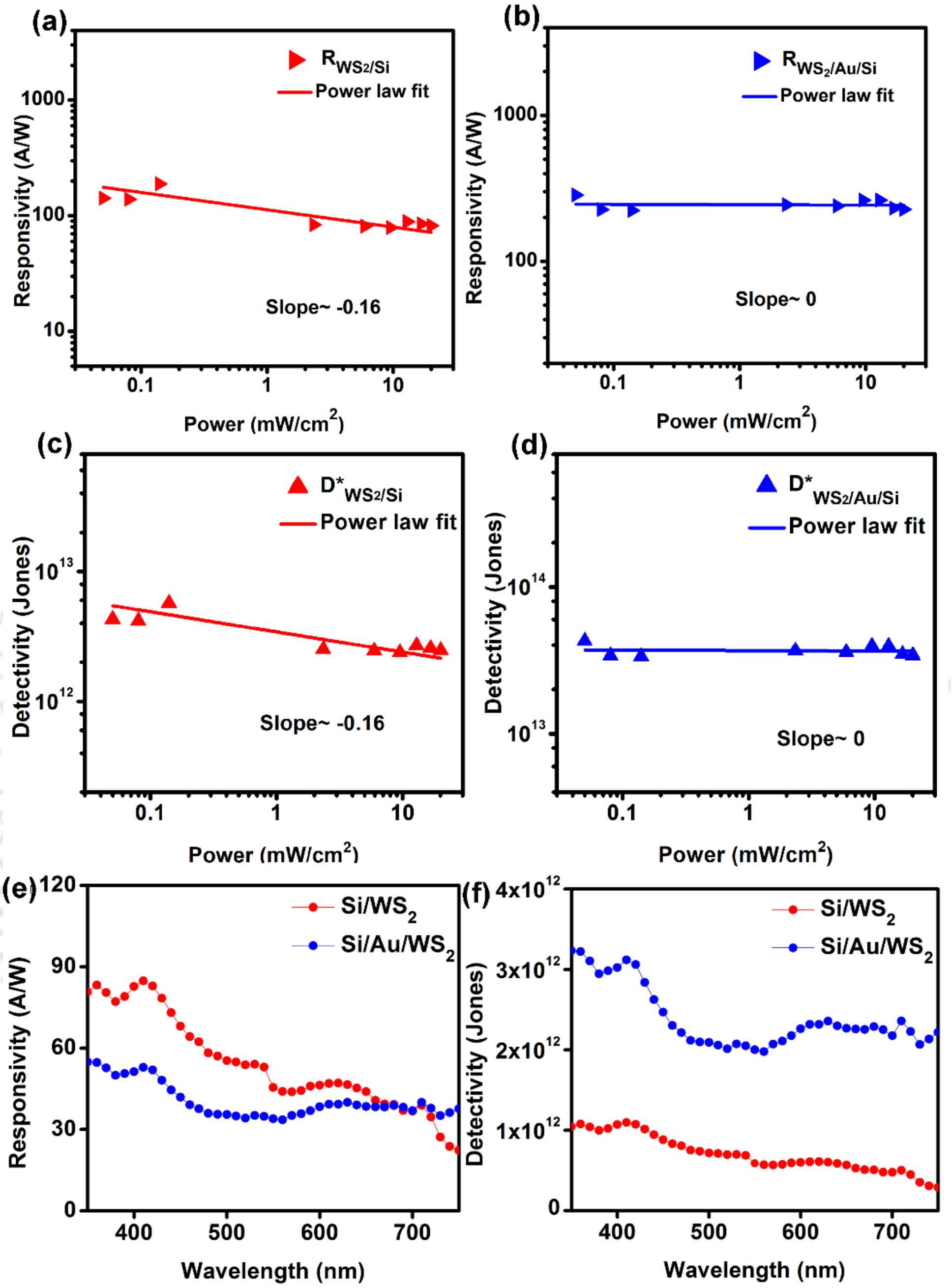

Fig. 4.10. The responsivity of the (a) Si/WS_2 and (b) Si/Au/WS_2 heterojunction photodetectors as a function of the power of illumination of 405 nm laser. Specific detectivity of the (c) Si/WS_2 and (d) Si/Au/WS_2 heterojunction photodetectors as a function of the power of illumination of 405 nm laser. (e) Comparative spectral responsivity of Si/WS_2 and Si/Au/WS_2 heterojunction PDs. (f) Comparative spectral detectivity of Si/WS_2 and Si/Au/WS_2 heterojunction PDs.

Additionally, we measure the wavelength dependence of responsivity (R_λ) as well as detectivity (D*) of the Si/WS_2 and Si/Au/WS_2 photodetectors, in the wavelength range of 350 nm to 750 nm, as shown in **Fig. 4.10(e, f)**. For both the PDs, the wavelength-dependent response is almost constant throughout the entire range for -5V bias. A peak responsivity of

~85 A/W was obtained for the p-n junction PD. In the wavelength range of 350-750 nm, the responsivities of both the PDs are more or less of the same order and spectral variation can be directly correlated with the respective absorption spectra presented in **Fig. 4.5(a).** The Schottky type Si/Au/WS_2 PD exhibits pronounced detectivity throughout the spectral range, owing to the ultralow dark current compared to the Si/WS_2 PD (**Fig. 4.10(f)**). It is to be noted that a Xenon lamp with an illumination power of the order of ~0.16-0.66 mW/cm^2 was used to conduct the spectral response experiment. To demonstrate the superior performance of the Si/Au/WS_2 heterojunction PD over the previously reported WS_2-based PDs, a summary of the photodetection performances of the WS_2 based PDs is presented in **Table 1**. Remarkably, the Si/Au/WS_2 heterojunction device shows promise as an optimal, highly responsive, and fast response photodetection device.

Table 1. Comparison of the present device with those of the reported device parameters for WS_2 based photodetectors.

Device layers	**I_{on}/I_{off}**	**R (AW^{-1})**	**D* (Jones)**	**Photocurrent growth/decay time constants**	**Reference**
Si/Au/WS_2	$\sim 1.3\times10^5$	276.2	$\sim 4.3\times10^{13}$	4.4/43.5 μs	This work
Si/WS_2	227	186.6	$\sim 5.4\times10^{12}$	55.1/139.8 μs	This work
WS_2/Si	10^6	0.22	1.5×10^{12}	16/29 μs	[21]
WS_2/Si	$\sim 10^2$	5.70		670/998 μs	[12]
WS_2		0.51	2.7×10^9	4.1/4.4 s	[11]
MoS_2/Au/WS_2	$\sim 10^4$	1.3×10^{-2}			[19]
WS_2/graphene	~21	1814.3	7.5×10^{12}	2/2.9 s	[5]
WS_2/MoS_2	10^2	4.36×10^{-3}	4.4×10^{13}	4/4 ms	[15]

4.3.5. Working Principle of the Photodetectors

The charge transfer across the heterojunction can be explained through an appropriate band diagram based on the relative positions of the Fermi levels of WS_2 and p-Si, as depicted in **Fig. 4.11(a)**[4, 49-51]. For the Si/Au/WS_2 PD, the proposed band diagram is depicted in **Fig. 4.11(b)**[4, 49].

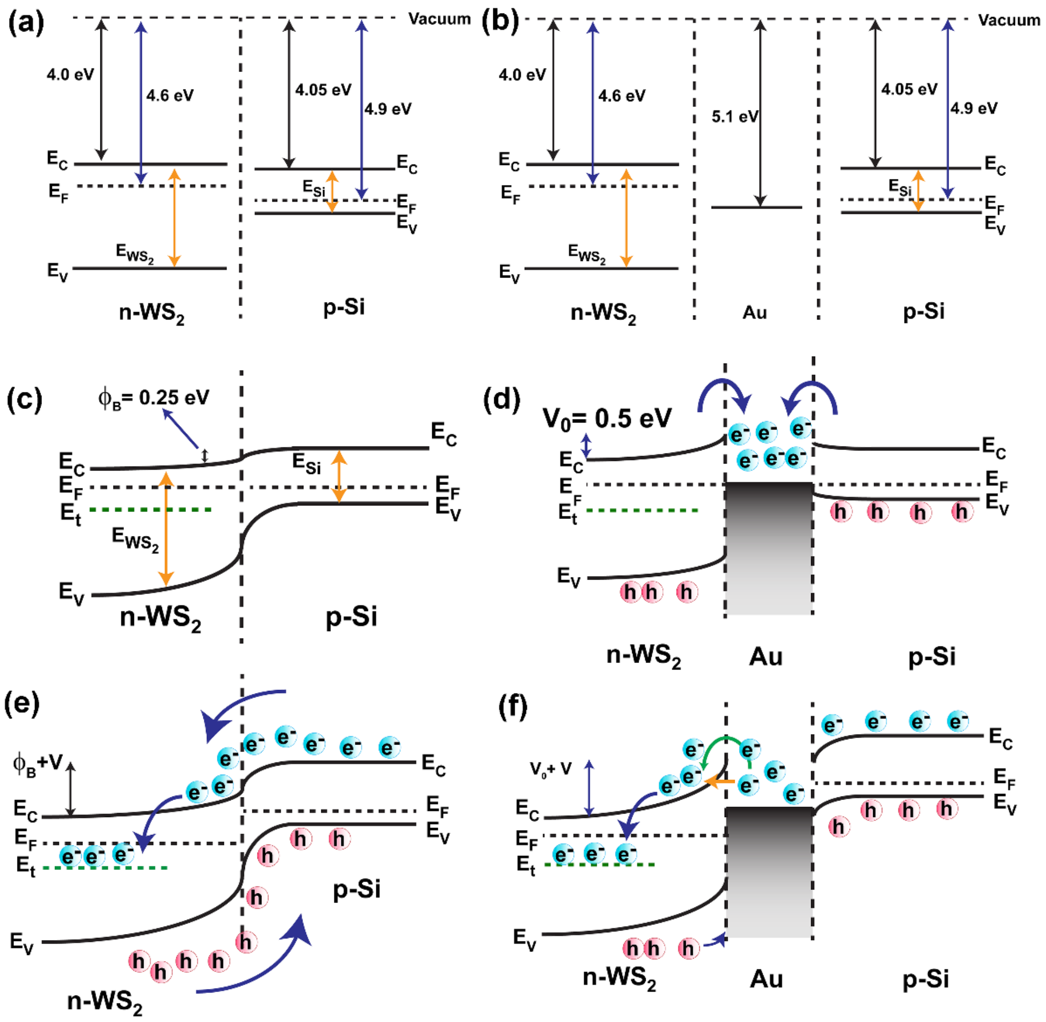

Fig. 4.11. Energy band diagrams of (a) Si/WS_2 and (b) Si/Au/WS_2 before the formation of a junction. Schematic of energy band diagram of (c) Si/WS_2 and (d) Si/Au/WS_2 heterojunctions at equilibrium without external bias. Schematic of energy band alignment of (e) Si/WS_2 heterojunction and (f) Si/Au/WS_2 heterojunction under reverse bias (V). The arrows indicate the movement of charge carriers.

It is noteworthy that Au film is used as the top electrode in the fabrication of the heterojunction PD, which is deposited by thermal evaporation. There may be a possibility of some deposited Au atoms passing through the QDs layer if the QD layer is discontinuous and forming direct contact with the Si, which would result in the effective formation of Au/p-Si/Au junction. However, an Ohmic contact is formed at p-Si/Au interface owing to the relative position of the Fermi level of p-Si with the work function of Au. It follows that the device would not exhibit any rectification, unlike the present scenario[49]. We have shown from the AFM analysis (**Fig. 4.2**) that the WS_2 QD layer is sufficiently thick and uniform to block the Au atoms to come in direct contact with the bottom Si layer. In the case of Si/WS_2, the positions of the Fermi levels facilitate the band alignment of a type II heterojunction. At equilibrium, i.e., at zero bias condition, a potential barrier $\Phi_B \sim 0.25$ eV develops at the interface of p-Si. The Fermi levels of the p-Si and n-WS_2 get aligned at the same energy value, as shown in **Fig. 4.11(c)**. Upon illumination of the p-n heterojunction with 405 nm laser at zero bias, charge carriers get photoexcited, and charge transfer excitons are formed. These excitons further dissociate aiding in effective charge separation, which explains conduction at zero bias condition[4].

For Si/Au/WS_2, there are two interfaces in question. At the Au/WS_2 interface, a Schottky junction is formed between the WS_2 QDs and the Au NPs. On the other hand, at the p-Si/Au interface, an Ohmic contact is formed, which does not partake in any rectification[49]. During the RTA process, Au atoms from the Au layer diffuse into the Si layer and form a disordered Au-Si alloy with low resistivity. Thus, when the Au electrode is deposited on the Au NPs, the contact with the Si layer becomes uniform and this ensures low contact resistance resulting in a reasonably good Ohmic contact with Si layer. From the positions of the Fermi levels of WS_2 as well as Si, the electrons transfer from the respective conduction bands to the Au NP. At equilibrium, a built-in potential of 0.5 eV (V_{bi}) develops on the WS_2 side (**Fig. 4.11(d)**). Likewise, due to the alignment of the Fermi levels, the conduction band of Si bends as well, resulting in no net flow of electrons in the system in equilibrium. Thus, the Au NPs act as a reservoir of electrons, in equilibrium and in absence of light. Upon irradiation, Au NPs offer an abundance of electrons that can overcome the barrier height (Φ_0=1.1 eV) to transfer it to the conduction band of WS_2 QDs. This is made possible in two ways: (1) The presence of hot electrons in the plasmonic Au NPs, owing to plasmon-enhanced absorption, that possess sufficiently high energy and can transfer to the conduction band of WS_2 QDs[45]. (2) Since the WS_2 QDs are mostly monolayered (~0.8 nm), electrons from the Au NPs can tunnel through the depletion width[52]. These collectively result in high photoconductivity even in the zero-bias condition.

A schematic illustration of the band alignment in reverse bias condition is presented in **Fig. 4.11(e, f)**. In the case of the p-n heterojunction device, Si/WS_2, the reverse bias results in an enhanced electric field across the junction, which increases the effective potential barrier (**Fig. 4.11(e)**). This in turn results in higher effective transport of the photoexcited charge carriers to the opposite electrodes, thus, leading to enhanced conductivity[4]. In the case of the Si/Au/WS_2 Schottky detector (**Fig. 4.11(f)**) under reverse bias conditions, as the Fermi level of the WS_2 QDs goes down, there is elevated electron tunneling. Moreover, upon irradiation, in addition to the escalated transport of photoexcited charge carriers across the junction, there is effective hot electron transfer from the Au NPs to the WS_2 QDs as electrons gain energy. Further, under the reverse bias, the Fermi level of Si goes up, and the electrons flow from its conduction band to Au NP and subsequently to the WS_2 QDs. Thus, conduction takes place via electron tunneling as well as hot electron transfer. However, in dark conditions, on the application of the external bias, the conduction only takes place mainly via electron tunneling, leading to a much smaller dark current. The suppressed dark current ensures a high photocurrent on/off ratio and superior detectivity of the Schottky PD. At this point, it is important to note that the Au NPs in the system lead to LSPR aided electric field enhancement causing the ~6 fold enhancement in the PL intensity. Inevitably, there are losses due to recombination at the various interfaces. Thus, it is likely that there is a competition between the two phenomena in the system. We argue that Au NPs act primarily as carrier sink in the Si/Au/WS_2 system, which leads to significant suppression of the dark current. When operated under reverse bias, the recombination in the system is minimized and the carrier separation dominates over the carrier loss due to recombination. Thus, the incorporation of Au NPs greatly boosts the overall performance of the PD with ultralow dark current, which is very good for practical application.

4.4. Conclusion

In summary, we have demonstrated the superior performance of Au nanoparticle embedded Si/Au/WS_2 QD-based photodetectors in this work. Ultra-small WS_2 QDs of monolayer thickness were synthesized using a liquid phase exfoliation technique and utilized for photodetection. An array of Au NPs (average size ~6.7 nm) was uniformly grown on a p-Si substrate and self-powered photodetectors based on Si/WS_2 QD and Si/Au/WS_2 heterostructures were fabricated through a simple drop-casting technique. The Schottky type Si/Au/WS_2 PD is demonstrated as a much superior device compared to p-n Si/WS_2 PD. For the Si/Au/WS_2 PD, the integration of Au NPs leads to a highly improved I_{on}/I_{off} ratio of $\sim 1.3\times10^5$, by the suppression of the dark current accompanied by an increase in the photocurrent. Also, the Schottky PD exhibited an ultrafast response with photocurrent rise/fall time of~4.4/43.5 μs as well as superior responsivity of 276.2 A/W and detectivity of $\sim 4.3 \times 10^{13}$ Jones, which are very significant. This improved device performance is attributed to the incorporation of the Au NPs which serve as a carrier tunneling pathway and the generation and transport of hot electrons for ultra-fast transport of photo-generated charge carriers. Most importantly, these WS_2 QD-based vertical hybrid devices can be operated without any external bias. Thus, the incorporation of plasmonic NPs in TMD-based hybrid structures paves way for designing heterojunction devices with distinctive performances for cutting-edge optoelectronic applications.

References:

1. Borzda, T., et al., Charge Photogeneration in Few-Layer Mos2. *Advanced Functional Materials* **2015**, *25*, 3351-3358.
2. Qiao, S.; Cong, R.; Liu, J.; Liang, B.; Fu, G.; Yu, W.; Ren, K.; Wang, S.; Pan, C., A Vertically Layered Mos2/Si Heterojunction for an Ultrahigh and Ultrafast Photoresponse Photodetector. *Journal of Materials Chemistry C* **2018**, *6*, 3233-3239.
3. Liu, B., et al., High Performance Photodetector Based on Graphene/Mos2/Graphene Lateral Heterostrurcture with Schottky Junctions. *Journal of Alloys and Compounds* **2019**, *779*, 140-146.
4. Mukherjee, S.; Maiti, R.; Katiyar, A. K.; Das, S.; Ray, S. K., Novel Colloidal Mos2 Quantum Dot Heterojunctions on Silicon Platforms for Multifunctional Optoelectronic Devices. *Scientific Reports* **2016**, *6*, 29016.
5. Singh, V. K.; M. Yadav, S.; Mishra, H.; Kumar, R.; Tiwari, R. S.; Pandey, A.; Srivastava, A., Ws2 Quantum Dot Graphene Nanocomposite Film for Uv Photodetection. *ACS Applied Nano Materials* **2019**, *2*, 3934-3942.
6. Ghosh, J.; Mawlong, L. P. L.; G. B, M.; Pattison, A. J.; Theis, W.; Chakraborty, S.; Giri, P. K., Solid-State Synthesis of Stable and Color Tunable Cesium Lead Halide Perovskite Nanocrystals and the Mechanism of High-Performance Photodetection in a Monolayer Mos2/Cspbbr3 Vertical Heterojunction. *Journal of Materials Chemistry C* **2020**, *8*, 8917-8934.
7. Gusakova, J.; Wang, X.; Shiau, L. L.; Krivosheeva, A.; Shaposhnikov, V.; Borisenko, V.; Gusakov, V.; Tay, B. K., Electronic Properties of Bulk and Monolayer Tmds: Theoretical Study within Dft Framework (Gvj-2e Method). *physica status solidi (a)* **2017**, *214*, 1700218.
8. Zhu, B.; Chen, X.; Cui, X., Exciton Binding Energy of Monolayer Ws2. *Scientific Reports* **2015**, *5*, 9218.
9. Peimyoo, N.; Shang, J.; Cong, C.; Shen, X.; Wu, X.; Yeow, E. K. L.; Yu, T., Nonblinking, Intense Two-Dimensional Light Emitter: Monolayer Ws2 Triangles. *ACS Nano* **2013**, *7*, 10985-10994.
10. Gutiérrez, H. R.; Perea-López, N.; Elías, A. L.; Berkdemir, A.; Wang, B.; Lv, R.; López-Urías, F.; Crespi, V. H.; Terrones, H.; Terrones, M., Extraordinary Room-Temperature Photoluminescence in Triangular Ws2 Monolayers. *Nano Letters* **2013**, *13*, 3447-3454.
11. Yao, J. D.; Zheng, Z. Q.; Shao, J. M.; Yang, G. W., Stable, Highly-Responsive and Broadband Photodetection Based on Large-Area Multilayered Ws2 Films Grown by Pulsed-Laser Deposition. *Nanoscale* **2015**, *7*, 14974-14981.
12. Lan, C.; Li, C.; Wang, S.; He, T.; Jiao, T.; Wei, D.; Jing, W.; Li, L.; Liu, Y., Zener Tunneling and Photoresponse of a Ws2/Si Van Der Waals Heterojunction. *ACS Applied Materials & Interfaces* **2016**, *8*, 18375-18382.
13. Kim, H.-S.; Patel, M.; Kim, J.; Jeong, M. S., Growth of Wafer-Scale Standing Layers of Ws2 for Self-Biased High-Speed Uv–Visible–Nir Optoelectronic Devices. *ACS Applied Materials & Interfaces* **2018**, *10*, 3964-3974.
14. Tan, H.; Xu, W.; Sheng, Y.; Lau, C. S.; Fan, Y.; Chen, Q.; Tweedie, M.; Wang, X.; Zhou, Y.; Warner, J., Lateral Graphene-Contacted Vertically Stacked Ws2/Mos2 Hybrid Photodetectors with Large Gain. *Advanced Materials* **2017**, *29*.
15. Wu, W.; Zhang, Q.; Zhou, X.; Li, L.; Su, J.; Wang, F.; Zhai, T., Self-Powered Photovoltaic Photodetector Established on Lateral Monolayer Mos2-Ws2 Heterostructures. *Nano Energy* **2018**, *51*, 45-53.
16. Xue, Y., et al., Scalable Production of a Few-Layer Mos2/Ws2 Vertical Heterojunction Array and Its Application for Photodetectors. *ACS Nano* **2016**, *10*, 573-580.
17. Du, W.; Zhao, J.; Zhao, W.; Zhang, S.; Xu, H.; Xiong, Q., Ultrafast Modulation of Exciton–Plasmon Coupling in a Monolayer Ws2–Ag Nanodisk Hybrid System. *ACS Photonics* **2019**, *6*, 2832-2840.

18. Huang, H.; Sheng, Y.; Zhou, Y.; Zhang, Q.; Hou, L.; Chen, T.; Chang, R.-J.; Warner, J. H., 2d-Layer-Dependent Behavior in Lateral Au/Ws2/Graphene Photodiode Devices with Optical Modulation of Schottky Barriers. *ACS Applied Nano Materials* **2018**, *1*, 6874-6881.
19. Lin, Z.; Luo, P.; Zeng, W.; Lai, H.; Xie, W.; Deng, W.; Luo, Z., Improvement of Photoelectric Properties of Mos2/Ws2 Heterostructure Photodetector with Interlayer of Au Nanoparticles. *Optical Materials* **2020**, *108*, 110191.
20. Pak, Y., et al., Enhanced Photoresponse of Ws2 Photodetectors through Interfacial Defect Engineering Using a Tio2 Interlayer. *ACS Applied Electronic Materials* **2020**, *2*, 838-845.
21. Wu, E.; Wu, D.; Jia, C.; Wang, Y.; Yuan, H.; Zeng, L.; Xu, T.; Shi, Z.; Tian, Y.; Li, X., In Situ Fabrication of 2d Ws2/Si Type-Ii Heterojunction for Self-Powered Broadband Photodetector with Response up to Mid-Infrared. *ACS Photonics* **2019**, *6*, 565-572.
22. Wang, Z., et al., Giant Photoluminescence Enhancement in Tungsten-Diselenide–Gold Plasmonic Hybrid Structures. *Nature Communications* **2016**, *7*, 11283.
23. Zeng, Y.; Li, X.; Chen, W.; Liao, J.; Lou, J.; Chen, Q., Highly Enhanced Photoluminescence of Monolayer Mos2 with Self-Assembled Au Nanoparticle Arrays. *Advanced Materials Interfaces* **2017**, *4*, 1700739.
24. Hao, Q.; Pang, J.; Zhang, Y.; Wang, J.; Ma, L.; Schmidt, O. G., Boosting the Photoluminescence of Monolayer Mos2 on High-Density Nanodimer Arrays with Sub-10 Nm Gap. *Advanced Optical Materials* **2018**, *6*, 1700984.
25. Cao, E.; Lin, W.; Sun, M.; Liang, W.; Song, Y., Exciton-Plasmon Coupling Interactions: From Principle to Applications. *Nanophotonics* **2018**, *7*, 145.
26. Pramanik, A.; Davis, D.; Patibandla, S.; Begum, S.; Ray, P.; Gates, K.; Gao, Y.; Chandra Ray, P., A Ws2-Gold Nanoparticle Heterostructure-Based Novel Sers Platform for the Rapid Identification of Antibiotic-Resistant Pathogens. *Nanoscale Advances* **2020**, *2*, 2025-2033.
27. Barman, B.; Dhasmana, H.; Verma, A.; Kumar, A.; Chaudhary, S. P.; Jain, V. K., Formation of Plasmonic Silver Nanoparticles Using Rapid Thermal Annealing at Low Temperature and Study in Reflectance Reduction of Si Surface. *Advances in Natural Sciences: Nanoscience and Nanotechnology* **2017**, *8*, 035010.
28. Iqbal, m. w.; Iqbal, M.; Khan, M.; Shehzad, M. A.; Seo, Y.; Park, J.; Hwang, C.; Eom, J., High-Mobility and Air-Stable Single-Layer Ws 2 Field-Effect Transistors Sandwiched between Chemical Vapor Deposition-Grown Hexagonal Bn Films. *Scientific Reports* **2015**, *5*, 10699.
29. Berkdemir, A., et al., Identification of Individual and Few Layers of Ws2 Using Raman Spectroscopy. *Scientific Reports* **2013**, *3*, 1755.
30. Molas, M. R.; Nogajewski, K.; Potemski, M.; Babiński, A., Raman Scattering Excitation Spectroscopy of Monolayer Ws2. *Scientific Reports* **2017**, *7*, 5036.
31. Xu, S.; Li, D.; Wu, P., One-Pot, Facile, and Versatile Synthesis of Monolayer Mos2/Ws2 Quantum Dots as Bioimaging Probes and Efficient Electrocatalysts for Hydrogen Evolution Reaction. *Advanced Functional Materials* **2015**, *25*, 1127-1136.
32. Lin, L.; Xu, Y.; Zhang, S.; Ross, I. M.; Ong, A. C. M.; Allwood, D. A., Fabrication of Luminescent Monolayered Tungsten Dichalcogenides Quantum Dots with Giant Spin-Valley Coupling. *ACS Nano* **2013**, *7*, 8214-8223.
33. Gao, J., et al., Transition-Metal Substitution Doping in Synthetic Atomically Thin Semiconductors. *Advanced Materials* **2016**, *28*, 9735-9743.
34. Perrozzi, F.; Emamjomeh, S. M.; Paolucci, V.; Taglieri, G.; Ottaviano, L.; Cantalini, C., Thermal Stability of Ws2 Flakes and Gas Sensing Properties of Ws2/Wo3 Composite to H2, Nh3 and No2. *Sensors and Actuators B: Chemical* **2017**, *243*, 812-822.
35. Ganguly, A.; Benson, J.; Papakonstantinou, P., Sensitive Chronocoulometric Detection of Mirna at Screen-Printed Electrodes Modified by Gold-Decorated Mos2 Nanosheets. *ACS Applied Bio Materials* **2018**, *1*, 1184-1194.
36. Sylvestre, J.-P.; Poulin, S.; Kabashin, A. V.; Sacher, E.; Meunier, M.; Luong, J. H. T., Surface Chemistry of Gold Nanoparticles Produced by Laser Ablation in Aqueous Media. *The Journal of Physical Chemistry B* **2004**, *108*, 16864-16869.

37. Zhao, W.; Ghorannevis, Z.; Chu, L.; Toh, M.; Kloc, C.; Tan, P.-H.; Eda, G., Evolution of Electronic Structure in Atomically Thin Sheets of Ws2 and Wse2. *ACS Nano* **2013**, *7*, 791-797.

38. Yin, W.; Bai, X.; Chen, P.; Zhang, X.; Su, L.; Ji, C.; Gao, H.; Song, H.; Yu, W. W., Rational Control of Size and Photoluminescence of Ws2 Quantum Dots for White Light-Emitting Diodes. *ACS Applied Materials & Interfaces* **2018**, *10*, 43824-43830.

39. Dhakal, K. P.; Duong, D. L.; Lee, J.; Nam, H.; Kim, M.; Kan, M.; Lee, Y. H.; Kim, J., Confocal Absorption Spectral Imaging of Mos2: Optical Transitions Depending on the Atomic Thickness of Intrinsic and Chemically Doped Mos2. *Nanoscale* **2014**, *6*, 13028-13035.

40. Mawlong, L. P. L.; Bora, A.; Giri, P. K., Coupled Charge Transfer Dynamics and Photoluminescence Quenching in Monolayer Mos2 Decorated with Ws2 Quantum Dots. *Scientific Reports* **2019**, *9*, 19414.

41. Bora, A.; Mawlong, L. P. L.; Das, R.; Giri, P. K., Understanding the Excitation Wavelength Dependent Spectral Shift and Large Exciton Binding Energy of Tungsten Disulfide Quantum Dots and Its Interaction with Single-Walled Carbon Nanotubes. *Journal of Colloid and Interface Science* **2020**, *561*, 519-532.

42. Ji, W.; Jing, P.; Zhao, J., Improving the Efficiency and Reducing Efficiency Roll-Off in Quantum Dot Light-Emitting Devices by Utilizing Plasmonic Au Nanoparticles. *Journal of Materials Chemistry C* **2013**, *1*, 470-476.

43. Tanabe, K., Field Enhancement around Metal Nanoparticles and Nanoshells: A Systematic Investigation. *The Journal of Physical Chemistry C* **2008**, *112*, 15721-15728.

44. Mawlong, L. P. L.; Paul, K. K.; Giri, P. K., Direct Chemical Vapor Deposition Growth of Monolayer Mos2 on Tio2 Nanorods and Evidence for Doping-Induced Strong Photoluminescence Enhancement. *The Journal of Physical Chemistry C* **2018**, *122*, 15017-15025.

45. Gosciniak, J.; Atar, F. B.; Corbett, B.; Rasras, M., Plasmonic Schottky Photodetector with Metal Stripe Embedded into Semiconductor and with a Cmos-Compatible Titanium Nitride. *Scientific Reports* **2019**, *9*, 6048.

46. Narayan, M.; Singh, J., Study of the Mechanism and Rate of Exciton Dissociation at the Donor-Acceptor Interface in Bulk-Heterojunction Organic Solar Cells. *Journal of Applied Physics* **2013**, *114*.

47. Scharber, M. C.; Mühlbacher, D.; Koppe, M.; Denk, P.; Waldauf, C.; Heeger, A. J.; Brabec, C. J., Design Rules for Donors in Bulk-Heterojunction Solar Cells—Towards 10 % Energy-Conversion Efficiency. *Advanced Materials* **2006**, *18*, 789-794.

48. Zeng, L.; Tao, L.; Tang, C.; Zhou, B.; Long, H.; Chai, Y.; Lau, S. P.; Tsang, Y. H., High-Responsivity Uv-Vis Photodetector Based on Transferable Ws2 Film Deposited by Magnetron Sputtering. *Scientific Reports* **2016**, *6*, 20343.

49. Metal-Semiconductor Contacts. In *Physics of Semiconductor Devices*, pp 134-196.

50. Wang, K., et al., Interlayer Coupling in Twisted Wse2/Ws2 Bilayer Heterostructures Revealed by Optical Spectroscopy. *ACS Nano* **2016**, *10*, 6612-6622.

51. Rawat, A.; Jena, N.; Dimple; De Sarkar, A., A Comprehensive Study on Carrier Mobility and Artificial Photosynthetic Properties in Group Vi B Transition Metal Dichalcogenide Monolayers. *Journal of Materials Chemistry A* **2018**, *6*, 8693-8704.

52. Das, R.; Sugimoto, H.; Fujii, M.; Giri, P. K., Quantitative Understanding of Charge-Transfer-Mediated Fe3+ Sensing and Fast Photoresponse by N-Doped Graphene Quantum Dots Decorated on Plasmonic Au Nanoparticles. *ACS Applied Materials & Interfaces* **2020**, *12*, 4755-4768.

Chapter 5

Photoluminescence Modulation and Doping of CVD grown Monolayer WS_2 by Heterostructuring with non-van der Waals 2D Bi_2O_2Se quantum dots

In this chapter, we discuss the significant role played by the neutral and charged exciton dynamics in comprehending the optical inter-band transitions in two-dimensional monolayer TMDs. Bi_2O_2Se quantum dots are decorated on the monolayer WS_2 (1L-WS_2) film grown using chemical vapor deposition (CVD) to modulate its photoluminescence properties. The high photoluminescence (PL) emission of 1L-WS_2 gets systematically quenched on the variation of the concentration of the QDs. We study the associated charge transfer dynamics in the system using a four-energy level model. The PL measurements at different QD concentrations show that the exciton decay becomes faster in WS_2 as the QD concentration increases. Likewise, the trion formation rate increases. The trion decay involves trapping by defect states, which plays an important role in the coupled charge transfer dynamics. Thus, the evolution of the emission features of 1L-WS_2 in the heterostructure (HS) is attributed to the conversion of neutral excitons to negatively charged trions via electron transfer from the Bi_2O_2Se QDs. The simulation-based on a set of decay rate equations replicates the experimental data for different concentrations of the QDs. The 1L-WS_2 becomes n-type doped, with an increase in the electron density by $\sim 6.6 \times 10^{13}$ cm^{-2}. The charge transfer from Bi_2O_2Se to WS_2 due to the type-II band alignment is confirmed by Kelvin Probe Force Microscopy (KPFM). The study lays out a suitable approach to tune the optical properties of 1L-WS_2 by doping using QDs. The charge transfer potentially enables researchers to further study the fundamentals of light-matter interaction at nanoscale heterostructures.

5.1. Introduction

Monolayer TMDs are sub-nanometer scale thin semiconducting materials similar to the two-dimensional graphene, that have garnered a great deal of research interest on account of their unique optical and electronic properties and tremendous potential for various applications[1-5]. Much like its sister TMD, MoS_2, WS_2 undergoes a transition from indirect optical bandgap in bulk to direct bandgap at monolayer level with the band edge located at energy-degenerate valleys (K, K')[6]. Due to broken inversion symmetry in the 1L regime and giant spin-orbit coupling, 1L-WS_2

gives rise to myriad avenues for research in the emerging area of valley physics[6-8]. The strong excitonic features at room temperature, owing to reduced dielectric screening in 1L-WS_2 result in enhanced Coulomb interactions. The system thus favors the formation of prominent many-body quasiparticles such as trions, biexcitons, etc. Trions are formed in presence of residual electrons or holes. At room temperature, these trions occupy an energy level lower than that of the neutral excitons and serve as relaxation pathways for the latter. Whereas, biexcitons which are essentially a pair of excitons, are formed in monolayer TMDs when there is a high exciton density attributable to lack of dielectric screening[9]. However, the signature of biexcitons is barely observed at room temperature[10]. The presence of these states can largely modify the PL spectrum of the monolayer TMDs. The experimental investigation and understanding of the carrier recombination dynamics have been carried out in the past based on techniques such as time-resolved PL[11-13] and ultrafast pump-probe spectroscopy[14-16]. Consequently, the optical properties of 1L-TMDs have been tuned and investigated by controlling the charge density by methods of doping[17-21]. Mawlong et al. have demonstrated the manipulation of the PL emission of 1L-MoS_2 via interfacing with WS_2 QDs and comprehensively probed the coupled charge transfer involved[22]. Roy et al. fabricated a heterostructure composed of $MoSe_2$ QDs and 1L-MoS_2 or WSe_2 and studied the charge dynamics in the system[23]. Unlike the extensively studied TMDs, QDs made from a new class of non-van der Waals 2D materials are yet to be explored. One such material is 2D Bi_2O_2Se, in which individual layers are bound by weak electrostatic force[24]. Although there have been recent reports on the various outstanding properties of 2D Bi_2O_2Se and applications[25-27], the optical properties of Bi_2O_2Se QDs mostly remain unexplored, to the best of our knowledge. Additionally, there have been no reports on the influence of these Bi_2O_2Se QDs on the PL emission properties of 1L-WS_2. The presence of QDs leads to recombination via different available channels by providing a higher density of residual charge carriers. In this chapter, we present a thorough study on the photoinduced charge transfer and a theoretical model involving coupled rate equations to have a better understanding of the carrier relaxation dynamics in the 1L-WS_2/Bi_2O_2Se QD HS.

5.2. Experimental details

5.2.1. CVD growth of 1L-WS_2

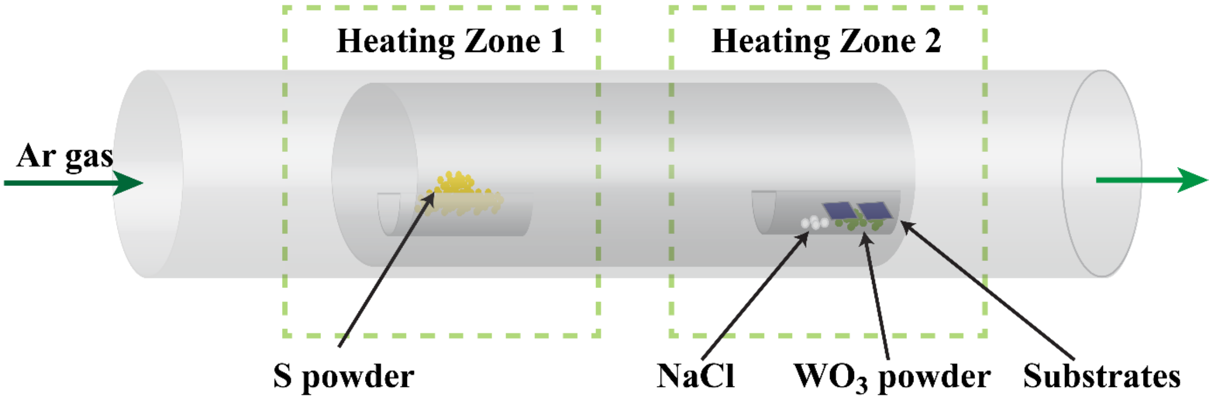

Fig. 5.1. Schematic diagram of the CVD setup for the growth of 1L-WS_2.

Monolayer WS_2 single crystals were grown on Si/SiO_2 substrates by a CVD process using a 2-inch quartz tube-based two-zone muffle furnace. A one-end closed tube of a smaller diameter is placed inside the 2-inch Quartz tube. 10 mg of WO_3 powder is placed in a quartz boat towards the closed end of the inner quartz tube, ensuring that it lies in the center of heating zone 2. For better lateral growth, an optimized quantity of NaCl is mixed with the WO_3 powder[28]. The substrates are placed face down right above the precursor as shown in **Fig. 5.1**. At the upstream zone, 150 mg of S is kept in another quartz boat. The temperature of zone 2 is ramped at a rate of 17 °C/min up to 940 °C. At this stage, the temperature at the S boat position reached 150 °C. For growth, these temperature conditions were maintained for 15 min. The furnace was then allowed to cool down naturally. The growth procedure is described in detail in **Chapter 2 (Section 2.4.2).** The morphology, chemical composition, and crystal structure are studied via TEM, AFM, XPS, and micro-Raman analyses.

5.2.2. Synthesis of Bi_2O_2Se QDs and decoration on the 1L-WS_2

Bi_2O_2Se quantum dots (QDs) were synthesized using a two-step process. Firstly, Bi_2O_2Se nanosheets (NS) were synthesized using a typical solvothermal-based chemical synthesis protocol. 90 mg of $Bi(NO_3)_3 \cdot 5H_2O$ and 15 mg of Se powder and 3 ml of hydrazine were added to 50 ml of DI water at room temperature and allowed to be completely dissolved with the help of a magnetic stirrer. Then, 100 mg of KOH and 160 mg of NaOH were added to get a homogeneous solution. The solution was loaded into a stainless-steel autoclave and kept at 150 °C for 6 h to synthesize Bi_2O_2Se NS. Centrifugation was carried out and the products obtained were washed several times with DI water and finally dried at 80°C overnight. Chemical exfoliation of the as-synthesized NS was carried out in N-methyl-2-pyrrolidinone (NMP) using a tip sonicator with ultrasonic frequency for 1 h. The supernatant obtained post-sonication contained the Bi_2O_2Se QDs. The QDs were subsequently dried and redispersed in water in various concentrations (0-40 mg/l) for further experiments. For the decoration and formation of the HS, the QDs of different concentrations are spin-coated on the 1L-WS_2 and dried before performing the optical characterizations.

5.2.3. Characterization techniques

The morphology and structural properties of the CVD-grown 1L-WS_2 have been studied using a transmission electron microscope (TEM) (JEOL-JEM 2100 operated at 200 kV). The CVD-grown 1L-WS_2 was transferred from the SiO_2 substrates to carbon-coated Cu-grids. To transfer the film, the sample was coated with polymethylmethacrylate (PMMA) by spin coating at 1500 rpm for 60 s, and then baked at 140 °C for 10 min. The PMMA-coated sample was then treated with 6 M NaOH solution for one hour to etch out the PMMA-supported 1L-WS_2 film, which was then repeatedly washed with DI water. Then, the film was fished out onto a Cu grid and allowed to air-dry. The PMMA was removed from the WS_2 film with the help of acetone. X-ray Photoelectron Spectroscopy (XPS) was employed to study the elemental composition of the as-prepared 1L-WS_2 and the Bi_2O_2Se QDs (Ulvac-Phi, Inc.). The X-ray diffraction (XRD) patterns of the Bi_2O_2Se NS and QDs were collected to determine their crystalline phase and quality (Rigaku RINT 2500 TTRAX-III, Cu kα radiation). The details of the AFM and micro-Raman and PL measurements have been discussed in detail in **Chapter 2 (Section 2.2.3)**. Kelvin Probe Force Microscopy (KPFM) measurements were carried out for the 1L-WS_2 and the HS (Cypher, Oxford Instruments using a conductive Ti/Ir coated Silicon probe) to estimate the work function. UV-Vis-NIR absorbance spectroscopy measurements of the HS as well as its counterparts were recorded using a commercial spectrophotometer (PerkinElmer, UV win Lab).

5.3. Results and discussion

5.3.1. Morphology studies

Fig. 5.2(a) displays the optical image of triangular-shaped monolayered WS_2 grown on a SiO_2 substrate. Uniform WS_2 grains laterally grow from a seed to form a large continuous monolayer film in the shape of triangular crystals with uniformity on a scale of hundreds of micrometers, as apparent from **Fig. 5.2(a).** The AFM image of a triangular monolayer WS_2 is displayed in **Fig. 5.2(b).** The height profile along the blue line reveals a thickness of ~0.8 nm, which corresponds to monolayer WS_2 (inset of **Fig. 5.2(b)**).

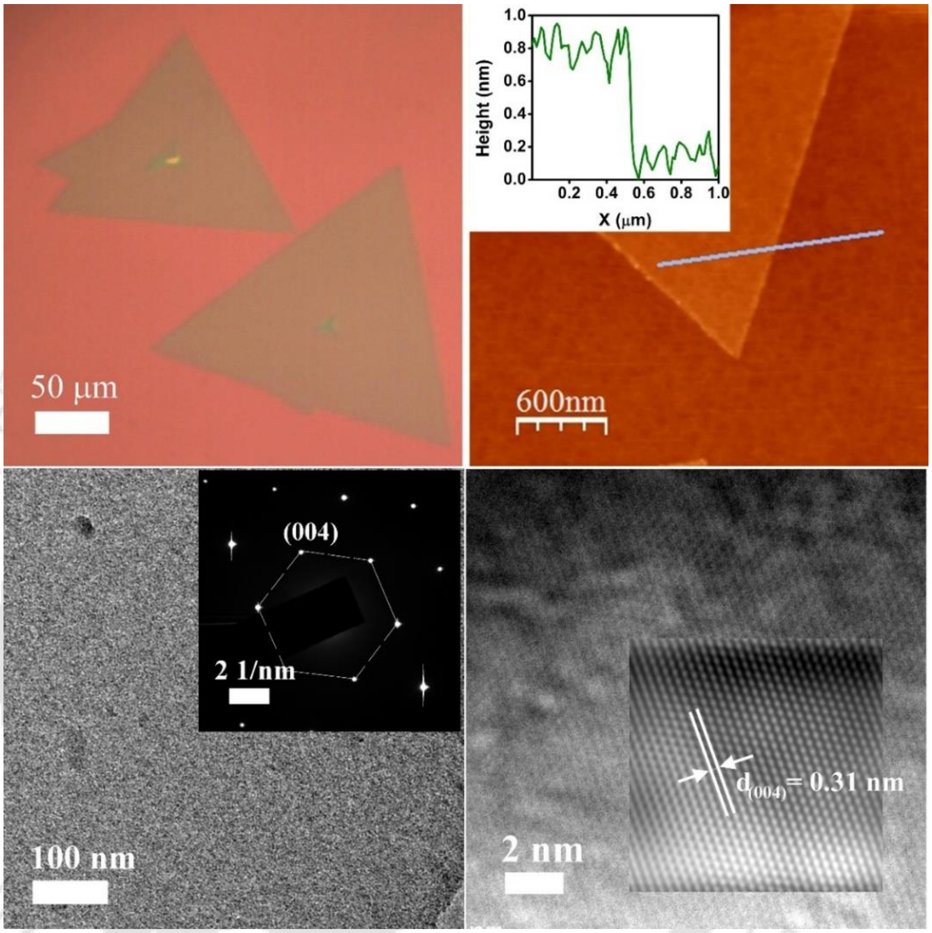

Fig. 5.2.: (a) Optical microscopy image of CVD grown WS_2 monolayer over a large area. (b) AFM image of 1L-WS_2 on SiO_2. The inset displays the height profile along the blue line. (c) FETEM micrograph of monolayer WS_2. The inset shows the corresponding SAED pattern. (d) High-resolution-TEM image of 1L-WS_2. Inset depicts the corresponding IFFT showing a d-spacing of 0.31 nm of the (004) plane of WS_2.

Fig. 5.2(c) shows the TEM micrograph of the CVD-grown WS_2 film transferred onto a Cu grid. The inset shows the selected area electron diffraction (SAED) pattern that indicates the single-crystalline nature of the as-grown WS_2 monolayer. The high-resolution TEM (HR-TEM) image is displayed in **Fig. 5.2(d).** The hexagonal lattice structure is evident from the corresponding IFFT as depicted in the inset. The lattice d-spacing is ~0.31 nm, consistent with the (004) plane of crystalline WS_2.

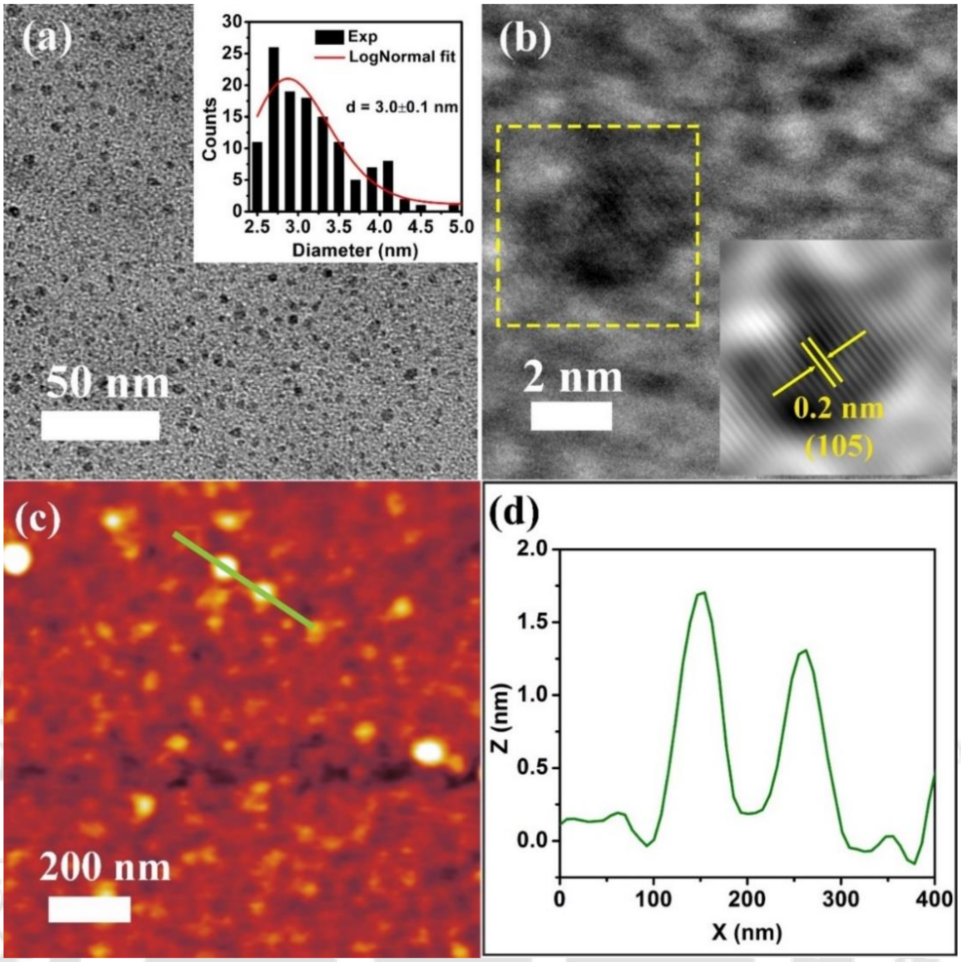

Fig. 5.3. (a) TEM image of Bi_2O_2Se QDs. The inset displays the corresponding size distribution. (b) High-resolution-TEM image of Bi_2O_2Se QDs. Inset depicts the corresponding IFFT showing a d-spacing of 0.2 nm of the plane (105). (c) AFM image of Bi_2O_2Se QDs. (d) Height profile of the QDs across the green line on (c).

The typical morphological properties and size distribution of the as-prepared Bi_2O_2Se QDs were studied via TEM. **Fig. 5.3(a)** shows the bright field image of the Bi_2O_2Se QDs showing nearly uniform sizes (diameter 2-5 nm). The log-normal function fitting of the data yields an average diameter of ~ 3.0 ± 0.1 nm, as shown in the inset of **Fig. 5.3(a). Fig. 5.3(b)** exhibits the high-resolution TEM (HRTEM) image of Bi_2O_2Se QDs depicting their crystalline nature. The lattice d-spacing is measured as 0.2 nm, which corresponds to the (105) plane of the Bi_2O_2Se crystal. The AFM image of the synthesized Bi_2O_2Se QDs is shown in **Fig. 5.3(c).** The height profile along the green line revealed that the average thickness of the Bi_2O_2Se QDs is ~2 nm (**Fig. 5.3 (d)**), indicating the QDs are of few (2-3) layered type.

5.3.2. Structural and compositional analysis

5.3.2.1. XRD and XPS Analysis

The XRD patterns of the Bi_2O_2Se NS and the QDs were recorded and their comparison is displayed in a stacked plot in **Fig. 5.4(a).** The positions of the diffraction peaks ascertain the tetragonal crystal phase in the as-synthesized Bi_2O_2Se NS[25, 29-30]. The pattern corresponding to the QDs however, unveils diffraction peaks of much lower intensities. This could be attributed to the loss of crystallinity and reduction in the layer number during chemical exfoliation of the NS to obtain the QDs.

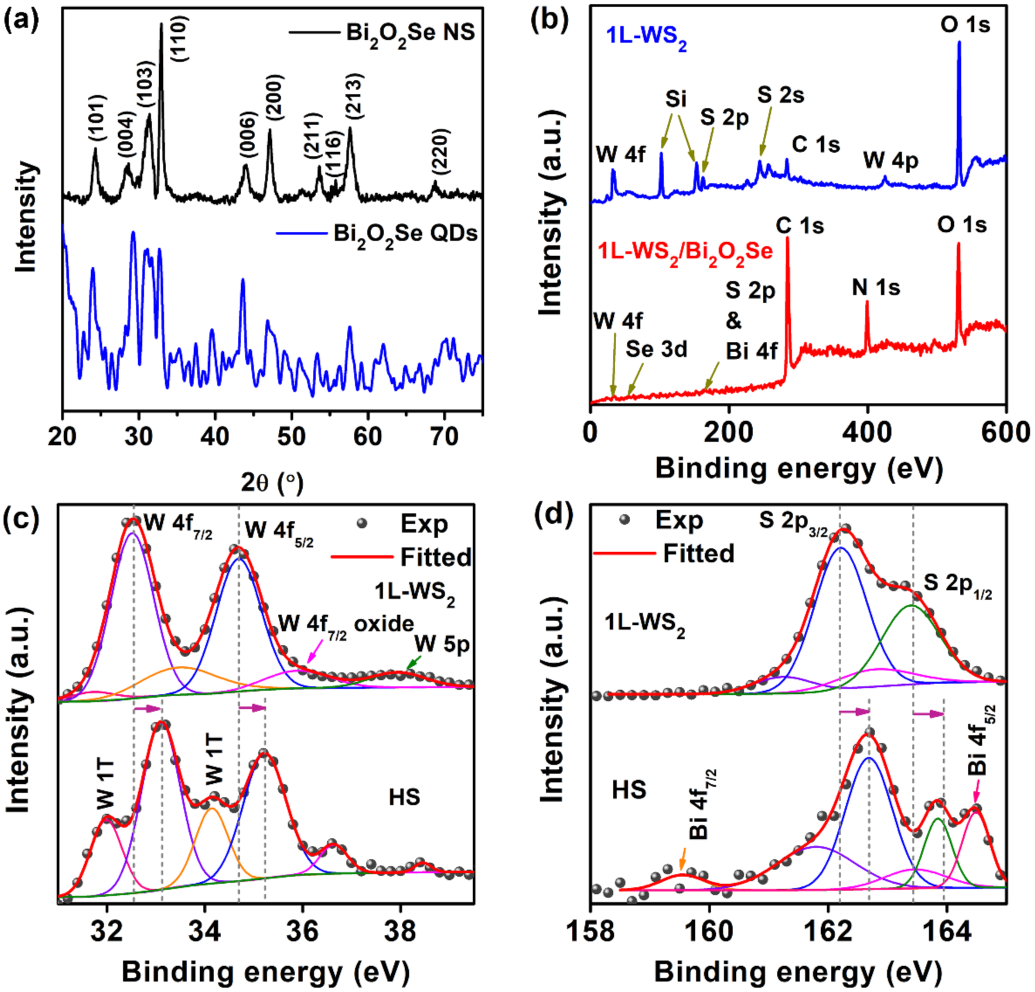

Fig. 5.4. (a) XRD patterns of Bi_2O_2Se nanosheets and Bi_2O_2Se QDs in a stacked plot. (b) XPS survey scan spectra of 1L-WS_2 and 1L-WS_2/Bi_2O_2Se QD. The high-resolution XPS spectra of (c) W 4f and (d) S 2p of 1L-WS_2 and 1L-WS_2/Bi_2O_2Se QD.

The chemical environment of the 1L-WS_2 grown on SiO_2 substrate as well as the HS 1L-WS_2/Bi_2O_2Se QD is studied via X-ray photoelectron spectroscopy. The core-level XPS survey scans of the pristine 1L-WS_2 and the HS are displayed in **Fig. 5.4(b).** The survey scan corresponding to 1L-WS_2 indicates the presence of W and S along with signatures of C and O. The oxygen peak may be due to the WO_3 residue on the substrate from the growth process. In the case of the HS, additional peaks corresponding to Bi and Se are apparent, confirming the HS formation. **Fig. 5.4(c)** displays a stacked plot of the high-resolution XPS spectra of W 4f for the 1L-WS_2 and the HS 1L-WS_2/Bi_2O_2Se QD. The peaks at 32.5 eV and 34.7 eV are ascribed to W $4f_{7/2}$ and W $4f_{5/2}$, respectively, which confirm the formation of highly crystalline 2H-WS_2. The additional peaks at 31.7 eV and 33.5 eV correspond to the W^{4+} state of the metallic 1T-phase of WS_2, which is consistent with earlier reports[31-32]. The presence of the precursor WO_3 is shown by the appearance of the small shoulder peak at 35.9 eV which corresponds to the W^{6+} state of the oxide. The spectrum corresponding to the HS 1L-WS_2/Bi_2O_2Se QD shows the presence of all the aforementioned peaks. However, there is a blueshift in the W $4f_{7/2}$ and W $4f_{5/2}$ peaks by 0.5 eV. This could be an indication of the transfer of electrons from the Bi_2O_2Se QD to the 1L-WS_2, which leads to a shift in the Fermi level of the latter towards the conduction band[22, 33]. The S 2p core-level spectra of the 1L-WS_2 and the HS are depicted in **Fig. 5.4(d).** The doublet at 162.2 eV and 163.4 eV are consistent with the S^{2-} states, S $2p_{3/2}$ and S $2p_{1/2}$, respectively[31, 34]. The peaks at lower binding energies 161.2 eV and 162.7 eV denote the presence of sulfur vacancies in the CVD grown 1L-WS_2[35]. The S 2p spectrum of the HS exhibits a clear blue shift of ~0.4 eV. Thus, there is an overall upshift in the binding energy in the HS, confirming the electron transfer from the QD to the 1L-WS_2. Furthermore, the shoulder peaks at 159.5 eV and 164.4 eV correspond to Bi $4f_{7/2}$ and Bi $4f_{5/2}$[24]. This further ascertains the successful formation of the hybrid 1L-WS_2/Bi_2O_2Se.

5.3.2.2. Raman Analysis

Micro-Raman measurement was carried out on 1L-WS_2**,** Bi_2O_2Se QDs, and 1L-WS_2/Bi_2O_2Se systems using a 488 nm Ar laser. The characteristic Raman spectra of 1L-WS_2 and the HS 1L-WS_2/Bi_2O_2Se are depicted in **Fig. 5.5(a)**. The in-plane vibrational mode of WS_2, E_{2g} (Γ) is blue-shifted to 358.6 cm^{-1} and the out-of-plane vibrational mode, A_{1g} (Γ) is red-shifted (419.9 cm^{-1}) with respect to bulk WS_2. The frequency difference or Δk between A_{1g} and E_{2g} modes is used to identify the number of layers in layered TMDs[36]. For our CVD-grown WS_2 film, Δk = 61.5 cm^{-1}, which confirms monolayer growth[37]. The features are common to both 1L-WS_2 and the HS 1L-WS_2/Bi_2O_2Se. Remarkably, there is a ~10-folds enhancement in the intensities of the individual modes of 1L-WS_2 in the HS sample. This is believed to be due to the surface-enhanced Raman scattering (SERS) effect exhibited by the Bi_2O_2Se QDs, via electromagnetic field enhancement[38].

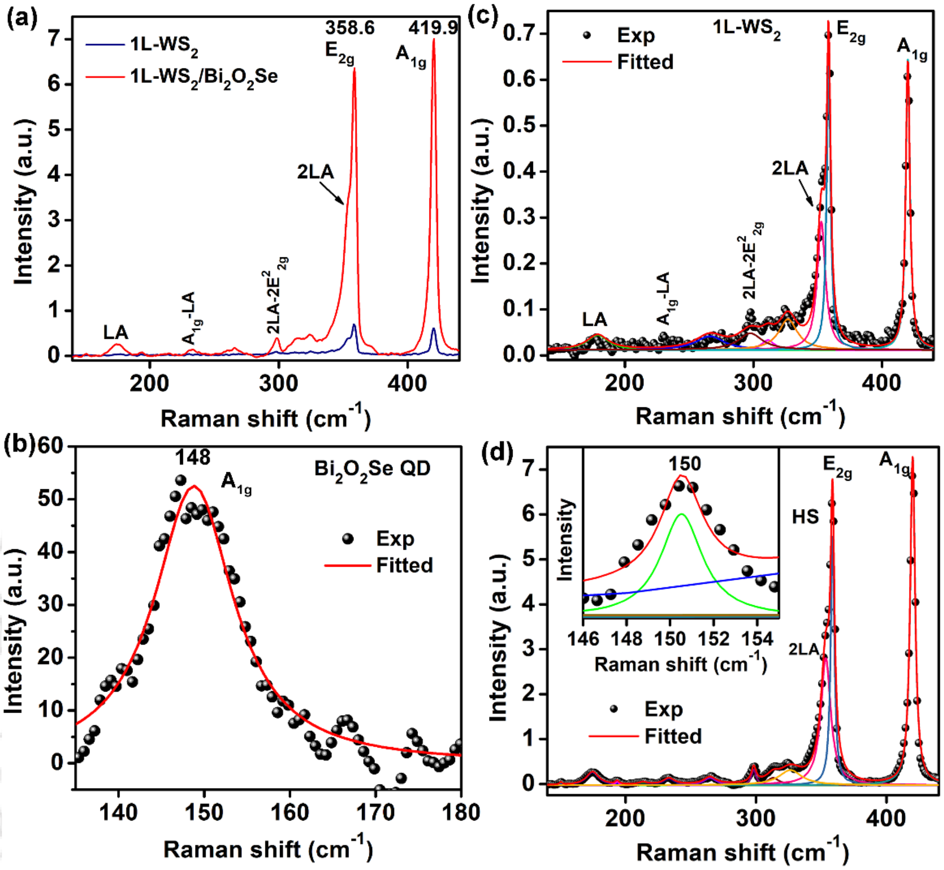

Fig. 5.5. (a) Comparative micro-Raman spectra of 1L-WS_2 and 1L-WS_2/Bi_2O_2Se QD acquired using 488 nm excitation. (b) Micro-Raman spectrum of Bi_2O_2Se QD. Deconvoluted Raman spectra of (c) 1L-WS_2 and (d) 1L-WS_2/Bi_2O_2Se QD. Inset shows the magnified spectra in the range 146-155 cm^{-1}.

The Raman spectrum of Bi_2O_2Se QDs is presented in **Fig. 5.5(b)**, which exhibits the characteristic A_{1g} mode at 148.8 cm^{-1}. The A_{1g} mode is reported to be at ~158 cm^{-1}, for CVD-grown few-layer Bi_2O_2Se[24]. The Raman spectrum in **Fig. 5.5(b)**, however, shows a significant red-shift in the A_{1g} vibrational mode of the exfoliated Bi_2O_2Se QDs, which can be argued to be due to a decrease in the layer thickness from multilayer to bilayer or trilayer as well as reduced lateral size. The FWHM of the mode is about 11.3 cm^{-1}, which is higher than the multilayer flakes as reported by Hossain et. al[24]. This is possibly due to loss of crystallinity during the exfoliation process. Additionally, since the A_{1g} mode is sensitive to the electron density of the system, the shift could be partly attributed to any doping effect induced during the process of synthesis. The Raman spectra for 1L-WS_2 and 1L-WS_2/Bi_2O_2Se are deconvoluted and presented in **Fig. 5.5(c, d)**. Along with the optical modes of WS_2, another peak at ~353 cm^{-1} is assigned to the 2LA mode, i.e., the second-order longitudinal acoustic mode[37, 39]. Other Raman modes of 1L-WS_2 are summarized in **Table 1**.

Table 1. Summary of the deconvolution parameters of the Raman spectra of the 1L-WS_2 and 1L-WS_2/Bi_2O_2Se QDs

Raman modes	**1L-WS_2**		**Bi_2O_2Se QDs**		**1L-WS_2/Bi_2O_2Se**	
	Position (cm^{-1})	*FWHM (cm^{-1})*	*Position (cm^{-1})*	*FWHM (cm^{-1})*	*Position (cm^{-1})*	*FWHM (cm^{-1})*
Bi_2O_2Se						
A_{1g}	-	-	148.8	11.3	150.5	2.3
WS_2						
LA	178.8	20.2	-	-	174.8	11.5
2LA	352.7	7.7	-	-	353.4	9.2
E_{2g}	358.4	3.6	-	-	358.6	3.4
A_{1g}	419.9	3.9	-	-	420.0	4.5

The presence of these Raman modes confirms good crystallinity in the as-prepared 1L-WS_2[40]. The A_{1g} mode of Bi_2O_2Se QDs is evident in the inset of **Fig. 5.5(d)** from the Lorentzian fitting of the spectrum. This confirms the formation of the heterojunction, 1L-WS_2/Bi_2O_2Se QDs. The A_{1g} mode, however, is blue-shifted to 150.5 cm^{-1}. It is well established that the A_{1g} mode couples strongly with electrons. Thus, the blueshift of 1.7 cm^{-1} is indicative of an effective p-type doping effect of the Bi_2O_2Se QDs by means of electron transfer to the 1L-WS_2[22, 25]. The charge transfer should be accompanied by a redshift in the A_{1g} peak of the 1L-WS_2. However, no significant shift in the Raman mode is observed. We notice a decrease in the FWHM of the A_{1g} mode of Bi_2O_2Se in the hybrid sample, which may be related to the passivation of defects in Bi_2O_2Se QDs.

5.3.3. Optical analysis of 1L-WS_2 and Bi_2O_2Se QDs

To explore the optical characteristics of the 1L-WS_2, we acquired the diffused reflectance spectra (DRS). The Kubelka-Munk function (F(R)) was computed from the DRS data, which is a comprehensive measure of their absorbance. **Fig. 5.6(a)** depicts the layered plot of F(R) of the 1L-WS_2 and the micro-PL spectrum acquired using a 488nm laser excitation. The F(R) plot clearly shows the characteristic absorption peaks of WS_2 corresponding to B and A excitons. The B (512 nm) and A (624 nm) excitons arise from the splitting of the valence band of WS_2 at the K point of the Brillouin zone, due to pronounced spin-orbit coupling. The PL emission peak of 1L-WS_2 is observed at 630 nm. For a better understanding of the origin of the PL, we have deconvoluted the PL spectrum with three Gaussian components: the neutral exciton (A_0), the negative trion (A_{tr}), and the defect-bound exciton (X) (**Fig. 5.6(b)**).

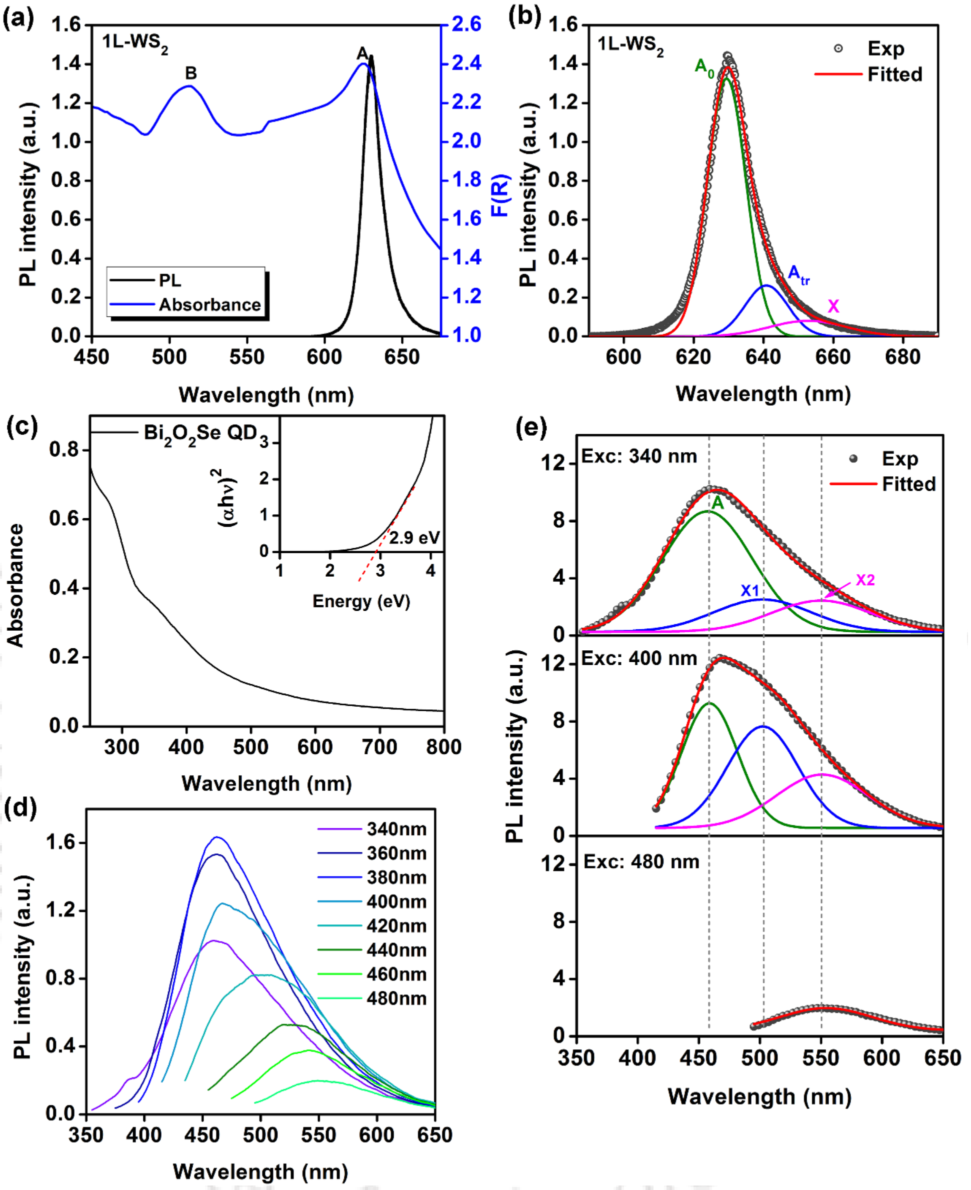

Fig. 5.6. (a) PL emission spectrum and Kubelka-Munk F(R) plot of 1L-WS_2. PL spectrum is acquired for excitation of 488nm. (b) Gaussian deconvolution of the PL spectrum of 1L-WS_2 with 3 components. (c) UV-Vis absorption spectrum of Bi_2O_2Se QD. Inset displays the corresponding Tauc plot. (d) Excitation-dependent PL spectra of Bi_2O_2Se QDs. (e) Stacked Gaussian deconvolutions of the PL spectra of Bi_2O_2Se QDs for the excitation wavelengths 340, 400, and 480 nm.

The A_0 exciton peak at ~629.4 nm, arises from the direct band gap transition from the conduction band to the valence band in WS_2. The A_{tr} peak at ~640.8 nm, the transition from the trions, is caused by light n-type doping from the substrate or the charged impurities in the CVD grown 1L-WS_2 film. The trion binding energy, thus, amounts to ~35 meV, which agrees well with literature[41]. The third component is the X exciton peak (653 nm), attributed to the radiative recombination of the bound excitons. The spectral weight corresponding to the A_0 dominates the fitting, with a significant 74.5% of the PL spectrum. The spectral weight of A_{tr} amounts to 16.4% of the spectrum.

The UV-Visible absorption spectrum of Bi_2O_2Se QDs is displayed in **Fig. 5.6(c)**. The QD absorption spectrum is contrasting with respect to that of CVD-grown two-dimensional Bi_2O_2Se film. The QDs exhibit high absorbance in the UV region with a tail in the visible region. Bi_2O_2Se has an indirect band gap. However, in the QD regime, we presume the band gap becomes quasi-direct, due to the evolution of the band structure. The Tauc plot reveals a band gap of 2.9 eV for the QDs, while the bulk bandgap is much lower. **Fig. 5.6(d)** depicts the excitation wavelength-dependent PL spectra of the Bi_2O_2Se QDs for the excitation range of 340-480 nm, which exhibits typical QD characteristics of quantum confinement. Due to the step-down process of chemical exfoliation, it is understood that defects are created in the system, such as Se vacancies, topological defects, edge effects, etc.[32, 42] We have deconvoluted the PL spectra corresponding to the excitation wavelengths 340 nm, 400 nm and 480 nm with three Gaussian components- the A exciton (~457 nm) corresponding to direct transition from the conduction band to the valence band and two defect excitons X1 (~500 nm) and X2 (~550 nm) (**Fig. 5.6(e)**). The position of the A exciton varies slightly with excitation energy owing to quantum confinement. At λ_{ex}=480 nm, the PL is only contributed by the radiative defect bound exciton X2. This is similar to the behavior of WS_2 QDs discussed in **Chapter 3**.

For a further in-depth investigation of its excitonic properties, we carry out temperature-dependent PL measurements on 1L-WS_2 using an excitation of 488 nm. **Fig. 5.7(a)** displays the temperature-dependent PL spectra in the range of 193-273 K. There is a decrease in PL emission intensity with ascending temperature, accompanied by a spectral red-shift. This decrease in the PL intensity is understood to be due to an increase in the non-radiative recombination processes at higher temperatures[43]. To estimate the thermal activation energy, or in our case, the exciton binding energy (E_b), we carry out the Arrhenius fitting of the PL data in the temperature range 213-273 K, using the Arrhenius equation, $I(T) = \frac{I(0)}{1+Ce^{(\frac{-E_b}{k_B T})}}$. Here, I(T) and I(0) are the PL intensities at T and 0 K, respectively. C is a proportionality constant. The exciton binding energy of 1L-WS_2 is estimated to be ~699.7 ± 5.5 meV (inset of **Fig. 5.7(a)**). Theoretically, the exciton binding energy is estimated to be around 0.7 eV[41]. Thus, our estimation agrees well with the reported values. The redshift in PL emission wavelength, associated with an increase in the temperature from 113-293 K, is depicted in **Fig. 5.7(b)**. The temperature-induced shift in the emission energy is fitted with the Varshni formula, $E(T) = E(0) - \frac{\alpha T^2}{\beta + T}$, as shown in the inset of **Fig. 5.7(b)**. *E(T)* and *E(0)* are the bandgaps of WS_2 at temperatures T and 0 K, respectively. We find *E(0)*= 2.03 eV and α and β are phenomenological constants. Through the best fitting of the data, we obtain $\alpha = 3.59 \times 10^{-4}$ eV K^{-2} and $\beta = 216.3$ K, which agree well with the Debye temperature of bulk WS_2[44-46].

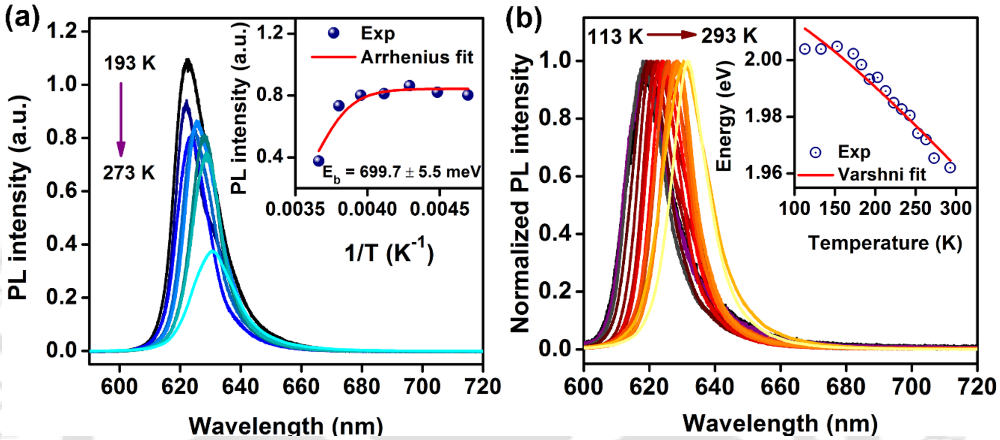

Fig. 5.7 (a) Temperature-dependent PL spectra of 1L-WS_2 in the temperature range of 193-273 K. Inset shows the Arrhenius fit that yields E_b= 699.7 meV. (b) The normalized PL spectra in the temperature range 113- 293 K. Inset depicts the Varshni fit which yields E(0)= 2.03 eV.

5.3.4. Photoluminescence modulation and charge transfer dynamics

To investigate the change in the absorption features of the HS with respect to the pristine 1L-WS_2, the comparative Kubelka-Munk function plot is presented in **Fig. 5.8(a)**. WS_2 exhibits absorption bands corresponding to B and A excitons at 512 nm and 624 nm, respectively, which amounts to the giant spin-orbit splitting of ~ 435 meV. The B and A excitonic bands are marginally redshifted for the HS (inset of **Fig. 5.8(a)**). The shift in B exciton peak is ~28 meV whereas for A exciton it is ~ 6 meV. This redshift in the HS is argued to be due to the n-type doping effect on WS_2 owing to charge transfer from the QDs[22, 47]. **Fig. 5.8(b)** depicts the representative PL emission spectra of 1L-WS_2, Bi_2O_2Se QDs, and their HS. The laser excitation of 488 nm was used for the measurement. The PL emission intensity of the 1L-WS_2 decreases by ~71% with a slight redshift of ~10 meV, with the integration of Bi_2O_2Se QDs (of concentration 5 mg/l). Also, the PL linewidth of the HS visibly broadens with respect to the spectrum corresponding to 1L-WS_2. We have discussed in our previous work (**Chapter 3**) that the change in the PL line shape and shift in peak position can be attributed to selective carrier recombination at different levels[48]. Additionally, the PL spectra of the Bi_2O_2Se QDs appear to be broader and of much lower intensity than the 2D WS_2 film. The emission spectrum matches with the PL spectrum shown in **Fig. 5.6(e)**.

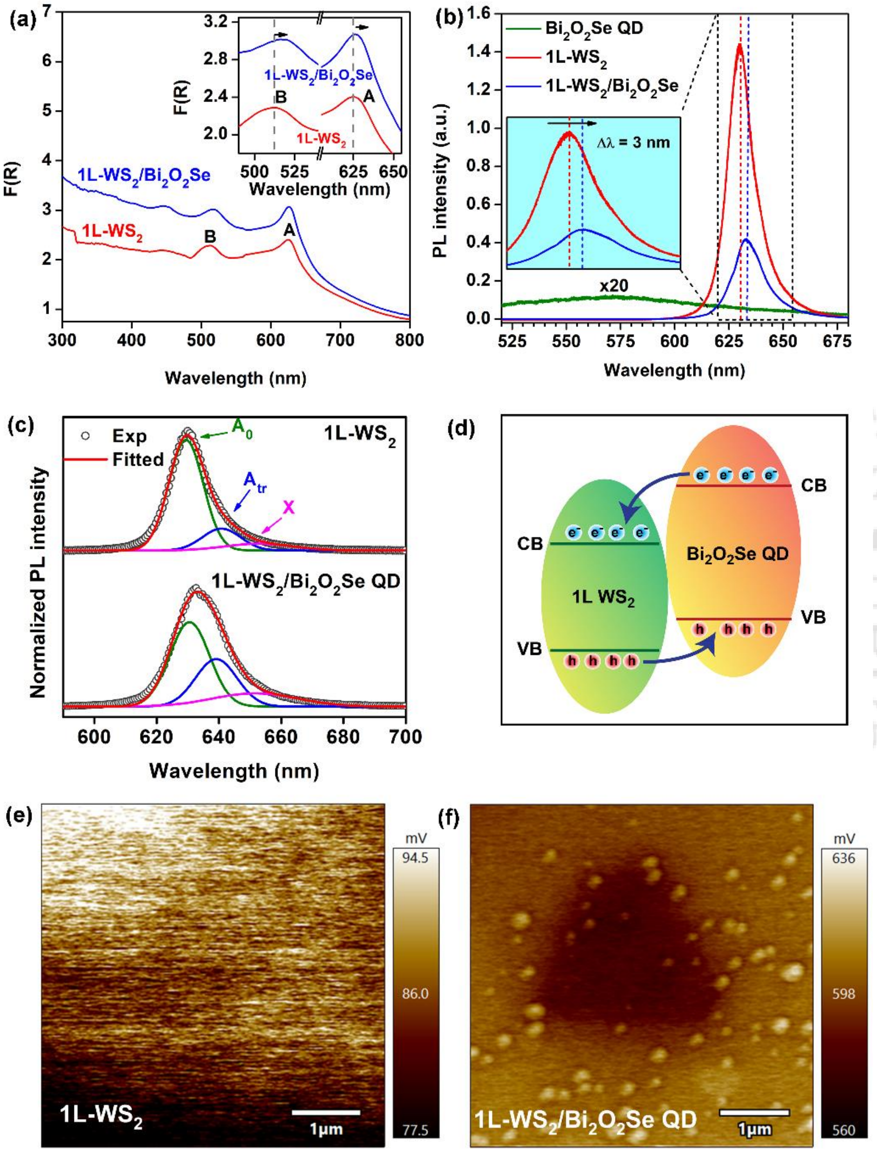

Fig. 5.8. (a) Comparative Kubelka-Munk plots of 1L-WS_2 and 1L-WS_2/Bi_2O_2Se QDs. The inset displays the magnified spectra; the arrows indicate the shift in the peak position. (b) Comparative PL spectra of 1L-WS_2, Bi_2O_2Se QD and 1L-WS_2/Bi_2O_2Se QD, at laser excitation of 488 nm. (c) Gaussian deconvolution of PL emission spectra of 1L-WS_2 and 1L-WS_2/Bi_2O_2Se QD. (d) Proposed energy band diagram (alignment) of the 1L-WS_2/Bi_2O_2Se QD heterojunction. KPFM potential profiles on (e) 1L-WS_2 and (f) 1L-WS_2/Bi_2O_2Se QDs.

To shed light on the evolution of the PL emission properties of the 1L-WS_2 with the incorporation of the Bi_2O_2Se QDs, we present the deconvoluted PL spectra in a stacked plot, in **Fig. 5.8(c),** for comparison. The spectra have been deconvoluted with three components: the A_0 exciton (~630 nm), the A_{tr} trion (~641 nm), and the defect-bound exciton (~653 nm). The positions of the components relatively remain unchanged; however, there is a drastic trade in the respective spectral weights of the exciton and the trion with the QDs decoration. The A_0 exciton dominates the PL of the 1L-WS_2 with 74.5% weight, while the trion contribution is ~16.4%. Whereas upon formation of the 1L-WS_2/Bi_2O_2Se QD HS, the excitonic contribution to the PL emission drops to ~52%, and the trion spectral weight rises to ~30.5%. It may be noted that a QD concentration of 30 mg/l was used for the measurement. This shift in the spectral weights is attributed to excess electrons in 1L-WS_2, due to charge transfer from the Bi_2O_2Se QDs[22, 47, 49]. This is aided by the specific band alignment at the 1L-WS_2/Bi_2O_2Se QDs junction, as displayed in **Fig. 5.8(d)**. The CVD-grown 1L-WS_2 exhibits PL emission predominantly due to neutral excitons. The incorporation of Bi_2O_2Se QDs leads to the transfer of electrons from the defect trap states of the QDs that are excited upon illumination with a 488 nm laser. These surplus electrons lead to the conversion of the neutral excitons into negative trions, thus leading to a reduction of the neutral exciton emission intensity. This results in n-type doping of the 1L-WS_2, which manifests in the evolution of the PL line shape and the redshift in the PL peak position. Additionally, on the formation of the HS, X defect exciton spectral weight increases from ~9.1 to 17.5%.

To support our hypothesis of charge transfer from the QDs to the 1L-WS_2, we have carried out a Kelvin Probe Force Microscopy (KPFM) measurement. The work functions of the 1L-WS_2 and the 1L-WS_2/QD HS are estimated from the contact potential difference (V_{CPD}) obtained from the potential profiles, depicted in **Fig. 5.8(e, f)**, respectively. The work function of the tip used (Φ_t) is ~ 4.992 eV. The relation between the contact potential difference and the work functions is given by the relation, $eV_{CPD} = \Phi_t - \Phi_s$, where Φ_s is the work function of the sample. In **Fig. 5.8(e),** the potential profile is obtained over a uniform flake of 1L-WS_2. The average V_{CPD} for 1L-WS_2 is ~86 mV. Thus, the work function of 1L-WS_2 is estimated to be ~ 4.906 eV. The computed $\Phi_{1L\text{-}WS2}$ shows that the as-grown 1L-WS_2 is only slightly n-doped, consistent with its sharp PL emission due to mainly the neutral exciton with minor trion contribution. Thus, CVD grown 1L-WS_2 here is not particularly n-doped contrary to the CVD grown 1L-MoS_2[43]. However, the effect of excess electrons due to the Bi_2O_2Se QDs in the 1L-WS_2/Bi_2O_2Se QD HS would lead to a shift in the work function. The average V_{CPD} of the HS is ~570 mV, considering the area of darker contrast in **Fig. 5.8(f)**. Therefore, the Φ_{HS} is ~4.422 eV. A significant decrease in the work function is expected due to surplus electron density in the 1L-WS_2, due to effective n-type doping caused by the QDs.

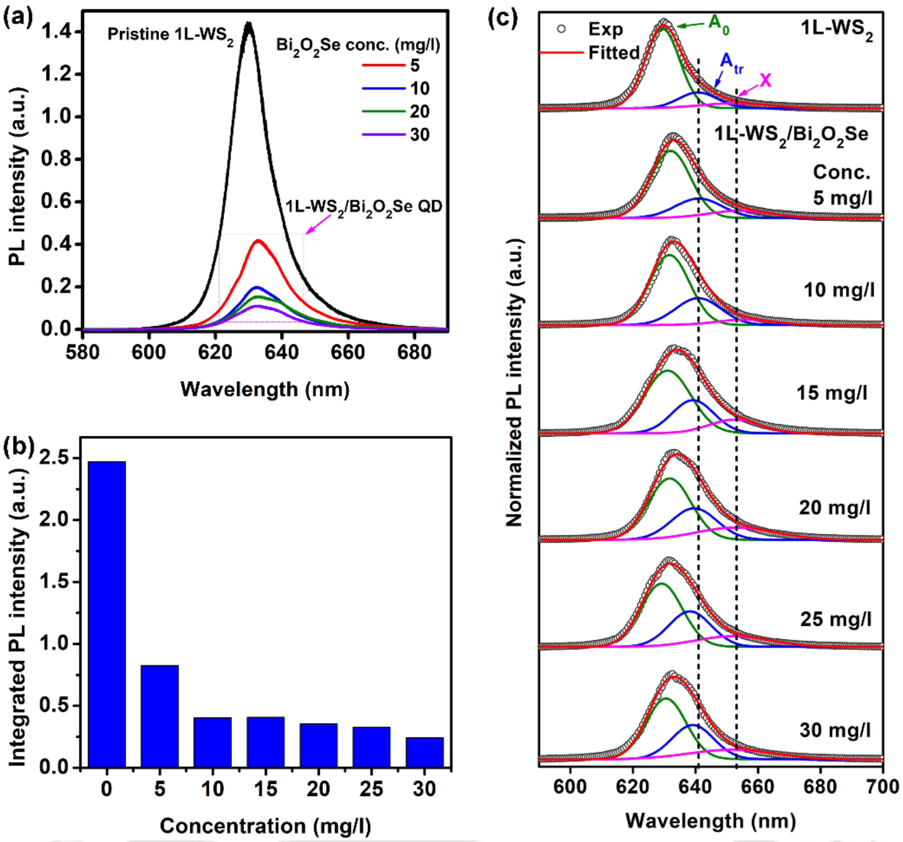

Fig. 5.9. (a) Variation of the PL spectra of the CVD-grown 1L-WS_2 on the decoration of Bi_2O_2Se QDs of different concentrations. (b) Integrated PL intensity of 1L-WS_2 as a function of the concentration of Bi_2O_2Se QDs. (c) Deconvoluted PL spectra of 1L-WS_2 acquired at different QD concentrations. The Gaussian components of the deconvolution are neutral exciton (A_0), negative trion (A_{tr}) and defect-bound exciton (X).

We further investigate the doping level that is achieved by charge transfer, by recording the PL spectra of the 1L-WS_2 by varying the concentrations of the Bi_2O_2Se QDs (5-30 mg/l). It may be noted that the KPFM measurement was carried out with a high concentration of Bi_2O_2Se QDs (30 mg/l). **Fig. 5.9(a)** shows the evolution of the PL spectra of the 1L-WS_2 with different concentrations of the QDs. The systematic quenching of the PL is accompanied by broadening and spectral redshift. There is a substantial change in the total integrated PL intensity as soon as the HS is formed with the Bi_2O_2Se QDs (see **Fig. 5.9(b)**). At 5 mg/l, the integrated PL intensity drops down by ~ 67%. However, with a gradual increase in the concentration of the QDs, there is no further spectral change noticeable. For better comprehension, we study the relative change in the contributions of the neutral exciton, trion, and defect-bound exciton. **Fig. 5.9(c)** shows the stacked plot of the deconvoluted PL spectra of the 1L-WS_2 with different concentrations of the QDs. For clarity, the PL spectra are normalized. The broadening of the PL due to increased trionic contribution is apparent in **Fig. 5.9(c),** especially at concentrations $\geq$ 15 mg/l. The trionic spectral weight increases to ~27.5%, whereas the excitonic contribution reduces to ~58.4%. At higher concentrations, the spectral weight of the exciton further reduces to ~52%, while that of the trion approaches saturation ~32.5% at 30 mg/l. Thus, there is an overall broadening of the PL spectra and an apparent redshift in the PL peak position of ~ 8 meV.

From the PL fitting, we obtain the integral PL intensities corresponding to the exciton (I_{A0}), trion (I_{Atr}), and the defect exciton (I_X) of the 1L-WS_2 HS at different concentrations of the Bi_2O_2Se QDs. The variation of these parameters is plotted with respect to the QD concentrations in **Fig. 5.10(a)**. We notice that the intensity of the neutral excitons I_{A0} decreases dramatically on the decoration of Bi_2O_2Se QDs even at low concentrations and then exhibits somewhat saturation at higher concentrations (>20 mg/l). The integrated intensity of the trion, however, shows a minor change. There is a decrease in the intensity, partly because of charge separation at the interface of the QDs and the 1L-WS_2, and secondly, because of conversion of the neutral exciton to trion. At further higher concentrations of the QDs, there is a saturation of trion emission/population, after a certain doping level due to Pauli blocking effect, in which nearby states become forbidden for the occupation of electrons[50-51].

Next, we discuss the exciton and trion relaxation dynamics with rate equations based on a four-energy level model, as shown in **Fig. 5.10(b),** proposed by our group in a previous study on 1L-MoS_2[22]. This is crucial for a detailed understanding of the evolution in the integrated PL intensities of the neutral exciton I_{A0}, trion I_{Atr}, and defect bound-exciton I_X, and the subsequent doping effect. The four levels are namely the levels about the A_0, A_{tr}, X, and the ground level. Here, G represents the rate of generation of neutral excitons, whereas, $\Gamma_1(\delta)$ characterizes the decay rate of the excitons, to the ground level. The exciton decay, in this work, is closely related to the different doping concentrations (δ) of Bi_2O_2Se QDs. For better modeling of our data, we have assumed that Γ_1 is directly proportional to δ. Now, the trions are inherently formed from excitons on the addition of electrons from a dopant or other external factors. Thus, the formation rate of trion from the exciton is given by $k_{tr}(\delta)$, which is dependent on the δ of the Bi_2O_2Se QDs.

The decay of the trion population with increasing δ is closely associated with the decay of neutral excitons as well. Due to charge separation in a type II band alignment, the e-h recombination is bound to be hindered. Thus, the direct dependence of Γ_1 on the doping concentration δ is well accounted for. The trions, on the other hand, decay through two pathways: (1) directly to the ground state at the rate of Γ_2 and (2) through defect trap states with a decay rate of Γ_3. Additionally, the defect excitons decay to the ground level with a decay rate of Γ_4. Since the degree of evolution in defect-related intensity is relatively smaller, Γ_3 and Γ_4 are assumed to be independent of the doping concentration.

The corresponding rate equations for the population of neutral excitons N_0, trions N_{tr}, and the defect-bound excitons N_X can be expressed as:

$$\frac{dN_0}{dt} = G - [\Gamma_1(\delta) + k_{tr}(\delta)]N_0 \tag{1}$$

$$\frac{dN_{tr}}{dt} = k_{tr}(\delta)N_0 - (\Gamma_2 + \Gamma_3)N_{tr} \tag{2}$$

$$\frac{dN_X}{dt} = \Gamma_3 N_{tr} - \Gamma_4 N_X \tag{3}$$

$$k_{tr}(\delta) = k_{tr}(0)\left(1 + \frac{s\alpha\delta}{\alpha\delta+1}\right) \tag{4}$$

$$\Gamma_1(\delta) = \Gamma_1(0)(1 + \beta\delta) \tag{5}$$

The rates of change of populations of different entities are dependent on their formation rate as well their decay rates. We consider that in the process of adsorption of Bi_2O_2Se QDs onto the 1L-WS_2, the Langmuir law is followed, i.e., a uniform layer of Bi_2O_2Se molecules covers a 1L-WS_2 crystalline flake. As such, the formation rate of trions from excitons can be described as $k_{tr}(\delta)$ (Eq. (4)), which is a modified version of the expression[18, 52], assuming there is an increase in the rate of trion formation with increasing doping concentration. Here, α is a measure of the adsorption probability of the Bi_2O_2Se QDs onto the 1L-WS_2, and *s* (~85%) reflects the ability of charge transfer from Bi_2O_2Se QD to 1L-WS_2. In Eq. (5), β is a proportionality constant. Doping concentration δ is increased in steps of 5 mg/l in our experiment. We obtain the relations for the neutral exciton, trion, and defect-bound exciton densities, under steady-state, upon solving the above rate equations analytically within the framework of the four-level model:

$$N_0(\delta) = \frac{G}{\Gamma_1(\delta)+k_{tr}(\delta)} \tag{6}$$

$$N_{tr}(\delta) = \frac{k_{tr}(\delta)}{\Gamma_2+\Gamma_3}N_0 = \frac{k_{tr}(\delta)}{(\Gamma_2+\Gamma_3)}\frac{G}{(\Gamma_1(\delta)+k_{tr}(\delta))} \tag{7}$$

$$N_X(\delta) = \frac{\Gamma_3}{\Gamma_4} N_{tr} = \frac{\Gamma_3}{\Gamma_4}\frac{k_{tr}(\delta)}{(\Gamma_2+\Gamma_3)}\frac{G}{(\Gamma_1(\delta)+k_{tr}(\delta))} \tag{8}$$

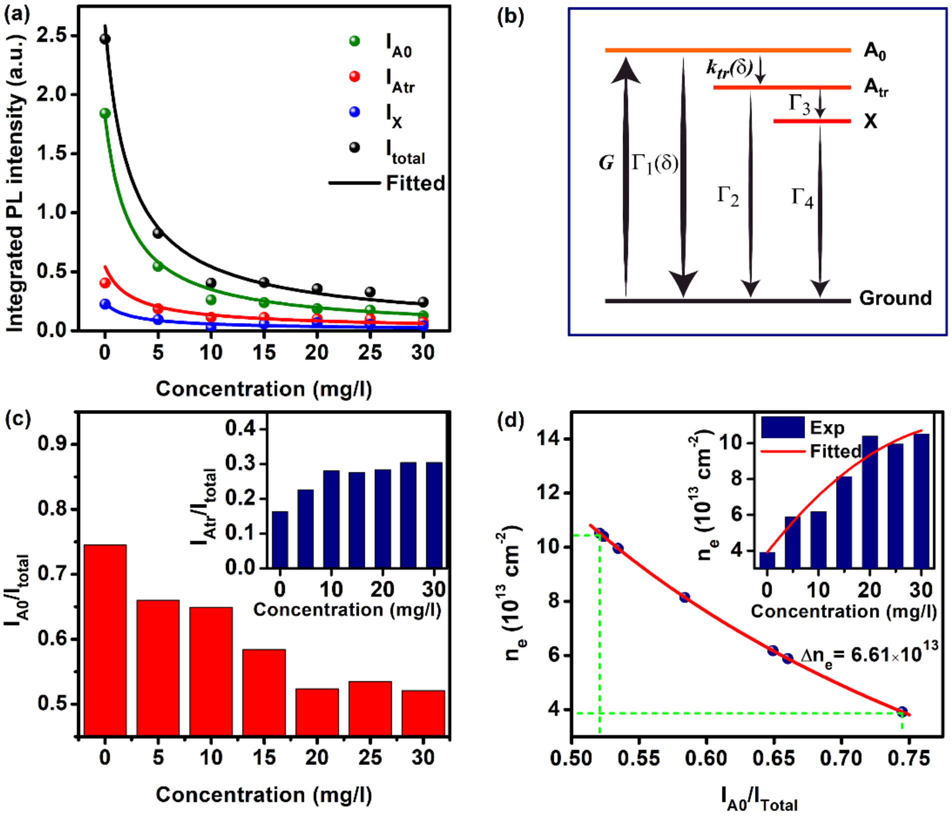

Fig. 5.10.: (a) Integrated PL intensities of the neutral exciton (I_{A0}), trion (I_{Atr}), and defect bound exciton (I_X) and their total (I_{total}) as a function of the concentration of Bi_2O_2Se QDs. Symbols represent the experimental data, while the solid lines are analytically fitted data. (b) Schematic representation of transitions in a four-level energy diagram involving the neutral exciton (I_{A0}), trion (I_{Atr}), and defect-bound exciton (I_X) and the ground state. (c) The spectral weight of A_0 (I_{A0}/I_{Total}) as a function of the concentration of Bi_2O_2Se QDs. The inset depicts the variation of the trion spectral weight with the doping concentration. (d) The change in n_e based on the law of mass action depicted as a function of neutral exciton spectral weight (I_{A0}/I_{Total}). The inset shows the electron density (n_e) calculated from the law of mass action, as a function of the QD concentration.

The steady-state PL intensities of the neutral exciton (I_{A0}), trion (I_{Atr}), and defect-bound exciton (I_X) are directly related to the respective population densities of these entities and can be represented as follows:

$$I_{A_0}(\delta) = \frac{AG\gamma_0}{\Gamma_1(\delta)+k_{tr}(\delta)} \tag{9}$$

$$I_{A_{tr}}(\delta) = \frac{k_{tr}(\delta)}{(\Gamma_2+\Gamma_3)}\frac{AG\gamma_{tr}}{(\Gamma_1(\delta)+k_{tr}(\delta))} \tag{10}$$

$$I_X(\delta) = \frac{\Gamma_3}{\Gamma_4}\frac{k_{tr}(\delta)}{(\Gamma_2+\Gamma_3)}\frac{AG\gamma_X}{(\Gamma_1(\delta)+k_{tr}(\delta))} \tag{11}$$

Here, A is a constant that reflects the collection efficiency of luminescence. The radiative decay rates of the neutral exciton, trion, and defect-bound exciton, respectively, are taken as γ_0, γ_{tr}, and

γ_X. **Fig. 5.10(a)** depicts the fitted parameters from our proposed model, which agree excellently well with the variation of the experimentally obtained PL intensities I_{A0}, I_{Atr}, and I_X with concentration. The neutral excitons exhibit a fast decay rate, $\Gamma_1(0) = 0.002$ ps^{-1}, while the trion formation rate in this analysis is given by $k_{tr}(0) = 0.5$ ps^{-1}, based on earlier reports[14, 18]. Other decay rates are $\Gamma_2 = 0.02$ ps^{-1} and $\Gamma_3 = 0.05$ ps^{-1} based on the intermediate lifetimes of the processes involved. The values of the decay rates for 1L-WS$_2$ are obtained from literature[14, 18]. We have assumed an intermediate decay rate from the defect trap state, $\Gamma_4 = 0.01$ ps^{-1} for a good fit to the carrier recombination dynamics. The ratios of the fitting parameters of $AG\gamma_{tr}/AG\gamma_0$ and $AG\gamma_X/AG\gamma_0$ to match the experimental data are 0.042 and 0.0036, respectively, which implies that $\gamma_{tr} \ll \gamma_0$ and $\gamma_X \ll \gamma_0$, i.e., the radiative rates of the trions and defect excitons are significantly lesser than that of the neutral excitons, suggesting strong PL emission from the neutral excitons[18, 53]. Our value of γ_{tr}/γ_0 is in good agreement with the reported value ($\gamma_{tr}/\gamma_0 = 0.06$)[18]. The charge transfer process is aided by the specific band alignment between the CVD grown 1L-WS$_2$ and the Bi$_2$O$_2$Se QDs. The contribution of the trions in the evolution of the PL is much greater than that of the defects, however, it becomes crucial to consider the role of the defects while modeling the experimental data. We depict the variation of the excitonic spectral weight with respect to changing QD concentrations in **Fig. 5.10(c).** The inset of **Fig. 5.10(c)** represents the saturation of the trion spectral weight with increasing doping concentrations. Furthermore, to quantify the doping effect discussed in this work, we calculate the change in the electron density in the system, with the assumption of the validity of the law of mass action. The relationship between the population densities of the neutral exciton (N_0), trions (N_{tr}), and the charge density (n_e) at any given doping stage, is expressed as:

$$\frac{N_0 n_e}{N_{tr}} = \left(\frac{16\pi m_{A0} m_e}{h^2 m_{tr}}\right) k_B T \exp\left(-\frac{E_b}{k_B T}\right) \tag{12}$$

Here, h is Planck's constant, k_B is the Boltzmann constant, T is the ambient temperature (300 K) and E_b is the trion binding energy (~35 meV). The effective masses of the electron (m_e) and hole (m_h) are 0.44 m0 and 0.45 m_0, where m_0 is a free electron mass. Therefore, the effective masses of a neutral exciton (m_{A0}) and a trion (m_{tr}) are given by 0.89 m_0 and 1.33 m_0, respectively. Therefore, from the above equation, the calculated excitonic spectral weight of the exciton can be expressed as

$$\frac{I_{A0}}{I_{total}} = \frac{I_{A0}}{I_{A0}+I_{Atr}+I_X} = \frac{1}{1+\frac{\gamma_{tr} N_{tr}}{\gamma_0 N_0}+\frac{\Gamma_3 \gamma_X N_X}{\Gamma_4 \gamma_0 N_0}} \approx \frac{1}{1+8.75\times10^{-15} n_e} \tag{13}$$

The values of γ_{tr}/γ_0 and γ_X/γ_0 from the fitting are substituted here. The change in the electron density is depicted with respect to the variation in the excitonic spectral weights in **Fig. 5.10(d).** For pristine 1L-WS$_2$, the electron density is ~3.91 × 10^{13} cm^{-2}. After doping induced by Bi$_2$O$_2$Se QDs at the concentration of 30 mg/l, the calculated electron density of the 1L-WS$_2$/Bi$_2$O$_2$Se QD HS increases to 1.052 × 10^{14} cm^{-2}. Thus, there is a significant increase in the electron density after the formation of the HS i.e., Δn_e ~ 6.61 × 10^{13} cm^{-2}, which approximately estimates the density of doped electrons in 1L-WS$_2$. Additionally, the electron density n_e in the hybrid system at different QD concentrations is computed and presented in the inset of **Fig. 5.10(d)**. In a study conducted by our group related to doping of 1L- MoS$_2$, the electron density of the WS$_2$ QD decorated 1L-MoS$_2$ (2.05 × 10^{13} cm^{-2}) almost quadrupled with respect to that of the pristine sample (5.50 × 10^{12} cm^{-2})[22]. Whereas, in this work, the electron density of the doped 1L-WS$_2$ is ~2.7 times the pristine film implying relatively weaker doping. This is attributed to weak adsorption of the Bi$_2$O$_2$Se QDs onto the 1L-WS$_2$ film surface, owing to their non-van der Waals nature. It has to do partly with the electrostatic interaction/force between the layers of Bi$_2$O$_2$Se that causes lesser charge flow.

Thus, we have demonstrated the effective doping in 1L-WS$_2$ simply by the decoration of Bi$_2$O$_2$Se QDs. This paves the way for achieving control over the electrical and optical properties of CVD grown 1L-WS$_2$. The effective tuning of the electron density leads to the conversion of neutral excitons to trions, altering the shape of the PL emission spectrum. These straightforward ways of systematic doping of these 2D systems become essential while developing potential optoelectronic and electronic devices.

5.4. Conclusion

To summarize, controlled doping of monolayer WS$_2$ is possible via the decoration of 2D material quantum dots. The process requires no microfabrication techniques and higher-level doping can be achieved simply by controlling the concentration of the Bi$_2$O$_2$Se QDs. The quenching of the PL emission is accompanied in the process due to the conversion of neutral excitons to trions owing to the surplus electrons in the system. The variation in the electron density amounts to Δn_e ~ 6.6 × 10^{13} cm^{-2}, which is almost one order higher than the pristine 1L-WS$_2$. This indicates an n-type doping effect in the CVD grown 1L-WS$_2$ by a simple technique. Our results suggest an effective way to manipulate the electron density through the decoration of QDs, which is advantageous to tune the optical and electrical properties of monolayer TMD systems. We believe this study would potentially facilitate further research in understanding the fundamentals of light-matter interactions in 2D heterostructure systems and pave way for myriad applications in optoelectronics, electronics, and so on.

References

1. Shi, J., et al., Controllable Growth and Transfer of Monolayer Mos2 on Au Foils and Its Potential Application in Hydrogen Evolution Reaction. *ACS Nano* **2014**, *8*, 10196-10204.

2. Yang, X.; Li, B., Monolayer Mos2 for Nanoscale Photonics. *Nanophotonics* **2020**, *9*, 1557-1577.

3. Chen, J., et al., Synthesis of Wafer-Scale Monolayer Ws2 Crystals toward the Application in Integrated Electronic Devices. *ACS Applied Materials & Interfaces* **2019**, *11*, 19381-19387.

4. Zhang, Z.; Qian, Q.; Li, B.; Chen, K. J., Interface Engineering of Monolayer Mos2/Gan Hybrid Heterostructure: Modified Band Alignment for Photocatalytic Water Splitting Application by Nitridation Treatment. *ACS Applied Materials & Interfaces* **2018**, *10*, 17419-17426.

5. Lan, C.; Zhou, Z.; Zhou, Z.; Li, C.; Shu, L.; Shen, L.; Li, D.; Dong, R.; Yip, S.; Ho, J. C., Wafer-Scale Synthesis of Monolayer Ws2 for High-Performance Flexible Photodetectors by Enhanced Chemical Vapor Deposition. *Nano Research* **2018**, *11*, 3371-3384.

6. Zhu, B.; Zeng, H.; Dai, J.; Gong, Z.; Cui, X., Anomalously Robust Valley Polarization and Valley Coherence in Bilayer Ws₂. *Proceedings of the National Academy of Sciences* **2014**, *111*, 11606-11611.

7. Gao, F.; Gong, Y.; Titze, M.; Almeida, R.; Ajayan, P. M.; Li, H., Valley Trion Dynamics in Monolayer ${\Mathrm{Mose}}_{2}$. *Physical Review B* **2016**, *94*, 245413.

8. Mai, C.; Barrette, A.; Yu, Y.; Semenov, Y. G.; Kim, K. W.; Cao, L.; Gundogdu, K., Many-Body Effects in Valleytronics: Direct Measurement of Valley Lifetimes in Single-Layer Mos2. *Nano Letters* **2014**, *14*, 202-206.

9. Kim, M. S.; Yun, S. J.; Lee, Y.; Seo, C.; Han, G. H.; Kim, K. K.; Lee, Y. H.; Kim, J., Biexciton Emission from Edges and Grain Boundaries of Triangular Ws2 Monolayers. *ACS Nano* **2016**, *10*, 2399-2405.

10. Upadhyay, B.; Thakur, D.; Pramanick, B.; Bhandari, S.; Balakrishnan, V.; Pal, S. K., Anomalous Emission Behavior of Excitons at Low Temperature in Monolayer Ws₂. *Journal of Physics D: Applied Physics* **2022**, *55*, 235105.

11. Lagarde, D.; Bouet, L.; Marie, X.; Zhu, C. R.; Liu, B. L.; Amand, T.; Tan, P. H.; Urbaszek, B., Carrier and Polarization Dynamics in Monolayer ${\Mathrm{Mos}}_{2}$. *Physical Review Letters* **2014**, *112*, 047401.

12. Wang, G.; Palleau, E.; Amand, T.; Tongay, S.; Marie, X.; Urbaszek, B., Polarization and Time-Resolved Photoluminescence Spectroscopy of Excitons in Mose2 Monolayers. *Applied Physics Letters* **2015**, *106*, 112101.

13. Wang, L.; Xu, C.; Li, M.-Y.; Li, L.-J.; Loh, Z.-H., Unraveling Spatially Heterogeneous Ultrafast Carrier Dynamics of Single-Layer Wse2 by Femtosecond Time-Resolved Photoemission Electron Microscopy. *Nano Letters* **2018**, *18*, 5172-5178.

14. Shi, H.; Yan, R.; Bertolazzi, S.; Brivio, J.; Gao, B.; Kis, A.; Jena, D.; Xing, H. G.; Huang, L., Exciton Dynamics in Suspended Monolayer and Few-Layer Mos2 2d Crystals. *ACS Nano* **2013**, *7*, 1072-1080.

15. Zereshki, P.; Valencia-Acuna, P.; Zhao, H., All-Optical Control of Charge Transfer and Interlayer Excitons in Transition Metal Dichalcogenide Heterostructures. *Physical Review B* **2021**, *103*, 165416.

16. Yang, J., et al., Identifying the Intermediate Free-Carrier Dynamics across the Charge Separation in Monolayer Mos2/Rese2 Heterostructures. *ACS Nano* **2021**, *15*, 16760-16768.

17. Ross, J. S., et al., Electrical Control of Neutral and Charged Excitons in a Monolayer Semiconductor. *Nature Communications* **2013**, *4*, 1474.

18. Tao, Y.; Yu, X.; Li, J.; Liang, H.; Zhang, Y.; Huang, W.; Wang, Q. J., Bright Monolayer Tungsten Disulfide Via Exciton and Trion Chemical Modulations. *Nanoscale* **2018**, *10*, 6294-6299.

19. Feng, Q.; Li, Y.; Gao, F.; Sun, Y.; Yan, J.; Liu, W.; Xu, H.; Liu, Y., Manipulating Transfer and Separation of Photocarriers in Monolayer Ws2 Via Cdse Quantum Dot Doping. *ACS Photonics* **2020**, *7*, 1857-1865.

20. Wang, Y.; Slassi, A.; Stoeckel, M.-A.; Bertolazzi, S.; Cornil, J.; Beljonne, D.; Samorì, P., Doping of Monolayer Transition-Metal Dichalcogenides Via Physisorption of Aromatic Solvent Molecules. *The Journal of Physical Chemistry Letters* **2019**, *10*, 540-547.

21. Kuechle, T.; Klimmer, S.; Lapteva, M.; Hamzayev, T.; George, A.; Turchanin, A.; Fritz, T.; Ronning, C.; Gruenewald, M.; Soavi, G., Tuning Exciton Recombination Rates in Doped Transition Metal Dichalcogenides. *Optical Materials: X* **2021**, *12*, 100097.

22. Mawlong, L. P. L.; Bora, A.; Giri, P. K., Coupled Charge Transfer Dynamics and Photoluminescence Quenching in Monolayer Mos2 Decorated with Ws2 Quantum Dots. *Scientific Reports* **2019**, *9*, 19414.

23. Roy, S.; Neupane, G. P.; Dhakal, K. P.; Lee, J.; Yun, S. J.; Han, G. H.; Kim, J., Observation of Charge Transfer in Heterostructures Composed of Mose2 Quantum Dots and a Monolayer of Mos2 or Wse2. *The Journal of Physical Chemistry C* **2017**, *121*, 1997-2004.

24. Hossain, M. T.; Giri, P. K., Temperature-Dependent Raman Studies and Thermal Conductivity of Direct Cvd Grown Non-Van Der Waals Layered Bi2o2se. *Journal of Applied Physics* **2021**, *129*, 175102.

25. Hossain, M. T.; Das, M.; Ghosh, J.; Ghosh, S.; Giri, P. K., Understanding the Interfacial Charge Transfer in the Cvd Grown Bi2o2se/Cspbbr3 Nanocrystal Heterostructure and Its Exploitation in Superior Photodetection: Experiment Vs. Theory. *Nanoscale* **2021**, *13*, 14945-14959.

26. Wu, J., et al., High-Performance Waveguide-Integrated Bi2o2se Photodetector for Si Photonic Integrated Circuits. *ACS Nano* **2021**, *15*, 15982-15991.

27. Liu, X.; Li, R.; Hong, C.; Huang, G.; Pan, D.; Ni, Z.; Huang, Y.; Ren, X.; Cheng, Y.; Huang, W., Highly Efficient Broadband Photodetectors Based on Lithography-Free Au/Bi2o2se/Au Heterostructures. *Nanoscale* **2019**, *11*, 20707-20714.

28. Singh, A.; Moun, M.; Sharma, M.; Barman, A.; Kumar Kapoor, A.; Singh, R., Nacl-Assisted Substrate Dependent 2d Planar Nucleated Growth of Mos2. *Applied Surface Science* **2021**, *538*, 148201.

29. Wu, J., et al., High Electron Mobility and Quantum Oscillations in Non-Encapsulated Ultrathin Semiconducting Bi2o2se. *Nature Nanotechnology* **2017**, *12*, 530-534.

30. Drbaar, e.; Ruleova, P.; Benfa, L.; Lpbeák, P., Preparation and Transport Properties of Bi2o2se Single Crystals. *Journal of Electronic Materials* **2012**, *41*, 2317-2321.

31. Loh, T. A. J.; Chua, D. H. C.; Wee, A. T. S., One-Step Synthesis of Few-Layer Ws2 by Pulsed Laser Deposition. *Scientific Reports* **2015**, *5*, 18116.

32. Lin, L.; Xu, Y.; Zhang, S.; Ross, I. M.; Ong, A. C. M.; Allwood, D. A., Fabrication of Luminescent Monolayered Tungsten Dichalcogenides Quantum Dots with Giant Spin-Valley Coupling. *ACS Nano* **2013**, *7*, 8214-8223.

33. Gao, J., et al., Transition-Metal Substitution Doping in Synthetic Atomically Thin Semiconductors. *Advanced Materials* **2016**, *28*, 9735-9743.

34. McCreary, K. M.; Hanbicki, A. T.; Jernigan, G. G.; Culbertson, J. C.; Jonker, B. T., Synthesis of Large-Area Ws2 Monolayers with Exceptional Photoluminescence. *Scientific Reports* **2016**, *6*, 19159.

35. Perrozzi, F.; Emamjomeh, S. M.; Paolucci, V.; Taglieri, G.; Ottaviano, L.; Cantalini, C., Thermal Stability of Ws2 Flakes and Gas Sensing Properties of Ws2/Wo3 Composite to H2, Nh3 and No2. *Sensors and Actuators B: Chemical* **2017**, *243*, 812-822.

36. Molina-Sánchez, A.; Wirtz, L., Phonons in Single-Layer and Few-Layer Mos${}_{2}$ and Ws${}_{2}$. *Physical Review B* **2011**, *84*, 155413.

37. Berkdemir, A., et al., Identification of Individual and Few Layers of Ws2 Using Raman Spectroscopy. *Scientific Reports* **2013**, *3*, 1755.

38. Pramanik, A.; Davis, D.; Patibandla, S.; Begum, S.; Ray, P.; Gates, K.; Gao, Y.; Chandra Ray, P., A Ws2-Gold Nanoparticle Heterostructure-Based Novel Sers Platform for the Rapid Identification of Antibiotic-Resistant Pathogens. *Nanoscale Advances* **2020**, *2*, 2025-2033.

39. Molas, M. R.; Nogajewski, K.; Potemski, M.; Babiński, A., Raman Scattering Excitation Spectroscopy of Monolayer Ws2. *Scientific Reports* **2017**, *7*, 5036.

40. Xu, S.; Li, D.; Wu, P., One-Pot, Facile, and Versatile Synthesis of Monolayer Mos2/Ws2 Quantum Dots as Bioimaging Probes and Efficient Electrocatalysts for Hydrogen Evolution Reaction. *Advanced Functional Materials* **2015**, *25*, 1127-1136.
41. Zhu, B.; Chen, X.; Cui, X., Exciton Binding Energy of Monolayer Ws2. *Scientific Reports* **2015**, *5*, 9218.
42. Dhenadhayalan, N.; Lin, T.-W.; Lee, H.-L.; Lin, K.-C., Multisensing Capability of Mose2 Quantum Dots by Tuning Surface Functional Groups. *ACS Applied Nano Materials* **2018**, *1*, 3453-3463.
43. Mawlong, L. P. L.; Paul, K. K.; Giri, P. K., Direct Chemical Vapor Deposition Growth of Monolayer Mos2 on Tio2 Nanorods and Evidence for Doping-Induced Strong Photoluminescence Enhancement. *The Journal of Physical Chemistry C* **2018**, *122*, 15017-15025.
44. Peng, B.; Zhang, H.; Shao, H.; Xu, Y.; Zhang, X.; Zhu, H., Thermal Conductivity of Monolayer Mos2, Mose2, and Ws2: Interplay of Mass Effect, Interatomic Bonding and Anharmonicity. *RSC Advances* **2016**, *6*, 5767-5773.
45. Yip, C. T.; Lo, T. W.; Zhu, S.-C.; Jia, G. Y.; Sun, H.; Lam, C.-H.; Lei, D., Tight-Binding Modeling of Excitonic Response in Van Der Waals Stacked 2d Semiconductors. *Nanoscale Horizons* **2019**, *4*, 969-974.
46. Dumcenco, D. O.; Hsu, H. P.; Huang, Y. S.; Liang, C. H.; Tiong, K. K.; Du, C. H., Optical Properties of Tungsten Disulfide Single Crystals Doped with Gold. *Materials Chemistry and Physics* **2008**, *111*, 475-479.
47. Feng, R.; Xu, S.; Liu, W.; Gao, P.; Zhang, J.; Tong, L., Local Modulation of Excitons and Trions in Monolayer Ws2 by Carbon Nanotubes. *Nano Research* **2020**, *13*, 1982-1987.
48. Bora, A.; Mawlong, L. P. L.; Das, R.; Giri, P. K., Understanding the Excitation Wavelength Dependent Spectral Shift and Large Exciton Binding Energy of Tungsten Disulfide Quantum Dots and Its Interaction with Single-Walled Carbon Nanotubes. *Journal of Colloid and Interface Science* **2020**, *561*, 519-532.
49. Carmiggelt, J. J.; Borst, M.; van der Sar, T., Exciton-to-Trion Conversion as a Control Mechanism for Valley Polarization in Room-Temperature Monolayer Ws2. *Scientific Reports* **2020**, *10*, 17389.
50. Lin, T. N.; Santiago, S. R. M.; Caigas, S. P.; Yuan, C. T.; Lin, T. Y.; Shen, J. L.; Chen, Y. F., Many-Body Effects in Doped Ws2 Monolayer Quantum Disks at Room Temperature. *npj 2D Materials and Applications* **2019**, *3*, 46.
51. An, J. M.; Franceschetti, A.; Zunger, A., Pauli Blocking Versus Electrostatic Attenuation of Optical Transition Intensities in Charged $\Mathrm{Pbse}$ Quantum Dots. *Physical Review B* **2007**, *76*, 161310.
52. Mouri, S.; Miyauchi, Y.; Matsuda, K., Tunable Photoluminescence of Monolayer Mos2 Via Chemical Doping. *Nano Letters* **2013**, *13*, 5944-5948.
53. Peimyoo, N.; Yang, W.; Shang, J.; Shen, X.; Wang, Y.; Yu, T., Chemically Driven Tunable Light Emission of Charged and Neutral Excitons in Monolayer Ws2. *ACS Nano* **2014**, *8*, 11320-11329.

Chapter 6

Photoluminescence Modulation of Monolayer WS_2 by ZnO encapsulation and Study of the Quantum Well Effect

In this chapter, we investigate the effect of ZnO encapsulation on the PL emission from CVD grown 1L-WS_2 films. We construct a sandwich-like structure on 1L-WS_2 using the high bandgap semiconductor ZnO. A thin film of ZnO is grown via radio frequency (RF) magnetron-sputtering on SiO_2 and quartz substrates. The 1L-WS_2 is then transferred onto the ZnO film and subsequently, another layer of ZnO film is deposited via RF sputtering to fabricate an encapsulated 1L-WS_2 quantum well (QW). We explore the quantum confinement and the tuning of the PL emission from the sub-nanometer scale 1L-WS_2 film. In this work, we incorporate power-dependent and temperature-dependent PL spectroscopy as tools to understand the role of neutral excitons, trions, biexcitons, and defects. The PL of 1L-WS_2 is largely affected by factors such as strain and doping. A quantum well would basically lead to the enhancement in PL emission. However, the large bandgap semiconductor ZnO injects carriers onto the 1L-WS_2 which leads to conversion to neutral excitons from trions and biexcitons. The biexciton emission becomes dominant at low temperatures and high laser powers for monolayer WS_2. Thus, the large enhancement in excitonic PL emission due to the QW effect becomes prominent only at low laser powers. This work offers detailed insight in order to understand the carrier dynamics in 1L-WS_2 based QW structure by ZnO encapsulation and the tunability in the PL emission.

6.1. Introduction

In the previous chapters, we have touched upon how WS_2 undergoes a transition from indirect to direct bandgap at its 1L level with the band edge located at the K, K' valleys of the Brillouin zone[1]. In addition, 1L-WS_2 exhibits giant spin-orbit coupling and broken inversion symmetry. The weakened dielectric screening in monolayer limit as well as quantum confinement facilitate the formation of many-body quasiparticle states with unusual binding energies[2]. Since an n-doped system implies excess background electrons, the three-body quasiparticle or the trion dominates the PL emission, as covered in **Chapter 5**. However, the formation of the two electron-hole pair quasi-states, i.e., biexcitons is not as straightforward. Although, their occurrence is mostly explored in cryogenic systems, at room temperatures the emission from the biexciton channel is only achieved at high laser excitation powers[2]. McCreary et al. have demonstrated the enhanced trion emission in transferred 1L-WS_2 samples with an increase in the power of laser excitation[3]. Here, we have constructed a quantum well by encapsulation of the 1L-WS_2 by a higher bandgap ZnO in a sandwich structure. Charge transfer takes place from ZnO to the 1L-WS_2 under photoexcitation. Thus, even though the signature of biexcitons is rarely observed at room temperature[4], the lack of dielectric screening and quantum confinement in the QW system aids in a high exciton density[1]. As such we have been successfully able to observe rich PL characteristics in the QW system, discussed below in detail.

6.2. Experimental details

6.2.1. Growth of ZnO Thin film

The ZnO thin film was grown via a physical deposition/growth process. Firstly, the film was deposited on various substrates, such as SiO_2 and quartz, using the RF magnetron sputtering technique. A high-purity ZnO sputter target (99.99%) of 2-inch diameter was used for the process. The RF power was set at 60 W and the deposition was carried out for 1.5 h in an Ar gas atmosphere at a chamber pressure of 0.1 mbar. The substrate holder was kept on rotation mode for a uniform deposition which resulted in the growth of ZnO thin films of thickness ~5 nm, on various substrates.

6.2.2. Growth of 1L-WS_2 and Formation of ZnO/WS_2/ZnO heterostructure

Monolayer WS_2 films were grown on various substrates (sapphire, SiO_2, quartz) by a NaCl-assisted CVD process using a 2-inch quartz tube-based two-zone muffle furnace, as mentioned in **Chapter 2**. 10 mg of WO_3 powder is placed in a quartz boat towards the closed end of the inner quartz tube, ensuring that it lies in the center of heating zone 2. The temperature of zone 2 is ramped up to 940 °C. At the upstream zone, i.e., zone 1, 150 mg of S is kept in another quartz boat. During growth, the temperature at the S boat is maintained at 150 °C, which is a requisite for optimum growth of 1L-WS_2. The growth procedure is described in detail in **Chapter 2 (Section 2.4).** The morphology, chemical composition and crystal structure are studied via TEM, AFM, XPS, and micro-Raman analyses. The 1L-WS_2 is then transferred onto the RF sputtered ZnO film by the standard PMMA-aided transfer procedure. Subsequently, another layer of ZnO film is deposited directly onto the 1L-WS_2 via RF sputtering to fabricate a QW-like encapsulated ZnO/WS_2/ZnO heterostructure. **Table 1** mentions the sample codes used in the chapter.

Table 1: Summary of the sample codes used in the chapter.

Sample code	Sample description
as-WS_2-SiO_2	CVD-grown 1L-WS_2 on SiO_2
as-WS_2-Sap	CVD-grown 1L-WS_2 on sapphire
t-WS_2	Transferred 1L-WS_2 on SiO_2
ZnO/WS_2/ZnO	1L-WS_2 sandwiched between ZnO thin films to form a quantum well structure

6.2.3. Characterization techniques

The details of the AFM, micro-Raman, micro-PL, and XPS measurements have been discussed in **Chapter 2 (Section 2.4.3)**. The morphology and structural properties of the CVD-grown 1L-WS_2 have been studied using a transmission electron microscope. The morphology of the ZnO film is studied using FESEM. X-ray diffraction (XRD) pattern for the ZnO thin film was collected to determine its crystalline quality (Rigaku RINT 2500 TTRAX-III, Cu kα radiation). UV-Vis-NIR absorbance spectroscopy measurements of the HS as well as its counterparts were recorded using a commercial spectrophotometer (PerkinElmer, UV win Lab). The details have been discussed in **Chapter 5 (Section 5.2.3).** Kelvin Probe Force Microscopy (KPFM) measurements were carried out for the 1L-WS_2 and the HS to estimate the work function.

6.3. Results and discussion

6.3.1. Morphology studies

The morphology of the 1L-WS_2 and the ZnO/WS_2/ZnO QW is first studied using an optical microscope. **Fig. 6.1(a)** depicts a single 1L-WS_2 triangular flake of the order of ~40 μm grown on an SiO_2 substrate. For comparison, the OM image of the ZnO/WS_2/ZnO is displayed in **Fig. 6.1(b)**. For clarity, the triangular 1L-WS_2 flakes of dimensions in the range ~ 10-50 μm are marked with white dashed lines.

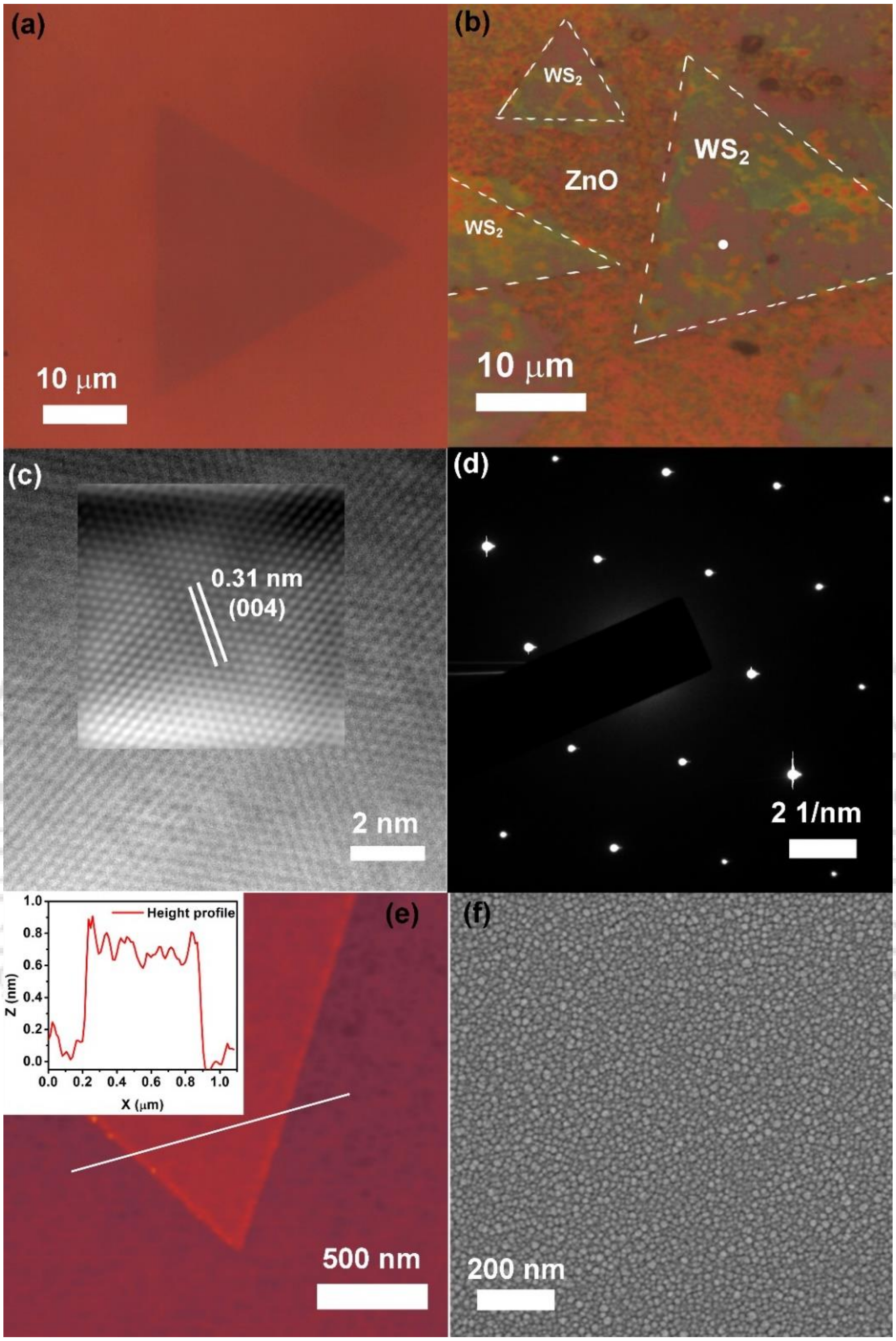

Fig. 6.1.: Optical microscopy images of (a) WS_2 monolayer and (b) $ZnO/WS_2/ZnO$ HS. (c) High-resolution-TEM image of 1L-WS_2. Inset depicts the corresponding IFFT showing a d-spacing of 0.31 nm. (d) The SAED pattern of the WS_2. (e) AFM image of 1L-WS_2 on SiO_2. (c) The height profile along the blue line. The inset shows the height profile along the white line. (f) FESEM image of the RF sputtered ZnO film.

High-resolution-TEM imaging of the CVD grown 1L-WS_2 was carried out (see **Fig. 6.1(c)**), which shows the high crystallinity in the sample. Further image processing (inset) reveals the presence of the (004) planes of WS_2 that correspond to a lattice spacing of 0.31 nm. The same is reflected in the electron diffraction pattern, in **Fig. 6.1(d)**, which confirms good overall crystalline quality. AFM is carried out to verify that the film has monolayer thickness (**Fig. 6.1(e)**). The inset depicts the height profile of the WS_2 layer along the white line. **Fig. 6.1(f)** shows the FESEM image of the RF sputtered ZnO thin film. The film consists of closely spaced uniform nano-islands of ZnO. Thus, we consider a uniform ZnO film growth achieved via RF sputtering.

6.3.2. Compositional and structural analysis

6.3.2.1. XPS Analysis

Fig. 6.2 displays the high-resolution XPS spectra of W 4f for the CVD grown 1L-WS_2. The peaks at 32.0 eV and 34.1 eV are ascribed to the W^{4+} state of W $4f_{7/2}$ and W $4f_{5/2}$, respectively, which confirm the formation of 2H-WS_2 (**Fig. 6.2(a)**). In addition, the presence of the metallic 1T-phase of WS_2 is affirmed by the presence of the peaks at 31.1 eV and 33.1 eV[5-6]. The appearance of the small shoulder peak at 35.2 eV is attributed to the W^{6+} state of the unreacted WO_3. The S 2p core-level spectrum of the 1L-WS_2 is depicted in **Fig. 6.2(b).** The S envelope has been fitted following Gaussian deconvolution – the peaks at 162.2 eV and 163.4 eV correspond to the S^{2-} states, S $2p_{3/2}$ and S $2p_{1/2}$, respectively[5, 7]. The as-grown 1L-WS_2 film consists of S vacancies confirmed by the peaks at lower binding energies 161.2 eV and 162.7 eV[8]. **Fig. 6.2(c)** displays the W 4f core level spectrum corresponding to the HS ZnO/WS_2/ZnO which shows the presence of all the characteristic peaks, mentioned earlier. However, there is a pronounced blueshift in the W $4f_{7/2}$ and W $4f_{5/2}$ peaks by 2.5 eV. This could be a clear indication of the transfer of electrons from ZnO film to the 1L-WS_2, leading to a shift in the Fermi level of the WS_2 towards the conduction band[9-10]. Similarly, the S 2p spectrum of the ZnO/WS_2/ZnO QW exhibits the signature of all the characteristic peaks (**Fig. 6.2(d)**). However, the spectral weight corresponding to S vacancies increases from 31.8% in the as-grown 1L-WS_2 to 41.5% in ZnO/WS_2/ZnO. This may be due to the transfer process of the 1L-WS_2 film onto ZnO to fabricate the QW. No pronounced shift in peak position is observed. **Fig. 6.2(e)** shows the Zn 2p core-level spectrum for the RF sputtered ZnO film consisting of the characteristic peaks 1020.9 eV (Zn $2p_{3/2}$) and 1043.9 eV (Zn $2p_{1/2}$). The inset displays a redshifted spectrum of the ZnO/WS_2/ZnO QW indicating electron transfer from the ZnO film to 1L-WS_2. **Fig. 6.2(f)** presents the Gaussian deconvoluted spectrum corresponding to O 1s of the ZnO film. The peaks at binding energies 528.4 eV and 531.0 eV are ascribed to the lattice oxygen and oxygen vacancies in the as-grown sample[11]. The downshift of these peaks in the HS (inset) further supports the assertion of the charge-transfer aided shift in the Fermi level away from the conduction band for ZnO.

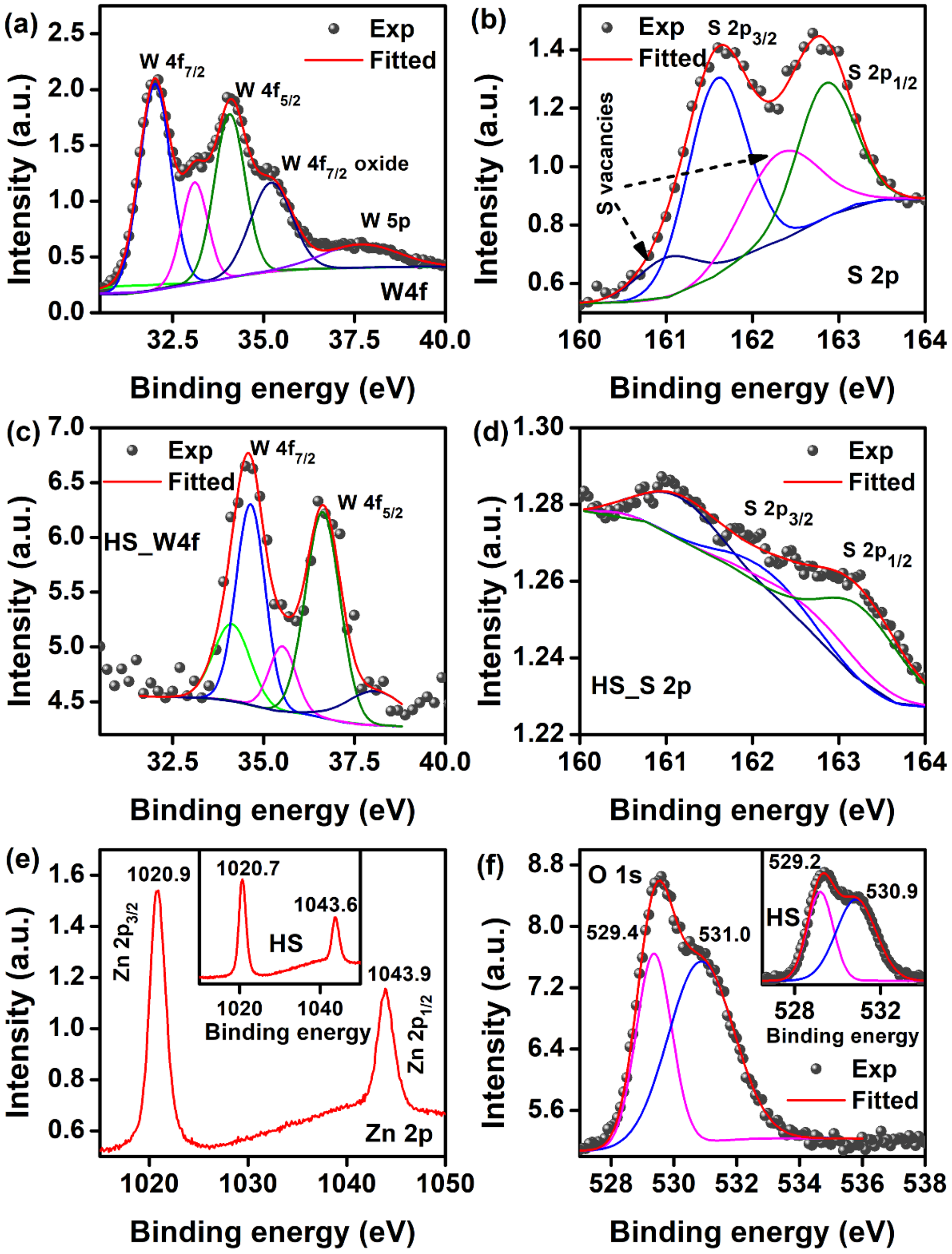

Fig. 6.2. High-resolution XPS spectra corresponding to (a) W 4f and (b) S 2p of the CVD grown 1L-WS_2. High-resolution XPS spectra corresponding to (c) W 4f and (d) S 2p of the ZnO/WS_2 HS. High-resolution XPS spectra of (e) Zn 2p and (f) O 1s of the sputtered ZnO film. Insets show the respective spectra for Zn 2p and O 1s corresponding to the ZnO/WS_2.

6.3.2.2. XRD and Raman Analysis

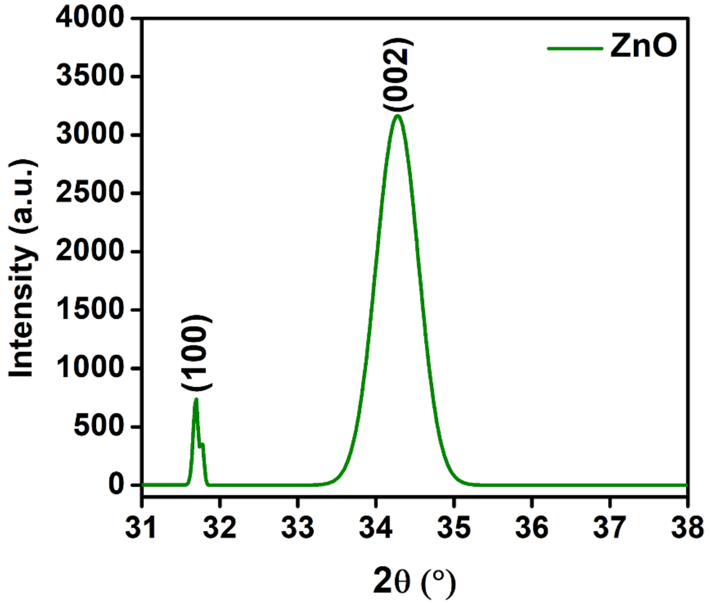

Fig. 6.3. XRD pattern of the RF-sputtered ZnO thin film.

The XRD pattern of the ZnO thin film is displayed in **Fig. 6.3.** The diffraction peaks at 31.7° and 34.3° correspond to the (100) and (002) lattice planes of the hexagonal wurtzite crystal phase of the as-synthesized ZnO thin film[12].

Micro-Raman measurement was carried out on different 1L-WS_2 samples (as-WS_2-SiO_2, as-WS_2-Sap, and t-WS_2) and the ZnO/1L-WS_2/ZnO QW. The laser excitation of 488 nm was used and for comparison, the spectra are presented in a stacked plot in **Fig. 6.4(a)**. The characteristic optical Raman modes E_{2g} and A_{1g} appear at 356.5 cm^{-1} and 418.3 cm^{-1}, respectively, for as-WS_2-SiO_2. Sapphire presents itself as a strain-free system for CVD grown 1L-WS_2, as discussed in **Chapter 2, Section 2.4.4**. Thus, the E_{2g} mode in as-WS_2-Sap exhibits a redshift to 357.7 cm^{-1}, while the A_{1g} mode almost remains unaltered. The release of strain in a transferred 1L-WS_2 film, with respect to as-grown 1L-WS_2, is further confirmed by the stiffening of the E_{2g} mode for t-WS_2. One might argue the doping effect that may be induced by PMMA that has been used as a transfer agent. However, utmost care has been taken to remove its traces from the transferred samples, in order to minimize any chances of electron transfer from PMMA to the WS_2. Thus, no shift in the A_{1g} mode is observed in t-WS_2 with respect to as-WS_2-SiO_2. In the Raman spectrum corresponding to ZnO/WS_2/ZnO, the A_{1g} mode softens. For better understanding, we carry out Lorentzian deconvolution of the spectra of t-WS_2 and ZnO/WS_2/ZnO. The deconvoluted Raman spectra for t-WS_2 film and ZnO/1L-WS_2/ZnO QW are stacked in a vertical plot in **Fig. 6.4(b)**. For t-WS_2, the characteristic E_{2g} and A_{1g} modes appear at 357.2 cm^{-1} and 418.6 cm^{-1}, respectively. The frequency difference Δk amounts to 61.4 cm^{-1}, which is characteristic of 1L-WS_2. However, for the ZnO/1L-WS_2/ZnO QW, the in-plane E_{2g} mode exhibits a slight redshift to 356.8 cm^{-1}, indicative of an induced strain in the system.

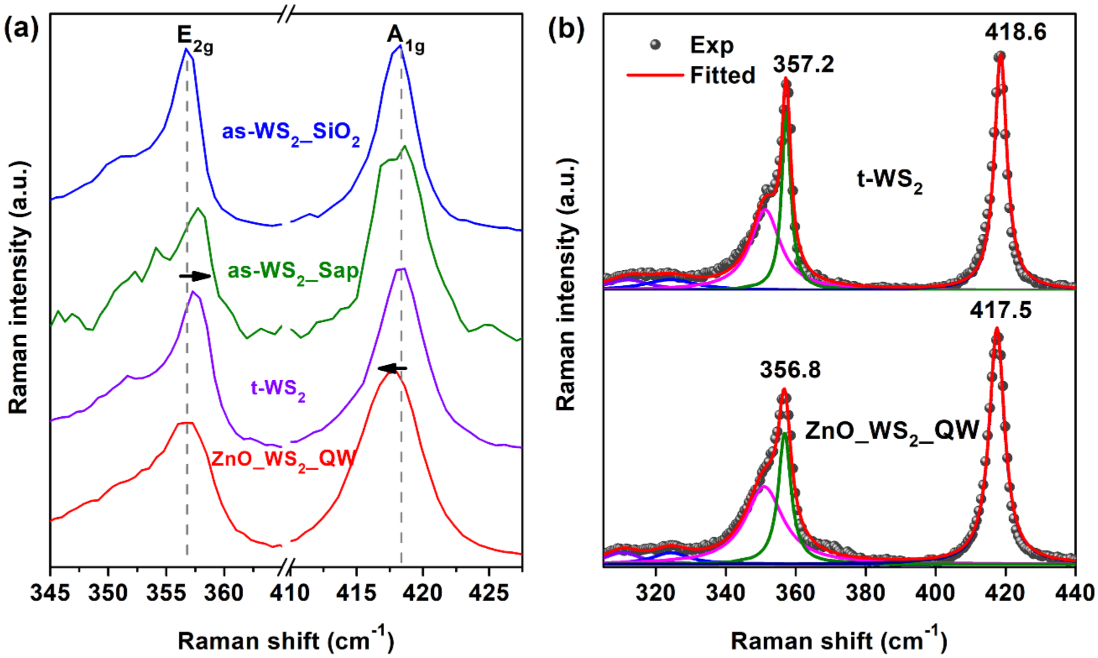

Fig. 6.4. (a) Comparative micro-Raman spectra corresponding to CVD grown 1L-WS_2 on SiO_2, Sapphire, transferred 1L-WS_2 film (on SiO_2), and ZnO/1L-WS_2/ZnO. (b) Deconvoluted Raman spectra for 1L-WS_2 film (on SiO_2) and ZnO/1L-WS_2/ZnO QW structure. The excitation wavelength used is 488 nm.

Likewise, the A_{1g} mode downshifts to 417.5 cm^{-1}. Since the out-of-plane A_{1g} mode is highly sensitive to doping, this redshift implies there is a transfer of electrons from ZnO to WS_2, making it more n-type doped. This hypothesis is further backed by the increase in the FWHM of the A_{1g} mode from 4.5 cm^{-1} in pristine t-WS_2 to 5.3 cm^{-1} in the HS[13]. Along with these optical modes of WS_2, another peak at ~353 cm^{-1} is assigned 2LA mode, i.e., the second-order longitudinal acoustic mode of WS_2[14-15].

6.3.3. Optical analysis of as-grown and transferred 1L-WS_2

The absorption characteristics or the Kubelka-Munk function (F(R)) of the CVD grown 1L-WS_2 is plotted in **Fig. 6.5(a)**. The characteristic B (514 nm) and A (622 nm) excitons arising from the splitting (~419 meV) of the valence band of 1L-WS_2 at the K point of the Brillouin zone are apparent in the spectrum. Furthermore, we compare the PL emission spectra of as-grown and transferred samples of 1L-WS_2, in this section.

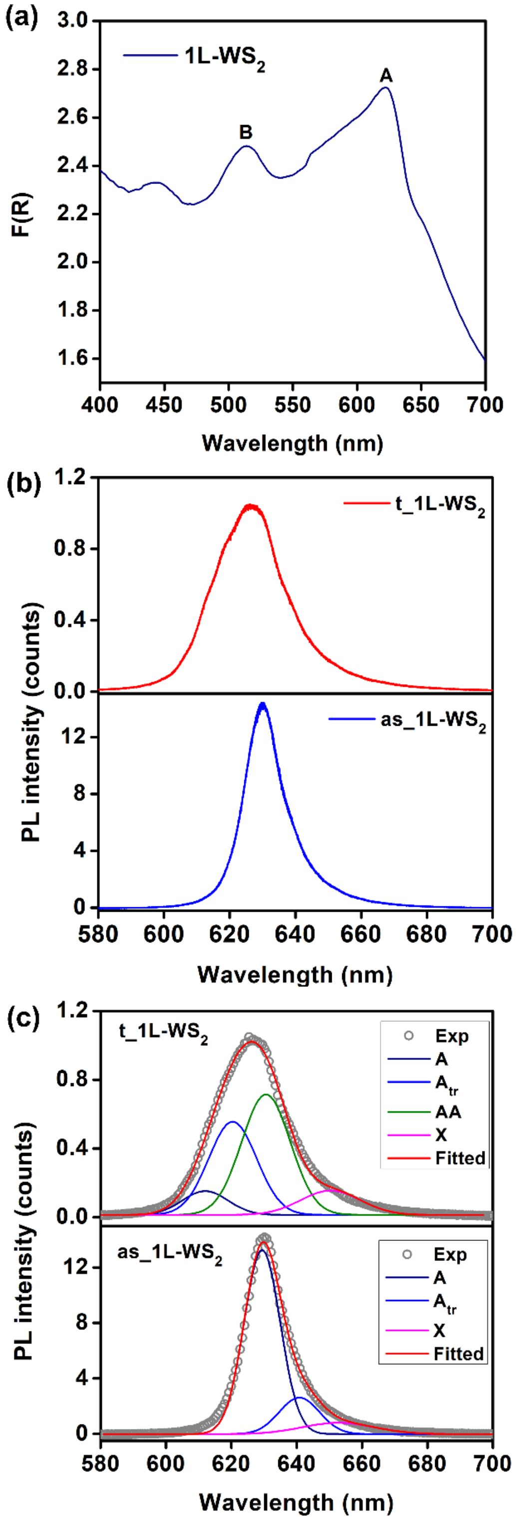

Fig. 6.5. (a) Kubelka Munk function plot of 1L-WS$_2$. (b) Comparative PL spectra of the transferred 1L-WS$_2$ on SiO$_2$ and CVD grown 1L-WS$_2$ on SiO$_2$. (c) Deconvoluted PL spectra of the transferred 1L-WS$_2$ and CVD grown 1L-WS$_2$ on SiO$_2$ substrates.

Fig. 6.5(b) displays a stacked plot of the micro-PL spectra of t-WS_2 and as-WS_2-SiO_2 that were acquired using a 488 nm laser excitation. The as-WS_2 exhibits a sharp PL emission peak, whereas the t-WS_2 shows a broad PL spectrum that is slightly blue-shifted, with respect to the former. Note that the laser power used is ~42 µW. It has been well established that an increase in the incident laser intensity can cause an enhancement in the trion as well as biexciton emission in WS_2[3, 16]. The emission intensity decreases here implying a transition from neutral exciton to trion-dominated emission in the t-1L-WS_2. The apparent blue shift is mainly due to the release/absence of the uniaxial strain. We have deconvoluted the PL spectra and presented them in a stacked plot for comparison (**Fig. 6.5(c)**). The sharp PL of the as-WS_2 is attributed to the dominating A_0 emission (at ~629.4 nm), as evident from the fitted peaks. The Gaussian peaks corresponding to A_{tr} and X emissions constitute only ~25.5% of the spectra. On the contrary, for t-WS_2, we have carried out deconvolution into 4 Gaussian peaks- A_0 emission (~612 nm), A_{tr} (~620.4 nm), an additional peak associated with the biexciton AA (~630.6 nm), and the defect exciton X (~650.4 nm). The A_0 peak exhibits a pronounced blue shift of ~56 meV. Such a variation between as-grown and transferred 1L-WS_2 is comparable with earlier reports and is argued to be due to the removal of tensile strain during the transfer process. The presence of tensile strain reduces the band gap, which leads to a red shift in the PL peak. The strain present in the as-WS_2 is quantifiable from the shift in the A_0 peak and is estimated to be ~0.28% for the shift of ~ 56 meV[3, 17]. Biexcitons are quasi-states of a pair of excitons. Additionally, the A_0 peak accounts for barely ~8% of the spectra in the t-1L-WS_2, while the A_{tr} and the AA emissions constitute ~34.7% and ~45.6%, respectively. The shift of the spectral weight from the neutral to charged exciton with the transfer can be attributed to the difference in the adsorption/desorption of ambient oxygen[3, 18]. To explore the emission from the quasiparticles of the 1L-WS_2, we have constructed a quantum well structure and studied the power and temperature-dependent PL emission characteristics, in the next section. To eliminate the effect of strain, we have used only t-1L-WS_2 for comparison with the quantum well.

6.3.4. Photoluminescence tuning and Quantum Well effect

Fig. 6.6(a) displays the comparative UV-Vis absorbance spectra of the ZnO and the ZnO/1L-WS_2 on quartz substrates. The spectrum corresponding to the HS exhibits a small absorption peak at 635 nm, which corresponds to the 1L-WS_2, however, the peak exhibits a redshift. The shift can be attributed to the charge transfer from the ZnO to the WS_2[19]. The ZnO thin film has an optical band gap of 3.2 eV, as estimated from the Tauc plot (see inset), while the 1L-WS_2 has a band gap of 2 eV. We study the power-dependent PL emission characteristics of the ZnO/1L-WS_2/ZnO QW and compare them with the PL spectra of the t-1L-WS_2, in this section. **Fig. 6.6(b-d)** display the comparative PL spectra at powers 7.5, 80.1, and 250 µW, respectively. At the lowest power, P=7.5 µW, the QW exhibits almost ~6-fold enhancement in the PL intensity with an apparent blue shift of the peak. Additionally, the PL line shape visibly changes with respect to 1L-WS_2, which may be ascribed to interfacial defects in the QW. With the increase in the laser excitation power, the enhancement of PL becomes less apparent. At 250 µW, the blue shift can be clearly observed, however, the PL emission from the QW is only about ~1.2 times that of the 1L-WS_2. Thus, the emission features of the QW require further careful examination.

We have carried out Gaussian deconvolution of the PL spectra of 1L-WS_2 and ZnO/WS_2/ZnO QW. The emission spectrum of 1L-WS_2 consists of 4 Gaussian peaks- A_0 exciton, A_{tr} trion, AA biexciton, and X defect bound exciton, whereas the QW spectrum contains an additional X′ interfacial defect state. **Fig. 6.6(e)** shows the stacked plot of the fitted spectra for P=7.5 µW. The intensity of the A_0 exciton thus is amplified ~10 times in the QW, with an increase in the spectral weight from 16.6% to 45.1%. The A_{tr} emission dominated the PL emission of the transferred 1L-WS_2 with 46.7% weight, closely followed by the AA emission at ~26.3%. As we have seen in the previous section that the transferred 1L-WS_2 exhibits a different emission behavior compared to the as-grown film under similar excitation conditions. Thus, the transferred 1L-WS_2 is established to be more n-type resulting in large trionic emission. However, as the 1L-WS_2 is encapsulated with ZnO thin films, the electron transfer is accompanied by the hole transfer leading to pronounced exciton recombination and thus, causing a distinct enhancement in the overall PL intensity. This is the Quantum well effect on the carrier recombination in the system. The ~10-fold enhancement is attributed to the fact that at low excitation powers, the PL of t-1L-WS_2 is dominated by trions, which are known to produce lower intensity PL, given the dominated non-radiative recombination mechanisms[3, 20]. Nevertheless, as the laser excitation power is increased to 250 µW (**Fig. 6.6(f)**), the PL spectra of the t-1L-WS_2 become more dominated by the biexciton, AA. The biexciton-dominated emission is due to surplus exciton density in the system, at high incident powers, and the superior quality of the sample, i.e., lesser number of trap centers[21].

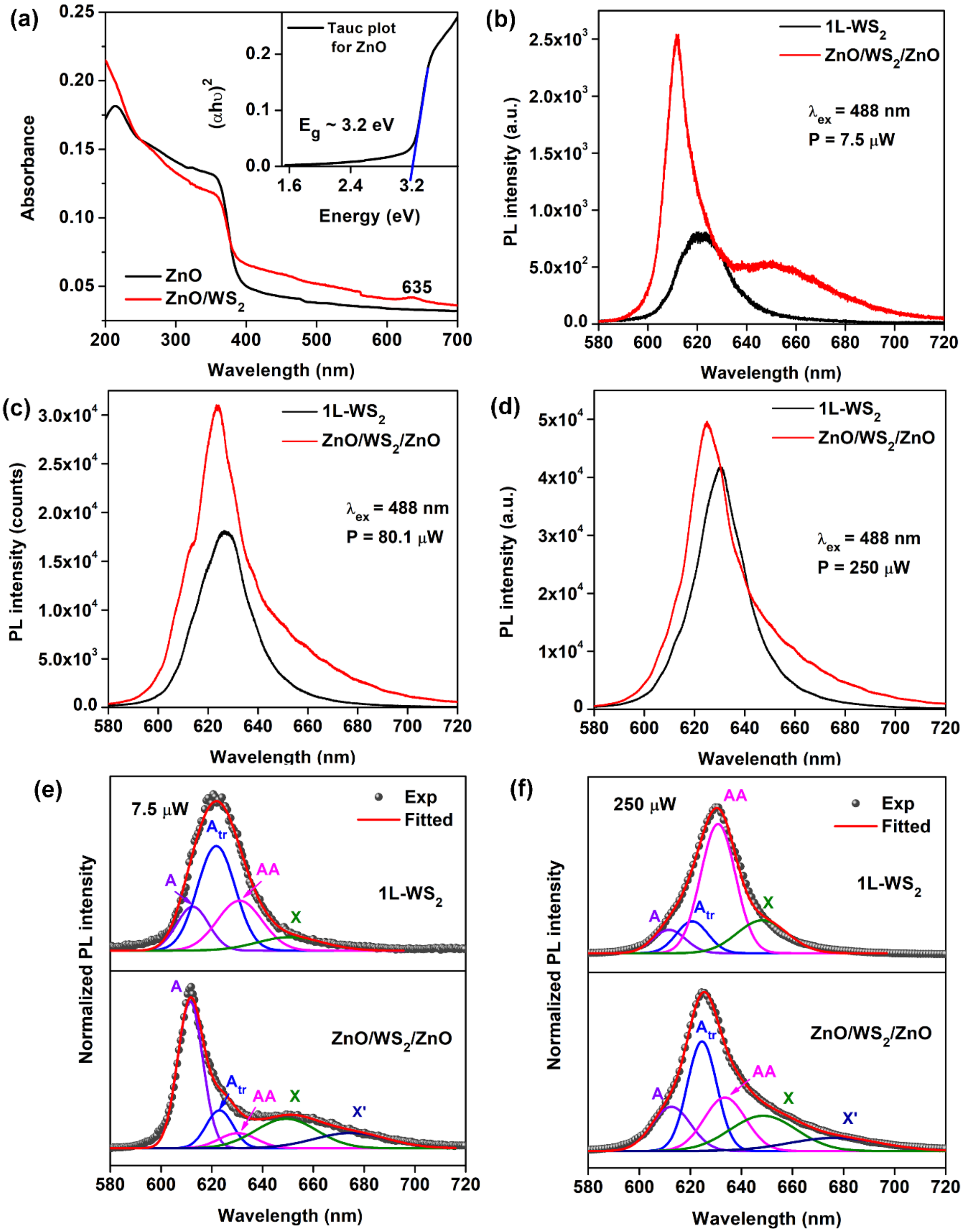

Fig. 6.6. (a) UV-Visible absorption spectra of ZnO film and ZnO/WS$_2$ HS. Inset shows the Tauc plot for the ZnO thin film. Comparative PL spectra of the transferred 1L-WS$_2$ on SiO$_2$ and ZnO/WS$_2$/ZnO QW at an excitation of 488 nm and incident powers: (b) 7.5 μW, (c) 80.1 μW, and (d) 250 μW. Comparative deconvoluted PL spectra of transferred 1L-WS$_2$ and ZnO/WS$_2$/ZnO QW at incident powers: (e) 7.5 μW and (f) 250 μW.

However, with the construction of the QW, the electron transfer from the ZnO leads to the conversion of the excitons to trions. As a result, the enhancement of the PL intensity is limited. The fitting parameters for the spectra of 1L-WS_2 and ZnO/WS_2/ZnO are presented in **Table 2**.

Table 2: PL fitting parameters for 1L-WS_2 and ZnO/WS_2/ZnO for the powers 7.5 µW and 250 µW.

Laser Power	**Sample**	**A_0**		**A_{tr}**		**AA**		**X**		**X´**	
		Peak (nm)	Weight (%)	Peak (nm)	Weight (%)	Peak (nm)	Weight (%)	Peak (nm)	Weight (%)	Peak (nm)	Weight (%)
7.5 µW	1L-WS_2	612.5	16.6	621.8	46.7	631	26.3	650.8	10.4	-	-
	ZnO/WS_2/ ZnO	611.5	45.1	623.1	12.3	630.2	6.9	649.3	22.0	674.7	13.7
250 µW	1L-WS_2	611.7	9.7	620.7	12.6	630.8	56.7	648.1	21.0	-	-
	ZnO/WS_2/ ZnO	612.6	16.0	624.6	30.3	633.5	20.7	648.5	21.8	676.6	11.2

To discern the effect of the incident power on the emission characteristics of the QW, **Fig. 6.7(a)** displays the comparative PL spectra of the ZnO/WS_2/ZnO HS at two laser excitation powers 7.5 µW and 250 µW.

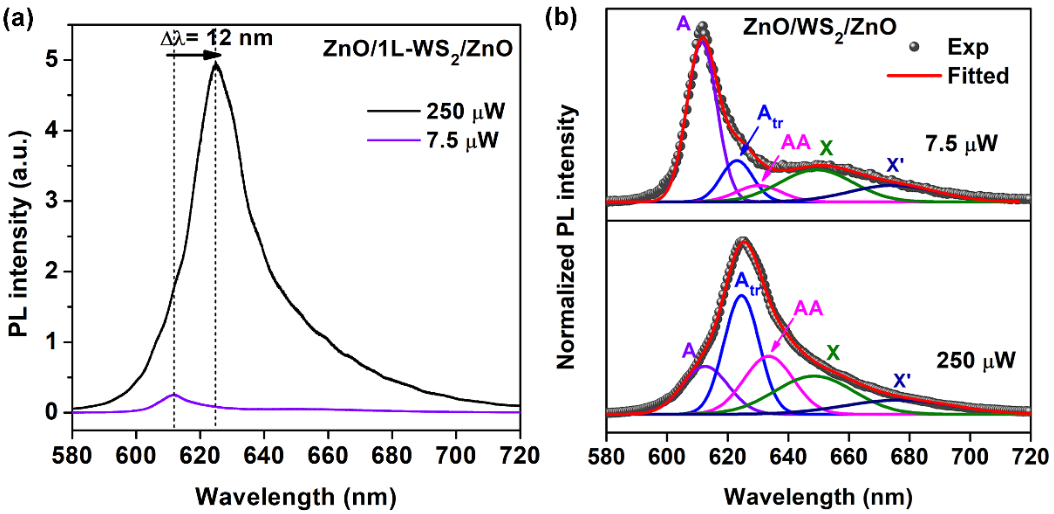

Fig. 6.7. (a) Comparative PL spectra of ZnO/WS_2/ZnO QW at incident powers 7.5 µW and 250 µW. (b) Deconvoluted PL spectra of ZnO/WS_2/ZnO QW at incident powers 7.5 µW and 250 µW.

Note that owing to the increase in the incident laser power, there is a ~20-fold PL enhancement. However, this enhancement is accompanied by a spectral red shift of Δλ ~ 12 nm. It has been well established that increased intensity of the incident laser induces emission from multibody quasi-states such as trions and biexcitons. The fitted spectra are presented in a stacked plot in **Fig. 6.7(b)**. The positions of the peak remain mostly unchanged irrespective of the incident power. However, at the low excitation power, 7.5 µW, the spectrum is dominated by the excitonic emission at a spectra weight of ~ 45.1 %. There is a shift of spectral weight from A_0 to A_{tr} as well as AA, with the increase in the laser power. The electron transfer from ZnO to 1L-WS_2 is accompanied by an increased exciton density at higher power. This explains the modulation along with the redshift in the PL spectra.

Fig. 6.8(a, b) depict the variation of the integrated intensities of A_0, A_{tr}, and AA with respect to the incident laser power. The plots are double logarithmic. The PL intensities are then fitted with respect to the power-law using the equation, $I \propto P^m$. In the case of the 1L-WS_2, the A_0 and A_{tr} show an almost linear behavior with *m*~1 and 0.8, respectively, which is anticipated for transitions related to excitonic, trionic states[22-23]. The AA emission peak, on the contrary, exhibits a super-linear behavior, with *m*~1.4. Ideally, the slope, *m* is expected to be ~2, at thermal equilibrium[22]. The super-linear nature of the increase in the PL intensity is a signature of biexciton emission. However, the kinetics of the biexciton formation in the system and lack of thermal equilibrium lead to *m* being in the range of 1.2-1.9[1, 21-22, 24]. A similar trend is observed in the case of the QW, ZnO/WS_2/ZnO, although the slope *m* for the AA emission is reduced to ~1.2, which can be attributed to the increased defect trap centers in the system[22]. The super-linearity of the trion emission is ascribed to the loss of carrier population from the trion state to localized defect states[25]. **Fig. 6.8(c, d)** display the variation of the biexciton integrated intensity with respect to the exciton integrated intensity. The almost quadratic relationship (*m*~1.4 and 1.7 for 1L-WS_2 and the QW, respectively) strongly supports our assignment of biexcitons[25-27]. Additionally, we have plotted the peak positions of the neutral excitons, trions, and biexcitons with respect to the incident laser power for the 1L-WS_2 and the QW (see **Fig. 6.8(e, f)**). On average, the peaks corresponding to A_0 (~612 nm), A_{tr} (~621 nm), and AA (~631 nm) exhibit negligible spectral shifts with the variation of power in the range of ~7.5 – 250 µW. The average trion binding energy is, thus, about ~30 meV and likewise, the estimated biexciton binding energy is ~60 meV, which agree well with literature[3, 22]. The Haynes factor, which is the ratio of the biexciton binding energy to the exciton binding energy (E_b), is in the order of ~ 0.09, assuming the E_b ~ 700 meV, as estimated in **Chapter 5**. The estimated Haynes factor falls in the range consistent with quantum-well systems and monolayer TMDs, in general[21-22, 25].

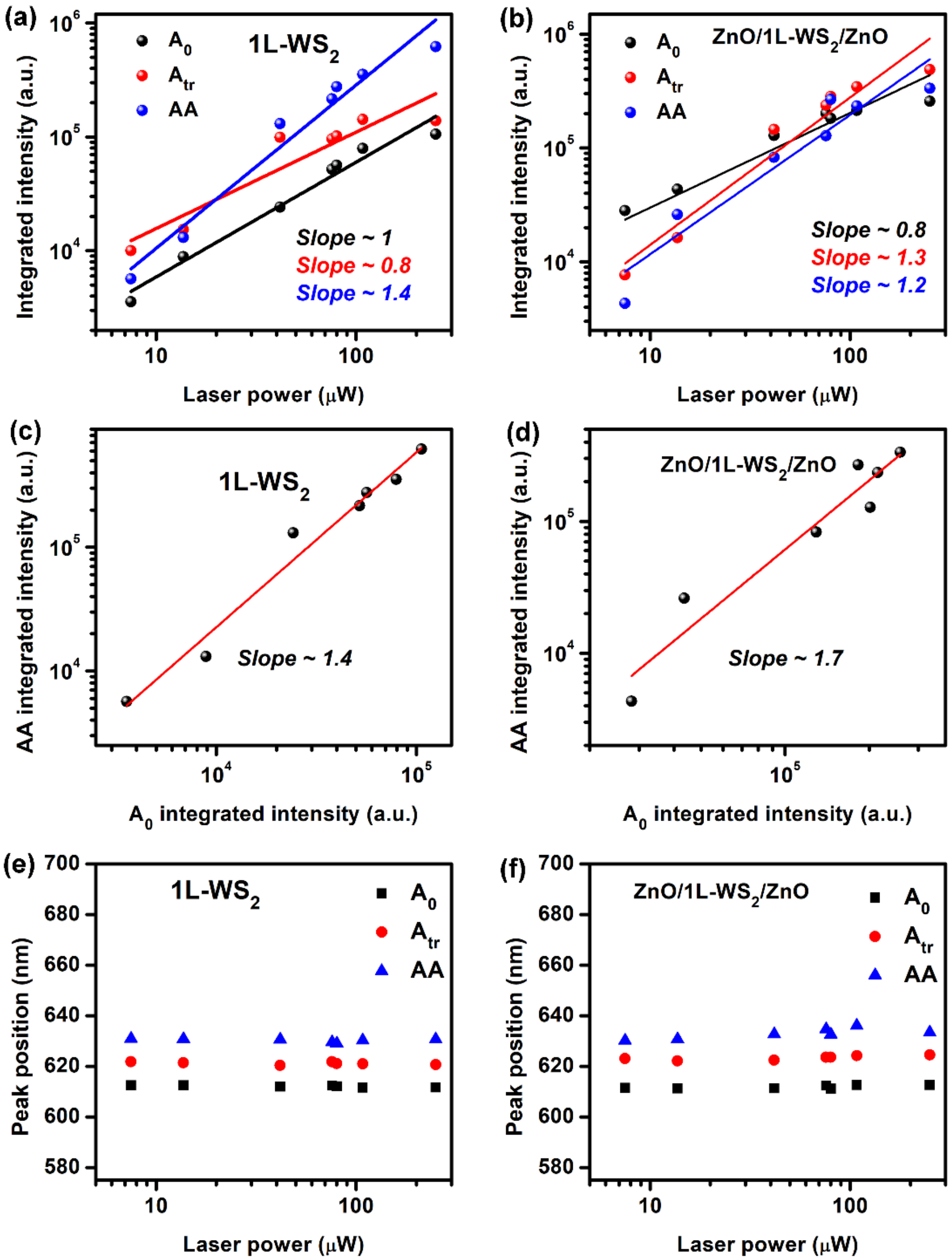

Fig. 6.8. The integrated intensities of deconvoluted PL peaks of neutral excitons (A_0), trions (A_{tr}), and biexcitons (AA) as a function of excitation laser power for (a) 1L-WS_2 and (b) $ZnO/WS_2/ZnO$. The biexciton integrated intensity (AA) as a function of the exciton integrated intensity (A_0) for (c) 1L-WS_2 and (d) $ZnO/WS_2/ZnO$. Peak positions of neutral excitons (A_0), trions (A_{tr}), and biexcitons (AA) for (e) 1L-WS_2 and (f) $ZnO/WS_2/ZnO$. All the plots are logarithmic.

6.3.5. Temperature-dependent PL study

To further explore the excitonic states in 1L-WS_2 and the QW, we acquired the temperature-dependent PL spectra. **Fig. 6.9(a, b)** display the temperature dependence of the PL emission spectra corresponding to as-1L-WS_2 and the ZnO/WS_2/ZnO, respectively.

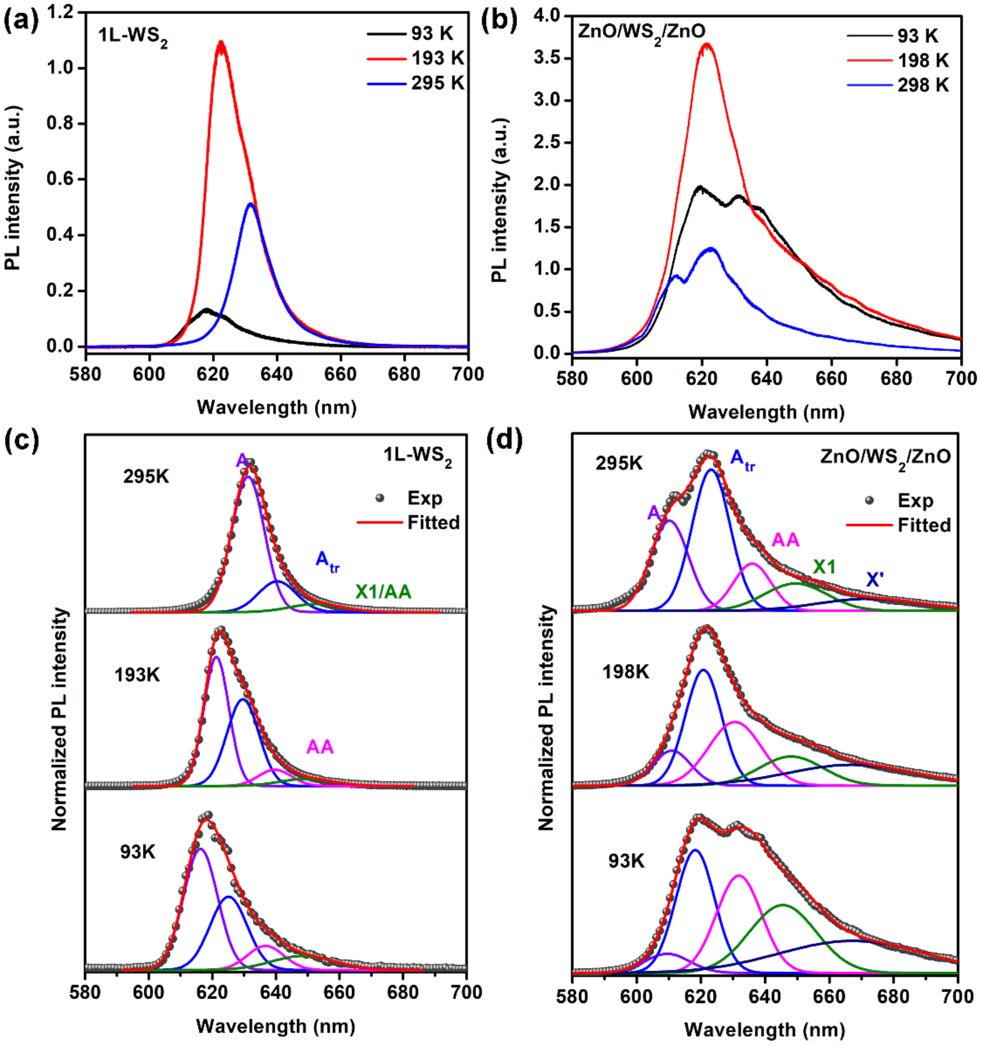

Fig. 6.9. Temperature-dependent PL emission spectra of (a) as-grown 1L-WS_2 and (b) ZnO/WS_2/ZnO QW. Stacked deconvoluted PL spectra of (c) as-grown 1L-WS_2 and (d) ZnO/WS_2/ZnO QW at temperatures 93 K- 295 K.

For 1L-WS_2, as shown in **Fig. 6.9(a)**, the PL emission first increases ~2-folds with the decrease of the temperature from 295 K to 193 K, accompanied by a blue shift. However, this increase is not monotonic and with a further decrease in the temperature to 93K, the PL intensity is reduced. In the case of the ZnO/WS_2/ZnO (**Fig. 6.9(b)**), the PL emission is almost 3 times enhanced with a decrease in the temperature from 295 K to 198 K, whereas the PL is quenched with further cooling to 93 K. The reduction of the PL intensity of 1L-WS_2 at temperatures lower than ~200 K is ascribed to the presence of the spin-forbidden “dark” excitonic state, arising from the strong spin-orbit coupling[26]. The spin allowed “bright” exciton recombines radiatively leading to emission, which increases with the lowering of temperature. On the contrary, the formation of the dark excitonic state causes the overall reduction of PL emission at low temperatures[23, 26]. It is to be noted that the PL line shapes vary significantly with temperature in the ZnO/WS_2/ZnO system, compared to the 1L-WS_2. We have deconvoluted the spectra to understand the variation of the excitonic features with temperature. The parameters of deconvolution are tabulated (see **Table 3**).

Table 3: Temperature-dependent PL fitting parameters for as-1L-WS_2 and ZnO/WS_2/ZnO.

Sample	**Temperature (K)**	**A_0**		**A_{tr}**		**AA**		**X**		**X´**	
		Peak (nm)	Weight (%)	Peak (nm)	Weight (%)	Peak (nm)	Weight (%)	Peak (nm)	Weight (%)	Peak (nm)	Weight (%)
1L-WS_2	295	631.2	73.5	640.4	19.4	-	-	652.7	7.1	-	-
	193	621.3	46.6	629.6	39.9	639.7	7.8	649.8	5.7	-	-
	93	616.3	48.0	625.1	31.4	636.7	10.2	648.6	10.4	-	-
ZnO/WS_2/ ZnO	295	610.2	25.3	623.2	39.8	636	13.1	649.5	12.8	672.7	9.0
	198	611.0	9.9	620.8	31.7	630.6	25.3	648.1	14.0	667.0	19.1
	93	609.5	4.6	618.2	25.1	631.8	23.3	645.5	24.0	667.1	23.1

When the ambient temperature of measurement changes from 295 K to 93 K, the A_0 of the 1L-WS_2 exhibits a blue shift of ~47.5 meV. The biexciton emission is absent in the as-grown 1L-WS_2 at room temperature. There is a clear increase in its spectral weight with a lowering of the temperature, which is expected (**Fig. 6.9(c)**). The combined spectral weight of A_0 and A_{tr} decreases with temperature, from ~92.9% at 295 K to ~86.5% at 193 K, finally to 79.4% at 93 K. We observe that the spectral features of the ZnO/WS_2/ZnO are in stark contrast to those of the as-grown 1L-WS_2 (see **Fig. 6.9(d)**). There is a gradual reduction in the spectral weight from ~25.3% to ~4.6%, as we go from room temperature to 93 K. Simultaneously, the biexciton spectral weight boosts up by ~10%. However, the interesting feature is the lack of any apparent blue shift in the excitonic emission peak with the lowering of the temperature, which has been observed by Lee et.al in their QW system[28]. Such different temperature-dependent excitonic properties in the systems can be argued to be owing to the difference in the dielectric screening by the surrounding environments in the transferred 1L-WS_2 and the ZnO/WS_2/ZnO[29-30].

6.3.6. Mechanism of Photoluminescence Modulation

Fig. 6.10(a, b) depict the KPFM potential profiles of the 1L-WS_2 and the ZnO thin films. As discussed in **Chapter 5, Section 5.3.4**, the work function of the tip used (Φ_t) is ~ 4.992 eV.

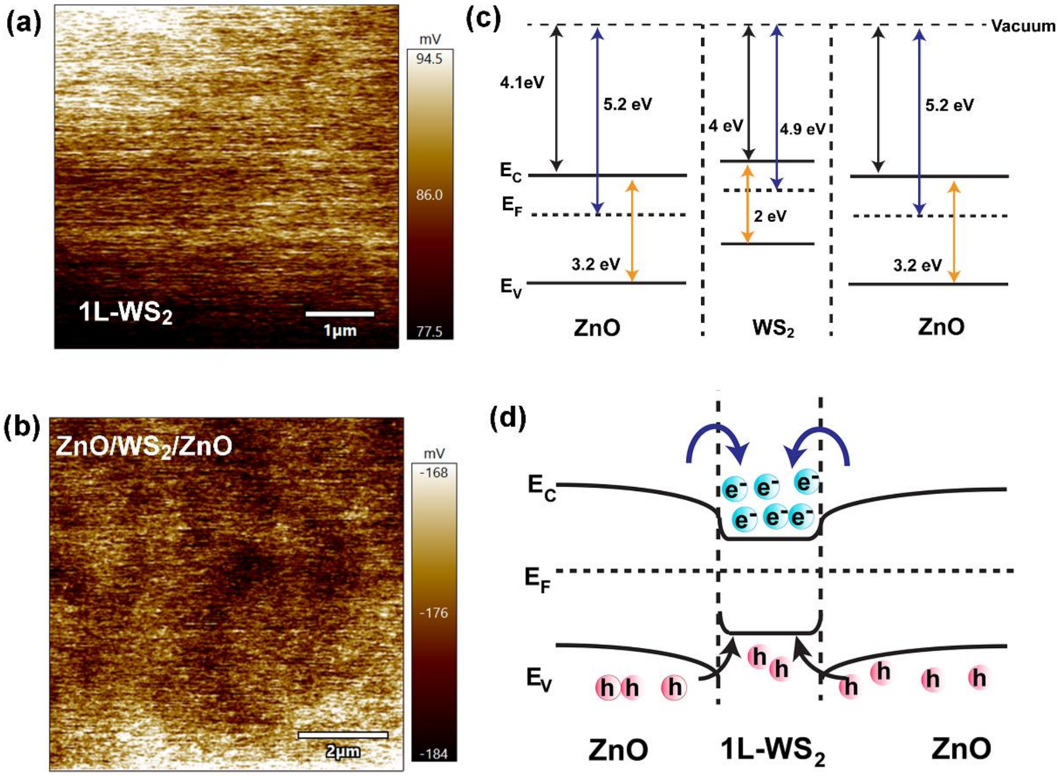

Fig. 6.10. KPFM potential profiles of (a) 1L-WS_2 and (b) ZnO films. (c) Schematic energy band diagram of the ZnO/WS_2/ZnO before the formation of QW HS. (d) Schematic energy band diagram of the ZnO/WS_2/ZnO at equilibrium. (The band diagrams are not drawn to the exact scale).

The relation between the contact potential difference and the work functions is given by, $eV_{CPD} = \Phi_t - \Phi_s$, where Φ_s is the work function of the sample. In **Fig. 6.10(a),** the average V_{CPD} over a uniform flake of 1L-WS_2 is ~86 mV. Thus, the work function of 1L-WS_2 is estimated to be ~ 4.9 eV. Similarly, for the ZnO thin film, the average V_{CPD} is ~ -176 mV (see **Fig. 6.10(b)**), which yields a work function of the order ~ 5.2 eV. The proposed band diagram based on the relative work functions of the 1L-WS_2 and ZnO is depicted in **Fig. 6.10(c)**[31-32]. The positions of the Fermi levels facilitate the specific band alignment on the formation of the junction at equilibrium, as shown in **Fig. 6.10(d)**. The presence of ZnO, which is a higher band gap semiconductor encapsulating the 1L-WS_2, leads to the electron as well as hole transfer to the 1L-WS_2. Thus, in addition to the conversion of neutral excitons to trions, in presence of surplus background electrons in the QW, we have observed the formation of biexcitons at higher excitation densities through the collision of excitons. These phenomena, in turn, alter the PL emission spectrum of the QW greatly. At low powers, the PL intensity of the QW is much higher than the 1L-WS_2 due to enhanced exciton recombination, facilitated by carrier transport from ZnO. The pronounced enhancement is also largely due to the essentially trion-dominated PL spectrum of the 1L-WS_2[3], at low powers. However, at higher powers, there is a higher possibility of the formation of biexcitons in the 1L-WS_2. Thus, the enhancement due to the QW effect induced by ZnO encapsulation is relatively low. Through investigation of power and temperature-dependent PL emission, we have observed not only PL enhancement due to the QW effect but also stark differences in the overall optical properties of the ZnO encapsulated 1L-WS_2. This is interesting for the applications in QW-based lasers and light-emitting diodes.

6.4. Conclusion

We have grown high-quality 1L-WS_2 films on sapphire, SiO_2, and quartz substrates by a CVD method. The as-grown 1L-WS_2 film shows a sharp PL emission at room temperature dominated by the neutral excitons. However, the low-temperature PL spectra are broader showing additional peaks originating from biexcitons. Interestingly, in the case of the transferred 1L-WS_2 film, there is a significant contribution from biexcitonic emission, even at room temperature. We further construct a quantum well structure using ZnO, which is a higher band gap semiconductor. Thus, we devise an effective way to manipulate the exciton and other quasiparticle densities in the system. The origin of the excitonic states and the overall spectral features of both systems are explored by careful examination of the power-dependent and temperature-dependent PL spectra. At low powers, the influx of charge carriers from ZnO to WS_2 aids in pronounced PL enhancement. Biexcitons are less likely to be formed at low excitation powers, through the collision of excitons, and also trion formation rate is comparatively low. However, at higher excitation powers, the possibility of trion formation dominates in ZnO/WS_2/ZnO, which hinders the enhancement of PL intensity. Additionally, the presence of trap states plays a vital role in the PL emission properties of the system. Higher the trap centers, the lesser the probability of biexciton formation. The preferential formation of trions or biexcitons in the QW system can either limit or facilitate PL enhancement, respectively. Thus, the fabrication of the ZnO/WS_2/ZnO QW allows us to successfully modulate the optical properties of monolayer WS_2. We believe this study would be highly relevant in enabling a deeper qualitative understanding of encapsulation-induced changes in the intrinsic properties of 1L-TMDs in quantum well-like systems.

References

1. Kim, M. S.; Yun, S. J.; Lee, Y.; Seo, C.; Han, G. H.; Kim, K. K.; Lee, Y. H.; Kim, J., Biexciton Emission from Edges and Grain Boundaries of Triangular Ws2 Monolayers. *ACS Nano* **2016**, *10*, 2399-2405.
2. Wang, K., et al., Interlayer Coupling in Twisted Wse2/Ws2 Bilayer Heterostructures Revealed by Optical Spectroscopy. *ACS Nano* **2016**, *10*, 6612-6622.
3. McCreary, K. M.; Hanbicki, A. T.; Singh, S.; Kawakami, R. K.; Jernigan, G. G.; Ishigami, M.; Ng, A.; Brintlinger, T. H.; Stroud, R. M.; Jonker, B. T., The Effect of Preparation Conditions on Raman and Photoluminescence of Monolayer Ws2. *Scientific Reports* **2016**, *6*, 35154.
4. Rawat, A.; Jena, N.; Dimple; De Sarkar, A., A Comprehensive Study on Carrier Mobility and Artificial Photosynthetic Properties in Group Vi B Transition Metal Dichalcogenide Monolayers. *Journal of Materials Chemistry A* **2018**, *6*, 8693-8704.
5. Loh, T. A. J.; Chua, D. H. C.; Wee, A. T. S., One-Step Synthesis of Few-Layer Ws2 by Pulsed Laser Deposition. *Scientific Reports* **2015**, *5*, 18116.
6. Lin, L.; Xu, Y.; Zhang, S.; Ross, I. M.; Ong, A. C. M.; Allwood, D. A., Fabrication of Luminescent Monolayered Tungsten Dichalcogenides Quantum Dots with Giant Spin-Valley Coupling. *ACS Nano* **2013**, *7*, 8214-8223.
7. McCreary, K. M.; Hanbicki, A. T.; Jernigan, G. G.; Culbertson, J. C.; Jonker, B. T., Synthesis of Large-Area Ws2 Monolayers with Exceptional Photoluminescence. *Scientific Reports* **2016**, *6*, 19159.
8. Perrozzi, F.; Emamjomeh, S. M.; Paolucci, V.; Taglieri, G.; Ottaviano, L.; Cantalini, C., Thermal Stability of Ws2 Flakes and Gas Sensing Properties of Ws2/Wo3 Composite to H2, Nh3 and No2. *Sensors and Actuators B: Chemical* **2017**, *243*, 812-822.
9. Gao, J., et al., Transition-Metal Substitution Doping in Synthetic Atomically Thin Semiconductors. *Advanced Materials* **2016**, *28*, 9735-9743.
10. Mawlong, L. P. L.; Bora, A.; Giri, P. K., Coupled Charge Transfer Dynamics and Photoluminescence Quenching in Monolayer Mos2 Decorated with Ws2 Quantum Dots. *Scientific Reports* **2019**, *9*, 19414.
11. Wu, W.; Zhang, Q.; Zhou, X.; Li, L.; Su, J.; Wang, F.; Zhai, T., Self-Powered Photovoltaic Photodetector Established on Lateral Monolayer Mos2-Ws2 Heterostructures. *Nano Energy* **2018**, *51*, 45-53.
12. Bindu, P.; Thomas, S., Estimation of Lattice Strain in Zno Nanoparticles: X-Ray Peak Profile Analysis. *Journal of Theoretical and Applied Physics* **2014**, *8*, 123-134.
13. Kim, H.; Lee, T.; Ko, H.; Kim, S. M.; Rho, H., Influence of Chemical Treatment on Strain and Charge Doping in Vertically Stacked Monolayer–Bilayer Mos2. *Applied Physics Letters* **2020**, *117*, 202104.
14. Berkdemir, A., et al., Identification of Individual and Few Layers of Ws2 Using Raman Spectroscopy. *Scientific Reports* **2013**, *3*, 1755.
15. Molas, M. R.; Nogajewski, K.; Potemski, M.; Babiński, A., Raman Scattering Excitation Spectroscopy of Monolayer Ws2. *Scientific Reports* **2017**, *7*, 5036.
16. Plechinger, G.; Nagler, P.; Kraus, J.; Paradiso, N.; Strunk, C.; Schüller, C.; Korn, T., Identification of Excitons, Trions and Biexcitons in Single-Layer Ws2. *physica status solidi (RRL) – Rapid Research Letters* **2015**, *9*, 457-461.
17. Su, L.; Yu, Y.; Cao, L.; Zhang, Y., Effects of Substrate Type and Material-Substrate Bonding on High-Temperature Behavior of Monolayer Ws2. *Nano Research* **2015**, *8*, 2686-2697.
18. Mitioglu, A. A.; Plochocka, P.; Jadczak, J. N.; Escoffier, W.; Rikken, G. L. J. A.; Kulyuk, L.; Maude, D. K., Optical Manipulation of the Exciton Charge State in Single-Layer Tungsten Disulfide. *Physical Review B* **2013**, *88*, 245403.
19. Feng, R.; Xu, S.; Liu, W.; Gao, P.; Zhang, J.; Tong, L., Local Modulation of Excitons and Trions in Monolayer Ws2 by Carbon Nanotubes. *Nano Research* **2020**, *13*, 1982-1987.

20. Zhu, B.; Chen, X.; Cui, X., Exciton Binding Energy of Monolayer Ws2. *Scientific Reports* **2015**, *5*, 9218.

21. Okada, M.; Miyauchi, Y.; Matsuda, K.; Taniguchi, T.; Watanabe, K.; Shinohara, H.; Kitaura, R., Observation of Biexcitonic Emission at Extremely Low Power Density in Tungsten Disulfide Atomic Layers Grown on Hexagonal Boron Nitride. *Scientific Reports* **2017**, *7*, 322.

22. Paradisanos, I.; Germanis, S.; Pelekanos, N. T.; Fotakis, C.; Kymakis, E.; Kioseoglou, G.; Stratakis, E., Room Temperature Observation of Biexcitons in Exfoliated Ws2 Monolayers. *Applied Physics Letters* **2017**, *110*, 193102.

23. Ye, Z.; Cao, T.; O'Brien, K.; Zhu, H.; Yin, X.; Wang, Y.; Louie, S. G.; Zhang, X., Probing Excitonic Dark States in Single-Layer Tungsten Disulphide. *Nature* **2014**, *513*, 214-218.

24. Kim, J. C.; Wake, D. R.; Wolfe, J. P., Thermodynamics of Biexcitons in a Gaas Quantum Well. *Physical Review B* **1994**, *50*, 15099-15107.

25. He, Z.; Xu, W.; Zhou, Y.; Wang, X.; Sheng, Y.; Rong, Y.; Guo, S.; Zhang, J.; Smith, J. M.; Warner, J. H., Biexciton Formation in Bilayer Tungsten Disulfide. *ACS Nano* **2016**, *10*, 2176-2183.

26. Upadhyay, B.; Thakur, D.; Pramanick, B.; Bhandari, S.; Balakrishnan, V.; Pal, S. K., Anomalous Emission Behavior of Excitons at Low Temperature in Monolayer Ws₂. *Journal of Physics D: Applied Physics* **2022**, *55*, 235105.

27. You, Y.; Zhang, X.-X.; Berkelbach, T. C.; Hybertsen, M. S.; Reichman, D. R.; Heinz, T. F., Observation of Biexcitons in Monolayer Wse2. *Nature Physics* **2015**, *11*, 477-481.

28. Lee, M.-J., et al., Measurement of Exciton and Trion Energies in Multistacked Hbn/Ws2 Coupled Quantum Wells for Resonant Tunneling Diodes. *ACS Nano* **2020**, *14*, 16114-16121.

29. Chernikov, A.; Berkelbach, T. C.; Hill, H. M.; Rigosi, A.; Li, Y.; Aslan, O. B.; Reichman, D. R.; Hybertsen, M. S.; Heinz, T. F., Exciton Binding Energy and Nonhydrogenic Rydberg Series in Monolayer WS2. *Physical Review Letters* **2014**, *113*, 076802.

30. Kajino, Y.; Arai, M.; Oto, K.; Yamada, Y., Dielectric Screening Effect on Exciton Resonance Energy in Monolayer Ws2 on Sio2/Si Substrate. *Journal of Physics: Conference Series* **2019**, *1220*, 012035.

31. Ma, J.; Amsalem, P.; Schultz, T.; Shin, D.; Xu, X.; Koch, N., Energy Level Alignment at the C60/Monolayer-Ws2 Interface on Insulating and Conductive Substrates. *Advanced Electronic Materials* **2021**, *7*, 2100425.

32. Hussain, B.; Aslam, A.; Khan, T. M.; Creighton, M.; Zohuri, B., Electron Affinity and Bandgap Optimization of Zinc Oxide for Improved Performance of Zno/Si Heterojunction Solar Cell Using Pc1d Simulations. *Electronics* **2019**, *8*, 238.

Chapter 7

Summary and Outlook

This chapter highlights the contributions of the present thesis and the new findings on the synthesis strategies of WS_2 quantum dots (QDs) and monolayer WS_2 films and their heterostructures with different materials like single-walled carbon nanotubes (SWCNT), plasmonic nanoparticles (NPs), other 2D materials like Bi_2O_2Se QDs, and high band-gap ZnO thin films and their applications in light emission and high-performance photodetection. The scope for future work is also discussed at the end.

7.1. Highlights of the Thesis

The dissertation presents the controlled growth protocols of monolayer WS_2 quantum dots (QDs) by chemical exfoliation and monolayer WS_2 film by chemical vapor deposition (CVD) method. For the QDs, we have achieved control over their size distribution by varying the centrifugation rates post exfoliation. On the other hand, for CVD, by controlling the various growth parameters such as the growth pressure, growth temperature, duration, and precursors, we have been able to obtain high-quality large-area monolayer WS_2 films over a variety of substrates (Chapter 2). Following the synthesis strategies, we have addressed the high photoluminescence (PL) quantum yield and the excitation-dependent emission of WS_2 QDs. We have also investigated the mechanism of the systematic quenching of the PL intensity of the QDs in presence of single-walled carbon nanotubes (SWCNTs) (Chapter 3). Further, we have fabricated a self-powered p-n heterojunction photodetector (PD) by using n-type WS_2 QDs and a p-type Si platform. By incorporating Au NPs in the system, we have developed a self-powered high-performance Si/Au/WS_2 Schottky PD with a highly suppressed dark current and fast photo-response (Chapter 4). Next, we synthesized highly luminescent monolayer WS_2 films using the CVD process and investigated the modulation of its PL simply by decorating them with non-van der Waals 2D Bi_2O_2Se QDs. An exhaustive analysis involving coupled charge transfer dynamics using the four-energy level model was employed to address the systematic PL quenching in the system and the n-type doping effect induced by charge transfer from the QDs to the 1L- WS_2 (Chapter 5). Finally, we constructed a ZnO/WS_2/ZnO quantum well (QW) by encapsulating the 1L-WS_2 film between

ZnO thin films. We studied the tuning of the PL emission of 1L-WS_2 when encapsulated by a higher bandgap ZnO and investigated the change in the exciton, biexciton, and trion dynamics using power-dependent and temperature-dependent PL measurements (Chapter 6).

The major contributions of the present thesis are summarized as follows:

A. Controlled Growth of Monolayer WS_2 quantum dots and film by Chemical Exfoliation and Chemical Vapor Deposition Method

Firstly, we have devised a synthesis protocol for highly luminescent monolayer and bilayer WS_2 quantum dots with controlled sizes using a straightforward chemical exfoliation technique followed by centrifugation. Spectroscopic tools such as UV-Visible-NIR absorption, Raman, and XPS analysis confirmed the growth of 2D QDs. Next, we have demonstrated the growth of triangular 1L-WS_2 flakes using the CVD technique at a relatively lower temperature ~750°C in a semi-confined growth system. The size of these 1L-WS_2 flakes was ~20 µm. By tuning the growth parameters such as carrier gas pressure, temperature, and duration, we were able to grow a larger area monolayer to bilayer WS_2. Finally, we have grown a large area of continuous 1L-WS_2 by using a NaCl-assisted CVD growth approach. The role of growth temperature, pressure, duration, precursors, and substrates is significant in the growth of highly crystalline 1L-WS_2. Moreover, controlling the vapor pressure locally using a one-end sealed quartz tube inside the system and the Na^+ ions from the NaCl ensure the growth of large-area and high-quality monolayer WS_2 on a variety of substrates. We have carried out systematic studies of the substrate-dependent Raman and PL spectra of the as-grown WS_2. The growth substrates have a significant impact on the PL line shape, peak position, and emission intensities. The sapphire substrates yield better quality 1L-WS_2 film in all aspects. Advancing the ability to grow continuous and defect-free monolayer WS_2 on at least 100 mm wafers is crucial to realize any applications for WS_2 as well as any other 2D materials. It can be realized in more high end sophisticated experimental setups such as the MOCVD.

B. Detailed Spectral Analysis of WS_2 Quantum dots and Study of Photoluminescence Quenching using Single-walled Carbon Nanotubes

We have demonstrated the optimized synthesis of ultra-small WS_2 QDs that exhibit a high PL quantum yield of ~15%, without any functionalization. The QDs have a high exciton binding energy and rich PL emission features. A detailed analysis reveals that the excitation wavelength-dependent broad PL emission results from different contributions from the excitonic transitions from the spin-orbit split valence band at the K, K´ point, and also from the defect states. The PL emission of WS_2 QDs is systematically quenched in the presence of single-walled carbon nanotubes (SWCNT). The quenching is pronounced in SWCNT with higher defect densities. XPS and Raman analyses support the formation of WS_2 QD/SWCNT complexes that lead to the overall improvement in the crystallinity of the SWCNTs, shown for the first time. The PL quenching is attributed to the formation of non-fluorescent ground state complexes, which leads to lesser availability of the highly fluorescent QDs in the system. The strong bonding between the WS_2 QDs and the SWCNTs allows charge transfer from the QDs to the SWCNTs, which is also partially responsible for the quenching. The results are insightful in understanding the interaction between WS_2 QD and SWCNTs and regulating the fluorescence intensity of WS_2 QDs, which is important for various applications in biomedical areas. *This work has been published in "J. Colloids & Interf. Sci., 2020, 561, 519."*

C. A High-Performance Si/Au/WS_2 QD-based Schottky Photodetector with Highly Suppressed Dark Current and Fast Photoresponse

We have fabricated a high-performance p-n junction photodetector (PD) by combining n-type WS_2 QDs with p-type Si platforms, for the first time. The I–V characteristics of PD confirm the formation of rectifying p-n heterojunction at the interface between the n-type WS_2 QDs and p-type Si. The hybrid Si/WS_2 QD PD acts as a self-powered photodetector and shows good photodetection performance. Furthermore, a Schottky Si/Au/WS_2 PD was fabricated using a p-Si substrate with a uniform array of Au NPs (average size ~6.7 nm) and the n-WS_2 QDs. The incorporation of Au NPs greatly improved I_{on}/I_{off} ratio (~1.3×10^5), by the suppression of the dark current by several orders of magnitude accompanied by an increase in the photocurrent. The Schottky PD exhibited a fast response with photocurrent rise/fall time of~4.4/43.5 μs. The device responsivity and detectivity were ~276.2 A/W and ~4.3×10^{13} Jones, respectively. The Au NPs serve as a carrier tunneling pathway and lead to the generation and transport of hot electrons for ultra-fast transport of photo-generated charge carriers. This PD can be operated without any external bias. Our findings pave way for designing 2D TMD and plasmonic NP-based heterojunction devices with superior performances for state-of-the-art optoelectronic applications. *This work has been published in "ACS Appl. Electron. Mater. 2021, 3, 11, 4891–4904."*

D. Photoluminescence Modulation and Charge Transfer Dynamics in Monolayer WS_2 Decorated with Bi_2O_2Se Quantum Dots

We have demonstrated the modulation in the light emission of the CVD grown 1L-WS_2 by decoration with non-van der Waals 2D semiconducting Bi_2O_2Se QDs. A systematic quenching of the PL intensity of 1L-WS_2 was observed by varying the concentration of the Bi_2O_2Se QDs. Kelvin Probe Force Microscopy (KPFM) was employed to estimate the work function of the as-grown 1L-WS_2. On being decorated with the Bi_2O_2Se QDs, the work function of 1L-WS_2 decreased, which provided direct evidence of charge transfer from the QD to the 1L-WS_2. A thorough analysis using a four-energy level model was carried out to explain the decrease in the PL intensity of the 1L-WS_2 and the accompanied redshift with an increase in the concentration of the Bi_2O_2Se QDs. The role of defects was also established in the doping density-dependent recombination dynamics of excitons in the system through quantitative analysis. The quenching of the PL emission is due to the conversion of neutral excitons to trions owing to the surplus electrons in the system. The doped electron density is as high as $\Delta n_e \sim 6.6 \times 10^{13}$ cm^{-2}, which indicates high n-type doping in the 1L-WS_2. Thus, controlled doping of 1L-WS_2 was achieved simply by varying the concentration of the Bi_2O_2Se QDs, for the first time. Our results potentially facilitate further research in understanding the fundamentals of light-matter interactions in 2D heterostructure systems and further, pave way for various electronic and optoelectronic applications. *This work has been published in "J. Phys. Chem. C 2022, 126, 30, 12623–12634."*

E. Photoluminescence Modulation in a Quantum Well of Monolayer WS_2 sandwiched between ZnO layers

Herein, we have grown high-quality 1L-WS_2 films on a variety of substrates by the CVD method. We studied the room temperature Raman and PL emission spectra of as-grown and transferred 1L-WS_2, which are largely affected by factors such as strain and doping. As grown 1L-WS_2 shows emission from biexcitons, at low temperatures. Interestingly, the PL spectra of transferred (unstrained) 1L-WS_2 consist of the signature of biexcitons even at room temperature. Subsequently, to tune the PL emission of 1L-WS_2, we constructed a quantum well (QW) structure using ZnO layers, which is a higher band gap semiconductor. The power-dependent and temperature-dependent PL emission characteristics of the ZnO/WS_2/ZnO QW and unstrained 1L-WS_2 film were carefully examined. The biexciton emission becomes dominant at low temperatures and high laser powers for 1L-WS_2. At low excitation powers, the influx of charge carriers from ZnO to WS_2 aids in a ~10 folds PL enhancement due to the QW effect. Biexcitons are less likely to be formed through the collision of excitons at low powers, and also the trion formation rate is comparatively low. At higher excitation powers, however, the possibility of the neutral exciton to trion formation dominates in ZnO/WS_2/ZnO, which hinders the enhancement of PL intensity. Therefore, through the fabrication of the ZnO/WS_2/ZnO QW, we were able to successfully tune the optical properties of 1L-WS_2 by manipulating the exciton and electron density of the system, for the first time. The temperature-dependent studies enabled interesting insights into the QW system. The results offer a detailed insight into the carrier dynamics in 1L-TMDs on encapsulation with higher band gap semiconductors, which will be beneficial in the development of future optoelectronic and photonic devices.

7.2. Scope for Future Work

In the present thesis, we have achieved a controlled synthesis of ultra-small and highly fluorescent WS_2 QDs by chemical exfoliation and highly crystalline large-area monolayer WS_2 by CVD technique. Additionally, we have presented thorough investigative studies on the fabrication of heterostructures of WS_2 QDs with SWCNTs and plasmonic Au NPs and of 1L- WS_2 with non-van der Waals Bi_2O_2Se QDs and ZnO thin film for applications in photoluminescence and photodetection. There is enormous scope to extend the present work to understand the fundamentals of light-matter interactions in 2D TMD systems and in turn, utilize them for a broad range of applications:

1. WS_2 QDs and monolayer WS_2 can be combined to form heterostructures with several other 2D materials, e.g., $MoSe_2$, WSe_2, h-BN, Bi_2O_2Se, $PdSe_2$, MXenes, and etc. to enable a wide range of device applications.
2. The monolayer and bilayer WS_2 nanosheets (a byproduct of chemical exfoliation), given their excellent absorption in the UV-visible region and large surface-to-volume ratio serve as a promising system to form hybrid structures with new-age 2D semiconductors for photoelectrochemical hydrogen production and photodetection.

3. Further investigative studies on 0D-2D WS_2 and other TMDs and their heterostructures to acquire a deeper understanding of charge dynamics and carrier trapping for future improvement in the optical and electrical properties
4. In-situ CVD growth of secondary and ternary TMD-based heterostructures for studies on the fundamental aspects as well as applications in different areas.
5. The stability of 1L-WS_2 and easy transfer procedures allow the fabrication of flexible heterojunction-based optoelectronic and electronic devices.
6. ZnO/WS_2/ZnO ternary heterostructure exhibited interesting PL emission characteristics owing to the quantum well effect. Thus, further investigation of similar ternary systems with other high band gap semiconductors can be promising for a fundamental understanding of multibody quasi-states of 1L-WS_2 and other TMDs and the development of next-generation photonic devices.